The Central Drift Chamber for the DØ experiment: Design, Construction and Test

E740

A Dissertation Presented

by

Ties Behnke

to

The Graduate School

in Partial Fulfillment of the Requirements

for the Degree of

Doctor in Philosophy

in

Physics

State University of New York

at

Stony Brook

August 1989

State University of New York
at Stony Brook

The Graduate School

TIES BEHNKE

We, the thesis committee for the above candidate for the Ph.D. degree, hereby recommend acceptance of the thesis.

Guido Finocchiaro

Advisor
Guido Finocchiaro
Professor
Department of Physics

Paul D. Grannis

Paul Grannis
Professor
Department of Physics

George Sterman

George Sterman
Professor
Department of Physics

Sam Aronson

Sam Aronson
Associate Director of the Physics Department
Brookhaven National Laboratory

This thesis is accepted by the Graduate School.

Graduate School

Abstract of the Dissertation

The Central Drift Chamber for the DØ experiment:

Design, Construction and Test

by

Ties Behnke

Doctor of Philosophy

in

Physics

State University of New York at Stony Brook

1989

A cylindrical drift chamber has been designed and built at the State University of New York at Stony Brook. This chamber is to be installed in the DØ detector which is being completed at the Fermi National Accelerator. In this dissertation the design, construction and testing of this chamber are described. The characteristic features of this chamber are cells formed by solid walls and a modular structure. Much discussion is given to the performance of and results from a chamber made from three final modules which was installed in the DØ interaction region during the 1988/1989 collider run. Using this chamber proton anti-proton interactions were measured at the DØ interaction point.

Table of contents

List of Figures

Acknowledgments

The design, construction and testing of the DØ central drift chamber involved many different people from Stony Brook and other institutions participating in the DØ experiment. The work presented here would not have been possible without the guidance and support from Prof. Guido Finocchiaro. The chamber would not have been built without the staff of the physics department, in particular Vito Manzella and Jack Steffens. It would still be a drawing if not for the department machine shop. Last but not least many thanks go to every member of the High Energy group.

1. Introduction

During the last two decades detectors in High energy physics became larger and larger. Increasing energy required deeper and larger detectors in order to be able to measure the interesting phenomena. The sucess of the standard model spured colliders of higher and higher energy with increasingly complex detectors.

This work describes the construction of a part of one of these detectors, the DØ detector at the Fermilab proton anti proton collider, the central drift chamber. Design, test and construction of this device spanned a period of over six years. The work was performed at the State University of New York at Stony Brook.

After discussing the general ideas of designing a drift chamber and the underlying physical principles, the implementation chosen for the DØ chamber is discussed. The prcess employed in constructing the chamber is described in some detail. The last part of this work reports on different tests performed using several generations of test chambers. It ends by describing results obtained from a recent run taken at the Fermilab Tevatron using a chamber identical to the final one but smaller mounted inside the DØ interaction point.

2. The DØ detector

The DØ detector is a general purpose 4π detector currently being constructed at the Fermi National Accelerator Laboratory in Batavia, Illinois. It will be the second large detector operated on the Tevatron $p - \bar{p}$ collider. About 180 physicists from the United states, France and the Soviet Union are collaborating on the task of construction and operation of this experiment.

DØ was formally started in the summer of 1983 as a counterpart/ complement to the other Tevatron detector, the CDF experiment. CDF at this time was already far advanced in design and under way in construction. The late start of DØ brought with it the major drawback, that the early physics runs of the Tevatron were missed, but it gave the collaboration the chance to start the design of a large detector for a $p - \bar{p}$ machine using the experiences of both CERN (UA1 and UA2) and the local competitor CDF. DØ is a detector of "the second generation". Techniques which were speculative during the UA1/UA2 and CDF design periods were well established and had proven their merit at the time when DØ was being designed. For example missing energy was accepted as the method of choice in finding and measuring many phenomena at hadron colliders- before the CERN UA* experiments this was a topic, whose importance has not been fully realized. DØ therefore could concentrate on designing a detector which was optimized for this type of physics.

DØ will address two classes of questions: It will measure known phenomena, improving the precision or confirming other measurements. The goal of this class of experiments may be summarized under the heading of tests of the standard model. Most prominently this includes precision measurements of the W-mass and width compared to the Z-mass and width. The other topic of interest to DØ is much less well defined. The new energy range of 2 TeV opens the possibility for new phenomena not embedded in a well established theory. Here the detector has to be flexible rather than specific so that it is sensitive to the broadest possible range of questions.

In the following chapter some of the physics topics relevant at the DØ experiment will be discussed briefly. Then a general description of the detector will be given and the role of the central drift chamber in the whole detector will be described.

2.1. Physics at DØ

During the last decade the so called Standard Model has come to be accepted as the best theory of weak, electro-magnetic and strong interaction. In the Glashow-Weinberg-Salaam model the unification of weak and electromagnetic forces has been

achieved. The discovery of the W and Z intermediate vector bosons in CERN in 1982 provided a spectacular confirmation of this theory. However a number of questions remain unanswered even in this "ideal" theory. In order to provide masses to the gauge bosons in the theory, "artificial" techniques have to be employed. The most frequently used one is the introduction of a massive scalar particle, the Higgs Boson, which through a process called spontaneous symmetry breaking provides a mass to the W and Z Bosons. However besides the fact that no experimental evidence exists for the Higgs no theoretical evidence exists either besides the statement "it works". Equally unsatisfactorily is the existence of some 28 free parameters in the theory which can not be calculated but have to be put in by hand. Particularly bothersome are the sizes of the different mass scales observed in nature. The electroweak theory happens below the 100 GeV threshold, with the W and the Z masses the heaviest observed objects so far. This has to be compared to a grand unification mass of the order of $10^{15} GeV/c^2$ for the simplest Grand Unification Models, or the Planck Mass ($10^{19} GeV/c^2$), if gravity is to be included. This tremendous step in energy requires that the different parameters which set the masses e.g. of the coupling vector bosons, have to be defined to an incredible accuracy of the order of 15 or 19 decimal places respectively. While not impossible it is not an appealing picture of nature.

Many models of unification exist. The simplest one- including only the electroweak and the strong interaction and combining them in a SU(5) theory are more or less ruled out by experiment. More complicated ones usually include gravity. The most commonly found feature of this class of theories is that they include a new symmetry, the so called supersymmetry. In supersymmetric theories fermions and bosons are treated on an exactly equal footing. This means in particular that every fermionic particle has a bosonic partner, and vice versa. Since supersymmetry is not readily observed in nature it has to be a broken symmetry. It can be shown that it is easier to keep the theory consistent with present experimental results if the mass spectrum of the supersymmetric particles lie in the 1 TeV range. Obviously this opens a whole new challenge for the experimenter in trying to find these new states.

More recently string theories have drawn a lot of attention as a possible candidate of the "final" unification of all forces. From the experimenters point of view string theories are not very attractive however. So far no unique description exists which would allow it to come down from the intrinsic string theory mass scale, which is of the order of the Planck mass, to something accessible by today's, or even tomorrow's, experiments. Additionally string theories reside naturally in more than three dimensions. Again no unique way has been found to compactify or otherwise break down the additional dimensions to come to a description of the observed world in four dimensions. At this point no experimental predictions exist which would show

the presence of string theories. Everything predicted by these theories in their low energy forms can be easily obtained by other non string models. An experimental confirmation of the existence or nonexistence of string theories seems very difficult, if not impossible. However in the opposite direction the discovery of some new phenomena at high energy might provide glimpses at which way to choose for a further unification of forces.

A very important experimental question at this time is the validity and the limits of the standard model. Measuring the W more precisely will allow a more stringent test of the model because higher order corrections will have to be taken into account. Finding the top quark or the Higgs would provide valuable information about the structure of the model.

In particular the following questions will be addressed by the DØ detector: Low p_t processes (minimum bias physics)

- mini jets
- multiplicity at high $\sqrt{s}$

Precision measurement of the W/Z properties

- mass difference
- decay widths
- production mechanism
- rare decays
- decay asymmetries

Test of QCD at very large q^2

- jet topological cross section
- compositeness searches
- direct photon study

Searches for new states, extensions of the standard model

- new families
- Higgs Sector
- heavy Leptons
- new quarks (including the top)
- additional gauge bosons

New phenomena at large q^2

- supersymmetry
- technicolor

- strings???
- ...

Many of the phenomena listed above share signatures which are principally similar. These are the measurement of missing transverse energy in the event, the measurements of an isolated electron and the measurement of muons. Missing transverse energy is used to induce and measure the role of non interacting neutral particles in the event. For "standard" topics this will mean the participation of a neutrino, for more exotic processes this might be a supersymmetric particle. These signatures are important because they allow to separate semileptonic decay modes of heavy particles from the QCD background of the $p - \bar{p}$ interaction. Transverse energy as opposed to total energy has to be used because some undetermined amount of the energy is flowing down the beam pipes and escapes the detector unseen. Making the detector as hermetic as possible will help increase the accuracy to which the transverse energy can be measured. Increasing the segmentation of the device will also help since it will be possible to measure the flow of energy in the detector more precisely.

Leptons can be equally important in pinpointing interesting reactions. The decay of a heavy quark e.g. into a lighter quark and a lepton/neutrino pair will produce a hadronic jet on one side of the event, a lepton and missing energy. Ideally the detector should be able to identify any lepton, even if it is surrounded by other hadronic energy, and to measure its energy. Practically this can be done only for muons not for electrons.

This summarizes the main requirements for the detector:

Hermeticity: The sensitive part of the detector should cover as large a fraction of the solid angle as possible. In order for the coverage to be useful no cracks or hot spots should exist within the covered region. The segmentation of the calorimeter should be fine both in depth and in the transverse direction.

Lepton identification: The detector should be able to identify and measure electrons and muons as precisely as possible.

A detailed monte carlo study has been performed by R. Raja at Fermilab to explore the performance of the DØ detector for W/Z physics [1]. Fig. [1] shows some of the results. The top plot shows the highest top quark possible as a function of total integrated Luminosity. The two lower plots explore two different scenarios, using the DØ detector. In the middle plot a total of $10pb^{-1}$ of data have been accumulated. The W-mass can be measured using the DØ detector to 0.25 GeV. A precise measurement can be used to put limits on the mass of a top.

In the bottom plot it is assumed that the W-mass has been measured to 0.125 GeV and that the top has been discovered. If this is the case the precise measurement

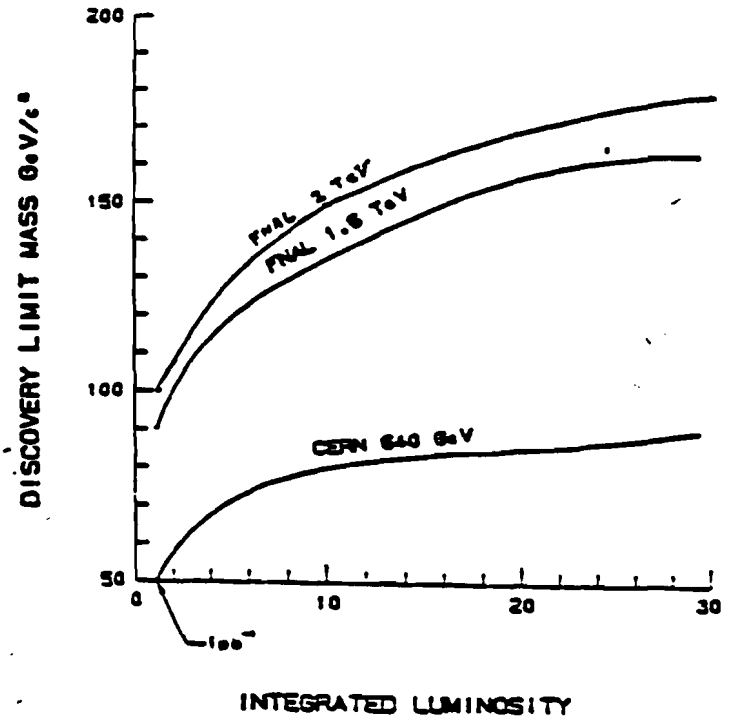

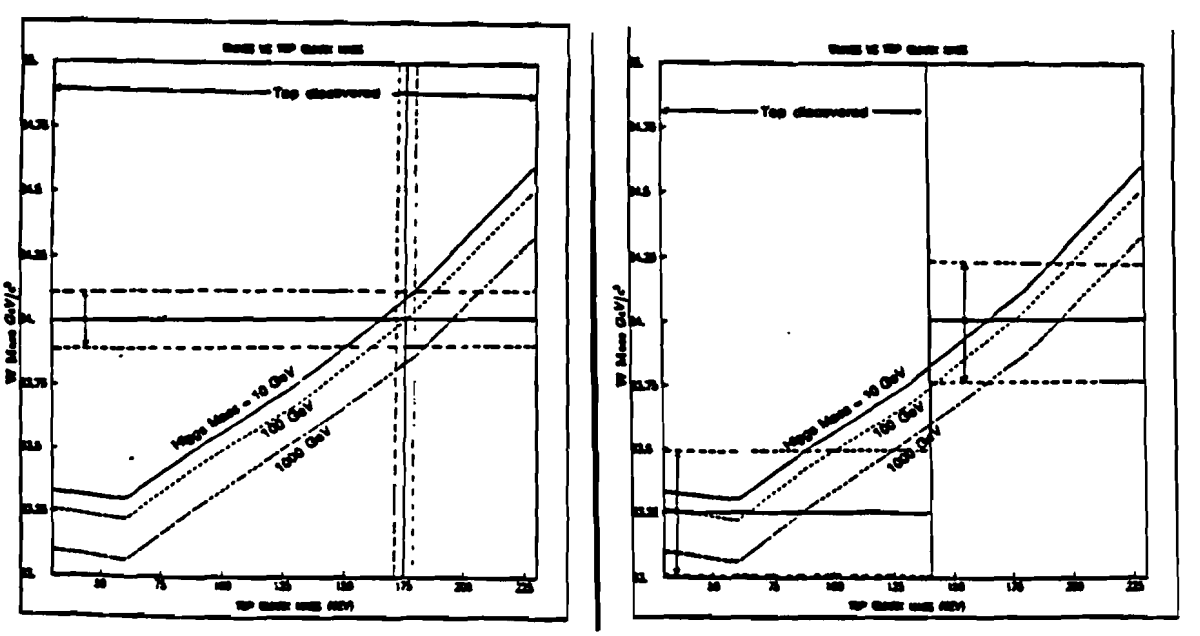

Figure 1 . Discovery limits for the top quark for as a function of integrated luminosity (top plot). Other plots: Implication of the w-mass on the top mass. Left bottom plot: $10pb^{-1}$ scenario at the Tevatron. Right bottom plot: $100pb^{-1}$ scenario.

	$\delta M_W(MeV)$
New heavy quark pair	
Large splitting	300
degenerate	-41
Heavy Lepton pair	
Large splitting, $m_\nu = 0$	300
Degenerate	-14
Heavy squark pair, slepton pair	
Large splitting	100
Degenerate	0
Winos	
$m_{3/2} << 100 GeV/c^2$	100
$m_{3/2} >> 100 GeV/c^2$	< 10
Technicolor	
$SU_8 x SU_8$	-500
O_{16}	-500

Table 1
Shift in the W mass due to effects beyond the standard model.

of both quantities can be used to indirectly set a limit on the Higgs mass as indicated in the plot. In this scenarios of course it was assumed that the standard model in its minimal formulation is correct. The introduction of for example more than one Higgs would change the situation.

To illustrate the importance of a precise knowledge of the W-mass table 1. lists a few implications of shifting the W-mass.

2.2. Description of the DØ detector

In order to match the above requirements with an actual detector design, the DØ detector was split into three very different and distinct subdetectors: the inner detector, the calorimetry and the muon system. The inner detector measures charged tracks and identifies electrons, the calorimeter measures the energy of all particles and the muon system identifies the muons in the event and determines their energy. DØ opted for an inner detector without a magnetic field. The magnetic field is usually used to measure the momentum of charged tracks. Omitting the field eliminates this possibility, but it allows a very compact inner detector with relaxed require-

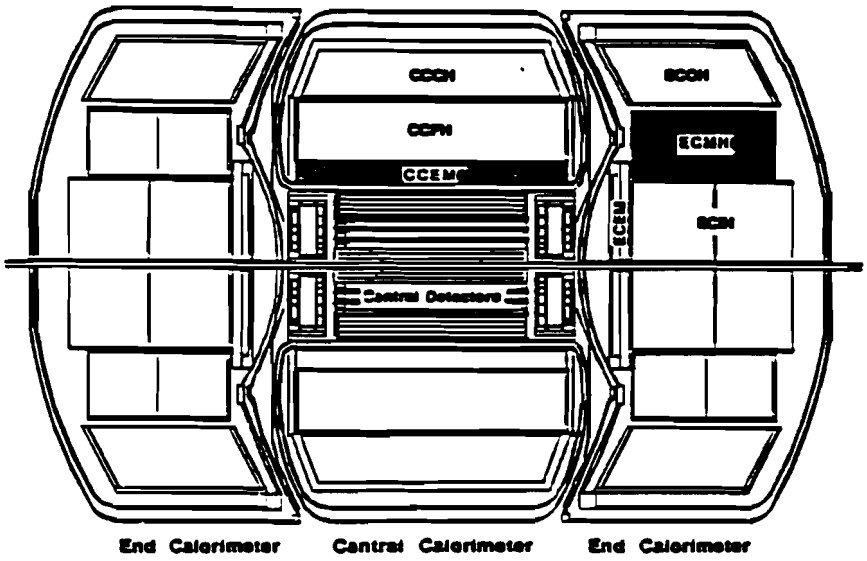

Figure 2 . Cross section through the calorimeter showing the central and the forward parts

ments about position resolution. A compact inner detector in turn allows for a larger calorimeter without driving costs to astronomical heights. Since at high energies calorimeters provide equal or better energy measurements than magnetic fields it was felt that the advantages of a very good and deep calorimeter are larger than the one of a magnetic field in the center of the detector. To partially compensate for the loss in particle ID a transition radiation detector was included in the inner detector. The transition radiation detector is able to distinguish an electron from other (heavier) charged particles. It detects radiation which is emitted if a highly relativistic particle traverses a boundary between two materials with different dielectric constants [2]. This device allows the identification of electrons in a crowded and noisy event with reasonably good accuracy.

2.2.1. The calorimeter

The DØ calorimeter is the central part of the whole detector. It consists of three main components, the central calorimeter, a forward and a backward calorimeter. Each is layered into three subparts, an electromagnetic part, a fine hadronic part and a coarse hadronic part. Fig. [2] shows a cross section of the calorimeter. The

electromagnetic section of the calorimeter covers the first 20.5 radiation length. This and the following fine hadronic section are Uranium liquid Argon calorimeter. The last section, the coarse hadronic one, is made from copper plates and is mostly meant to serve as a leakage calorimeter to confine the tails of high energy hadronic showers. The following table summarizes the data for the central calorimeter (a more detailed list can be found in [3]:

Module	λ_0	X_0	Segmentation name	$\Delta\eta$	$\Delta\Phi$	Absorber thickness	Sampling gap
CCEM	0.76	20.5	EMI	0.1	0.1	3 mm U	2*2.3 mm LAr
			EMII	0.1	0.1		
			EMIII	0.05	0.05		
			EMIV	0.1	0.1		
CCFH	4.3	96.0	FHI	0.1	0.1	6 mm U	2*2.3 mm LAr
			FHII	0.1	0.1		
			FHIII	0.1	0.1		
			FHIV	0.1	0.1		
CCCH	3.17	32.9	CHI	0.1	0.1	46.5 mm Cu	2*2.3 mm LAr

Table 1
Main parameter of the central calorimeter. X_0 means radiation length, λ_0 interaction length. For each part of the calorimeter the different segments in depth are shown.

A number of tests performed using prototypes of the different calorimeter modules have established the performance. The following list summarizes the results.

	CCEM	ECMH
linear response	$\leq 1/2\%$	$< 2\%$
energy resolution	$\approx \frac{15\%}{\sqrt{E}}$	$\approx \frac{21\%}{\sqrt{E}}$ for e^-
		$\approx \frac{48\%}{\sqrt{E}}$ for π^-
e/h ratio	$\langle e/h \rangle$	$= 1.04 \pm 0.03$

Table 2 lists the geometric data for the different calorimeters in the DØ detector.

Fig. [3] shows the result of a monte carlo analysis studying how often a simple 2-jet event will be mismeasured to be an event with missing energy. The missing energy in this plot is measured by a variable introduced by the UA1 collaboration [4] :

$$x = \frac{(p_t^{miss})^2}{0.5 * |E_t} \qquad (2-1)$$

	CCEM	CCFH	CCCH
Rapidity interval	-1.2 to 1.2	-1.0 to 1.0	-0.6 to 0.6
Inner Radius /cm	84.5	106.3	171.4
Outer Radius /cm	103.9	165.7	218.7
Absorber	U	U	Cu
Active Medium	LAr	LAr	LAr
# of modules in Φ	32	16	16
Minimum ionizing particle signal/tower(MeV)	157	685	178

Table 2
Partial specifications of the DØ central calorimeter. CCEM = central calorimeter electromagnetic section, CCFH= central calorimeter fine hadronic section, CCCH= central calorimeter coarse hadronic section.

	ECEM	ECIH	ECMH	ECOH
Rapidity interval	1.55 to 3.8	1.5 to 5.2	1.1 to 2.0	0.64 to 1.48
Inner Radius /cm	4.7	3.9	87.63	161.8
Outer Radius /cm	105.2	86.4	160.5	226.1
Absorber	U	Cu	Cu	Cu
Active Medium	LAr	LAr	LAr	LAr
Minimum ionizing particle signal/tower(MeV)	?	1859	1700	1070

Table 3
Partial specifications of the endcap DØ calorimeter. ECEM = endcap electromagnetic section, ECIH = endcap inner hadronic section, ECMH = endcap middle hadronic section. ECOH = endcap outer hadronic section.

For comparison the equivalent curve for the UA1 experiment is also drawn. Clearly DØ can expect to do considerably better than UA1. This is a result of the better resolution of the calorimeter.

2.2.2. The muon system

In order to be able to identify and measure muons as good as possible, a sophisticated muon system is being installed in DØ. It consists of a large Iron Toroid surrounding the whole detector which is magnetized to a field of approximately 2 T. In front and behind the toroid 3 layers of drift tubes are mounted which will measure the track of muons before and after the iron. This will allow a measurement of the moment of the particle by determining the bending angle. Muon chambers cover the solid angle down to 11° in Θ. A special small angle muon spectrometer (SAMUS) is inserted in the hole below 11° to extend the coverage down to the beam pipe.

The main part of the muon system is made from drift tubes. Vernier pads give the z-readout. Three layers of cells are combined into large planar chamber arrays. 1 set

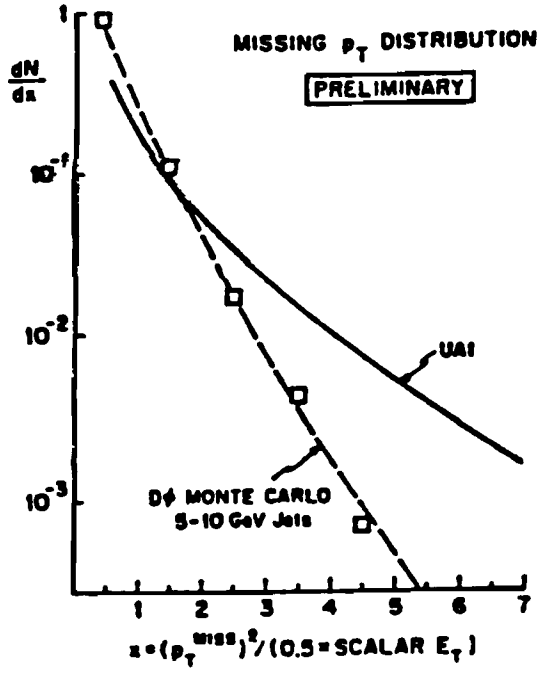

Figure 3 . Monte Carlo simulation of the fraction of 2-jet events mismeasured to have a missing transverse energy $x = (p_t^{miss})^2/0.5 * \sum E_t$.

of these drift tubes is mounted in front of the toroid, 2 spaced apart 1 m are mounted behind it. This way the bend and the exit direction of the muon can be measured. The entry direction can be determined by using information from the central drift chamber. Typical performance data from tests are:
resolution in drift $\approx 200\mu m$
resolution in $z \approx 3mm$
momentum resolution of the set of three chambers $\frac{\Delta p}{p} \approx 18\%, p \leq 300GeV$

2.2.3. The central detector

Fig. [4] shows a cross sectional view of the central detector. It has two distinct components: Drift chambers and a transition radiation detector. The later is sandwiched between two sets of drift chambers, the vertex chamber close to the beam pipe and the central drift chamber at the outside. The transition radiation detector allows the discrimination of electrons from other particles. For a detailed discussion on the functioning of transition radiation detectors see [4]. In [5] the special DØ implementation of this detector is described in detail. The important result is that

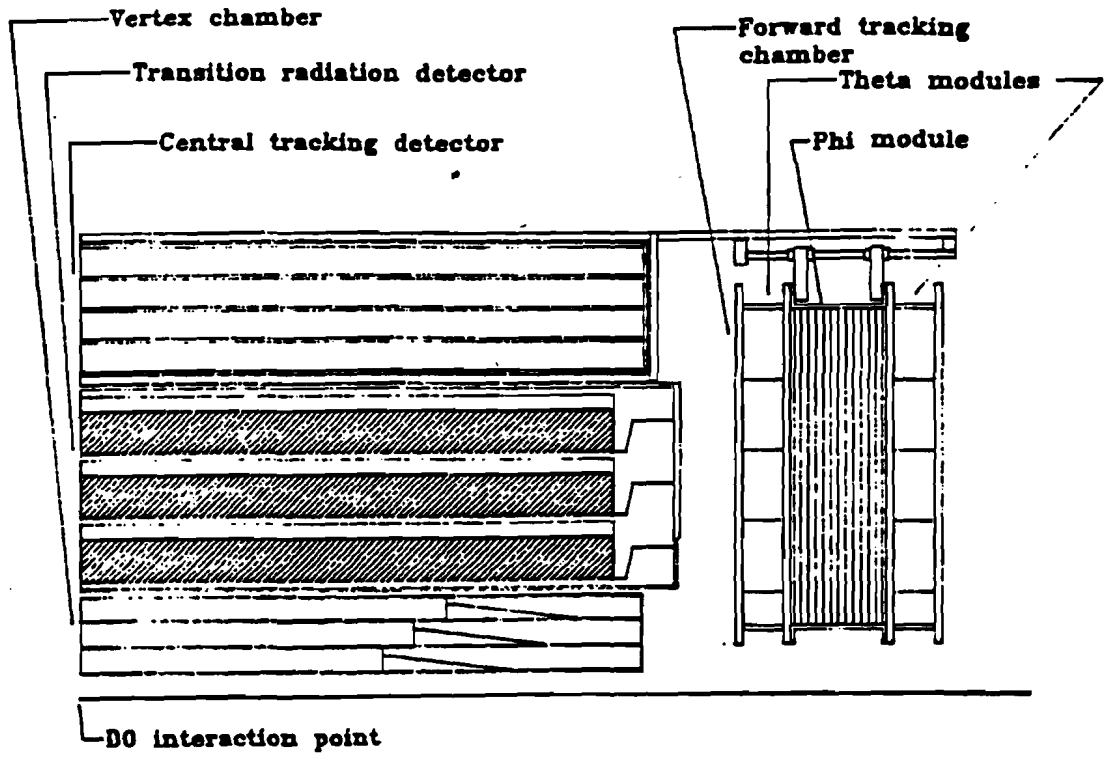

Figure 4 . Crossectional view of the central detector, including the forward drift chambers. One quarter of the whole detector is shown.

in tests a pion rejection at a 10% electron inefficiency of better than 50 has been achieved. This will greatly help in the identification of electrons in events, in particular of electron close to jets, where the calorimeter is no longer able to make a clear distinction.

The innermost part of the central detector is the Vertex Chamber. It is a high precision jet chamber like drift chamber. Its main purpose is the precise measurement of tracks close to the interaction point in order to be able to reconstruct vertices. The final goal of this would be to identify multiple interactions and secondary decays by measuring secondary vertices. To help in the identification of electrons in the event the chamber will also be used to veto "fake" electrons, which give a signal in the TRD, but which are really converted photons, therefore leaving no track in the Vertex chamber. The main performance data achieved with a test chamber in a fixed target test beam are listed below:

resolution	$50\mu m$ at 8 mm drift
2 track resolution	$700\mu m$ at 90 % efficiency

A detailed description of this chamber and its performance can be found in [6].

The forward and backward drift chambers cover the rapidity range below approximately $\eta = 1$. Three layers of cells are arranged in z, with wires in two cells running tangentially to a circle around the beam, in the middle module radially out from the beamline. Characteristics and performance of these chambers are very similar to the central drift chamber and will not be discussed here in detail. For a description of the mechanics of these chambers see [7].

Of most interest in this work is the central drift chamber. The central drift chamber covers the rapidity range from -1 to 1 and the radial range from 51.8 cm to 71.9 cm. It has two main purposes in the detector. The chamber should measure all charged tracks in space as accurately as possible in order to help in the reconstruction of the event and in the understanding of the event topology. It should help the TRD in distinguishing overlapping electron pairs from conversions or π_0 decays from single "real" electrons.

Since there is no magnetic field in the central region tracks are straight as they pass through the chamber. This greatly simplifies the task of reconstructing tracks. Since no momentum has to be measured the requirement on the resolution of the chamber can be relaxed. Events generally will look cleaner since low momentum tracks will not curl up and produce many space points. On the other hand any track will look straight, making it difficult to decide which one is a real track and which on is some low energy background radiation. Overlapping tracks will remain overlapping for the whole pass through the chamber making their recognition more difficult.

3. General Design of the Central Drift Chamber

Starting from the physics topics outlined in the last chapter and the role of the central drift chamber in this scenario a set of basic design parameters will be presented in this section. It should be noted that any design of a complicated object like a large drift chamber is a compromise between many factors. Besides the question whether a chosen design value will deliver the optimal performance possible, very often questions of practicability and cost have to be taken into account.

The central drift chamber in DØ is constrained by a number of factors. It has to fit into a small physical space, limited on one side by the TRD, on the other side by the calorimeter. It has to be as light and transparent as possible, while still being able to detect charged particles with a high efficiency. There is little space for electronics, cables or other peripheral devices.

On the other hand as much information as possible is to be extracted from this limited space. A number of basically different designs for drift chambers exist. The most common one at collider experiments is a chamber where all the field forming and all the electrodes are made from wires. Examples for this type of chamber are the SLD chamber [8]. These chambers are fairly easy to built and offer good mechanical accuracies. However in a tight space as given for the DØ chamber they have some drawbacks. Neighbour cells need to be separated from each other electrostatically. If only wires are forming the cells a fairly large distance between cells is needed for efficient separation. The other approach is to use closed cells, with solid walls separating cells. This is the basic design chosen for the DØ chamber. Solid walls allow to have less dead space between neighbour cells, because an efficient electric separation of the cells is guaranteed. It is now possible to use cells which are staggered in Φ for different layers.

The other basic design question to be resolved is the method used to determine the z-coordinate in the chamber. Wires strung at an angle to the beam direction alternating with wires strung along the beam are one possible approach (stereo layers). Again though the same problem appears. In order to decouple the stereo and the normal layers a large space is needed between them. In the DØ case this would mean the loss of a large part of the available room, and is therefore unacceptable. The method chosen for DØ is the use of delay lines for the z-coordinate. Delay lines are long coils which are mounted along a sense wire. A signal arriving on the sense wire will induce a signal on the delay line. This signal will propagate down the line towards both sides. By measuring the time at both ends a determination of the z-coordinate is possible. A more detailed discussion of the principle of delay lines will follow in the

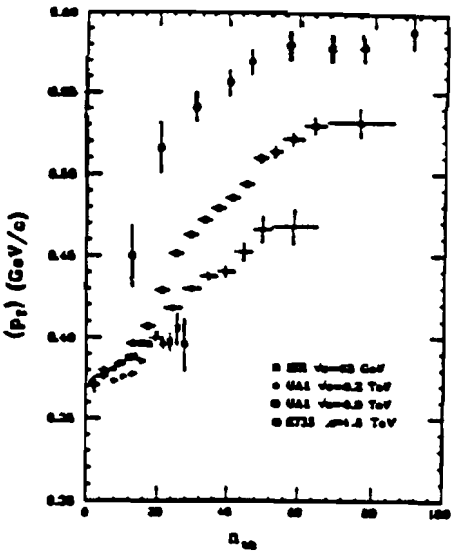

Figure 5 . Average multiplicity of charged tracks as a function of the average transverse momentum of the tracks

chapter on delay lines. A chamber with solid walls is ideally suited for delay lines. because the walls offer convenient surfaces on which to support the lines.

The requirements for the chamber were outlined in the last section. The absence of a need for extreme high precision allows the use of fairly large drift distances. With a nominal time between beam crossings of $3.5\mu s$ at 6 bunch operation and an assumed drift velocity of $40\mu m/ns$ this translates into drift gaps slightly more than 7 cm for $2.0\mu s$ maximum drift time. This allows about $1\mu s$ of total delay time on the z- read out elements. Taking this time and the radius of the chamber as about 60 cm 32 chambers around the circumference come closest to this requirement. This makes sense also in view of the average multiplicity of minimum bias events as observed e.g. by CDF at 1.8 TeV (see Fig. [5]). For interesting events a charged particle multiplicities around 30 is observed in a rapidity range $|\eta| \leq 1$. This would translate into an average occupancy of each cell in the chamber of 1 track per event. Of course for interesting events this can be locally much higher, in particular with the presence of jets many tracks will concentrate in a few cells. However it shows that on the average the chamber is run far below critical pile up conditions.

With drifts of the order of a few cm and normal drift gases, resolutions around

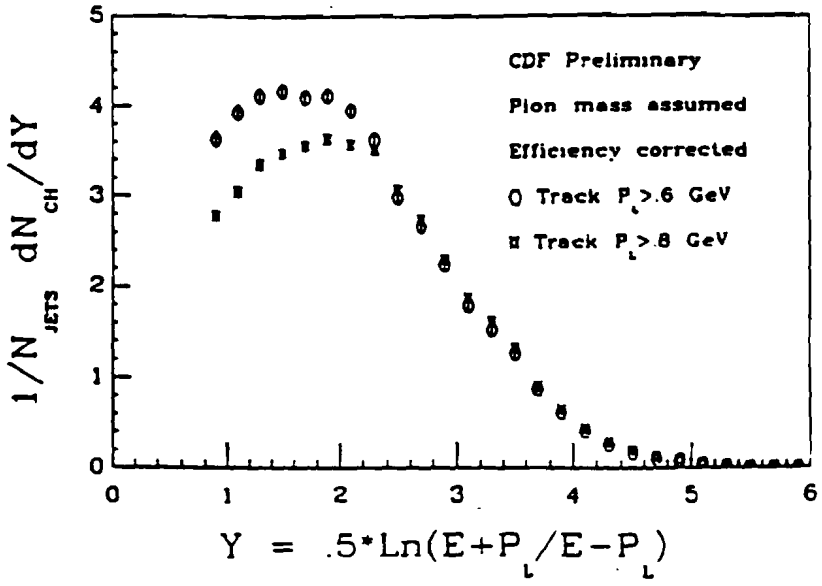

Figure 6 . Rapidity distribution for tracks participating in a jet, relative to the jet axis. CDF preliminary

$200\mu m$ are routinely obtained. In order to maximize the double pulse separation the signals on the sense wires should be digitized. Double pulse separation is of particular importance for jet physics, were many tracks are found in a small cone. Fig. 6 shows a plot of the rapidity distribution for tracks participating in a jet [9]. For a rapidity interval of 1 the number of charged tracks is around 4 for a longitudinal momentum cut of 600 MeV. Assuming the worst case scenario that all tracks are detected in one cell of the CDC, the average angular separation between the tracks is 2.25°. At an average distance from the beam pipe of 55cm this translates into a distance between tracks in drift of 2.2cm. A goal of a double track resolution of 2 mm therefore or a factor 10 better than the average separation is a good starting point. Assuming a drift velocity of 40 $\mu m/ns$ 2mm corresponds to 50 ns separation in time. This is realistically obtainable with drift chambers and digitization electronics.

In z basically the same criteria apply. In particular important is the ability to separate multiple hits as well as possible. The most common choice is charge division, which for gains around 10^4 will give a resolution of approximately 1% of the wire length. With 1.80 m long wires that would give about 18 mm resolution in the CDC. However the double hit resolution is poor for charge division systems.

inner radius	51.8 cm
outer radius	71.9 cm
length along z	179.4 cm
# of modules in Φ	32
Max drift distance	$d = 71.9cm * \tan 5.625^{\circ} = 7.08cm$
Max drift time	$1.8\mu s$
Max propagation time in z	$\leq 1.7\mu s$
Resolution in $r - \Phi$	$200\mu m$
Resolution in $r - z$	$\approx 10 * \sigma_{drift}$
Two track resolution in $r - \Phi$	2 mm
Two track resolution in $r - z$	$\approx 10cm$

Table 1
Expected/projected performance parameters for the CDC

A better choice turns out to be delay lines. The obtainable resolution is somewhat better than charge division, but mostly the double hit resolution is superior. This is being counterbalanced by a longer time needed to read the delay lines out and by the mechanical complications introduced by the lines and the additional material. For the length of the CDC and typical delay line velocities of 3 mm/ns total delay times in the range below $1\mu s$ are obtainable. At a beam crossing time of $3.5\mu s$ at the Tevatron and a maximal drift time of a little over $2\mu s$ this is acceptable. The reduced rate capability will not be a problem with the current Tevatron Luminosity. However if the collider should be upgraded to a higher collision rate pile up will occur and the delay lines will have to be replaced with faster ones.

Table 1 summarizes the performance criteria of the central drift chamber.

4. Physics of the Drift Chamber

4.1. Introduction

Detectors to measure the trajectories of charged particles play an important role in Particle Physics. During the last two decades gaseous detectors have dominated this field. Together with good spatial resolution they offer the possibility of a completely electronic readout, which is very important in todays high rate experiments. Only recently solid state detectors have started to replace gaseous detectors in some areas, notably, where extreme precision is required. Experiments to resurrect optical detectors are only in the early stages. (Scintillating fiber detectors, or detection of UV light of avalanches e.g.).

The more or less remote ancestor of all gaseous detectors is the "Geiger Müller Zählrohr". This is a device developed in the last century which uses avalanche multiplication to count charged particles. Descendants of this detector, which are in use in modern experiments, are the multiwire proportional chamber and the drift chamber. In its modern form theses detectors were pioneered in the 1960's by Charpak et.al. . [10] They showed that large chamber systems are possible without disastrous interference between neighbour cells and developed the first large chamber systems.

The first type of chamber used was the planar proportional chamber. Typically many parallel wires are strung in a plane, spaced usually a few mm apart. [11] Many of these planes can be put on top of each other and used alternately as anode and as cathode planes. A potential is applied between planes. If a particle traverses this arrangement, its trail of charge will be detected by the anode wires and the position of the hit wire will give the position of the particle. The more planes and the closer spaced the wires, the better precision can be achieved.

Proportional chambers have the advantage, that they can be operated at very high rates of incoming particles. Achieving a good spatial resolution however means a very large number of wires and readout channels. The next step in the development was the drift chamber, which offers nearly all the advantages of the proportional chamber, but allows a much more precise localization of the particle with fewer wires. The basic idea here is, that, in addition to recording the number and position of the wire hit one also measures the time it takes the charge from the moment of ionization to arrive on the sense wire. [1][12] Knowing the field configuration in the chamber one can deduce the drift path and therefore the distance at which the particle passed the wire. The gain in position accuracy is "payed for" by the necessity to control

the electric field in the chamber much more precisely than it was necessary in the proportional chamber and by some loss in rate capability. However if real three dimensional reconstruction of an event is required, drift chambers are unsurpassed. Especially in collider experiments of the last years spatial event reconstruction has been done nearly exclusively with drift chambers. These chambers often operate in a magnetic field, thereby allowing measuring of the particle momentum as well [13] [14]. Progress in the understanding of the drift process and the properties of gases resulted in the development of high precision drift chambers with accuracies of the order of 40 μm. [15] A rather complete discussion of proportional and drift chambers and the underlying physical processes can be found in [16] [17].

4.2. Ionization of gases by a charged particle

If a charged particle traverses a volume of gas, it will interact electromagnetically with the gas molecules / atoms and, if at sufficient energy, leave a trail of ions and electrons behind. In interacting with the gas the particle looses some of its energy. This energy loss is described by the Bethe Bloch formula (BBF): [18]

$$\frac{dE}{dx} = -k\frac{Z}{A}\frac{\rho}{\beta^2}\{\ln\frac{2mc^2\beta^2 E_M}{I^2(1-\beta^2)} - 2\beta^2\} \qquad (4-1)$$

$$k = \frac{2\pi N z^2 e^4}{mc^2}$$

where

N	Avogadro Number
m,e	electron mass and charge, respectively
Z,A, ρ	atomic number, atomic mass number, density of the medium
z, β	charge number, velocity of the projectile
E_M	maximum energy transfer between the projectile and the medium: $E_M = (2mc^2\beta^2)/(1-\beta^2)$
I	effective Ionization potential

Fig. 7 shows a plot of the BBF at atmospheric pressure for 2 model calculations and the measurements. For small β ($\beta < 0.97$ typ.) -the particle is not highly relativistic- dE/dx falls off sharply with increasing β. It then reaches a minimum and stays nearly constant for some range of β. Only for very relativistic particles dE/dx starts to increase again slowly (relativistic rise). A particle with a β such that dE/dx is minimal is called a minimum ionizing particle.

The Bethe Bloch Formula describes the mean energy loss of a particle for a given β. The actual energy of a specific individual particle is statistically distributed around

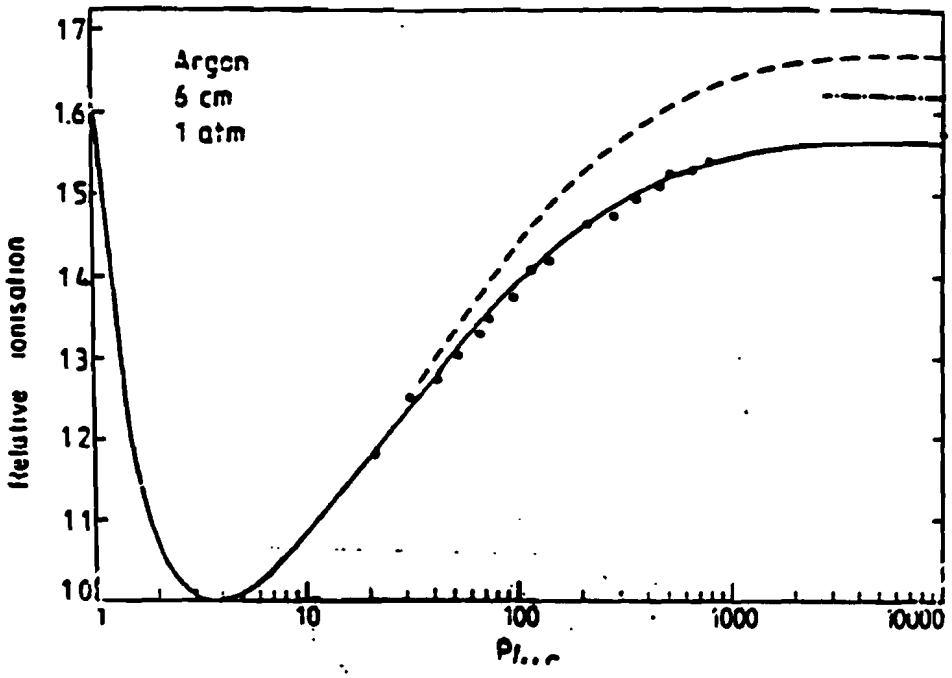

Figure 7 . Mean Energy Loss in Argon at atmospheric pressure relative to $\beta\gamma \approx 4$. Points in Argon/ 5% CH4; dashed line calculation of R.M. Sternheimer; solid line photo absorption model

this mean. The distribution is a rather broad one with a tail towards large energy losses due high energy knock out electrons (δ - rays) (Fig. [8]).

The above shown BBF is a simplified version. More sophisticated treatments were done e.g. by Landau and Sternheimer [19] Phys. Rev. B3,3681 (1971). The main source of uncertainty is the question how to treat the mean ionizing potential I. The best agreement so far between experiment and theory has been achieved with a model, that takes the shell structure of the atoms into account (Photo Absorption Ionization Model).

4.3. Primary/ Secondary Ionization

If a particle passes thru a gas volume, it will produce a number of Ion pairs. The number of pairs depends on the energy loss of the projectile and on the average energy needed to produce one ion pair. The number of this so called primary ion pairs n_p can not be easily computed, however there exist a number of measurements that can be used to estimate it (Fig. [9]). Some of the electrons produced in the collision with the projectile may have enough energy to ionize themselves another atom/ molecule

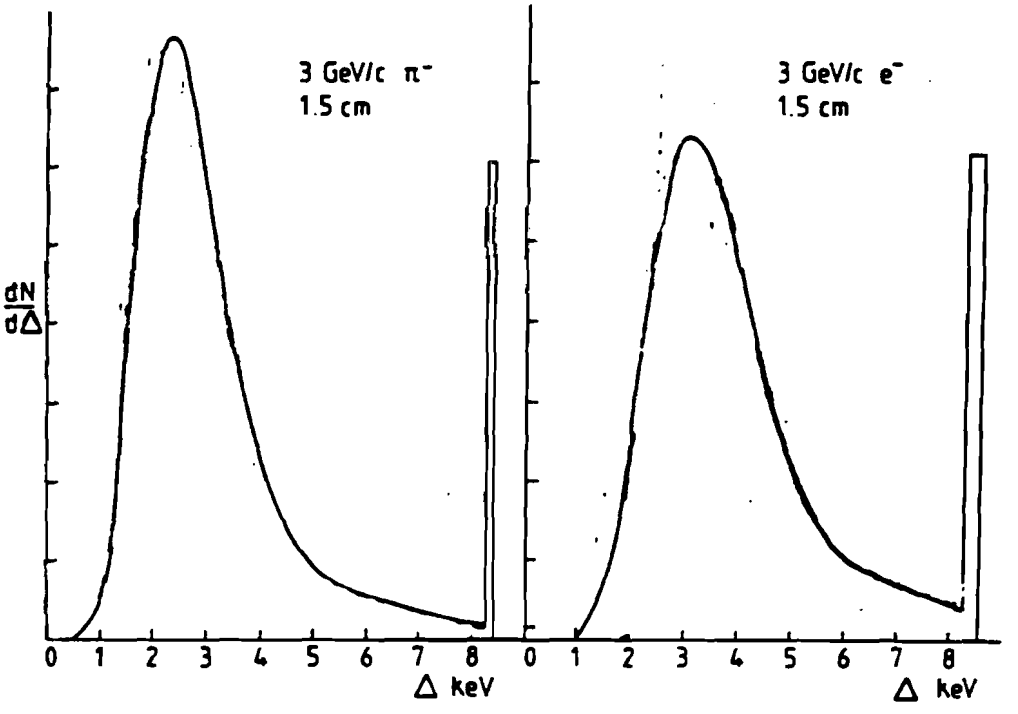

Figure 8 . Fluctuation about the mean energy loss for 3GeV electrons and pions for Argon-CH_4 mixture. [KL 82]

in the gas. These so produced pairs are called secondary ion pairs. The total number of Ions and electrons n_t can be written as:

$$n_T = \frac{\Delta E}{W_i} \qquad (4-2)$$

where

ΔE energy loss of the projectile

W_i average energy needed to produce one ion pair

For gas mixtures a simple linear law applies:

$$n_T = \sum_i \frac{\Delta E}{W_i} f_i \qquad (4-3)$$

where ΔE and W are defined as above, and f_i is the fraction of gas i in the mix. For example for the gas used in the DØ chamber, the MARK II gas (93% Argon, 4% CH_4,3%CO_2), the numbers are:

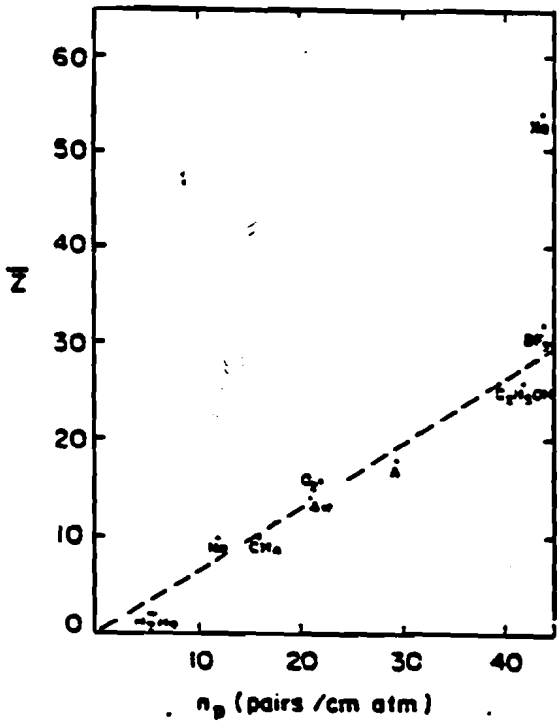

Figure 9 . Number of primary ion pairs produced by a fast projectile per unit length at normal condition in different gases, as a function of their average atomic number. [KL 82]

Gas	$\Delta E/dx(eV/cm)$	W_i	n_p
Ar	2.44	26	29.4
CO_2	3.01	33	34
CH_4	1.48	28	16

This yields for MARK II gas the numbers

$$n_P = 29 \text{ pairs/cm}$$
$$n_T = 93 \text{ pairs/cm}$$

For this gas the average distance between primary interactions is about 350 μm and every primary electron produces $\approx$ 3.2 secondary pairs. However as it has been pointed out in the case of the energy loss this process is a statistical one with large fluctuations around the mean, in particular with a large positive tail. Large fluctuations in the total number of ion pairs and therefore eventually in the pulse height of the detector are to be expected.

4.4. Drift of Ions and Electrons in Gases

4.4.1. Drift of Ions

Under the influence of an electric field, the electrons and the ions produced by a projectile in a gas volume will start to move in opposite directions. In addition they will randomly move around and collide with gas, loosing their energy and thermalizing quickly with the environment. In a constant field an equilibrium will be reached quickly and the electron/ion will move with a constant velocity $w^{\pm}$. It is customary to define a mobility for electrons/ ions as

$$\mu^{\pm} = \frac{w^{\pm}}{E} \qquad (4-4)$$

For Ions the drift velocity w increases linearly with the electric field, the mobility therefore is independent of E. For a mixture of different gases the effective mobility is given by

$$\frac{1}{\mu_i^+} = \sum_{j=1}^{n} \frac{f_j}{\mu_{ij}^+} \qquad (4-5)$$

where

p_j percentage of gas j in the mixture

If the different gases in a mixture have different ionization potentials, within typically 100 to 1000 collisions the charge of the ions will be transferred to the component with the lowest ionization potential . For a mean free path of the order of 10^{-5}cm this will have happened after drift lengths of 10^{-3} to 10^{-2} f^{-1} cm. where f denotes the percentage of the gas with the lowest ionization potential. As an example consider the above mentioned MARK II gas:

for Mark II	Gas	I /eV
	Ar	15.8
	CO_2	13.7
	CH_4	13.1

CH_4 has the lowest ionization potential and will therefore dominate the drift process. In Mark II gas the fraction of CH_4 is 3 %, and the mean free path less than $10^{-4}cm$. After $10^{-4}/3\%$ $cm = 330\mu m$ essentially only CH_4 ions will be drifting.

4.4.2. Drift of Electrons

The situation is slightly more complicated in the case of the electrons. Because of the very small mass electrons under the influence of electric fields may acquire substantial energies between collisions far exceeding the average energy. Complex

quantum mechanical processes take place if the de Broglie wavelength of the electron comes close to the wavelength of shells of the gas atoms/ molecules (Ramsauer effect). The elastic and inelastic cross sections acquire strong and non monotonic energy dependences, which are also material dependent. Small admixtures of different gases may substantially change the drift properties of the resulting mixture. As a result the drift velocity for electrons of most gas mixtures is strongly energy dependent. Typically for argon based mixtures the velocity first increases rapidly with the applied field, reaches a maximum and then becomes more or less saturated. Fig. [10] and Fig. [11] show some sample plots of drift velocities in different Argon based mixtures.

This strange behaviour of the drift velocity can be qualitatively understood following a path of reasoning proposed by Palladino et.al. in [20].

Let λ be the mean free path between collisions for electrons in a gas, v the instantaneous drift velocity. The average time between collisions is then given by:

$$t = \langle \frac{\lambda}{v} \rangle \qquad (4-6)$$

Naively the drift velocity w along the direction of the applied field is than given by

$$w = \frac{eE}{m} \langle \frac{\lambda}{v} \rangle, \qquad (4-$$

where the average is to be taken over the velocity distribution $f(v)$ of the electrons. Eq.(4- 7) is not completely correct, it can be shown, that the more general expression is

$$w = \frac{2}{3} \frac{eE}{m} \langle \frac{\lambda}{v} \rangle + \frac{1}{3} \frac{eE}{m} \langle \frac{d\lambda}{dv} \rangle \qquad (4-8)$$

In between two collisions the electron will gain an average energy per time of

$$\Delta\epsilon = eEw \qquad (4-9)$$

If $\Lambda(\epsilon)$ is the mean fractional energy loss between collisions, the energy lost in one collision is $\Lambda(\epsilon)\epsilon$, and the average energy loss per time

$$\Delta\epsilon = \Lambda(\epsilon)\epsilon \frac{w}{\lambda} \qquad (4-10)$$

Energy conservation requires, that [10] is equals to Eq.(4- 9), once an equilibrium has been reached:

$$eEw = \langle \Lambda(\epsilon)\epsilon \frac{v}{\lambda} \rangle \qquad (4-11)$$

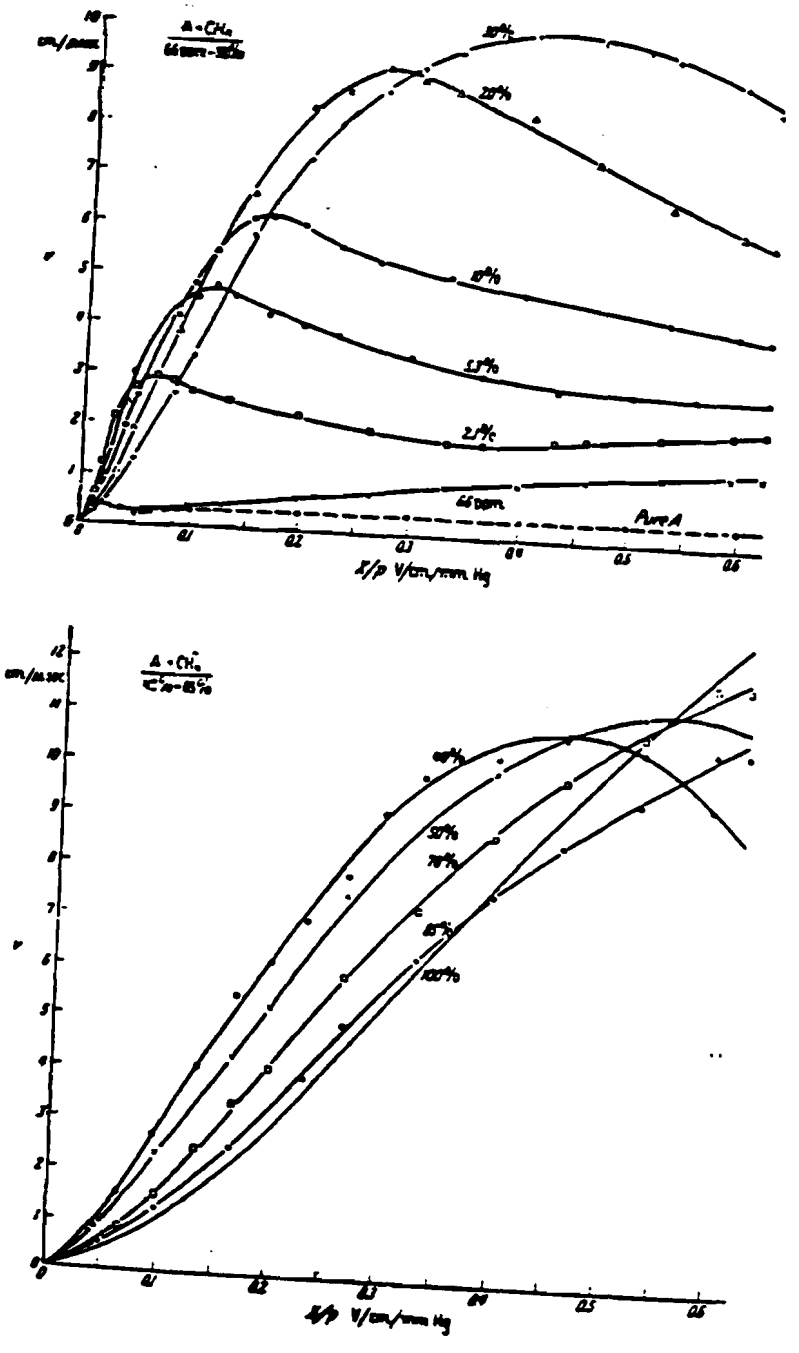

Figure 10 . Drift velocity vs. electric field for different argon based mixtures.

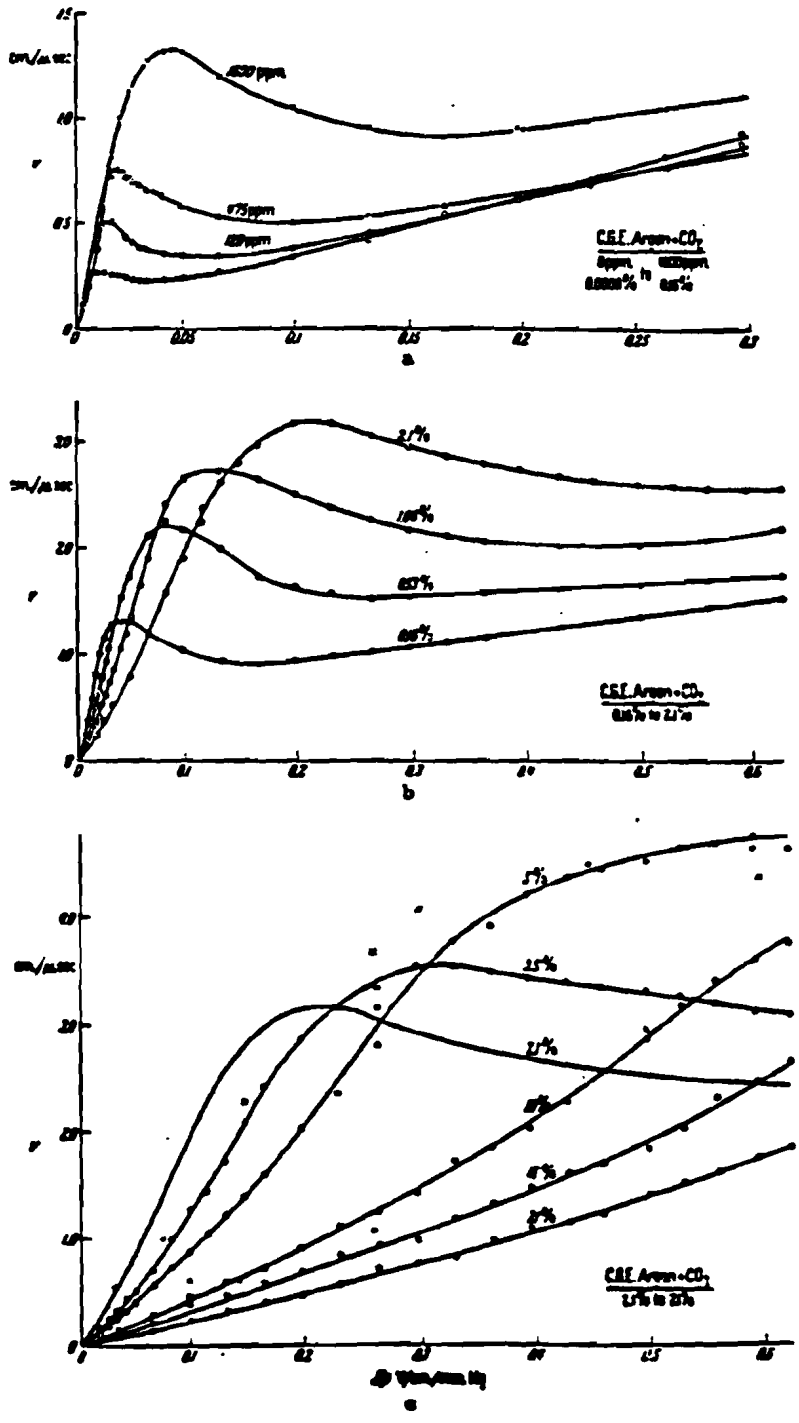

Figure 11 . Drift velocity vs. electric field for different argon based mixtures.

To calculate $\Lambda(\epsilon)$ one needs to know the energy distribution of the electron. Under the assumption that the momentum transfer mean free path is independent of the energy and that the energy is distributed according to a Maxwell like distribution one can calculate the averages and derive expressions for v,w,D and ϵ:

$$\epsilon = \frac{1}{2}mv^2$$

$$\Rightarrow \; eEw \approx \frac{1}{2}\Lambda m\frac{v^3}{\lambda}$$

from which follows

$$\begin{aligned} v &= [\frac{2eE\lambda}{m}\frac{1}{\sqrt{3\Lambda}}]^{1/2} \\ w &= [\frac{2eE\lambda}{3m}\sqrt{\frac{\Lambda}{3}}]^{1/2} = [\frac{1}{3}v\Lambda]^{1/2} \\ D &= [\frac{m\lambda}{6eE}\sqrt{\frac{\Lambda}{3}}]^{1/2} = [\frac{1}{3}\frac{\Lambda}{v}]^{1/2} \\ \epsilon &= \frac{eE\lambda}{\sqrt{3\Lambda}} = \frac{1}{2}mv^2 \\ \epsilon_K &= \langle\epsilon\rangle \end{aligned} \qquad (4-12)$$

The important parameter in this description are Λ and ϵ_K. Their behaviour in principle can be calculated from the electron cross section of the gases in question.

Fig. [12] shows the electronic cross section as measured for argon. Note the dip at energies around 0.3 eV; this is a consequence of the before mentioned Ramsauer effect. For electrons with energies below 0.3 eV, the cross section falls off rapidly with rising energy. One expects therefore that the average energy of the electron increases and the fractional loss decreases with a resulting strong rise in the drift velocity and ϵ_K. After the minimum the cross section starts to increase again rapidly. The increase in drift velocity therefore should slow down and quickly level out to a nearly constant value. As can be seen from Eq.(4- 12), that means that ϵ_K behaves similarly but with twice the slope of w. Only once a sizeable fraction of the electrons reaches an energy equal or above the ionization threshold of Argon, Λ will increase drastically with an resulting increase of w.

However the behaviour of Argon alone is not sufficient to explain the leveling of and -in some cases- falling off of the drift velocity observed in many Argon based mixtures. For this the contribution of the polyatomic gases are needed. Fig. [13] shows the excitation cross section for CO_2. CO_2 is a polyatomic molecule and has other degrees of freedom besides the electronic excitations. It can be excited into

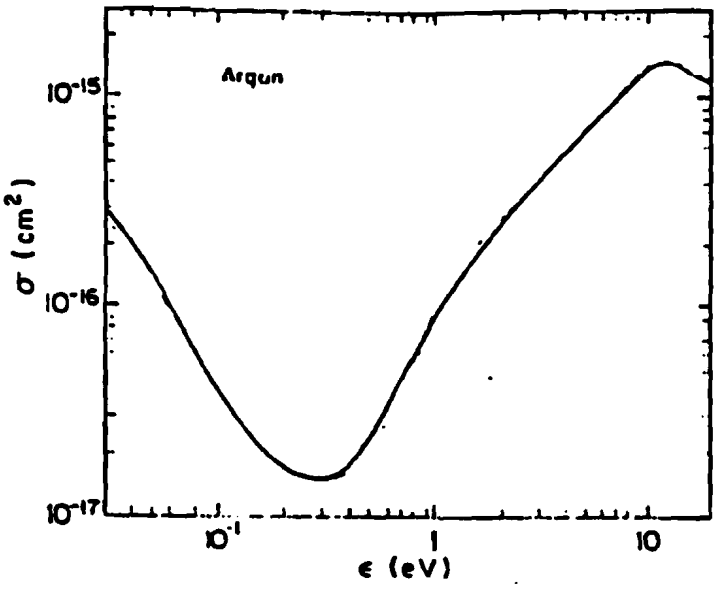

Figure 12 . Momentum transfer cross section in Argon.

rotational and vibrational modes as well. In the energy region from 0.1 to about 1 eV, vibrational excitations are rather large. For a few eV in this region they are the dominant effect in the total cross section. Here the fractional energy loss will be very large, since inelastic collisions dominate. Following the same argument as for argon this will yield the leveling off and eventual saturation of the drift velocity. As the energy increases however the vibrational excitations are no longer the dominant factor. The effective fractional energy loss becomes

$$\Lambda = \frac{\epsilon_{max}}{\epsilon} \qquad (4-13)$$

where ϵ_{max} is the highest vibrational energy. According to Eq.(4- 12) this means that w is approximately constant. This effect will dominate even once the energy crosses the ionization threshold for Argon.

The interplay between the Ramsauer dip in the argon cross section and the additional means of excitation available in polyatomic gases allow an qualitative explanation of the observed behaviour of drift velocities in Argon based mixtures. A more quantitative discussion can be found in the paper by Palladino and Sadoulet [20].

An important consideration for drift chambers is the question of how many of the

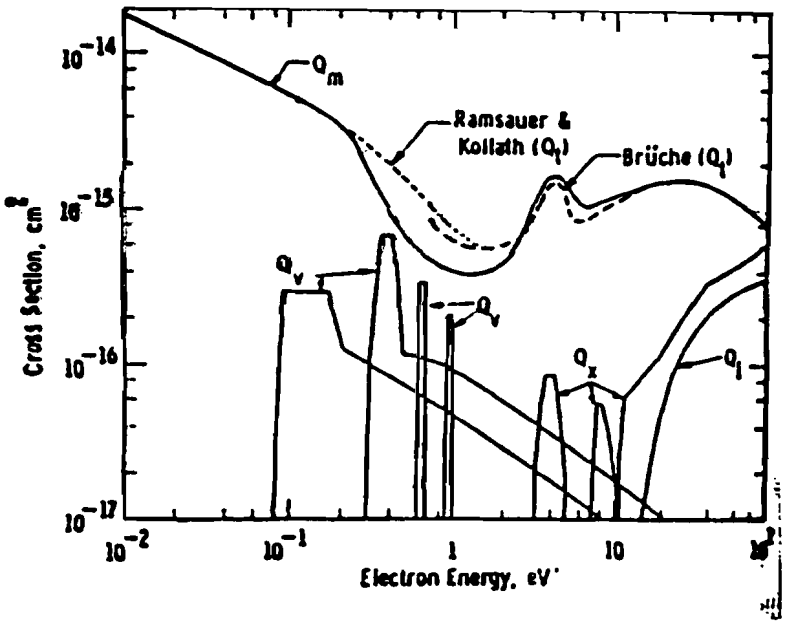

Figure 13 . Excitation spectrum for CO_2, showing the different contributions. Q_m is the momentum transfer cross section, Q_v the vibrational cross section, Q_x the electronic excitation cross section, Q_i the ionization cross section.

initially produced electrons will survive the drifting process, and how many will be lost along the way. The main process contributing is the attachment of the electron to an electro negative molecule. The electro negativity of gases varies widely; it is basically zero for noble gases, very large e.g. for oxygen. The following table shows the probability of attachment h, the number of collisions of an electron with the gas molecule under normal conditions without an electric field, and the average attachment time t.

Gas	h	N/s^{-1}	t/s
CO_2	$6.2\ 10^{-9}$	$2.2\ 10^{21}$	$0.71\ 10^{-3}$
O_2	$2.5\ 10^{-5}$	$2.1\ 10^{21}$	$1.9\ 10^{-3}$
H_2O	$2.5\ 10^{-5}$	$2.8\ 10^{21}$	$1.4\ 10^{-7}$
Cl	$4.8\ 10^{-4}$	$4.5\ 10^{21}$	$4.7\ 10^{-9}$

Both oxygen or water have rather short attachment times. Small amounts of either substance in the chamber gas may inhibit proper drifting over anything but very small distances and therefore keep the chamber from operating properly. Care has to be taken to keep these and other electronegative materials out of the chamber.

The number of electrons lost is given by an exponential law:

$$\frac{n}{n_0} = e^{-\frac{s}{\lambda_C}} \qquad (4-14)$$

λ_C denotes the mean free path for capture.

$$\lambda_C = \frac{w\lambda}{huf} \qquad (4-15)$$

where

w driftvelocity

u instant velocity, $u = \sqrt{2\mathrm{E}/m}$

λ electron mean free path

f fraction of the pollutant in the gas with $\lambda = (N\sigma(\mathrm{E}))^{-1}$, where N is the density of molecules, $\sigma(\mathrm{E})$ the electron cross section in the gas, one gets for λ_C:

$$\lambda_C = \sqrt{\frac{m}{2\mathrm{E}}}\frac{w}{Nhf\sigma(\mathrm{E})} \qquad (4-16)$$

If one assumes that the pollutant does not change the energy distribution of the drifting electrons significantly, for a pure Argon gas and 1% Water pollution one finds using:

$$\mathrm{E} = 6eV = 9.6126 * 10^{-19}\ J$$
$$w = 4 * 10^{3}\ ms^{-1}$$
$$\sigma(\mathrm{E}) = 5 * 10^{-20}\ m^{2}$$
$$h(H_2O) = 2.5 * 10^{-5}\ s^{-1}$$

that:

$$f\lambda_C = 8.18 * 10^{-2} cm$$
$$\frac{n}{n_0} = 0.11$$

1% water pollution in pure argon will absorb 11% of the drifting electrons after 1 cm drift.

4.5. Diffusion

A distribution of charges in free space without any external fields or forces will diffuse apart following a gaussian law:

$$\frac{dN}{N} = \frac{1}{\sqrt{4\pi Dt}} \exp -(x^2/4Dt)dx \qquad (4-17)$$

dN/N is the fraction of charge found in an element dx at a distance x from the origin after a time t, D is the diffusion coefficient. In other words, if at $t = 0$ all the charge is concentrated at $x = 0$, after a time t the resulting distribution has a σ of

$$\sigma_x = \sqrt{2Dt} \qquad (4-18)$$

If an electric field is applied to the charge distribution this formula remains true if one replaces D with $D(E)$ and if the fields are small. The presence of a nonzero electric field will increase the diffusion. $\sigma(D(E=0))$ is therefore sometimes called the thermal limit and describes the theoretical lower limit to the spread of a localized charge distribution with time. The application of an electric field will also split D into two components: one parallel, one perpendicular to the field. The perpendicular component will be essentially equal to $D(E=0)$, while the parallel one (sometimes called longitudinal diffusion) will change with the applied field. Diffusion is one of the main processes limiting the intrinsic accuracy of a drift chamber (see Fig. 14).

4.6. Avalanche Multiplication

The number of primary and secondary ions produced by a fast projectile in a gas is usually rather small. Typical numbers are of the order or less of 100 ion pairs per cm. In order to detect these charges more easily an amplification process within the chamber is employed. In very high fields (typically a few to tens of kV/cm) the drifting electrons acquire enough energy in one mean free path to ionize the next gas atom /molecule they collide with. This way the number of drifting electrons very quickly multiplies and reaches numbers like 10^4 to 10^5 for each initial charge. This process is called avalanche multiplication and is employed in virtually every gas filled particle detector.

One distinguishes four separate regions in the gain- voltage dependance. At very low voltages *no* amplification takes place. This area is utilized in ionization chambers. At somewhat higher voltages the number of collected ions is proportional to the number of initial ions. This region is called the proportional one and is used in

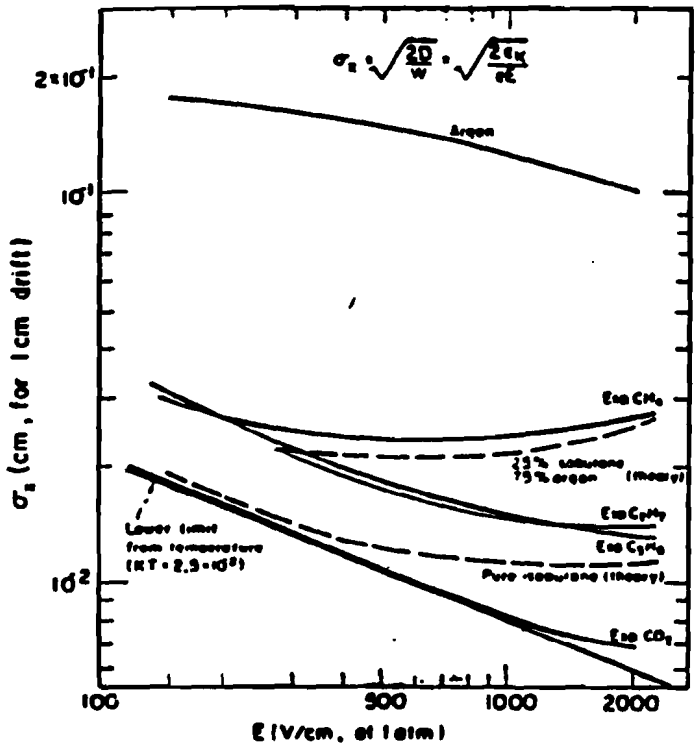

Figure 14 . Standard deviation of electron diffusion after one cm of drift in different gases at normal conditions. Solid lines are measurements, dashed ones from theory

proportional and drift chambers. At very high voltages the number of collected ions is independent of the initial number. This region is used in the Geiger- Müller counter. In between the proportional and the Geiger region there is a range of limited proportionality, which is the operating point e.g. for streamer chambers. At very low and at very high voltages proper operation is not possible, because the pairs recombine (low side) before drifting or because the counter discharges (high end).

If the average number of ionizations per unit length (Townsend coefficient) is called $\alpha(x)$, then

$$dn = n_0 \alpha(x) dx$$
$$n = n_0 exp(\int_{x1}^{x2} \alpha(x) dx) \qquad (4-19)$$

or

$$M = \frac{n}{n_0} = exp(\int_{x1}^{x2} \alpha(x) dx) \qquad (4-20)$$

M is called the multiplication factor. If one knows the Townsend coefficient, one can therefore by using Eq.(4- 20) calculate the expected gain in the chamber. Fig. [15] shows a typical collected charge- voltage curve for a gas counter.

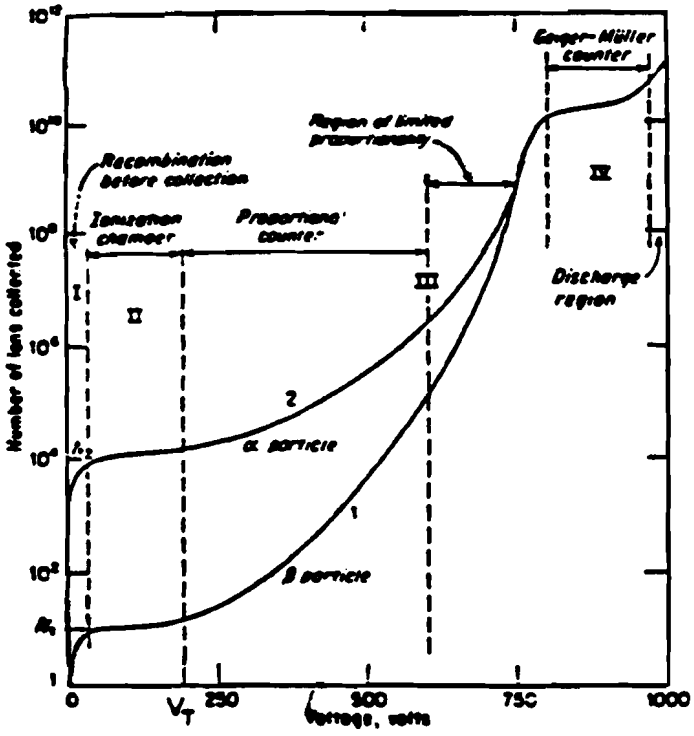

Figure 15 . Number of collected ions as a function of applied voltage for a proportional counter

4.7. The Drift Gas

In choosing a gas for a drift chamber a number of criteria should be observed. The gas or the gas mixture should show sufficient yield of ions for ionizing particles. It should have the correct drift velocity for the chosen application and it should allow a stable operation at reasonable gain. The later means gains of the order and larger of 10^4 for drift chambers, and usually 10^6 for proportional wire chambers. To minimize the attachment of drifting electrons a noble gas as the main component is favoured. The straight forward choice here is argon, both from a dE/dx point of view and from economical considerations.

Drift velocities in Argon can be adjusted by choosing the correct admixtures as discussed in the section on drift of electrons and ions. However there is another very important consideration that governs which components may be used. A pure argon filled chamber will not be a stable device. Since Argon is a noble gas and is stable in its atomic form, the only effective mechanism for an excited argon atom to return to its ground state is by radiating off a photon. Even for the lowest excited state this photon however has an energy of 11.6 eV, more than enough to extract electrons from

most metals (Copper e.g. requires 7.7 eV to extract one electron). In the process of avalanche multiplication plenty of excited argon atoms will be produced. They eventually will have to decay by emitting a photon, which in turn with some finite probability will get absorbed in the cathode or some other metal part of the chamber, possibly freeing an electron. If this happens a positive feedback mechanism is started which will very fast lead to the breakdown of the chamber.

Ion drift purely by Argon ions also presents a problem. The argon ions drift towards the cathode and neutralize there. The excess energy of the ion electron system will be either radiated off or will be dissipated by extracting an electron from the cathode. In both cases new electrons will be produced and the above described positive feedback mechanism initiated.

A solution to this problem is possible by adding small amounts of polyatomic molecules to the argon. Due to the complex structure of these molecules they have many ways to absorb energy and to dissipate off it without radiating photons. CH_4 e.g. will absorb photons in the energy range between 7.9 and 14.5 eV rather efficiently by exciting rotational and vibrational degrees of freedom. If the fraction of this so called quencher is high enough nearly all photons which were emitted by argon atoms during the process of forming the avalanche will get reabsorbed by the polyatomic substance. The positive feedback loop is then broken and the chamber can operate more reliably.

If the quencher is chosen such that its ionization potential is lower than that of argon it will also disrupt the second feedback loop described. Due to the above discussed charge transfer mechanism most all ions drifting will transfer their charge onto the quencher with the lowest ionization potential. At the cathode quencher molecules instead of argon atoms will arrive. Again because of the larger number of effective ways to dissipate energy open to the polyatomic substances, the number of electrons produced in the process of neutralization will be much smaller, the chamber therefore more stable.

As a general rule the more complicated the structure of the quencher molecule the more effective it will do its job. Hydro-carbon compounds are often used for quenchers, e.g. CH_4, or, for high gain operations, C_4H_{10}. Some anorganic substances also show quenching abilities, e.g. CO_2,BF_3 and others. For simpler molecules like CO_2 some secondary electron emission has been observed, which might result in occasional chamber breakdowns.

There is however a serious problem with the use of Hydro Carbons in a high radiation environment. In the process of quenching the molecule might break up and produce a very reactive radical, which will, depending on the substance, deposit

on the anode or the cathode and possibly polymerize into larger molecules. These resulting compounds will form a thin insulating layer on the electrode and seriously alter the behaviour of the system. In particular they might introduce a new path for a positive feedback between anode and cathode and induce discharge. The mechanism is the following. Since a thin insulating layer is deposited e.g. on the cathode the arriving ions no longer can neutralize readily. They will slowly leak thru the layer, but at a much reduced rate. If the rate of arrival of charge on the cathode is larger than the leakage current a charge will build up on the layer with a resulting electric field across it. If the field becomes large enough electrons will be extracted from the cathode thru the insulating layer and ejected into the chamber volume. These electrons then in turn will drift towards the anode, produce a new spurious avalanche and eventually more charge on the cathode. Again a positive feedback mechanism has been established and the chamber will discharge. This effect is known as the "Malter effect" [21]. Once the Malter effect starts the only way to reset the chamber is to switch off the High Voltage. However the chamber will be permanently damaged and will not be capable of high rate operation.

The onset of polymerization seems to depend on the radiation the chamber receives and on the concentration of the organic compound. It has been observed that e.g. a CH_4 concentration on less than 4 % will not show polymerization [22]. Using less than 4 % of any quencher however will not guarantee a stable operation of the chamber. One strategy to avoid polymerization has been followed in the MARK II or similar gases. Here two quencher gases are used, CO_2 and CH_4. Both by itself will not guarantee a stable operation -CH_4 because of its low concentration, CO_2 because by itself it does not suppress the secondary electron emission well enough- but together they yield an reasonably stable mixture. Both will absorb the photons emitted from the argon atoms rather effectively, together their concentration is high enough to yield essentially 100% absorption. Due to the lower ionization potential of the CH_4 however, it will eventually dominate the ion drift thereby solving the problem of secondary electron emission at the cathode due to CO_2 ions. Since the concentration of CH_4 is less than 4 %, the onset of polymerization is at least substantially delayed.

Another strategy often followed is to add some other component which has an even lower ionization potential than the quencher and which does not show the tendency to polymerize. Alcohols are the preferred choice.

The above discussion shows that the choice of the gas for a chamber will be a very important part of the chamber design. Often more than one addition to the basic gas will be necessary. It should be noted however that although some basic understanding of the properties of the resulting mixture can be obtained by following the reasoning outlined, so far the exact details can not be predicted with sufficient

precision but have to be measured.

4.8. Induced charge on the Anode wire

The signal of a drift chamber is read out from the anode wire. As the drifting electrons approach the anode wire, they induce an opposite charge onto it. For most of the drift distance this charge is very minute since the amount of charge drifting is very small. Only very close to the wire, after the avalanche multiplication has started, a sizable effect will be seen. Eventually the charge cloud arrives on the wire and gets neutralized. Now however the wire is surrounded with a cloud of positively charged ions, which slowly start to drift away from the anode towards the cathode. They in turn will induce a charge of negative sign on the wire, which will slowly saturate as the ions drift further and further away. As can be seen from this discussion there are three components to the signal detected on the anode:

- the induced charge due to the drifting electrons. This effect is very small and will be neglected in the following.
- the induced charge due to the positive ions as they drift towards the cathode. For the total charge this will be the dominant effect.

For simplicity a cylindrical geometry is assumed in the following. This is a rather good approximation for the electric field surrounding the anode wires up to distances of the order of the inter wire spacing. During the time it takes the ions to drift this distance however a large part of the charge will have been collected and the remaining drift will contribute only a small fraction to the total signal.

Let R_W, R_T be the wire radius and the radius of the tube, respectively. R_C be the average (center of mass) position of the ion charge produced in the avalanche. For most cases $R_C \approx R_W$.

If a charge Q moves a distance dr in the field, a work

$$\delta W = Q\frac{dV}{dr}dr$$

has to be performed. This work will be seen on the anode wire as

$$\delta W = Q_0\, dv. \qquad (4-21)$$

From this it follows:

$$\begin{aligned} Q\frac{dV}{dr} &= Q_0 dv \\ dv &= \frac{Q}{Q_0}\frac{dV}{dr}dr \end{aligned} \qquad (4-22)$$

If lC is the total capacitance of the system, V_0 the applied potential, and, in cylindrical geometry

$$V(r) = \frac{Q}{2\pi\epsilon_0} \ln \frac{r}{R_W} \qquad (4-23)$$

one gets:

$$\begin{aligned} v^+ &= \frac{Q}{lCV_0} \int_{R_C}^{r(t)} \frac{dV}{dr} dr \\ &= -\frac{Q}{2\pi\epsilon_0 l} \ln \frac{r(t)}{R_C} \end{aligned} \qquad (4-24)$$

where $r(t)$ denotes the radial position of the drifting ion charge. v^+ means the contribution to the signal due to the drifting positive ions. If one assumes that the electrons drift infinitely fast compared to the ions (v_{drift} for the ions is typically $1000 v^e_{\text{drift}}$), similar reasoning yields the expression for the contribution to the signal due to the electrons:

$$v^- = -\frac{Q}{2\pi\epsilon_0 l} \ln \frac{R_C}{R_W} \qquad (4-25)$$

In cylindrical geometry it is possible to calculate $r(t)$:

$$\frac{dr}{dt} = v = \mu \frac{E}{P}$$

Replacing E with

$$E = \frac{1}{2\pi\epsilon_0} CV_0 \frac{1}{r} \qquad (4-26)$$

and separating variables one gets:

$$\begin{aligned} \int_{R_C}^{r} r dr &= \int_0^t \frac{\mu C V_0}{2\pi\epsilon_0 P} dt \\ r(t) &= \left(\frac{\mu C V_0}{\pi\epsilon_0 P} t + R_c^2\right)^{1/2} \end{aligned} \qquad (4-27)$$

Inserting $r(t)$ into the equations for v^+ and v^- and adding them up to get the total induced voltage one finds:

$$\begin{aligned} v &= v^+ + v^- \\ &= -\frac{Q}{2\pi\epsilon_0 l} \frac{1}{2} \ln\left(1 + \frac{t}{t_0}\right) \end{aligned} \qquad (4-28)$$

$$\text{where} \quad t_0 = \frac{\pi \epsilon_0 P R_w^2}{\mu C V_0}$$

The induced charge then is easily obtained from $Q_i = vC$:

$$Q_i = \frac{1}{2} Q_e \ln \frac{R_w}{R_T} \ln (1 + \frac{t}{t_0}) \qquad (4-29)$$

As a special case let $t_{1/2}$ be the time it takes to develop half the total signal:

$$\begin{aligned} Q_i^{1/2} &= \frac{1}{2} Q_e \ln \frac{R_w}{R_T} \ln (1 + \frac{t_{1/2}}{t_0}) \\ &= \frac{1}{2} Q_e \end{aligned}$$

$$\begin{aligned} t_{1/2} &= t_0 (exp(\frac{1}{\ln \frac{R_w}{R_T} - 1})) \\ &\approx \frac{t_0}{\ln \frac{R_w}{R_T}} \end{aligned} \qquad (4-30)$$

In actual detectors one usually detects the current, not the charge: In the limit that the charge sees no resistance in the wire and the following readout electronics, $I(t) = dQ/dt$:

$$I(t) = \frac{1}{2} Q_e \ln(\frac{R_w}{R_T}) \frac{1}{t + t_0} \qquad (4-31)$$

$I(t)$ is maximal at $t = 0$ and decays then with a halftime t_0. For realistic systems one has to take into account that the current will see a RC network with a certain nonzero time constant. In the case of the DØ chamber the preamplifier will dominate this network. To arrive at the real chamber signal the response of the amplifier has to be folded with the pulse described by Eq.(4- 31).

4.9. Resolution of a drift chamber

The spatial resolution achievable with a drift chamber is limited by a number of processes. They split up in one group due to gas dependant contributions and another due to systematic effects. The main one are

- diffusion
- statistics of the primary ions/ electrons

- thermalization: the physical widening of the track due to δ rays
- systematic effects

The total uncertainty is given by the square of the sums of the individual contributions:

$$\sigma^2_{total} = \sigma^2_{diff} + \sigma^2_{ion\text{-}statistics} + \sigma^2_{thermalization} + \sigma^2_{systematic} \qquad (4-32)$$

The spread in space of the drifting electrons due to diffusions after a drift of distance x is given by

$$\sigma_x = \sqrt{\frac{2\epsilon_K x}{eE}}$$

(see the section on diffusion). Experimentally one finds that ϵ_K is, at least locally, proportional to $(E/p)^m$. Rewriting the expression for σ_x, one finds:

$$\sigma_x = \sigma_0 \left(\frac{E}{p}\frac{atm\ cm}{kV}\right)^{\frac{m-1}{2}} \left(\frac{x}{p}\frac{atm}{cm}\right) \qquad (4-33)$$

Typical values of m for drift gases are around 1.5. The dominant dependance of σ on the pressure is then

$$\sigma \sim \frac{1}{\sqrt{p}} \qquad (4-34)$$

σ_0 is the normalization constant describing the resolution at 1 cm of drift and 1 atm pressure at a field of 1kV/cm. Some typical numbers for σ_0 are:

Gas 1	Gas 2	Gas 3	σ_0 /μm
100% Ar			1200
100% CH_4			232
100% CO_2			83
50% Ar	50% CO_2		240
90% Ar	10% C_4H_{10}		380
90% Ar	10% CH_4		600
75% C_3H_8	25% C_2H_4		150
90% Ar	9% CO_2	1% CH_4	280

According to this description there are two ways to minimize the diffusion. The first is to operate the chamber at high pressure. Eq.[34] shows that this will make σ decrease as $1/\sqrt{p}$. The other way is to use a "cool" instead of a "hot" gas and try to make σ_0 as small as possible. The jump e.g. from Ar to CO_2 is quite dramatic. Experimentally it is found that even small additions of a cool gas to Ar will substantially decrease σ_0.

The actual position accuracy achievable with a given σ due to diffusion depends on the way in which the signal is collected and how the timing of the pulse is done. In the simplest case all the charge is collected and the center of mass of the resulting pulse is determined. In that case the spatial resolution σ_{diff} is given by

$$\sigma_{\text{diff}} = \frac{\sigma_x}{\sqrt{n}} \qquad (4-35)$$

For the Mark II gas the number of ion pairs at NTP is 93 pairs/cm. Therefore

$$\sigma_{\text{diff}} \approx 0.10\ \sigma_x$$

is achievable.

As the initial fast ionizing particle passes through the gas it randomly produces ions along its track. Each of these primary electrons in turn may have enough energy to ionize itself other gas atoms. The initial trail of ions looks therefore like a number of charge clusters of finite extension distributed randomly along the particle track.

The distribution of the j-th ion pair along a track with on the average n pairs per cm is given by (see Appendix for derivation):

$$A_j^n(x) = \frac{x^{j-1}}{(j-1)!} n^j\ e^{-nx} \qquad (4-36)$$

For the first detected pair j=1 and eq.[36] becomes:

$$A_1^n(x) = ne^{-nx} \qquad (4-37)$$

Eq.[37] describes the distribution of primary ion pairs and thereby the distribution of the clusters along the track. Moving a given cluster along the trajectory of the charged particle will change the field line along which it drifts towards the anode and therefore possibly the drift time. The effect is most pronounced close to the wire itself. Typically the FWHM of this distribution is about $200\mu m$. This translates in a possible timing error of the order or less of $10ns$, depending on the collection geometry and the field shape. An exact determination of the resulting resolution error can only be done with a Monte Carlo program.

Besides the uncertainty of the position of the cluster the extent of the cluster is another source of inaccuracy. The electrons produced in the ionization process have a finite range in argon. Most of them are rather low energy ones, the majority originating from the lowest electronic excitation of the argon atom. However there are a few higher energy ones with non negligible ranges, which will broaden up the

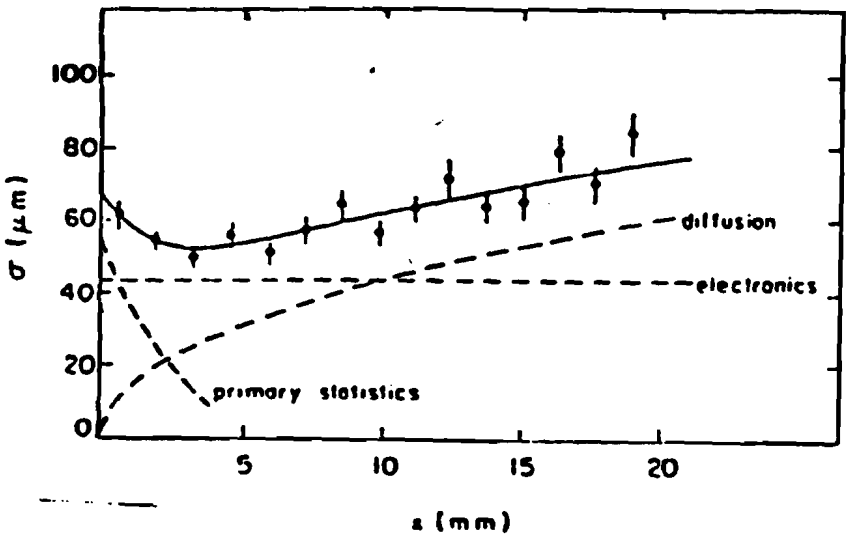

Figure 16 . Resolution of a drift chamber as a function of the drift distance. The dotted lines show the different contributions to the overall resolution. This plot shows a specific chamber under specific conditions, but the overall behaviour is similar for other drift chambers.

track and result in non gaussian tails to the distributions. Typically the ranges of these electrons is rather small and below a few μm for over 90% of them. The few high energy ones however will have ranges around $200\mu m$. Since the range of electrons is proportional to E/p the actual spatial uncertainty due to the sigma due to thermalization is $1/(\sqrt{n}p)$ smaller. Typical values for σ_{th}^{0} are $\approx 200\mu m$ in pure Argon and less than $20\mu m$ in polyatomic gases like CO_2. Fig. [16] shows a measurement of resolution in a specific drift chamber and the way this measured resolution splits up into the individual contributions. No effort has been made to fit the term due to ion statistics and clustering separately. For large drift distances the dominant effect is the diffusion, while at small x the ion statistics overwhelms everything. The constant term is due to the systematic effects like electronics etc.

5. The DØ central Drift chamber: Construction

5.1. Introduction

Compared to many other High Energy Experiments the inner drift chamber of the DØ experiment is a small chamber. It extends for 180 cm along the beam line and radially from about 50 to 70 cm. This small size is a result of a compromise between having a calorimeter at small radii, having a good central tracking chamber and still finding enough room for a transition radiation detector and a vertex chamber inside the tracker. The main design goal was to build a chamber in this limited space and extract as much information from this as possible.

The small space available resulted into a number of unusual design features. The most prominent one is the use of solid walls. These serve as dividers between neighbours layers and as supports for the delay lines. Because of the solid walls the space between neighbour layers can be smaller than it could be in conventional wire only chambers. Each cell forms a totally independent entity insulated from all the other cells. This also contains problems within one cell to this cell. If for example a wire breaks this wire at the worst will only shut down this one cell, and the neighbour cells will be unaffected.

The small space also advocated the use of delay lines over other methods of determining z. Without using extra space they provide two z-coordinate measurements per cell. The solid walls provide a support for them.

The main design goals were to construct a chamber with good spatial resolution in both $r\Phi$ and z, good dE/dx resolution and excellent double track reconstruction. The design eventually adopted can be characterized as follows:

- The detector consists of four layers of drift cells in r. Each layer is subdivided into 32 cells. Adjacent layers are staggered by half a cell to resolve left right ambiguities. Drift of the electrons is perpendicular to the beam axis tangentially to Φ. The two outer sense wires in each cell drive a delay line which provides the z-information.
- Only the sense- and potential wires are actual wires, all other electrodes are made by printing conductive lines on plastic film, thereby physically separating neighbour cells and layers.
- The whole assembly is held by an aluminium drum with Al end plates. This drum supports all the wire tensions. The two inner detectors, the TRD and the Vertex chamber, are hung from the CDC endplate.

5.2. The Mechanics of the CDC

5.2.1. Overview

Logically the inner drift chamber separates into 4 layers which surround the beam pipe. Each layer consists of 32 individual drift cells, each of which is a small self contained drift chamber with 7 anode wires. Each layer is rotated with respect to its neighbours by half a cell width. The result is a rather complicated looking arrangement of cells as shown in Fig. [17] .

Mechanically the complete circle has been broken up into 32 individual modules. Each module covers 11.25 ° in Φ, and extends from the inner to the outer radius. Due to the staggering cells are shared between neighbour modules. Each cell is contained to 75% in one module and to 25 % in the next one.

Each module forms a self contained unit, that is able to support the tension of all wires strung in that module. However in the final configuration the modules are mounted in an Aluminum support tube, which positions the modules precisely and takes the load from the wires.

This outer support tube consists of an Al- tube made from rolled 3/8 inch thick Aluminum, two end plates which engage the modules, and an inner tube, made from a light composite material, which closes the gas volume and provides additional mechanical stiffness to the assembly.

The anode wires of each cell are held by plastic end plugs, which sit on the surface of the modules and are engaged by precision machined holes in the Al-end plates. The wire terminations are accessible from the outside without interfering with the gas seal. The delay lines are brought to the outside of the chamber using these end plugs as well.

Amplifiers and cable connections are made on the Al- endplate. A 3/4inch thick space is available, making miniaturized cables and amplifiers necessary.

5.3. The Module

The Module is the basic building block of the central drift chamber. Essentially all important parts of the cells are contained within one module. The modules are made from composite materials with special attention to lightness and stiffness while still being strong enough to support the full tension of the wires and maintaining the mechanical accuracy required. Four sets of sense- and potential wires are housed in each module. Delrin end plugs are mounted on the module end plates and position

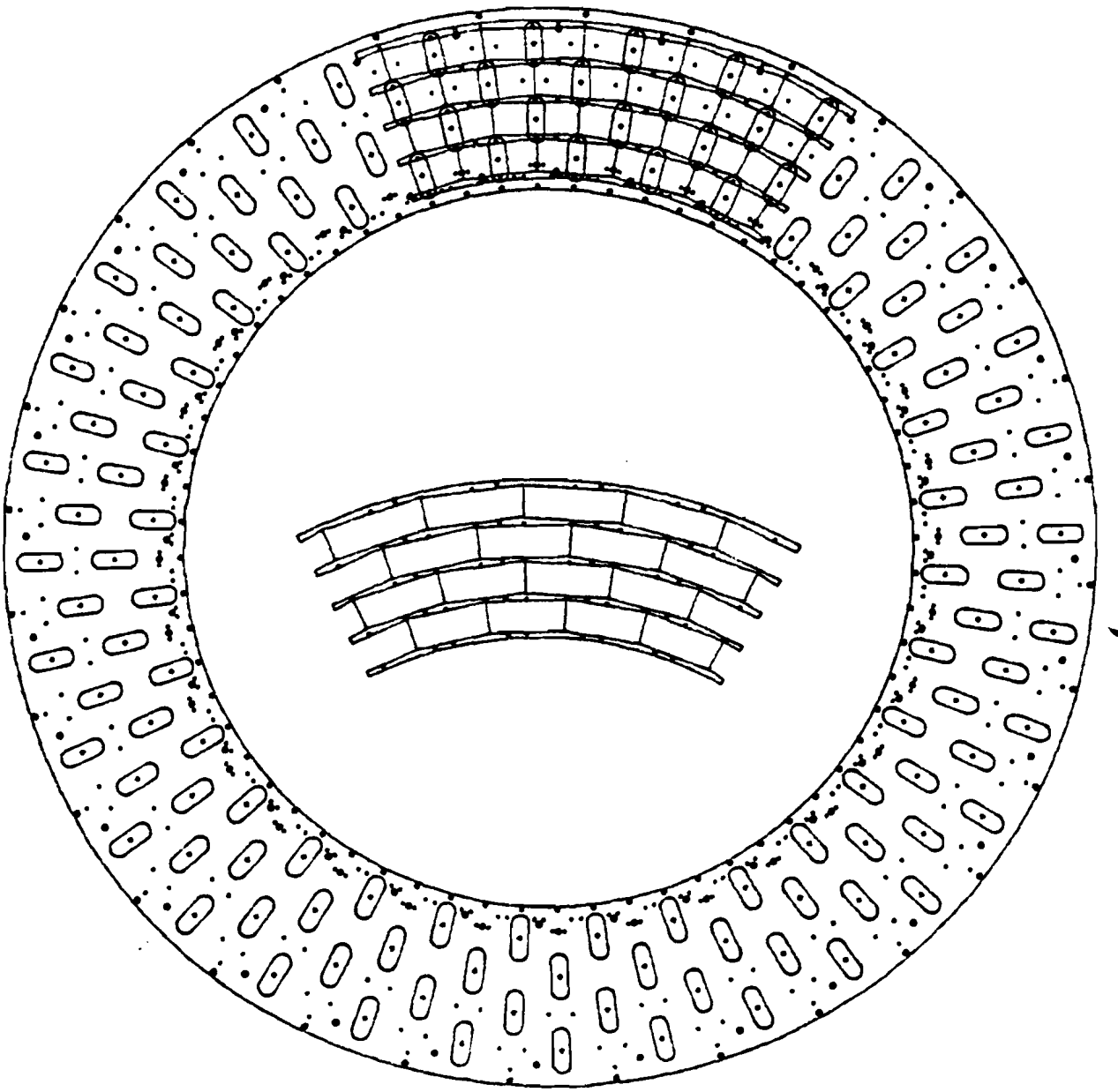

Figure 17 . Crossectional view of the CDC. Inside the chamber a 5-sector section of modules is shown. The large oval holes are for the end plugs, the smaller ones are gas inlets and mounting holes.

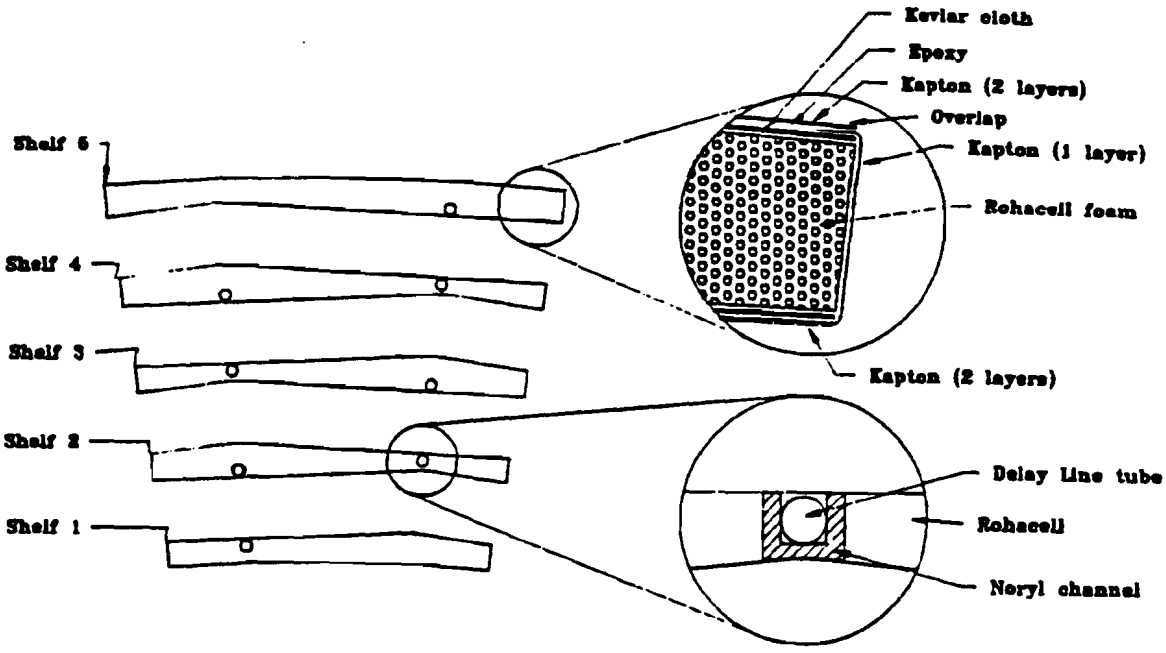

Figure 18 . Crossectional view of the five different shelves. One shelf has been enlarged to show the different materials used in the construction.

the wires through crimp pins. During the assembly period the modules form a self supporting independent system. Once they are inserted into the Al- shell the tension of the wires is transferred onto the Al-drum by pulling each end plug away from the modules with the help of two "bridges".

5.3.1. Shelves

Each module is built using five so called shelves, 4 septa strips and two end plates. The shelves are the dividers between layers and provide a surface for the fieldshaping strips and support the delay lines. Fig. [18] shows a cross sectional view of all five shelves. The innermost surface of shelf 1 and the outermost one of shelve 5 form a multifaced polygon to fit more tightly against the inner and outer shell, respectively.

Each shelf is made from a Rohacell core with a Kevlar-Epoxy skin on the top and bottom. Rohacell is a closed cell Polymethacrylimide rigid foam, which can be easily machined to good precision and which glues very well with epoxy. A plank of Rohacell is machined to the correct shape and dimensions using a special planer-like cutting machine. Two grooves are cut into the Rohacell plank to accommodate a teflon tube used for the delay lines. As can be seen in Fig. [18] delay lines are found

	Kevlar 49 Aramid	Du Pont Nylon	Dacron Polyester	E-HTS Glass	Stainless Steel
Tensile Strength* (MPa)	2758	986	1120	–	1724
**	3620	–	–	2413	–
Modulus (MPa)	124110	5516	12790	68950	199955
Elongation to Break (%)	2.5	18.3	14.5	3.5	2.0
Density (g/cm^3)	1.44	1.14	1.38	2.55	7.86

* Unimpregnated twisted yarn

** Impregnated strands

Data from: DuPont technical bulletin KEVLAR, page K-5

Table 1
Properties of commonly used fibers and steels

at the thinnest and at the thickest point of each shelf. At the thickest point a simple groove it cut, at the thinnest however space for an additional Noryl "U" channel is provided. The Teflon tube is laid in the "U" channel which is glued to the Rohacell. This lends additional mechanical support and in particular helps in insulating the thin part of the shelf against HV breakthrough.

The top and the bottom of each shelf is laminated with an epoxy saturated Kevlar cloth. Kevlar * is an aramid fiber developed by DuPont. It has a high tensile strength (2758 Mpa) and a high modulus (124 110 MPa) at only about one fifth of the weight of steel. Table 1 shows a comparison between different commonly used fibers, Kevlar and Steel.

The cloth is woven with seven times as many fibers in the longitudinal direction as in the transverse. This configuration shows superior stiffness against bending as illustrated in Table 2.

The whole shelf is wrapped with a sheet of Kapton foil for electrical insulation and to provide a good surface for the field shaping strips. The Kapton is doubled on the top and the bottom to minimize the chance that a pinhole will penetrate the skin of the shelf and cause High Voltage problems.

Each of these sandwiches is individually laid up by hand in a mold. A piece of Kapton cut to the correct dimensions is laid into the bottom part of the mold. A strip of Kevlar is laid up onto this followed by the two pieces of Rohacell, the Noryl

* Kevlar is a trademark of the DuPont Co. USA

Material of skin	thickness (1/1000")	Deflection/mil 24.7g	67.5g1)	Relative performance	
G10	10	9.5	27	22.5	1.4
Kevlar	4*	13	35	16	1
Kevlar	11**	4.5	13	48	2.9
Rohacell	0***	214	585	1	0.06

1) Measurements were done with the two listed weights applied to the center of a 45" long, 2.5" wide plank supported at the ends.

* Kevlar cloth with equal number of strands in transverse and in longitudinal direction.

** Kevlar cloth with 7 longitudinal fibers for every transverse fiber. Individual fiber size is equal for both samples.

*** Rohacell shelf is 30" long and 6.5" wide. It is listed here just for qualitative comparison.

Table 2
Measured deflections of different laminates

"U" channel and the Teflon tubes for the delay lines. Next the ends are molded by filling recesses with a premixed Epoxy–Silicon Powder compound (Shell 828 Epoxy with 40% V40 Hardener, thickened with Cabosil Silicon powder). A slot is molded in the ends which is used to key to shelf into the endplate during the assembly. After carefully checking for alignment and removing as many air pockets as possible the top piece of Kevlar is laid down into Epoxy and the Kapton folded over. Air bubbles are removed and the mold is closed. This procedure is repeated five times with five different molds for the five shelves. After closing the shelves are allowed to cure for 18 hours. They are then removed and the molds are prepared for the next batch. Since the epoxy used (Shell 815 epoxy with teta Hardener at a ratio of 10:1) needs 7 days to reach its ultimate strength, they are stored for at least one week on a flat surface to avoid distortions during the final curing process. Using a mold to do the final forming of the shelves guarantees closer mechanical tolerances of the final product and better reproducibility, although it complicates the production process somewhat and needs a rather expensive tooling.

5.3.2. Septa: Cathode sandwiches

The cathodes in the module are made from a thin laminate principally quite similar to the shelf. The Kevlar however has been replaced with a thinner fiberglas cloth. These laminates are made from a 1 mm thick Rohacell core, fiberglas and a strip of Kapton on both sides. They are produced in a big sheet using a vacuum bag as a press and "mold" and then cut down to size. The fiberglas is laid down with the fibers running at 45° to the long side to improve the stiffness against bending (see

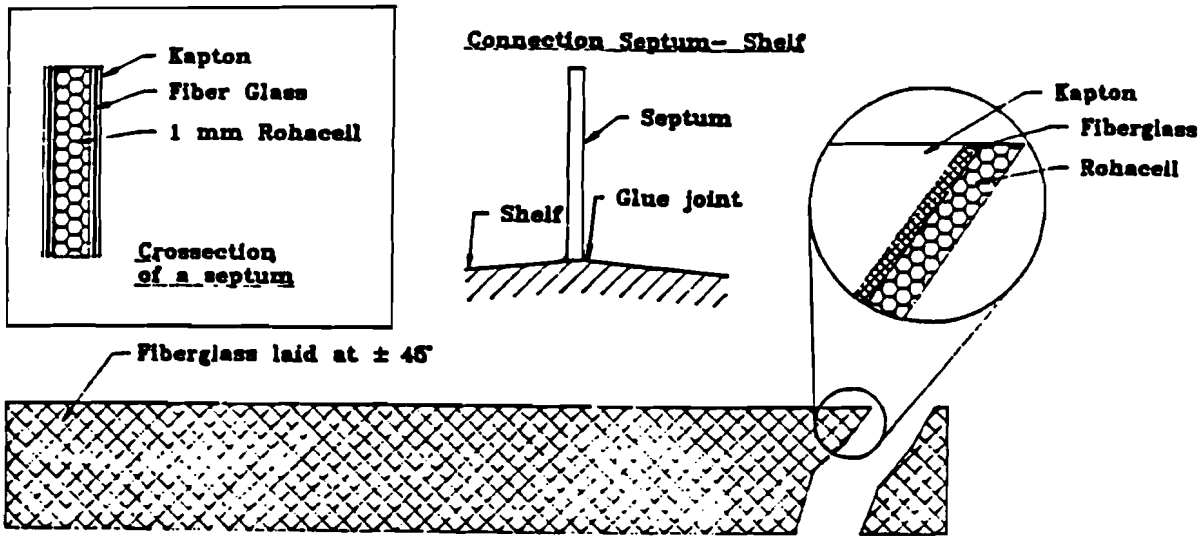

Figure 19 . A Septa strip: Layout of the fiberglas and cross sectional view

Fig. [19]).

5.3.3. End plates

The end plates have two purposes: they provide mechanical stiffness to the module, preventing shelves from "rotating" about the septa and the structure from collapsing, and they provide a support plane for the end plugs. They are strong enough so that the end plugs can rest on them with the whole wire tension applied. In the final assembly the plugs engage into the endplate and at the same time into the Al-endplate thereby positioning the module.

They are made from 0.25" thick G10. Four rectangular holes take the wire end plugs. On one side additional holes are foreseen for HV-feedthroughs for both cathode and central strip.

5.3.4. Assembly of a Module

Five shelves, 4 septa strips and two end plates get assembled into one module. The assembly is done using a special jig, which positions the shelves, septa and end

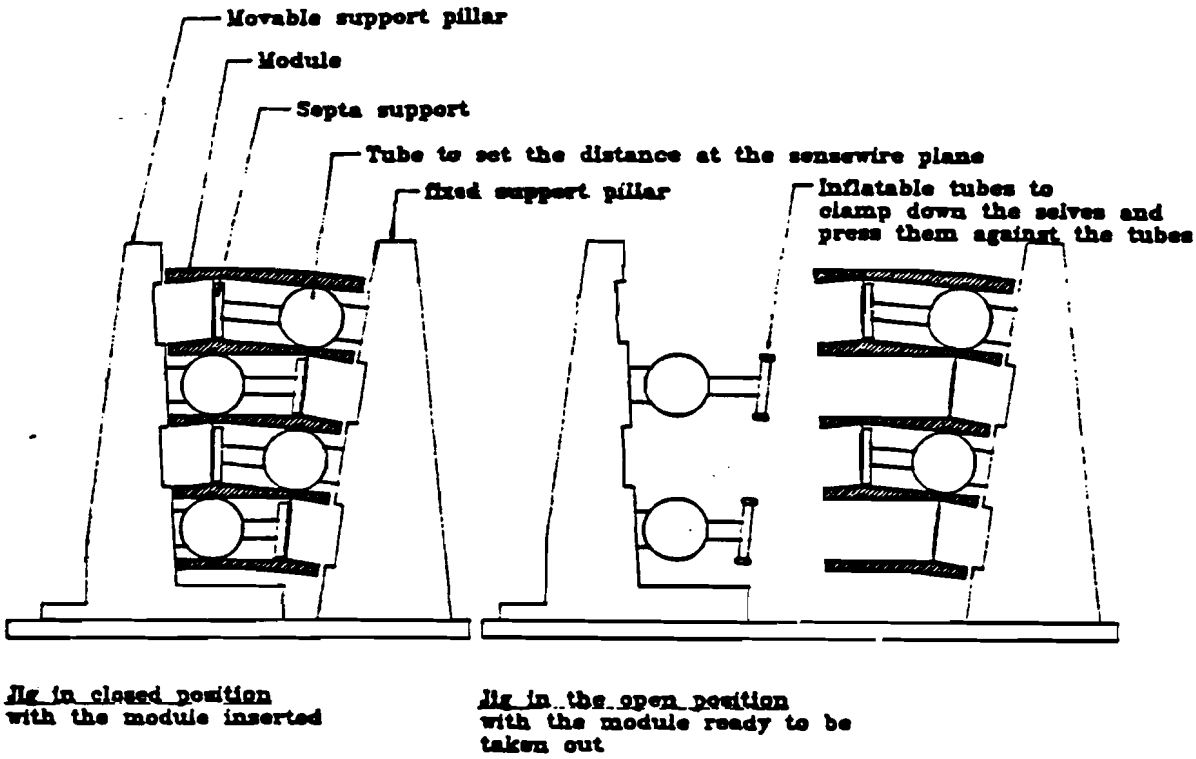

Figure 20 . 5 shelves being assembled in the assembly jig

plates. A cross sectional view of a module in this jig is shown in Fig. [20] . The critical measurement of the module is the height of each layer at the position of the sense wires. The jig provides precision machined cylinders which keep the shelves at the correct distance. Inflatable tubes press the shelves against the metal tubes and clamp them in the correct position.

After the shelves have been laid into the jig, the end plates are glued to the shelves and the septa connected to the shelf surface by a bead of Epoxy. Once cured the module is removed and a second bead of epoxy is applied to each septa.

Fig. [21] shows a complete module. Part of the endplate on the HV-side has been cut away to allow a better view of the inside. The staggered cathodes are clearly visible as are the ends of the tubes for the delay lines on two shelves.

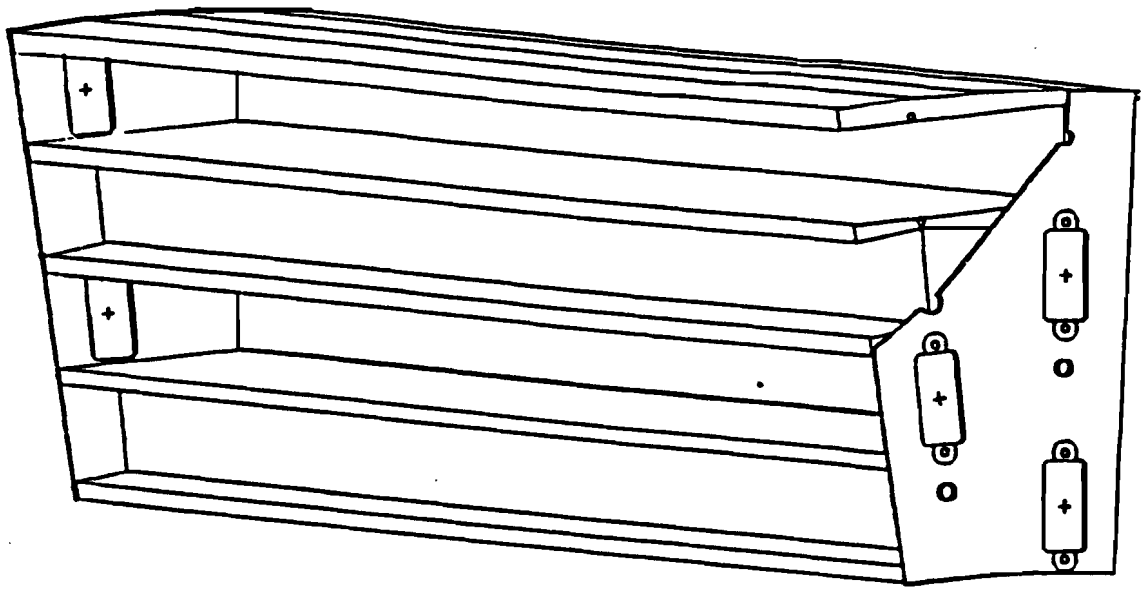

Figure 21 . Cutaway view of a module.

5.4. The End plug

Fig. [22] shows a drawing of the two end plugs used in the chamber. The end plugs are responsible for positioning the wire crimp pins, to key the module into the Al-endplate of the drum, to seal the gas volume inside the chamber, to bring out the delay lines and to feed the HV for the central strip into the chamber. The upper part of the plug is equipped with an "O"-ring and seals against a precision machined surface in the Al-endplate. The hole is machined to nominal 1/1000" clearance all the way around positioning the end plug to ±1/1000". The lower part of the end plug fits into a hole in the G10-endplate and keys the module to the Al-endplate. The plugs which are being used on the HV side of the chamber have longer "ears", which extend about 0.5" inside the active chamber volume close to the shelve surface. This protects the resistive divider strip, which is glued to the shelf surface, from discharge originating from the closest sense wires. The crimp pins to hold the different wires are press fit into holes in the end plug. The pins for the potential wires sit flush on the outer plug surface, while the sense wire pins are recessed by 0.2". This provides a longer discharge path between sense wire and potential wire pins, and allows the

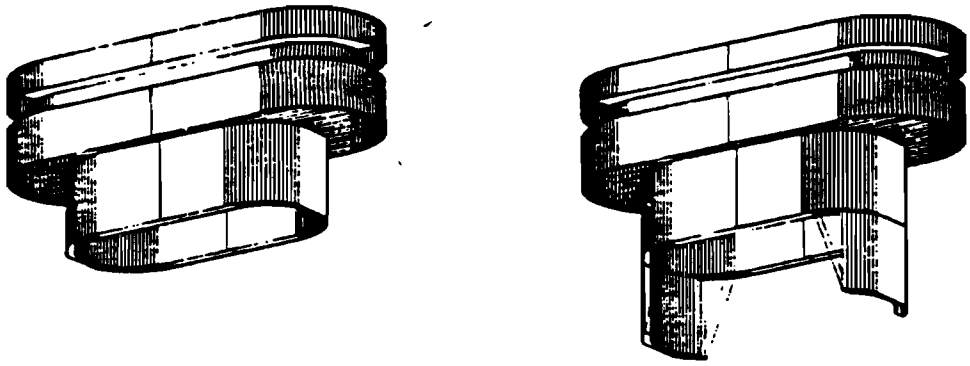

Figure 22 . a) end plug used on the HV side. The long ears are to protect the resistive dividers on the shelf against discharges from the wires. b) end plug used on the signal side of the chamber

use of an insulating connector to the sense wire pin to further safe guard against HV breakthrough (Fig. [23]).

Two holes are provided in the plugs for the delay line tubes. They are sealed with a gland "O"-ring seal and a special washer to keep the "O"-ring in place after insertion. The "O"-ring is a made from Viton V 884 compound with a hardness of 75 durometer [23]. On the HV side, the High Voltage for the central strip is fed in four locations to the module. Two each are located on top and on the bottom of each cell. A spring loaded probe is pressed into these holes and makes contact with a gold plated surface on the module. For redundancy two probes are always paired and serve the same potential.

Four threaded rods extend from the outer surface of the plug. These will be used by bridges after the final assembly of the chamber to pull the end plug away from the module and transfer the wire tensions onto the Al-drum. The bridges have openings for the delay line tubes and for the HV- connections to the central strip (Fig. [24]).

5.4.1. HV-plug and Pulling Screw

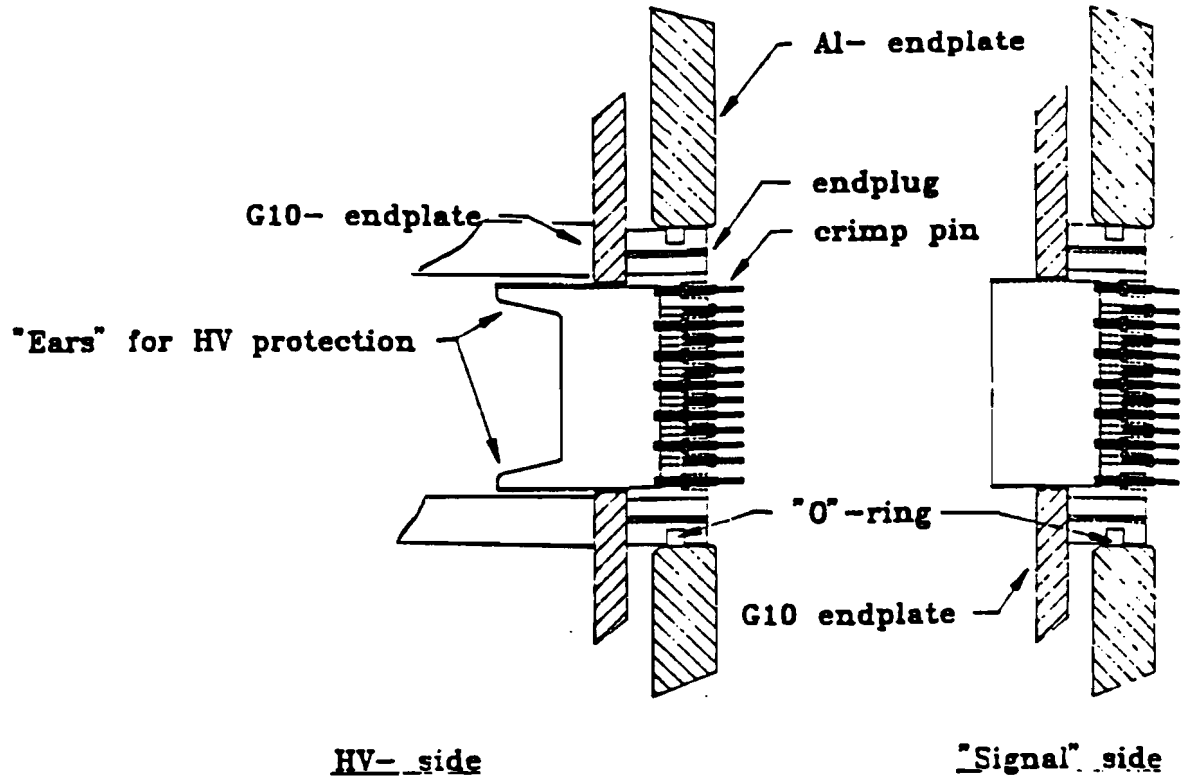

Figure 23 . Sideview of an end plug showing the crimp pins installed. The view shows the plu resting against the G10 endplate before being pulled.

On the HV side two other plugs connect to the module, the main HV feed through and a so called pulling screw. The later is simply a piece of Noryl with a threaded hole into which a screw from the outside engages. This pulls the module to a predefined position with respect to the Al-plate and keeps it from sliding back and forth.

The HV feedthrough is similar to the central strip connections, but self contained. A round piece of noryl fits into a hole in the Al-endplate, sealed with an "O"-ring, and extends into a matching hole of the G10 plate. A spring loaded probe mounted inside the noryl piece contacts a gold plated metal disk glued to the septa of the module and provides the contact for the main cathode high voltage.

5.5. Mechanical support system: The outer shell

The drum into which the modules are mounted is fabricated mostly from Aluminum with only the inner cylinder made from a lightweight composite. The outer cylinder is rolled from 3/8" thick Al, with 0.5" rings welded to the ends of it. Only the end rings are machined. The 0.5" thick end plates engage to the drum with a little lip and are bolted to it. A "O"-ring is captured in a groove in the endplate

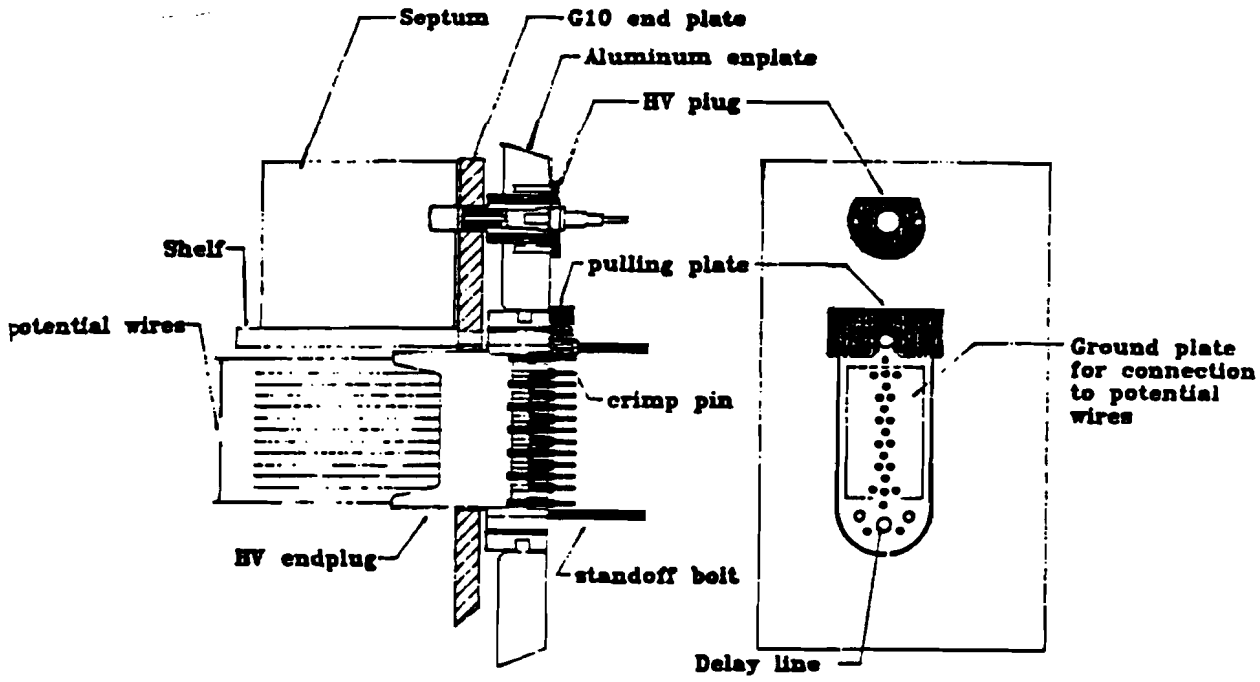

Figure 24 . View of a plug installed in its final position in the chamber. The plug has been pulled away from the G10 endplate and is now supported entirely by the bridges, which rest against the Al-endplate. The probes for the central strip HV are halfway extended to provide contact with the G10 endplate.

and seals the plate against the outer drum. On the inner radius a composite cylinder closes the volume. It is made from two thin Carbon Fiber skins with a sheet of Rohacell laminated in between. Again two metal rings are glued to the ends and provide a surface for the "O"-ring to seal against and material for bolts to be screwed into. Fig. [25] shows an assembly drawing of the whole system. Shown are also two extension cylinders which are attached to both ends of the central tracking shell and are used by the forward drift chambers.

The complete system is mounted inside the cyrostat on 4 feet attached to the ends of the extension cylinders. The other two inner chamber systems, the TRD and the Vertex chamber, are hung from spokes attached to the inner radius of the CDC endplate.

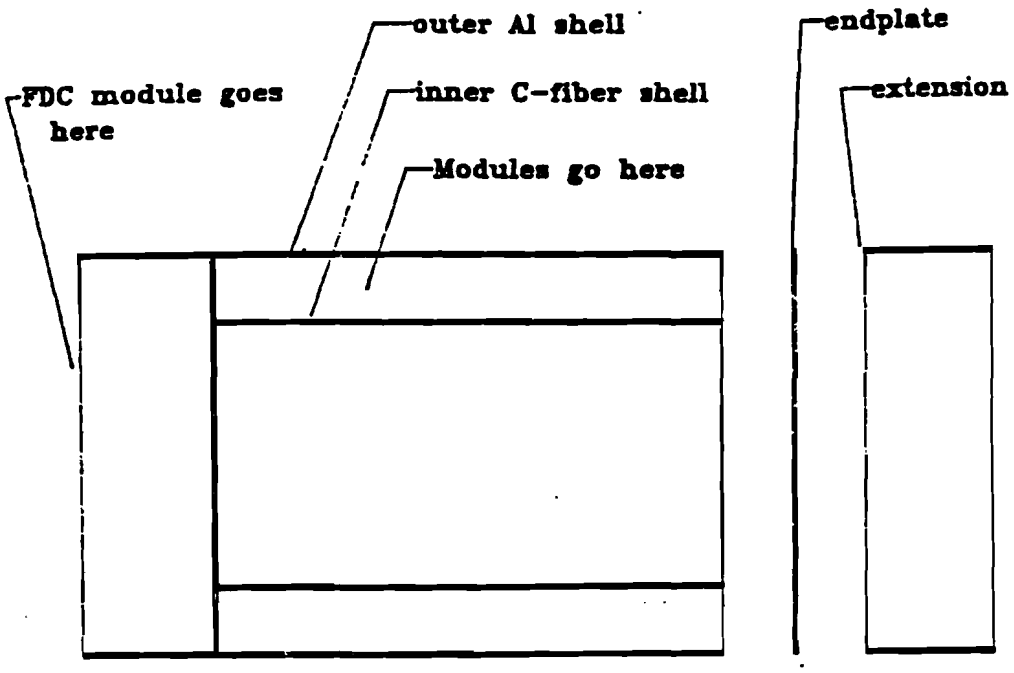

Figure 25 . CDC outer shell

5.6. The HV distribution in the Chamber

5.6.1. The field shaping cage

As mentioned earlier only the sense and potential wires are actually wires, all other electrodes are resistive lines printed on the shelf surfaces. Fig. [26] shows schematically the position and numbers of strips in one cell. A number of problems have to be addressed in the design of these strips. Since they cover a large part of the chamber, the amount of material introduced into the chamber by the strips should be kept as small as possible. Copper as the material is not favored because of too high density. Resistive plastics/Epoxies offer a better alternative with considerably less material involved.

Since the delay lines are mounted inside the shelves lines have to be printed on the surfaces in the immediate facinity of the delay lines. This has to be done in a way that does not interfere with the induction of a pulse onto the delay line. Electrostatic calculations indicate that a strip in the center of the chamber at the position of the delay line produces a favorable field configuration. However, since this line would be

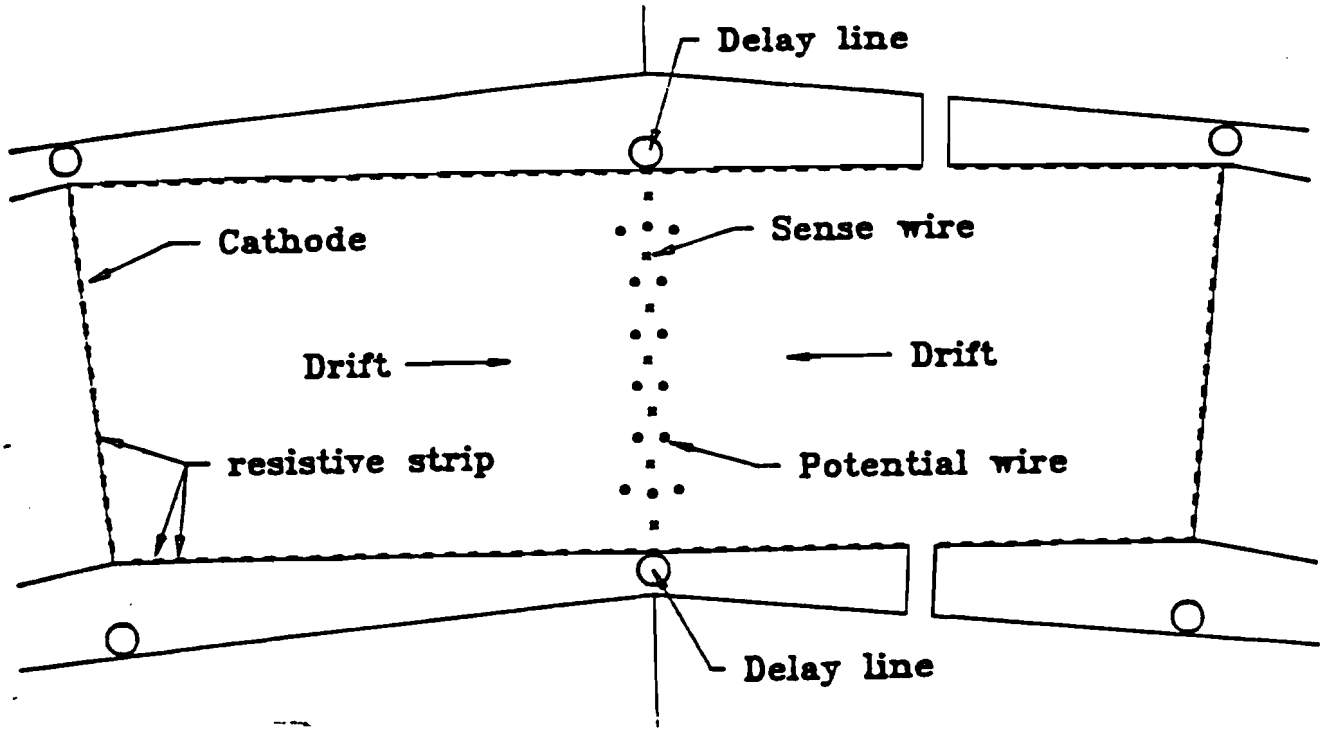

Figure 26 . Crossection of one cell showing the positions of the field shaping strips

positioned right on top of the delay line, it has to be investigated how this affects the signal seen by the line and how the signal propagation properties on the line are affected.

The only parameter which can be controlled is the resistivity of the field shaping strips. Too low a resistivity would attenuate the induced signal from the sense wires considerably and slow the rise time of the signal down. Two different sources of these effects have to be distinguished: The influence of the strip on the induction process, and the interaction between strip and signal after the induction when the signal starts propagating on the line.

The second question is addressed in table 1. A resistive line was printed onto a shelf on top of a delay line, but extending only for half the length of the line. A signal was then induced in the line with an antenna in a part of the line which was not covered by the strip. The rise time and attenuation of the signal after passing through the section of the line with the strip on top were measured.

The table shows that the intrinsic rise time of the delay line in the shelve is around 44ns (measured from 10 to 90 % of the signal). For line resistances around $1k\Omega/\square$ the rise times with and without strip are very similar. The slowing down of the signal

Input T_R/ns	$R = 220\Omega/\square$ T_R/ns	A/mV	$R = 803\Omega/\square$ T_R/ns	A/mV	no strip T_R/ns	A/mV
7	62	39	31	65	37	60
15	57	36	32	61	39	57
30	63	33	38	51	45	50
40	60	31.	44	44	46	44

Table 1

Rise times and Amplitudes of pulses propagating on delay lines with strips of different resistances close by, as a function of the rise time of the input pulse.

due to propagation of the signal in the environment of the resistive strip is negligible for lines with an resistance of more than $1k\Omega/\square$. This effect is important because the delay line is surrounded by strips of different resistivity: the strip immediately on top of the line. but also the strips printed on the septa on the other side of the shelve. The second effect is particularly important for those lines mounted at the thinnest part of the shelve.

However if one also takes the induction process into account considerably higher resistances are needed in order not to degrade the rise time appreciably. Due to technical difficulties no reliable data exist for the resistivity range from a few $k\Omega/\square$ to $\approx 20k\Omega/\square$. The following table gives an indication of the change in rise time as more and more lines are added in the field cage:

R/kΩ/□	no strip	56	+78	+78	22
T_R/ns	32	41	43	45	49

These measurements were done inducing the signal through the 1. line with $56k\Omega/\square$. The rise times quoted are measured for the fast part of the pulse by fitting a straight line to this part and taking the intersect of the baseline and of the 100% line as the timing points. Another important question is how the rise time changes with the distance of the strips to the delay line. Although the strip closest to the line is at a fixed distance, the previous table shows that adding lines has a non negligible effect on the rise time. In particular the septa will put some lines rather close to the delay line. The septa lines should ideally be of a low resistance, because they have to carry the cathode current.

The values eventually adopted in the chamber are $22k\Omega/\square$ for the inner lines on the septum and $80k\Omega/\square$ for the two edge line on each septum. For a Cathode current due to positive ions of 100nA this translates into a maximal voltage drop across the cathode of 15V or 5V respectively (assuming 1.80m long shelf and 1mm wide field shaping strip). To reduce the drop for the outer two lines they are connected in five points along the septum to the first of the low resistance strips. This lowers the actual

voltage drop on the outer strip in the worst case to the drop on the low resistance line plus one tenth of the possible drop of the high resistance line. In reality the potential drop will be normally lower than discussed, because the ions will be spread out along the strip and not the whole chamber current will arrive on one strip. Voltage drops below 5V along the cathode are about $\frac{1}{10\%}$ of the drift field and probably acceptable.

5.6.2. The Module: an electrical description

Two main groups of potentials have to be brought to each module and distributed: The sense wire/ potential wire voltages, and the voltages supplying the complete field cage. The former ones represent no big problem, since all the wires are easily accessible from the outside through the crimp pins. The later however is a fairly complicated problem, because the field cage consists of some 130 odd resistive lines printed on the different shelf surfaces, each of which has to be supplied with the correct potential. Only two voltages are applied externally: the cathode voltage and the central strip voltage. The central strip is the field shaping strip which is located directly on top of the delay line, and which is the endpoint of the field cage. The cathode voltage is applied to the top of each septum through the above described feed through connector. From there it is graded down by a resistive divider to the correct central strip potential. For this a surface mount resistive divider is glued to the end of each shelve. Two resistors in parallel connect each neighbouring field shaping lines. They are connected to the line with a carbon loaded conductive epoxy. Since each cell is shared between two neighbour modules connections have to be made from one module to the next at each shelf surface. This is done with little jumper wires, that plug into receptables mounted on the inside of the G10 endplate. Fig. [27] illustrates the different connections. At the central strip, a thin wire is soldered to the divider and guided along a groove in the opening for the plug to the outside of the G10 endplate, and connects to a gold plated metal disk which is glued into a recess of the plate. The spring loaded probes from the end plug "land" onto this disk and make the connection to the outside of the chamber.

The sense wires have to be connected twice: on one side the high voltage is connected to the, on the other side the signal are coupled through a capacitor to the preamp. The high voltage connections are made with a molded plug, with fits on all seven sense wires at once and connects them to the two different potentials. Resistors are molded into the HV-connector to protect the wires during possible discharges.

On the other side each wire is individually connected to a capacitor, which in turn feeds the sense wire signal into a preamp. On both sides the connection to the crimp pin is done with little square tubes, which slide over the thick part of the pin.

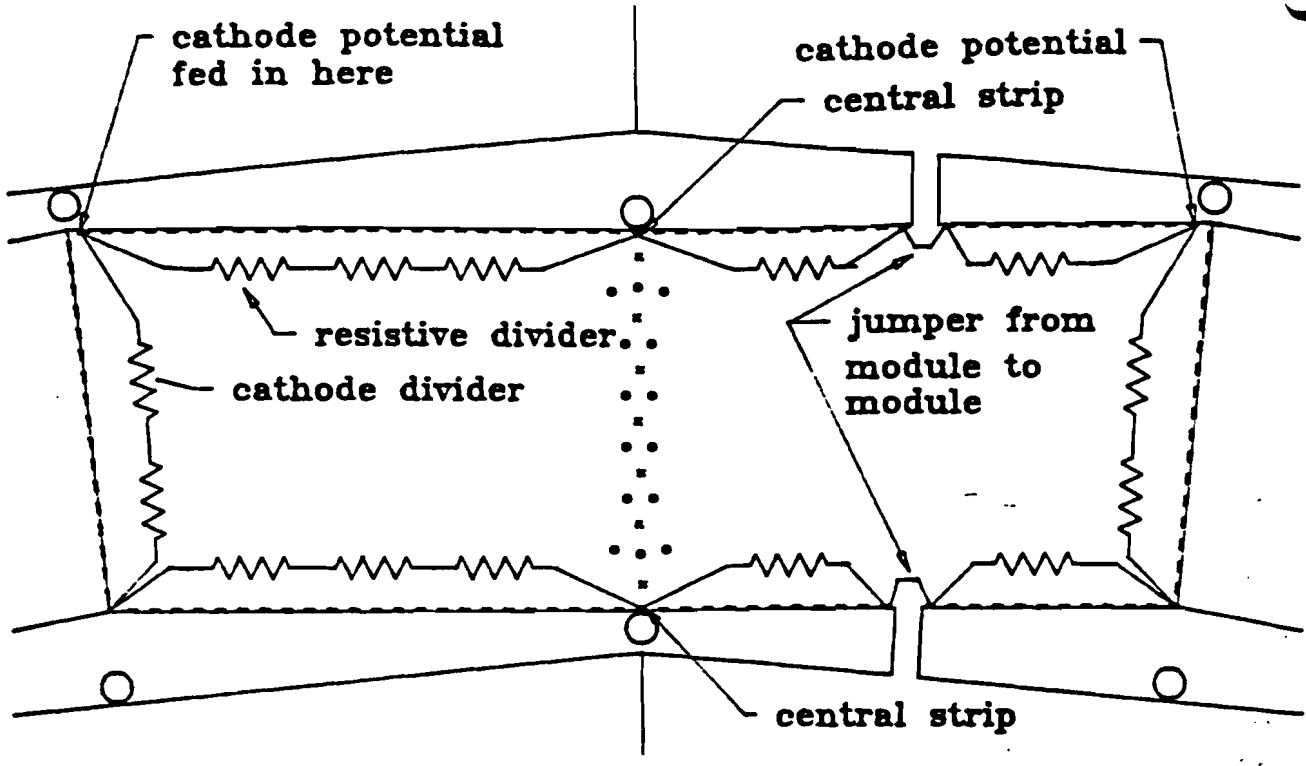

Figure 27 . Schematics of the electrical connections within a module and between neighbour modules

They are insulated with a teflon tube, which reaches to the bottom of the recessed hole in the plug.

The potential wires are all grounded. Before they are inserted into the end plug a printed circuit board is put on the plug. The pins rest with their shoulders on this board and make electrical contact. On the side where the signals are read out all the pins are connected together to form a good ground return for the signal, and are connected to a ground on the amplifier board. On the other side the traces are not interconnected, but they allow for easy access to the pins for testing and debugging of the chamber.

5.7. Wiring of the modules

2688 wires need to be strung in the Central Drift Chamber. Although small at the standard of many large drift chambers this is still a large enough number that a dedicated system to string the wires and to check them afterwards was developed and built. Due to the modular design of the chamber the wiring can be done one module at the time. This has the advantage that the wiring system can be considerably

simpler than if it would have to handle the full chamber at one time, and that the wires are easily accessible during the stringing process.

The system adopted is very closely modelled after one developed by Richardo De Salvo et. al. for the wiring of the CLEO upgrade central drift chamber ([24]) The basic idea of this system is to put the chamber vertical and to drop the wires through the chamber rather than to pull them along horizontally as in more conventional approaches.

At least two people are needed to string a wire in this scheme. One operates from the top of the chamber, the other from below the setup. The wire is kept on a spool which is driven by an electric motor suspended above the chamber. A metallic needle is connected to the wire and is threaded into the chamber. As the motor unwinds the wire the needle drops through the chamber. At the bottom a little permanent magnet is put through the feedthrough hole into the chamber. The needle is being attracted to the magnet and, if everything goes well, connects to it. An electrical circuit is closed by this contact and the motor stops abruptly. The needle and the magnet together are than fed through the bottom feedthrough by manually manipulating the motor.

Once the wire is fed through the chamber an additional foot or so is unwound from the spool to make sure that any part of the wire which might have been handled during the wiring process is not inside the chamber. The crimp pins are threaded onto the wire at the top and the bottom, pressed into their respective holes in the end plugs and the top pin is crimped. A weight is attached to the wire at the bottom and the second pin is crimped. Each wire is visually inspected for kinks or other irregularities before the next wire is started. After a module is completely wired all pins are recrimped at the ends with a "supercrimp". This is been done using a special crimp tool in order to clamp down on the end of the wire and avoid slippage.

Although in theory two people are able to operated the system, in practice three persons were usually involved. One person would work on the top of the chamber, one person sit below, and the third person would control the dropping down of the wire and inspect it after each operation.

Using this system and after some training it took about 60 seconds to completely string one wire, or roughly 2 hours for one complete module.

Fig. [28] shows a simplified drawing of the wiring stand. The oval objects at the side of the module are Helmholtz coils which were used to measure the tension of the wires after the stringing.

After the wiring was done, the wires were subjected to a period of over tension. The top plate of the wiring stand was moved away from the module to increase the

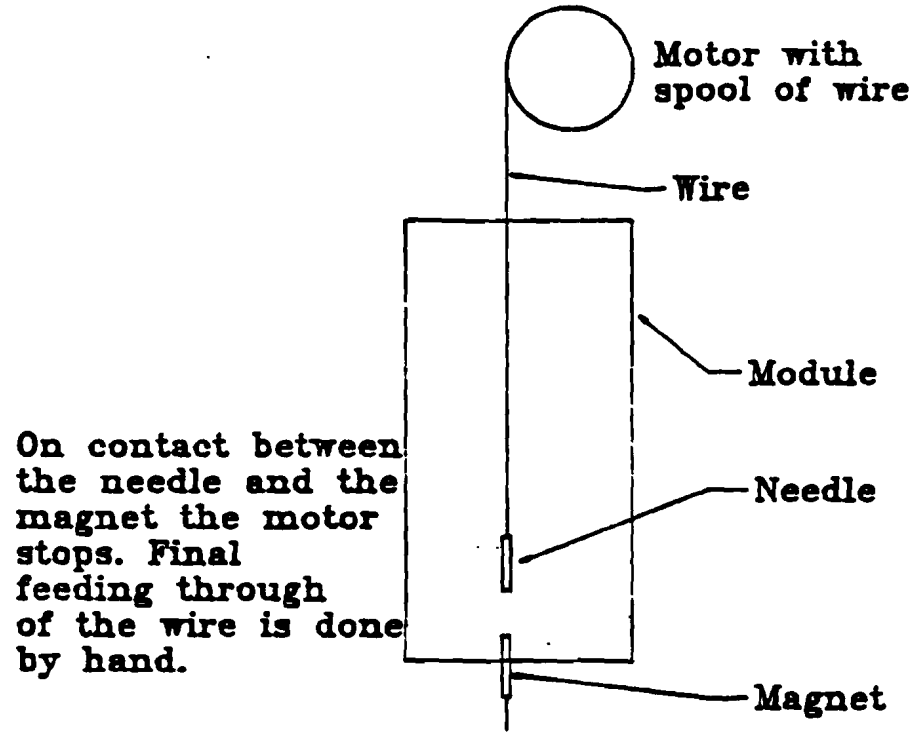

Figure 28 . Schematics of the wiring system

tension by about 10% for a couple of minutes. This was done to find any crimp pins who did not properly clamp on to the wire, and which later might start slipping.

After the over tension was relieved, the tension on the wires was measured. For this an PC based system was constructed (see [25] for a detailed description). A magnetic field is applied perpendicular to the wires and a current pulse is injected. The wire is deflected due to the resulting force and, after the pulse switches of, will vibrate at its natural frequency

$$\nu = \frac{1}{2l}\sqrt{\frac{T}{\mu}} \qquad (5-1)$$

where m is the mass of the wire, l the free length and T the Tension in the wire. Since the magnetic field is still switched on a current is induced in the wire with the frequency of the vibration. This current is digitized using a CAMAC based A to D converter, and read out by an IBM PC. A fast fourier transform is performed on the trace and the peak is found. The position of the peak in the fourier spectrum is the eigen frequency of the pulsed wire and is, according to Eq.(5- 1), directly related to the tension of the wire. Fig. [29] shows the measured distributions for wire tensions in sense wires and in potential wires respectively. These measurements were made 3

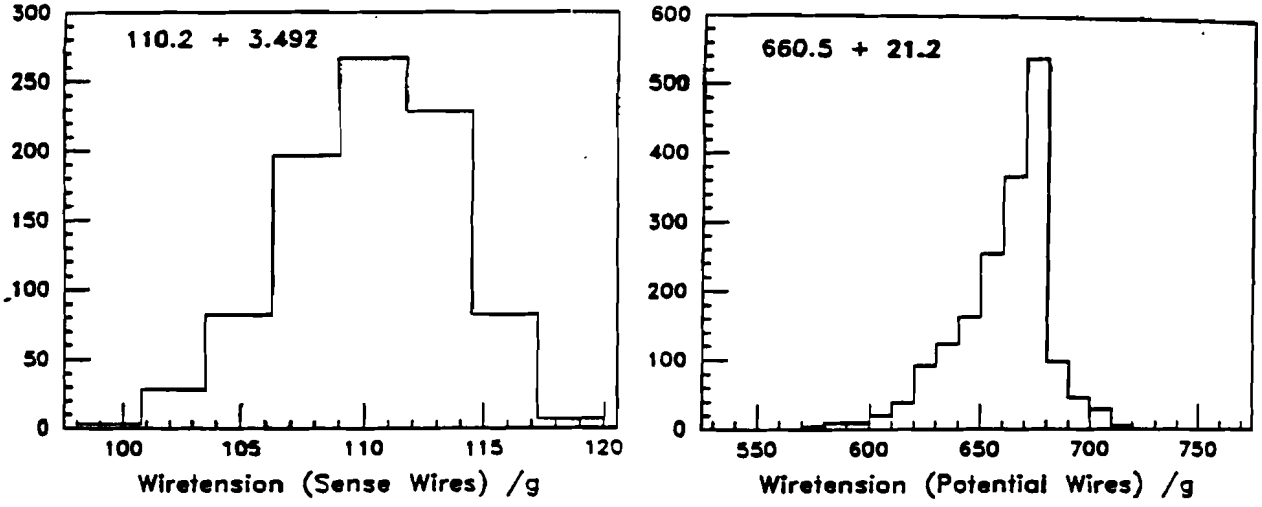

Figure 29 . Distribution of the measured wire tensions in the sense and potential wires. The nominal sense wire tension is 80 g, the nominal potential wire tension 600 g

months after the actual wiring of the chamber, after all modules had been installed in the CDC shell for a number of weeks. No slipped wire was found. The slightly asymmetrical shape of the distributions, in particular the potential wire one, indicates that some very limited slippage might have occurred immediately after the crimping, possibly in the period between the normal crimping and the super crimping. However the amount of slippage is very small around 7%. During the wiring any wire who deviated from the nominal tension by more than 5% was replaced. On the average this had to be done to about 1 wire per module. Once the modules passed the tension test the end plugs were released onto the G10 end plates and the module was removed from the wiring stand. They were stored in this state of reduced wire tension to avoid damage to the plastic shelves.

5.8. Assembly of the chamber

Once all the modules are assembled, wired and tested, they are ready to be inserted into the outer shell. For this, the endplate on the side of the preamps is mounted. The chamber is turned vertical. with the endplate at the bottom, and

the inner cylinder inserted and bolted to the endplate. Now the modules are inserted from the top one after the other and engaged into the lower endplate. However at this point they are not yet fully pushed into the holes, but rest lightly on the "O"-ring. As modules are being added the connections to neighbour modules are made. Once the ring of modules is closed the top endplate is carefully lowered onto the chamber. It will first engage with the standoff bolts from the drum, which positions the endplate with respect to the chamber. Then the 4 screws on each end plug will engage and key in each module to the endplate. They are now sitting completely to one side in the drum, with the "O" rings on all plugs not seated properly. Next each module is pushed up from the bottom until the modules is 0.2" away from the top endplate. This pushing is done in two steps, first about half the distance, then completely, so as to not stress the inter module connections more than necessary. At this point all "O"-rings are engaged in their respective holes and the top plate is bolted down. The pulling screws are inserted and the modules are fixed in this position.

The final step in the assembly of the chamber is the pulling out of the end plugs to their final position flush with the Al- endplate. Once this is done the whole wire tension is supported by the Al- drum, while the module only has to support its own weight. At this point the chamber is ready for mounting the electronics and connecting the HV systems.

6. The DØ central drift chamber: Delay lines

6.1. Introduction

A drift chamber as the DØ chamber easily measures the $r\Phi$ coordinates of a track, but not the z-coordinate along the sense wire. Different methods for doing this exist. One method, used for example in the MARK II upgrade chamber [26] is to use stereo layers for z-measurement. A set of sense wires is strung at an angle to the direction of the beam and allows together with the "normal" wires the reconstruction of the z-position of the track. Rather common is the use of charge division for the third coordinate. By reading out the signal on both sides of the sense wire, and by recording the pulse area in addition to the timing the z-coordinate can be calculated as essentially the ratio of the pulse heights. This method works best if resistive wires are used for the anode. The method chosen for the DØ central and forward/backward drift chambers is the readout of the third coordinate with delay lines. Here a long thin coil is run parallel to the sense wire and picks up the signal from the avalanche. The induced signal will start to propagate towards both sides on the delay line. By measuring the time on both sides the z-coordinate can be calculated. Delay lines offer some advantages over charge division, mostly in that they offer intrinsically a better z-resolution and pattern recognition power, however they introduce considerable material in the detector, need space next to the sense wires and complicate the construction of the chamber. Few experiment besides DØ so far has used delay lines for third coordinate readout in a drift chamber on a large scale [27], but other groups have done tests of such systems: [28]. The use of delay lines for third coordinate readout should not be confused with its use as a multiplexing device in proportional chambers (see e.g. [29]).

In the following chapter the basics of the operation of delay lines and their advantages, their disadvantages and the implementation in the case of the DØ chamber will be discussed.

6.2. Principles of Operation of Delay Lines

The delay lines used for position readout are essentially long and thin coils. They consist of a wound conductor, usually thin copper wire, and a ground return. The ground may be either on the outside of the line (this is e.g. the case for the lines of the CCOR group described in Ref. [1]) or in the inside of the line. This system forms electrically a transmission line with some distributed inductance, capacitance

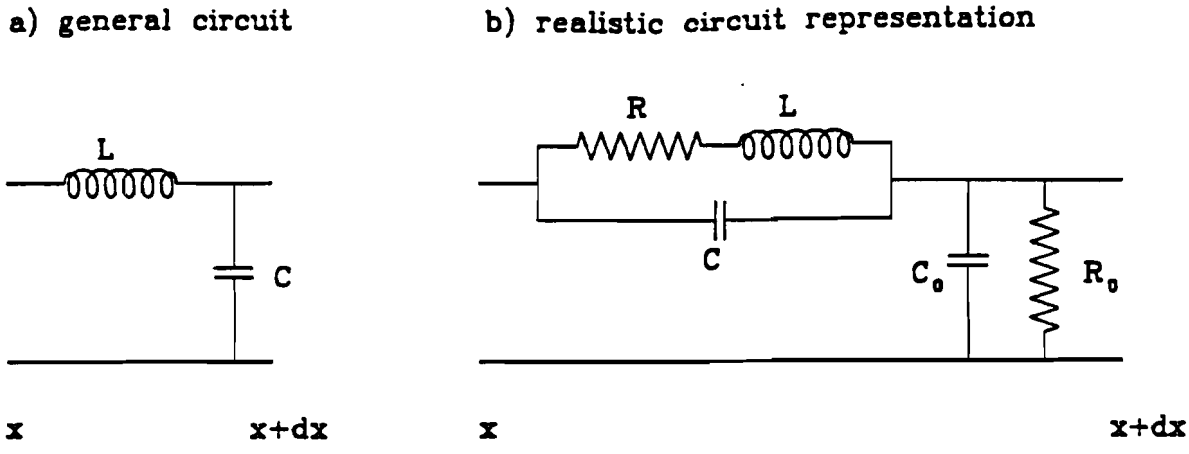

Figure 30 . Network representations for a delay line: a)general circuit b) realistic circuit. L=Inductance, C=Capacitance winding-core, R=ohmic resistance of the wire, C_0= Capacitance between neighbour windings

and resistance. A pulse induced on the line will travel down the line with a fixed velocity which is typically much slower than the speed of light.

Fig. [30] shows a generalized network with two complex resistances, one in series, the other in parallel. Z_1 is called the Impedance, $1/Z_2$ the admittance of the system. The diagram represents an infinitesimal length dx of the line. Applying the laws of Kirchhoff yields the following equations:

$$\frac{dV}{dx} = -Z_1(i\omega)I$$
$$\frac{dI}{dx} = -Y(i\omega)U(x) \qquad (6-1)$$
$$\text{where} \quad Y = \frac{1}{Z_2}$$

Taking the derivative with respect to x of both equations and replacing the single

x-derivatives one finds:

$$\begin{aligned} \frac{d^2I}{dx^2} &= Z(i\omega)Y(i\omega)I(x) \\ \frac{d^2U}{dx^2} &= Z(i\omega)Y(i\omega)U(x) \end{aligned} \qquad (6-2)$$

The general solution to this differential equation is:

$$U(x,i\omega) = Ae^{\gamma(i\omega)x} + Be^{-\gamma(i\omega)x} \qquad (6-3)$$

where

$$\gamma(i\omega) = \sqrt{Z(i\omega)Y(i\omega)} \qquad (6-4)$$

The current is connected to the voltage by:

$$\begin{aligned} I(x,i\omega) &= \frac{U(x,i\omega)}{Z_0} \\ Z_0 &= \sqrt{\frac{Z(i\omega)}{Y(i\omega)}} \end{aligned} \qquad (6-5)$$

Fig. [30] shows a realistic replacement circuit for a delay line. A piece of length dx of the line will have a certain characteristic impedance and ohmic resistance and a certain capacitance to ground. In addition this piece dx will capacitively couple to the next section dx' through the capacitance C_0. Since dielectric media are not perfect, there will be some losses to ground, described by the shunt conductivity G.

Using the generalized expressions for Z and γ derived above one finds:

$$\begin{aligned} Z(i\omega) &= i\omega L \frac{(1+\frac{R}{i\omega L})}{1-\omega^2 C_0 L\,(1+\frac{R}{i\omega L})} \\ \gamma(i\omega) &= i\omega\sqrt{LC}\,\{\frac{(1+\frac{R}{i\omega L})}{(1+\frac{G}{i\omega C})(1-\omega^2 C_0 L\,(1+\frac{R}{i\omega L})}\}^{1/2} \end{aligned} \qquad (6-6)$$

For the case of $|i\omega L| > R$ and $|i\omega C| > G$ (low loss approximation) one finds after

some algebra:

$$\begin{aligned}
\gamma &= \alpha + i\omega T \\
\alpha &= \sqrt{LC}\,\frac{1}{2(1-\omega^2 C_0 L)^{1/2}}\left(\frac{R}{L}+\frac{G}{C}\right) \\
T &= \sqrt{LC}\,\frac{1}{2(1-\omega^2 C_0 L)^{1/2}}\left(1+\frac{1}{8\omega^2}\left(\frac{R}{L}-\frac{G}{C}\right)^2\right) \\
Re\ Z &= \sqrt{\frac{L}{C}}\,\frac{1}{2(1-\omega^2 C_0 L)^{1/2}}\left(1+\frac{1}{8\omega^2}\left(\frac{R}{L}+\frac{G}{C}\right)^2\right) \\
Im\ Z &= \sqrt{\frac{L}{C}}\,\frac{1}{2(1-\omega^2 C_0 L)^{1/2}}\,\frac{1}{2\omega}\left(\frac{G}{C}-\frac{R}{L}\right)
\end{aligned} \qquad (6-7)$$

As long as $\omega^2 C_0 L$ is small compared to 1 both the total delay time T and the real part of the impedance do not depend explicitly strongly on the frequency. Only indirectly via a possible frequency dependance of L or C will either one change. For $\omega^2 C_0 L \leq 1$ no wave propagation is possible any more. An interesting special case is $R/L = G/C$. In this case $T = \sqrt{LC}/2(1-\omega^2 C_0 L)^{1/2}$ and the phase shift is proportional to ω. A transmission line with these properties is called a Heavyside cable.

6.3. Measuring z with Delay Lines

As pointed out in the introduction a delay line operates on a pulse induced from the sense wire. As the charge is accumulated on the sense wire a charge of opposite sign is induced on the delay line and starts traveling toward the end of the line. The signal is read out at both ends and timed with respect to the time of arrival of the electrons on the sense wire. In principle this method can also be used directly on the sense wire signal, but since the velocity v of the delay line is small compared to the velocity of propagation on a sense wire it is possible to measure the position of the pulse along the line more accurately that it can be done for a sense wire. The difference of those two times is proportional to the z-position along the line:

$$\begin{aligned}
t_1 &= t_l + t_d \\
t_2 &= t_r + t_d
\end{aligned} \qquad (6-8)$$

where t_l, t_r and t_d denote the time for the signal to reach the left side of the delay line, the right side of the delay line and the drift time of the electrons, respectively. The sum of the left and the right time ought to be constant and equal to the total

delay time T:

$$\begin{aligned} T &= t_l + t_r \\ &= t_1 + t_2 - 2\,t_d \\ &= const \end{aligned} \qquad (6-9)$$

The z position measured in a system where z=0 in the middle of the line is then given by:

$$\begin{aligned} \Delta z &= \frac{1}{2} v\,(t_1 - t_2) \\ &= \frac{1}{2} v\,(t_l - t_r) \end{aligned} \qquad (6-10)$$

For the z-position the dependance on the drift time cancels. An important question is how one knows which left and which right times belong to the same pulse. This is obvious if there is only one track in the chamber and therefore only one signal on the delay line. If however more than one avalanche arrives during a period of the order of the total delay time of the delay line, some confusion can arise. Eq.(6-9) allows in many cases to disentangle the different contributions. By requiring that after correcting for drift times left and right times add up to the total delay time of the line all but those signals which overlap in drift or overlap on the line can be resolved. Fig. 31] illustrates the different possibilities. Shown is an area in the chamber, with d the direction of drift and z the coordinate along the delay line. (0,0) in this plot is the actual position of a track in the chamber. A second track may lie anywhere in the $\Delta d\,\Delta z$ space limited only by the physical dimensions of the chamber. If the track lies outside of either strips, both signals on both sides of the delay line can be resolved. An unambiguous determination of z is possible. If the track falls within one of the strips, but outside of the central diamond, the signals can be differentiated on one side of the line, but not on the other. In this case the reconstruction of the two tracks is still possible, but at the cost of a somewhat larger calculation and error. If the second track lies within the central diamond, both pulses on either side overlap and no reconstruction is possible. This plot was made using a drift velocity of $40\mu m/ns$ and a delay line velocity of $0.24cm/ns$. It was assumed that two pulses can be distinguished if they are separated by 50 ns. This corresponds to a double track resolution of 2 mm in drift and 12 cm in z.

The cases in which pulses partially overlap warrant some special attention. In the following only the case of two tracks in one cell will be discussed. More than two tracks can be treated essentially in the same manner, the results however will be somewhat more complicated.

The first nontrivial case is the one, where both delay lines are separated and both pulses overlap in drift. Since the determination of z does not depend on the

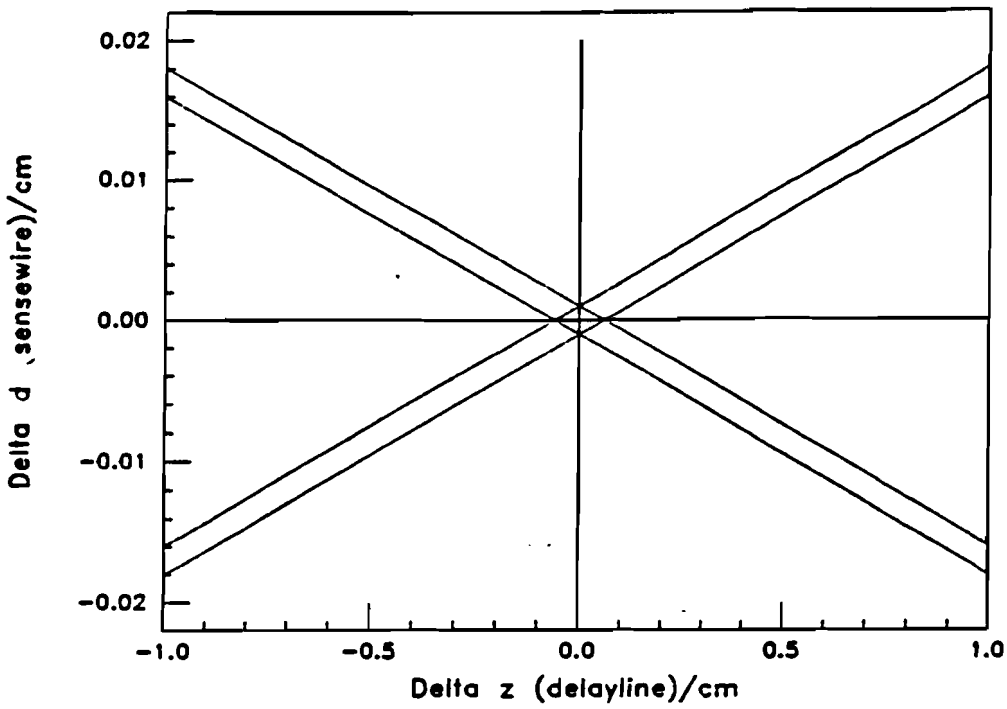

Figure 31 . Areas of overlap on the delay line for two tracks in the chamber. The first track lies at 0.0 in this plot, the second a distance Δd Δz away. If it falls in one of the strips one side on the line will overlap; it it falls into the diamond shaped area in the center both sides will overlap

knowledge of the drift time, this is no problem for calculating the z-coordinate. For the track with the shorter drift time, a full 3D point can be calculated, for the second track, only z will be known with normal precision.

The second possibility is that the signals measured on one side of the delay line overlap, but are separated on the other side and that the drift times for the two tracks are separated. In this case, the fact that the sum of the left and the right delay times have to be equal to the total delay time of the line allows to disentangle the two tracks. On the side on which the signals overlap the time of the first arriving pulse can be measured. By pairing this with both of the drift times, computing the resulting sums and requiring that they add up to the total delay time, it can be decided, which time on the other side of the delay line belongs to the same pulse. One then knows, which drift time pairs up with the other track, and using the measured delay time on the non overlapping side, can calculate the z-coordinate of this track as well. However because one needs to use explicitly the total delay time and the drift time this position will be somewhat less precise.

If the delay line pulses overlap on one side and both drift pulses overlap, only one

Description	measured	Δz	$\sigma^2_{\Delta z}$
drift & delay pulses resolved	t_{di}, t_{ri}, t_{di}	$\frac{1}{2}v(t_{di}-t_{ri})$	$(\frac{\Delta z^2}{v^2}\sigma_v^2+\frac{1}{2}v^2\sigma_t^2)=\sigma^2_{\Delta z,0}$
Drift overlaps, delay resolved	t_{di}, t_{ri}, t_{d2}	$\frac{1}{2}v(t_{di}-t_{ri})$	$\sigma^2_{\Delta z}$
delay ovlps. on one side, drift resolved	$t_{di}, t_{r1}, t_{di}, T$	$\frac{1}{2}v(t_{d1}-t_{r1})$	$\sigma^2_{\Delta z,0}$
		$\frac{1}{2}v(2t_{d2}-t_{d2}-T)$	$\sigma^2_{\Delta z,0}+\frac{5}{4}v^2\sigma_t^2$
Drift overlaps, delay overlaps on either side	$t_{d1}, t_{d1}, t_{r1}, T$	no individual reconstruction possible	$\approx \sigma^2_{2\ track}$

Table 1.

Measurable variables and expected resolution for two tracks seen by the delay line in one cell depending on whether all or only some of the four possible pulses can be resolved. A subscript "i" means, that for this variable all possible measurements can be done. "1", that the earliest arriving pulse can be measured, etc.. To simplify the table, it has been assumed, that the timing resolution for delay lines and sense wires is equal.

z-position can be determined. As before the early arriving track can be measured in drift. Following the procedure outlined for the second case, z can be calculated for this one (this is possible, because the pulse which arrives first in drift is also the one which will arrive first on the delay line side, where the pulses separate). For the second track, the z determination will be less precise, since the drift time is known only to within 1 $\sigma_{2\ track}$.

The last and worst case is the one, where both drift and delay line pulses overlap. Here not too much can be done. No statement is possible about which pulse pairs up with which. The z-position and the drift position can be determined only as an averaged position between the two tracks with an error comparable to the 2-track resolution in both drift and delay. Only if the tracks separate later in the chamber some degree of coordinate determination can be achieved by fitting a track and minimizing its χ^2. Table 1. summarizes the different cases.

As one can see, in most cases the track position can be reconstructed with good accuracy. Nearly always some part of the information can be recovered and used to arrive at some measurement of the z-position of the track. According to table 1. only in the case where both the delay line pulses and the sense wire pulses can not be separated, a sizeable deterioration of the resolution takes place. Even in the third case, where the delay line pulses overlap on one side, one track can be measured

with normal accuracy, the other one with somewhat smaller precision (typically for $\sigma = 2\,mm$ for the line, the second track would be determined with a σ of 3.5 mm).

The possibility to retrieve information on tracks with partially concealed information is one of the strong points in favor of delay lines. Charge division e.g. does not offer this possibility. In a system with charge division the sense wires are made from a resistive wire. The charge of the avalanche splits up between both sides of the wire. The measured charge depends on the distance traveled. If one measures the signal on both sides, the z-position can be determined as essentially the ratio of the two pulses [30]:

$$z_1 = l\,\frac{Q_2}{Q_1 + Q_2} \qquad (6-11)$$

where Q_1, Q_2 are the measured charges on either side and l the length of the wire. This formula is only correct for parts of the wire away from the immediate end. For single tracks accuracies of around 1% of the wire have been obtained.

The only measurable quantity here is the charge detected on both sides. If more than one track overlaps, it is impossible to tell the different contributions apart. Other than in the case of delay lines no additional constraints exist which would allow the disentangling of the two or more tracks.

Another possibility to measure the z-coordinate along the wire is the installation of "stereo layers" in the chamber. Stereo layers are sets of sense wires which are strung at an angle to the normal sense wire. In a collider environment with a cylindrical drift chamber like in DØ the stereo angle has to be kept small, if one doesn't want to separate stereo and non stereo layers by a thick dead region. The achievable resolution in z degrades like $1/sin(\theta)$ with the stereo angle. At practical angles of less than 5° this translates into a resolution of the order of cm.

Delay lines on the other hand allow resolutions of better than 0.2% of the line length. The drawback is that one has to introduce a rather large amount of material into the chamber and that one has to find a suitable way of mounting and supporting the lines parallel to the sense wires.

6.4. The 'Stony Brook' Delay lines

In table 2. a number of different delay lines are compared. # 1 and # 2 are early DØ prototypes, # 3 is a line built for the CCOR experiment, # 4 and # 5 are late designs showing the eventually adopted geometry but from somewhat opposite design philosophies.

Fig. [32] shows the attenuation for lines #1,3,4 and 5. It is interesting to note, that the cutoff frequency (the frequency, at which the signal is attenuated to half the

Line #	l cm	turns cm^{-1}	L $\mu H/cm$	C pF/cm	Z Ω	v cm/ns	$\frac{T_D}{T_R}$	$\nu_{1/2}$ MHz
1	48	167	6.88	18.65	540	0.096	10.4	10.5
2	44.4	152	9.68	10.36	1090	0.110	9.53	7.24
3	147	80	1.39	4.49	558	0.455	5.4	–
4	132	66	5.4*	18.9	285	0.18	18.0	14..
5	180	267	8.928	2.576	1530	0.235	32	20

Characteristic properties of a number of different delay line designs.
1 Insulating core, 2/1000" thick copper ground plate, 5/1000" Kapton dielectric, 2.4/1000" DIA. cu-wire.
2 Same as #1, except that the dielectric is 15/1000" thick
3 flat insulating core 2.5x 0.8 mm Vetronite, wire wound on core, Cu-vetronite strip glued to the outside of the line on one side as ground strip (CCOR collaboration)
4 1/16" C-fiber-epoxy core, 5/1000" heat shrink tubing as dielectric, 0.006"Cu wire
5 1/16" c-fiber-epoxy core, 16/1000" Teflon dielectric, 0.0015" Cu wire
Line # 5 is of the final design.
Cuttoff frequency is defined as the frequency, at which a pure sin-wave gets attenuated to half its amplitude normalized to a 1kHz signal. Capacitance and Inductance have been measured at a frequency of 10 kHz. Rise times are measured from 10% to 90% of the signal.
*For this line no direct measurement of the inductance was available. The cited value was calculated from the measured capacitance and impedances $L = Z^2C$

Table 2.

value at 1kHz) is rather similar for all the lines and seems to be weakly correlated to the number of turns on the line.

A rather good figure of merit for a delay line is the ratio delay time over rise time. This measures essentially the dispersion in the line and therefore the ability of the line, to propagate a short pulse without distortions. This is important, because a short pulse allows a more precise measurement of its timing. This also allows a harder shaping of the tail of the pulse, thereby making it possible to shorten the pulse more and improve the double track resolution. Ideally the line has a small enough dispersion and attenuation so that the pulse shape is dominated by the shape of the pulse on the inducing sense wire, rather than by the properties of the line itself. If this ideal is reached, the pulse shape will not vary as a function of position along the line and thereby the accuracy of measuring z will not depend on z. The delay time over rise time ratio is significantly better for the last two lines in the table, with line #5 being by far the best.

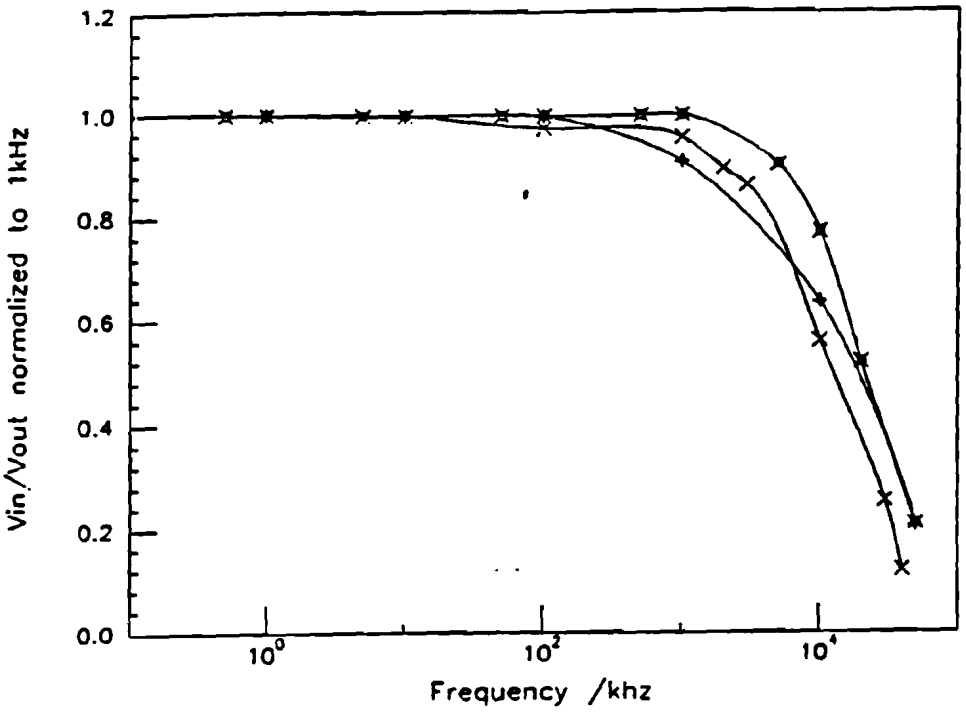

Figure 32 . Attenuation as a function of frequency normalized to the attenuation at 1 kHz for different delay lines

The main difference is the use of a carbon fiber rod as the core in lines #4 and #5. The carbon fiber rod is made of fibers running lengthwise in an epoxy matrix. Each individual fiber is conductive, but insulated from its neighbours by the epoxy. This produces a core material which has a low longitudinal resistance, but a high transverse one. (The use of Carbon fiber rods as cores for delay lines was first suggested by Mark Strovink, Berkeley).

Lines 4 and 5 are made with somewhat opposite design philosophies in mind. No. 4 stresses the capacitance in the line, thereby achieving a line with a low speed and low impedance. Line no. 5 has a comparatively much higher inductance and lower capacitance. The result is a line with low speed and very high impedance. Both lines use the carbon fiber core, and get good delay time over rise time ratios. The main difference between them is the use of a thick Teflon * dielectric in line #5.

The high impedance line is the favorable design. Frequency response and T_D/T_R are better.

There are however some problems with choosing a high impedance design. It is

* Teflon is a trademark of the DuPont Company, Delaware

not easy to extract a charge from a system with an impedance of more than $1k\Omega$. Typical preamp designs have input impedances of the order of 100Ω. These different impedances will have to be matched. The simplest solution is to put a resistor in series with the preamp input so, that this resistor and the input impedance of the preamp add up to the total impedance of the line. Now however the signal seen by the preamp is only 100/1500 of the signal on the line. In addition a series resistor represents a source of noise. The rms equivalent noise per $Hz^{1/2}$ is given by

$$\vec{e_s^2} = 4kTR_S \qquad (6-12)$$

where k is the Boltzmann constant, T the temperature in Kelvin and R_S the value of the effective series resistance of the system [31].

An alternative method for readout has been proposed by V. Radeka [-1]. Instead of using a real resistor to terminate the line, a capacitor in a feedback circuit can be used. This simulates a resistor without introducing the noise due to a real "warm" one. This method is called "cold termination". Theoretically the noise can be reduced by

$$\eta_f^2 = \frac{n^2 Z_o}{R_S}(1 + 2\,\frac{R_S}{Z_o}) \qquad (6-13)$$

For $Z = 1500\Omega$ and $R_S = 100\Omega$ this improves the signal to noise ratio by a factor 4.1. Fig. [33] shows the circuits for the two possibilities. Although the cold termination promises a sizable improvement of the signal to noise ratio, for the DØ chamber the easier way of using the same amplifier as on the sense wires was chosen. The main reason for this decision was the availability of a integrated charge sensitive amplifier, while for cold termination an equivalent circuit would have had to be developed. For a future upgrade of the chamber however this option is being explored.

6.5. Production of the Delay lines

In order to produce the 256 delay lines needed in the central drift chamber with consistent quality a machine was designed and built, which would accomplish this task. The machine consists of two main components: A system which moves the core of the delay line linearly upwards, and a winding head, which rotates around the core and winds the wire on it. The goal of the machine is to wind the wire on the core with constant tension and to lay every wire immediately next to the one before.

The basic idea of the delay line winder is that the core is slowly moved with respect to the winding head, but does not rotate. The head spins around the core and lays the wire, but does not move linearly. The whole system is mounted vertical

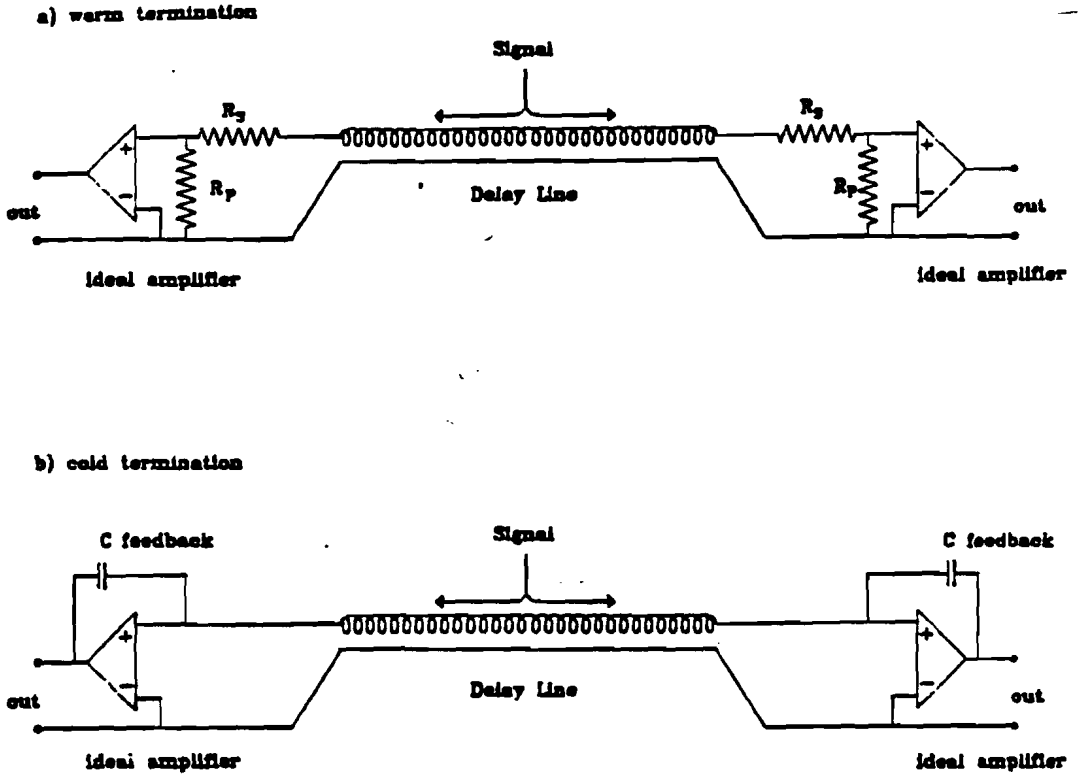

Figure 33 . Circuit diagrams for a) warm termination b)cold termination of delay lines

with the core moving up in order to minimize problems due to sagging of the core etc..

The linear upwards movement of the core is split into two tasks: a rough positioning of the core within a few mm to the right height and a fine correction of the core position to follow any variations in wire thickness etc. A linear actuator [32] is coupled to the motor which spins the winding heads and pulls a lever arm system slowly upwards. The speed is set such that for every revolution of the winding head the lever arm moves up by approx. the thickness of the wire. The core of the line to be wound is fixed to one side of the lever arm (see Fig. [34]). The other side of the arm is balanced by a weight which, as the line becomes longer and more wire is wound onto it, is continuously adjusted as to nearly balance the weight of the delay line. There is always a small remaining weight which pushes down on the line. As the winding head lays another turn of the wire on the core, the line itself constantly pushes down on the wire and makes sure that no spaces are left between the old and the new windings. In other words, as a new turn of the wire is laid, the wire itself pushes the line up by just the correct amount. The lever arm system makes sure that the push of the line on the wire is small and remains constant over the whole winding

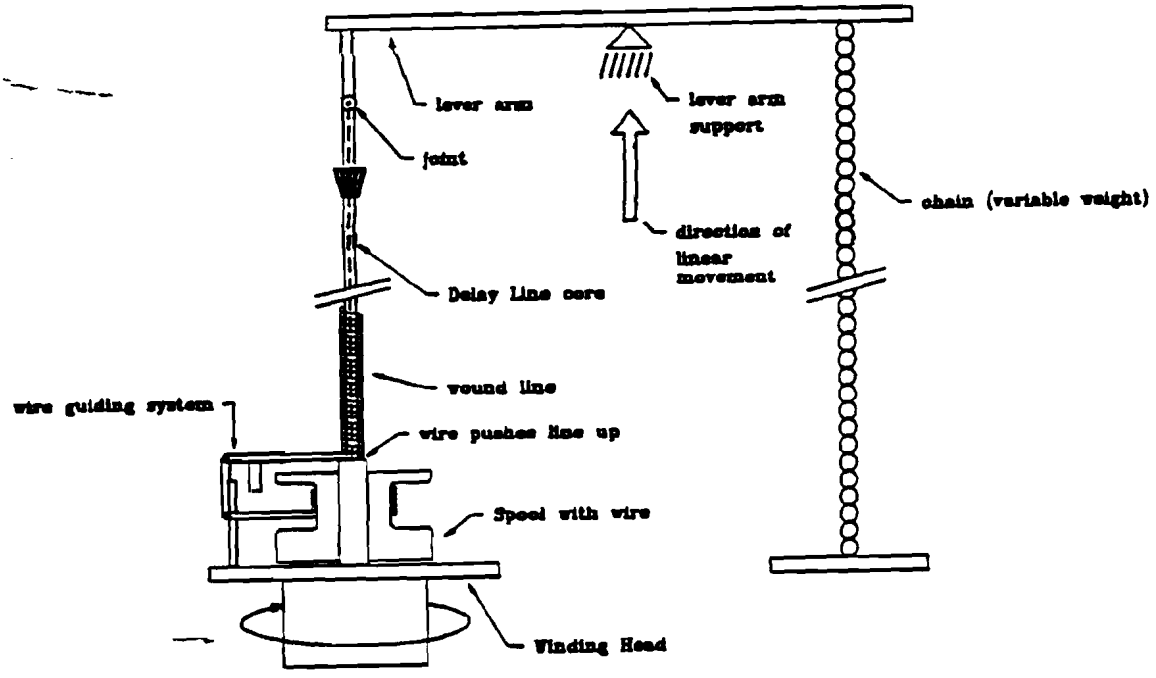

Figure 34 . The delay line winding machine (not to scale)

cycle.

The winding head is responsible for laying the wire down onto the core with a constant tension. For this a mechanical feedback system is installed which regulates the tension. Fig. [35] shows a drawing of the winding head. The core passes through the center of the plate. The coil with the wire sits in the center of the system, with the line passing through its center. The wire is guided through a system of wheels from the coil onto the brake arm (1) and then over the guide wheel (2) onto the core. A spring presses the brake arm on the wire coil. Only if there is tension on the wire will this brake be released. An adjustment mechanism (3) allows the tension to be set to the desired value.

Using this machine about 300 delay lines were produced. Fig. [36] shows the density of windings on the core as measured during the winding of the lines for 244 delay lines. Both a scatter plot relating the density of the windings to the serial number and thereby the production sequence and a distribution of the densities are shown. At around line # 280 there is a clear change and the spread becomes much larger. The reasons for this are not completely known, it does however coincide with a change of operator of the machine.

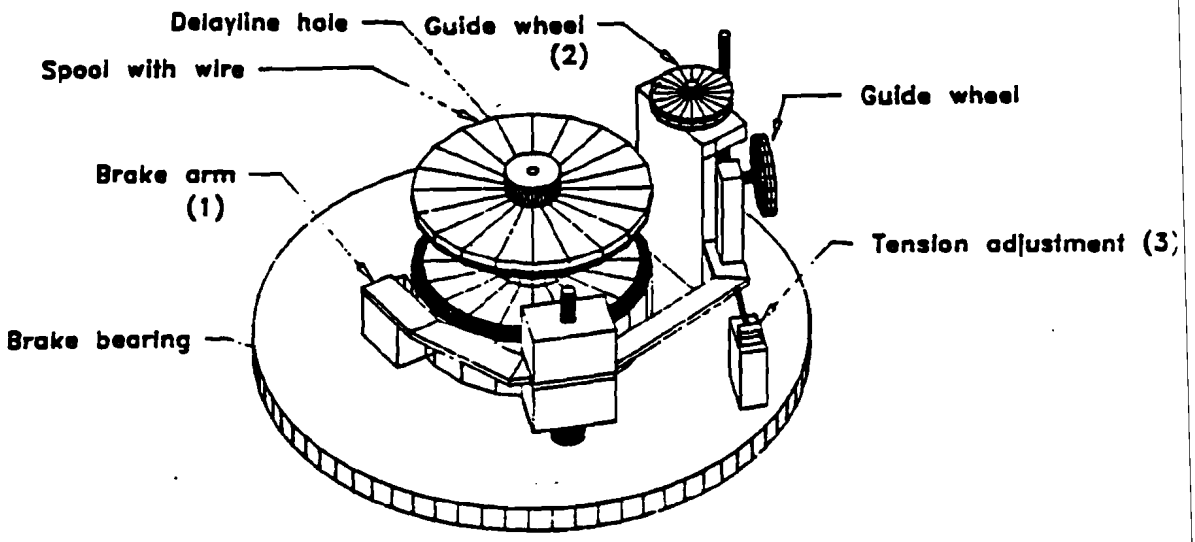

Figure 35 . Schematics of the winding head for the delay line winding machine.

If one assumes that the line can be described by an ideal very long and thin coil the standard formulas for the capacitance and inductance of a long thin coil apply:

$$C = \frac{2\pi\epsilon_0\epsilon_r}{l\ln(a_2/a_1)}$$
$$L = \frac{\mu_0\mu_r N^2\pi}{4l}(a_2^2 - a_1^2) \qquad (6-14)$$

where a_1 and a_2 are the radius of the core and of the windings respectively.

6.6. Calibration of delay lines

In order to be able to correct for the inhomogeneities of the delay lines discussed in the previous section, each line was individually calibrated after it was inserted into the module. A pulse was induced in the line on 16 points along z, and the timing of theses pulses were measured. From this an average velocity for each line was obtained, and a detailed plot of the deviation of the actual line velocity from this average as a function of z was made. Fig. [37] shows a schematics of the calibration system

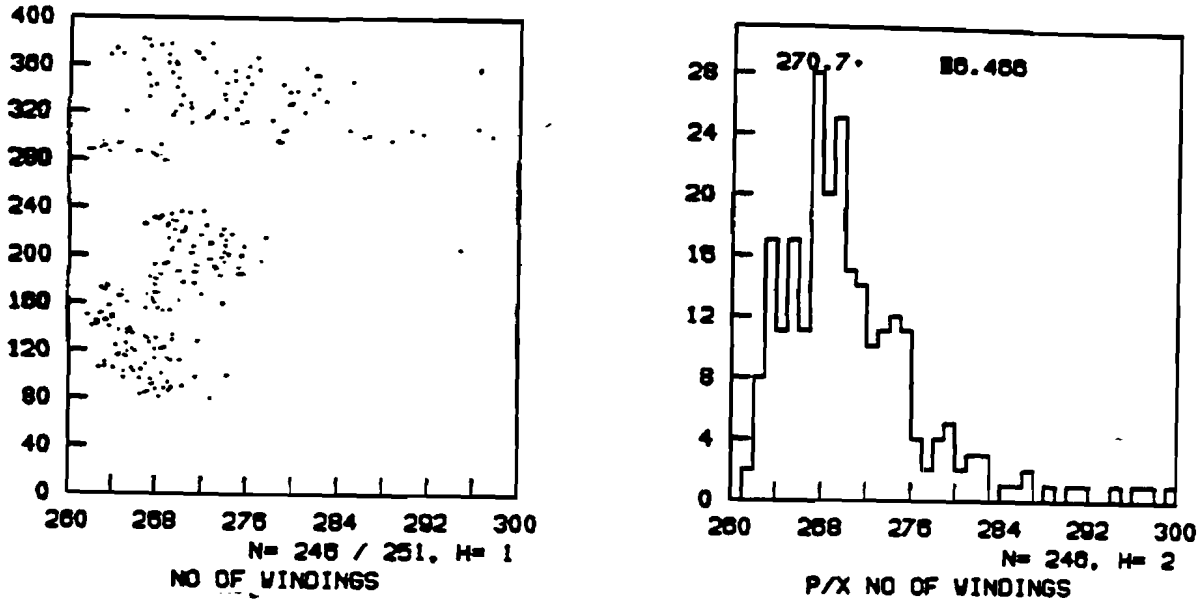

Figure 36 . Number of windings per cm on the delay lines as measured during the winding process and scatter plot of density of windings vs. serial number (=production time)

used. More details about the system can be gotten from [33]. Here only the results of the calibration shall be discussed.

Fig. [38] shows the deviations from a perfectly linear line, measured in mm. Two things should be noted: the deviations appear to be systematic, not randomly scattered around the mean, and they are within one sigma of the line resolution. It is therefore sensible to correct each delay line time as a function of z and try to improve the resolution, but for many applications a reasonable z determination is possible by using the average velocity.

In Fig. [39] shows a plot of the measured delay line velocities from the calibration. If one compares this with Fig. [37], it is interesting to note that both scatter plots have a "spike" towards smaller velocities / larger winding densities at around the same serial number 290. This might indicates that the observed deviations from the constant delay line velocity actually are caused by the nonuniform densities of windings. A definite statement however is difficult.

Fig. [40] shows the effects of the inhomogeneities on the overall performance of the lines. If one does not take the local variations of the velocities into account,but only uses the average individual velocities, the resulting residual distribution has a

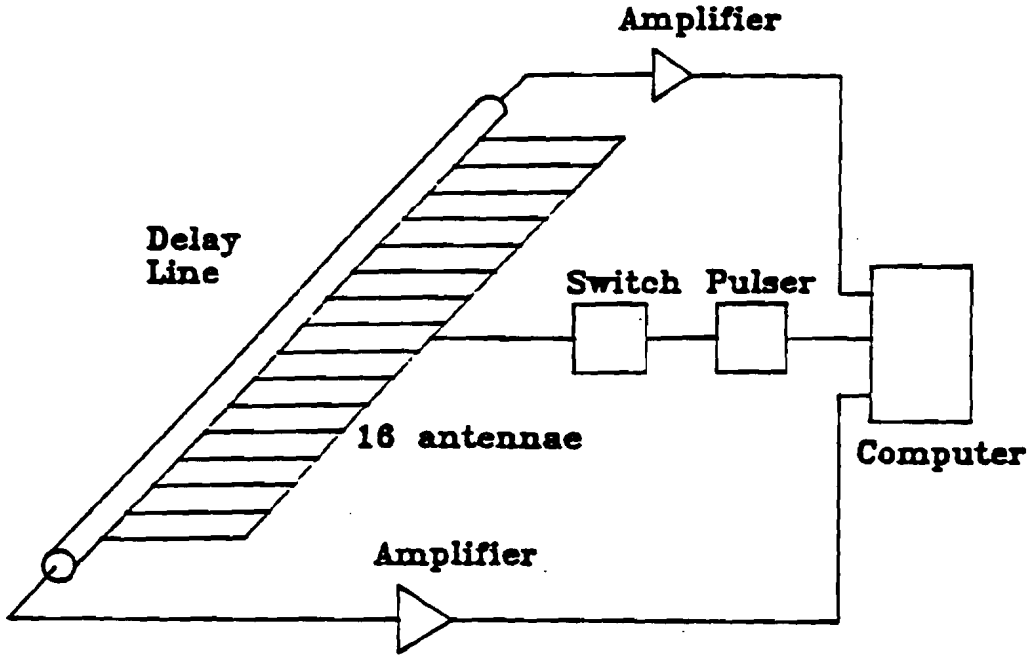

Figure 37 . System to calibrate the delay lines

sigma of 1.1 mm. This is about half the quoted sigma for the lines. For most purposes this is probably good enough and a deterioration of the line resolution from e.g. 2.5 to 2.75 mm will not be noticeable.

To summarize it has been shown that delay lines can be wound consistently with the density of windings constant on the 3 % level ($270.7cm^{-1} \pm 2.4\%$) . The measured variations in average velocity might be due in part to variations in winding density. Within one line the velocity varies locally in a not random manner. By measuring the velocity for 16 points along the line a individual line calibration is possible. However the average deviation from the straight line fit is of the order of $(1/2)\,\sigma$ of the intrinsic position resolution.

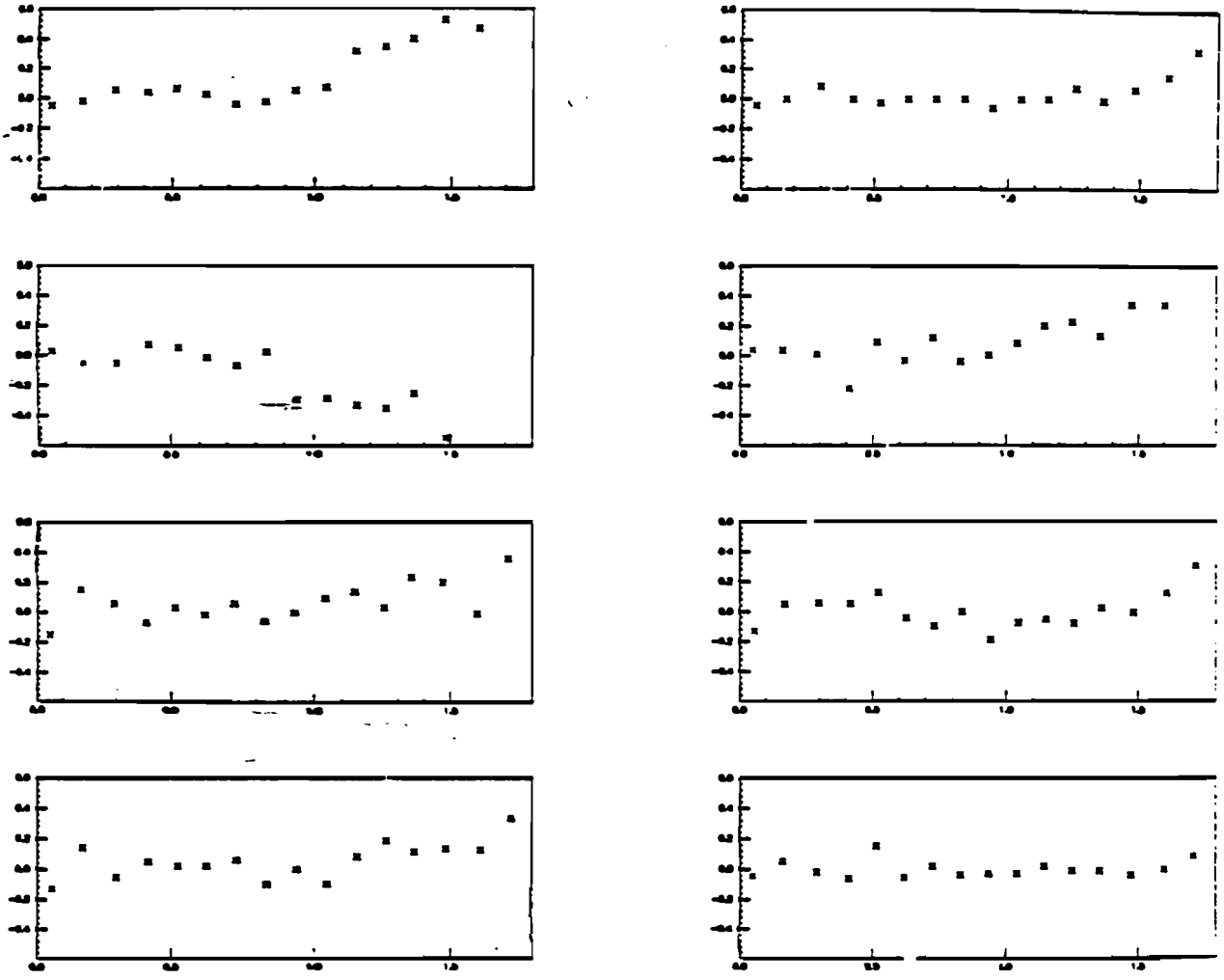

Figure 38 . Deviations from linearity for the delay lines in module #5. The horizontal scale is the z-coordinate in meter. the vertical one the z-deviations from an assumed perfectly linear line with the average velocity as measured in the calibration, in mm. Each row of 2 plots represents one layer in the module, with the top row corresponding to layer #0, the left top plot to line #0.

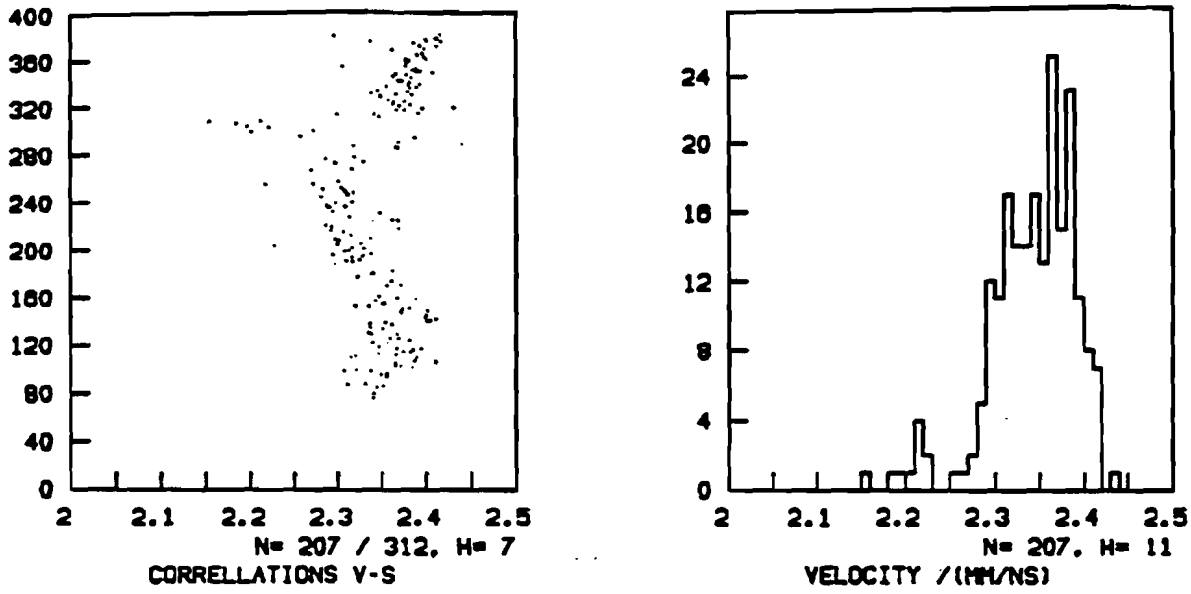

Figure 39 . Distribution of the velocities measured during the calibration, and scatter plot of velocities versus serial number of the line

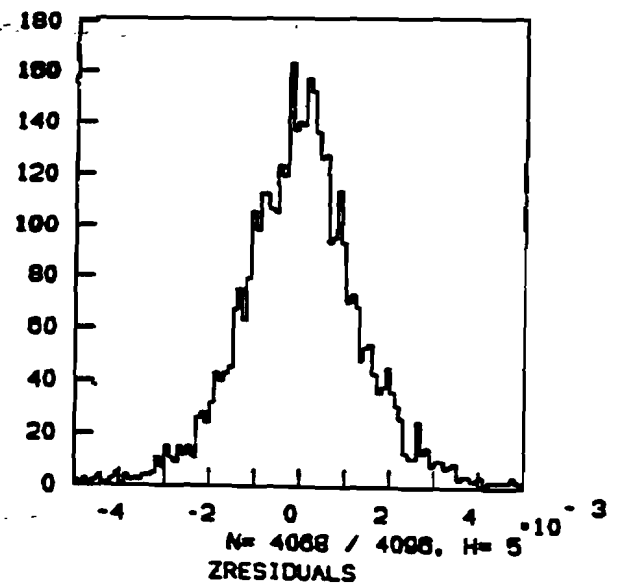

Figure 40 . Residuals (deviations of the calibration measurements from the ideal value (=line fitted with the average velocity)

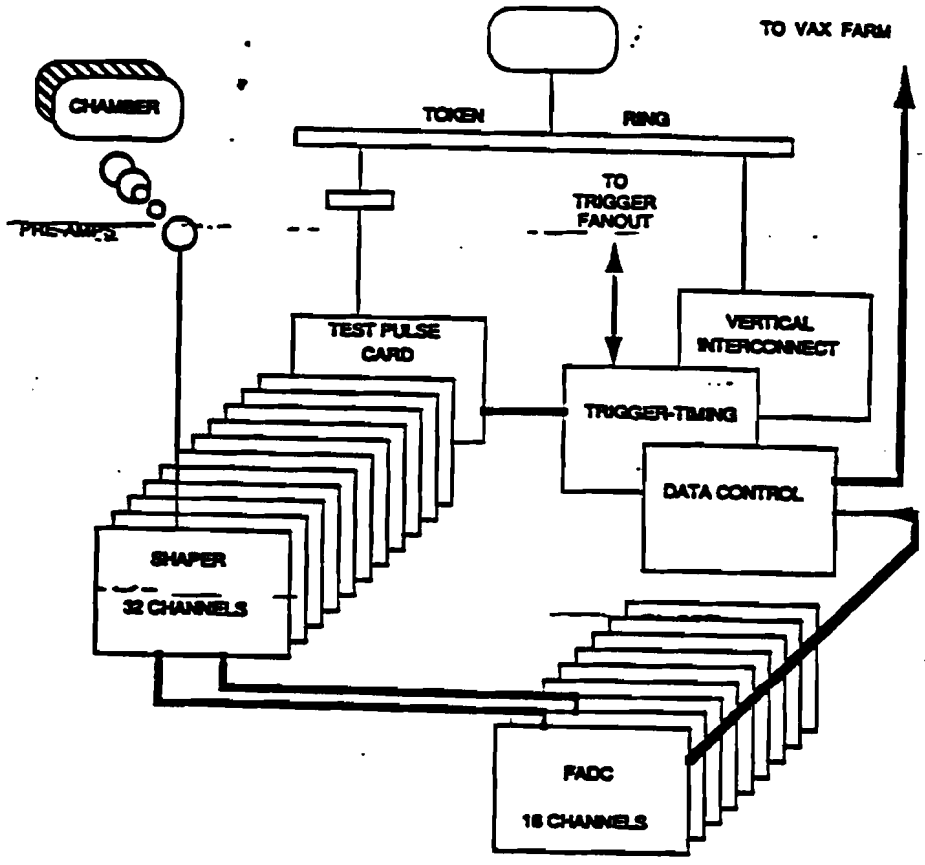

Figure 41 . Central tracking electronics

7. The DØ central Drift chamber: Electronics

In this chapter a brief description of the complete electronic chain starting at the sense wires/ delay lines and ending with the reading of the data into the computer is given. It is meant only to give an overview of the electronics involved, not to provide an in depth explanation of every component. For more detail a number of engineering notes exist [34], [35], [36], [37].

Fig. [41] shows a general layout of the central tracking electronics chain. Analog signals go through three stages: after the preamp they are amplified and shaped in the shaper amplifier, then sent to the analog part of the FADC, where they are once more amplified and, using a special bilinear amplifier, compressed to an 8 bit total dynamic range. After this the signals are digitized. They are compressed by removing those parts of the traces which are only base lines, and sent out to the μVax data acquisition system.

7.1. The Preamp

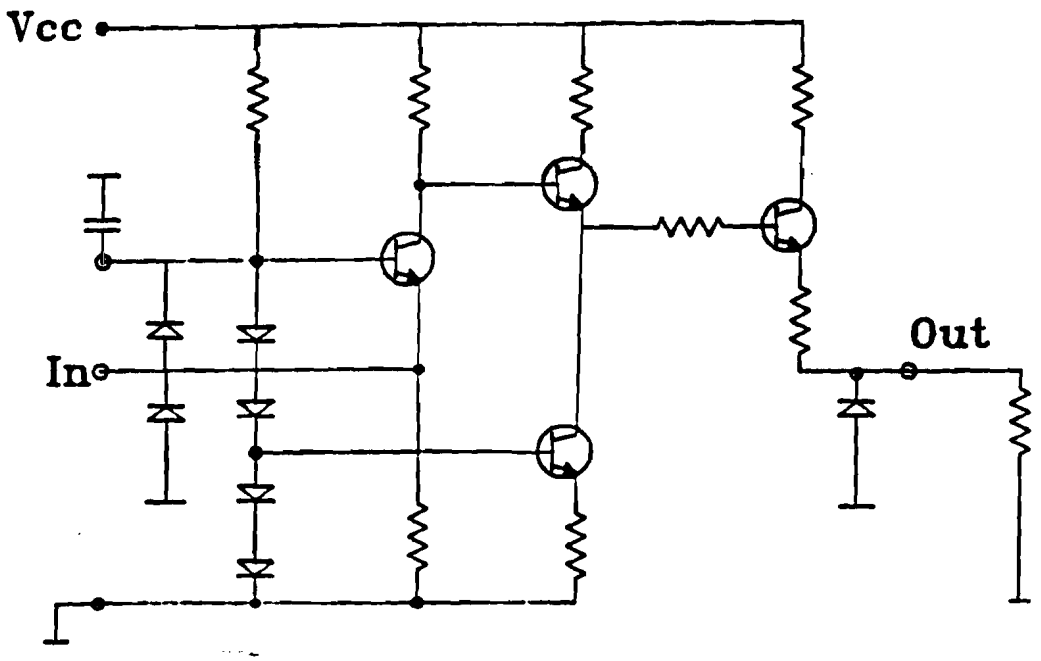

Figure 42 . Schematic of the Fujitsu MB43458 charge sensitive preamplifier

A special hybrid was developed for the DØ central tracking detectors with 8 channels of charge sensitive preamps, test pulse inputs and spark protection. The preamp is based on the Fujitsu MB43458 chip, a 4 channel charge sensitive preamplifier. Fig. [42] shows a schematic of one channel of this chip. This amplifier has a common base input stage followed by a two stage emitter follower. If a negative current arrives at the input, the current through the collector of the input transistor will increase by the same amount. This in turn drops the potential at the base of the first transistor of the emitter follower by $\Delta V_b = R_c * \Delta I_c$ for times large compared to the input time constant given by the 15kΩ resistor and the total capacitance of the collector to ground.

The two emitter followers simply act as a driver for the output line with a voltage swing of ΔV_b. The input current pulse ΔI_i is converted into an output voltage swing $\Delta V_o = R_c * \Delta I_c$. The input impedance of the amplifier is 150 Ω . A low input impedance is achieved by using the common base input stage. It is important for fast current pulses as expected from the drift chamber. The input of the device is protected by two diodes against large signals.

One Fujitsu chip has four of these preamps integrated into a small surface mount

package. Two of these chips are combined to a hybrid amplifier with eight channels. In addition to the built in protection circuits additional protection diodes and a small series resistor have been added to the input for further protection. In this configuration with an 50 Ω resistor in series the circuit survived sparking from a 2kV source through a 470pF capactitor.

7.2. The Shaper

The shaper is based on a crate with a VME bus. The crate is used to monitor the shaper board remotely and for controlling and setting the test pulse distribution. For this purpose the 32 channels of shaping amplifier on one board are divided into 4 quadrants, each of which can be addressed individually.

The shaper has two functions: it provides an amplification of the signal by a factor variable between 2 and 60, and it can be used to shape the pulses from the chamber. Two zero pole filters mounted on headers in the amplifier allow the users to adjust the shaping function to their particular needs. For the CDC the main use of this is to cut off the long tails of the sense wire pulses due to the ion drift. The aim is to produce a nearly symmetrical signal to improve the double track resolution. In Fig. [43] a simplified layout of the shaper card is shown. An input network suppl impedance matching between the cables and the amplifier, and decouples the ground of the shaper from the cable ground via a coupling transformer. The amplification is done in three stages. The first and the last stage are done by differential amplifiers equipped with one pole zero filter each for pulse shaping. The intermediate stage is a single ended amplifier. An RC network for compensation of losses and distortions in the cable is located here. Both zero pole filters, the cable compensation network and the input network are mounted on a removable header. This way a tuning of the parameter for the needs of the specific channel is easy. In the final experiment the shapers will be mounted underneath the detector on the so called platform. They will not be accessible under normal running conditions. Special care has been taken to design them reliable. A special card in the shaper crate provides a programmable test pulse system, which is controlled by a 1553 bus interfaced to the token ring to the main control room.

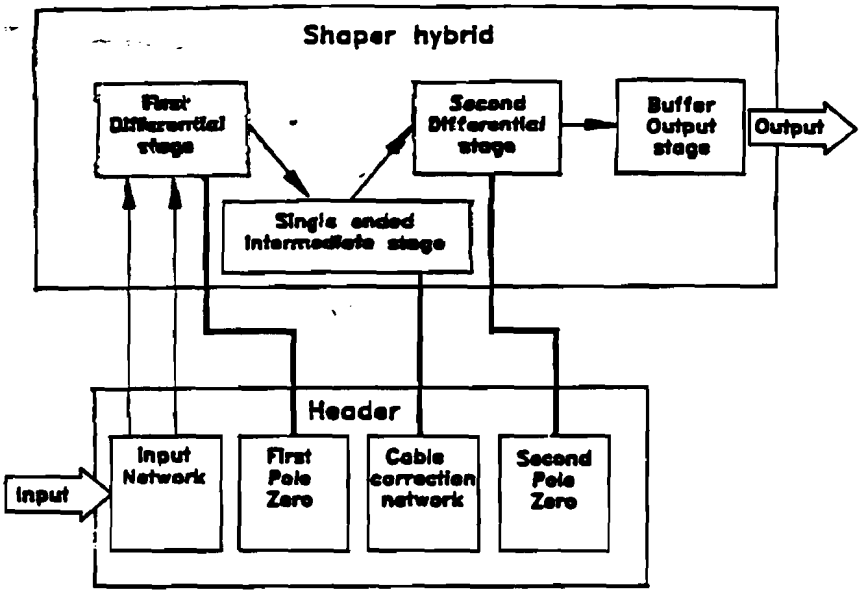

Figure 43 . Schematic layout of the shaper card

7.3. The FADC

As the shaper the FADC (Fast Analog to Digital Converter) is a VME bus based card. A 68000 crate μProcessor does all necessary crate and data management. Communication with the crate is done in two ways. Data are sent from the crate via a special high speed data cable to the rest of the data acquisition system. Control parameters can be set and read via an interface to a token ring network.

Fig. [44] shows a schematic layout of the FADC card. Three main functions can be distinguished: Input analog processing, actual digitization, and zero suppression.

The analog part mainly consists of a bilinear amplifier, the so called buffer amplifier. Fig. [45] is a simplified version of this circuit. The Buffer amplifier serves two different functions. It provides an adjustable gain input stage. The gain can be set via an input DC voltage and can be varied by a factor 2. Second a special circuit provides a bilinear response to the input signal. For low input signals a high amplification is used. If the input reaches a certain level, the gain changes to a lower value. The ratio of the two gains is 11, the break point is set at 192 FADC count equivalent. This way the range of the FADC which is normally 8 bit,is expanded to

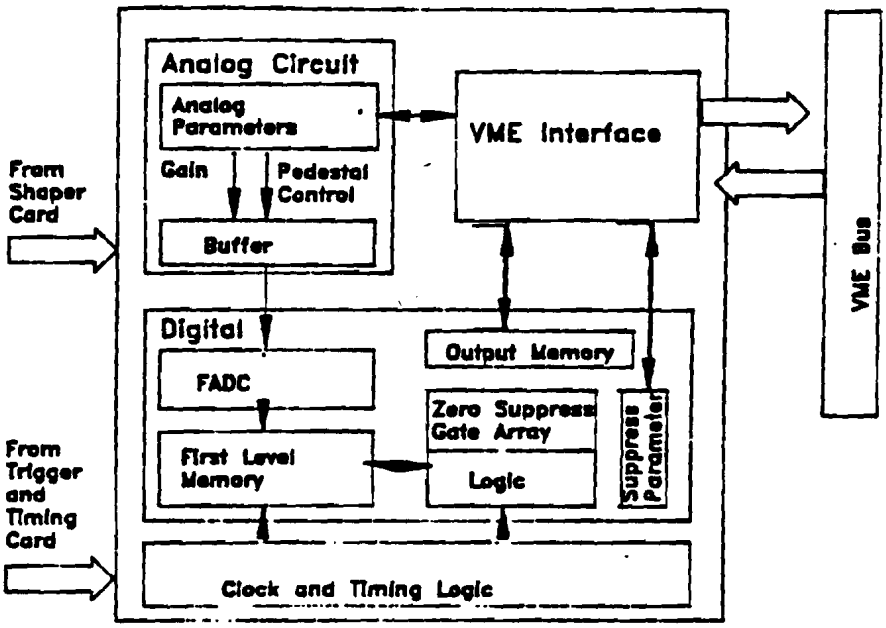

Figure 44 . Layout of the FADC card.

a total dynamic range of 9.5 bit, with reduced accuracy for the top part. Fig. [46] is a plot of the transfer function for the buffer amplifier. Above an input voltage of 0.129 V the output is compressed by a factor 11, expanding the range of possible inputs without saturating the output by a factor 3. After the amplification stage the offset of the output can be set via a control voltage.

Both control voltages, the gain and the offset or pedestal, are controlled via 8 bit DAC's. They are set by parameters sent to the crate via the token ring connection to the data acquisition system.

Signals from the buffers are digitized in the FADC's. These are 100 MHz 8 bit chips manufactured by SONY. They have an input range of 2 V. From the FADC the digitized signal is read into a first level fast memory. If a trigger arrives in time and declares the signal a good signal, the digitization cycle is stopped and the data in the fast memory are not overwritten. They are read into a special chip, the DØ zero suppress chip. The data are fed into a 8 bit wide 9 stages deep pipeline. As they are clocked down the pipeline they are compared to a number of levels for the absolute value and the difference between adjacent values. 4 thresholds (T1 to T4) and 3 slopes (differences, S1 to S3)) can be set from the outside individually for every

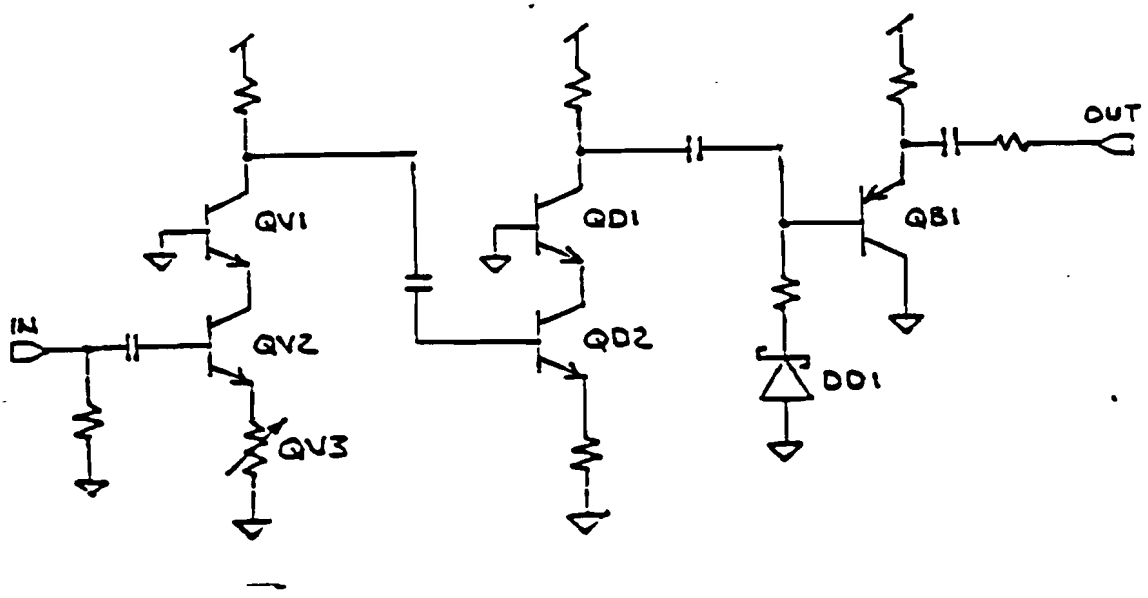

Figure 45 . Simplified schematics of the buffer amplifier

channel. The purpose of this chip is to find those areas in the data which are real pulses, and to eliminate all those where only base lines were measured. The exact conditions are as follows:
Let B_i be the $i-th$ data word, $D_i = B_i - B_{i-1}$. Six internal flags are set:

$$C1 = (B_{i-2} > T1) * (B_{i-1} > T1) * (B_i > T1)$$
$$C2 = (B_{i-2} \geq T2) * (B_{i-1} \geq T2) * (B_i \geq T2)$$
$$C3 = (B_{i-2} < T3) * (B_{i-1} < T3) * (B_i < T3)$$
$$C4 = (B_{i-2} < T4) * (B_{i-1} < T4) * (B_i < T4)$$
$$C5 = (D_{i-1} > S1) * (D_i > S1)$$
$$C6 = (S2 < D_{i-1} < S3) * (S2 < D_i < S3)$$

The leading edge and the trailing edge are then defined by the following two relations:

$$LE = C1 * C5 + C2$$
$$TE = C3 * C6 + C4$$

Only those data words which fall within a leading and a trailing edge are read out

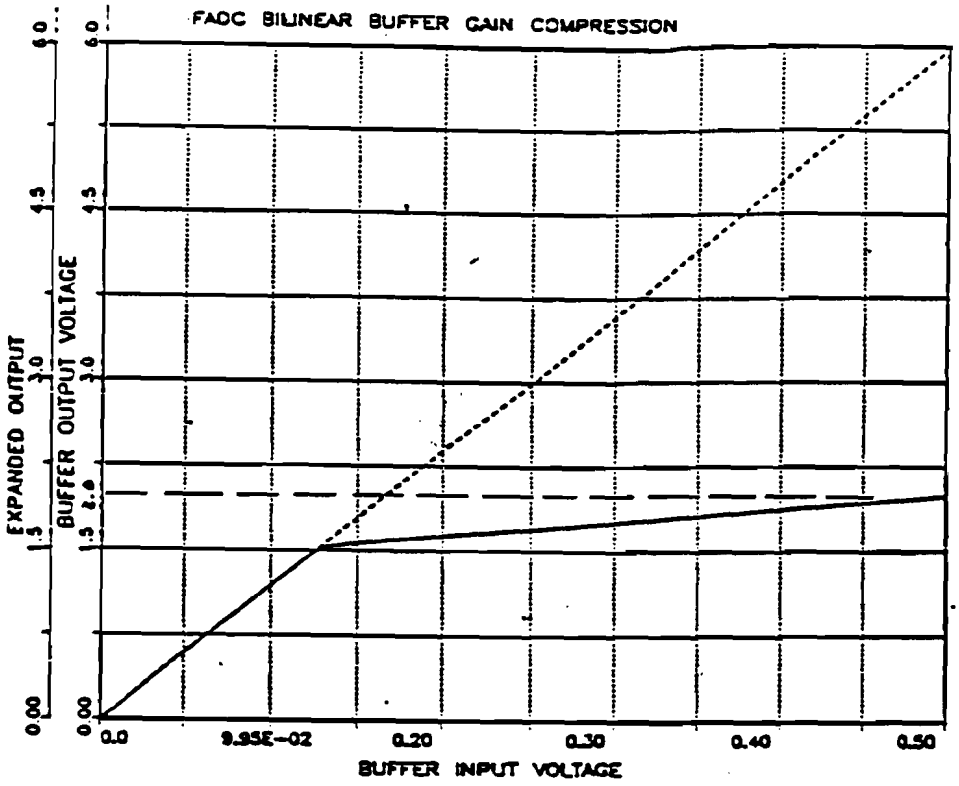

Figure 46 . FADC bilinear buffer amplifier transfer function. The 8 bit Sony FADC has a 2.0 V input range. corresponding to 256 bins. Using the bilinear response of the buffer this can be expanded to 768 bins or 9 1/2 bits.

from the pipeline. They are stacked from 8 to 16 bit and sent out onto the 16 bit data path. The data cable will sent the data as 32 bit words to the

7.4. Conclusions

A complete data readout system for the DØ detector has been designed and implemented at Fermilab. This system provides a fast and very flexible means of reading out information and digitizing them. A wide range of input signals sizes can be accommodated. A prototype version of this system was used at Fermilab for some time under realistic data taking conditions and performed satisfactorily.

8. The Electrostatics Program

8.1. Introduction

An important part of the design of the central drift chamber was played by a program that simulates the electrostatics of the chamber. This program - a more detailed description of which will follow- calculates the drift paths of electrons given a specific cell geometry and related quantities like drift time,potential etc.. In addition it allows the approximate calculation of induced pulses on wires and thereby the calculation of crosstalk and delay line pulses.

The information extracted from this program was used to explore the behaviour of the chamber under various operating conditions.

The goal of this study was to find a cell geometry, which, given the mechanical limitations imposed by the general design, allowed

- to find the potential distribution in the chamber that produces the best field configuration.
- to minimize the time dispersion.
- to find the optimal position of sense- and potential wires and the optimal number of potential wires so that crosstalk is minimized while disturbing the field as little as possible.
- to maximize the pulse induce on the delay line while minimizing the cross talk from the next neighbour sense wire.
- to minimize the electrostatic deflection of the wires.

The results obtained from the program were, wherever possible, compared to direct measurements on test cells or prototypes of the final detector.

In the following chapter the program will be discussed briefly. Then results from calculations will be presented and compared to experimental results.

8.2. The "Drift" Program

The program used to do the above outlined calculations is based on one written by Jerry Vav'ra, SLAC [38]. The underlying theory was first formulated by Erskine, CERN [39]. Other authors have written similar programs: [40], [41], [42]. The basic idea is to simulate a drift cell by an array of wires. which are infinitely long

The field in the chamber is then computed by superposition of ividual wires. This system was developed for chambers made up however works quite well for chambers like the DØ drift chamber, s with nearly continuous potential distributions everywhere but s, assuming that no charge is deposited on the insulating surfaces s.

of a single wire with radius r_w and charge per unit length $\tilde{Q}$ is

$$\vec{E} = \frac{1}{8\pi\epsilon_o}\tilde{Q}\,\frac{1}{r}\hat{r} \qquad \text{for } r > r_w \qquad (8-1)$$

where r is the distance from the center of the wire ($\hat{r}$ the unit vector in the radial direction).

The potential outside the wire is

$$\begin{aligned} V &= -\int_{r_o}^{r} E\,dr \\ &= -\frac{1}{2\pi\epsilon_o}\tilde{Q}\ln\frac{r}{r_o} + V_o \end{aligned} \qquad (8-2)$$

Since under normal conditions the potentials on the wires, but not the charges ar known, the first step in the chamber simulation is to calculate the charges . Once the charges are known, Eq.(8- 1) and Eq.(8- 2) can be used to calculate the field and potential at every point in the chamber by simple superposition of the individual wire contributions.

Given an array of n wires at known but possibly different potentials, the charges Q_i are connected to the potentials via the capacitance matrix C_{ij}:

$$\tilde{Q}_i = C_{ij}V_j \qquad (8-3)$$

where Q_i is the charge per unit length on wire # i; V_j the potential of wire # j; and C_{ij} is the capacitance per unit length between wires i and j . The capacitance matrix depends only on the geometry of the chamber (up to a scale factor, if the chamber is not in perfect vacuum). Rewriting Eq.(8- 2) by defining $Q = \tilde{Q}/2\pi\epsilon_o$ and $r = r/r_o$ yields

$$V = -Q\ln r + V_o \qquad (8-4)$$

The potential produced at the position of wire # i due to the contributions of all other wires is

$$V_i = -\sum_{j\neq i}(\ln r_{ij})\,Q_j + V_o \qquad (8-5)$$

where r_{ij} is the distance between the j^{th} to the i^{th} wire. To calculate the charges Eq.(8- 5) has to be inverted:

$$Q_j = (-\sum_{j \neq i} (\ln r_{ij}))^{-1} V_j + constant \qquad (8-6)$$

The program, rather than actually inverting the Matrix, solves Eq.(8- 5) for a given set of voltages. This methods is considerably faster than the inversion of a matrix with typically up to 100 * 100 entries. In order to normalize the system correctly an additional row and column is introduced in the matrix of equation Eq.(8- 6), with only the diagonal element non zero. This is equivalent to fixing the constant in Eq.(8- 6) in a way that the total charge in the system is 0.

8.3. The Drift Map

A helpful aid in visualizing the behaviour of the chamber is a drift map for the electrons or the ions. A drift map shows the paths of electrons (or ions) as they drift from their originating point towards the sense wire (cathode). To generate these plots the program deposits charges at constant intervals along the trajectory of a charged particle passing through the chamber. Each charge is then drifted along the field lines until it hits a wire. Electrons whose drift path converge on the same sense wire are collected into a bunch. For each bunch distances of equal drift time from the sense wire are calculated and plotted.

To actually calculate the drift path the program first determines the x and y component of the electric field at the location of the electron. It then steps the electron along the field vector some distance. The step size is varied so that the field at the new location in both magnitude and direction is different from the original one by less than some preset limit. Once this condition is fulfilled the electron is actually stepped to its new position, the drift time for this step is calculated and the new position is used as the starting point for the next step. In order to calculate the time an empirical relation between the electric field and the drift velocity for a specific gas is used.

Once the drifting electron approaches a sense wire to within twice the wire radius the drifting stops. Starting from a point on the drift path, that is exactly two radii away from the wire points of equal distance in time on the path are found by interpolating between the steps. Therefore the equal time lines which are plotted on the drift map are lines on which the electrons would have to start drifting should they all arrive on the wire at the same time.

The result of this calculations is a plot that shows for one quarter of the drift cell drift lines and equal time lines.

8.4. Time dispersion

The drifting electrons do not all arrive at the same time on the sense wires. This time spread, the time dispersion, is an important measure for the performance of the drift chamber.

The time dispersion depends on the geometry of the chamber- mostly on the width of the gap over which electrons are collected by a specific sense wire-, on the potential distribution of the surrounding wires and on the gas used. Of particular importance is the region immediately surrounding a sense wire up to distances of the order of the inter wire spacing.

Electrons get collected by a given sense wire over an extended part of the track of the ionizing particle. Electrons starting on different points on this primary track travel along different paths to arrive on the same sense wire. Those electrons which were freed just at the edge of the region which is collected by this sense wire will have the longest path while the ones starting in the center of the collection region have the shortest.

To calculate the time dispersion a consequence of gauss law is used, which states that the electric flux for the drift field is conserved. The field in the immediate surrounding of the sense wire is essentially a radial field, out in the drift volume it is uniform. A flux arriving through a given opening angle at the wire will have originated over a equivalent length of the track of the ionizing particle. For example all the charge produced over 10% of the track segment which drifts to one particular sense wire will arrive within 10 % of the opening angle of this bunch at the wire.

The program determines the part of the track which drifts towards one sense wire and calculates the drift time for the inner 90% of all charges on this track to arrive on the wire.

The difference between this time and the shortest drift time for these charges is then the time dispersion (90 %).

A small time dispersion is important because it enters directly into the rise time of the pulse. In principle a longer rise time is not necessarily a draw back, because in a system using digitization electronics as DØ does a longer rise time will actually mean a better precision. However as discussed in the section on the physics of drift chambers the deposition of the primary electrons is a statistical process resulting in the formation of clusters of electrons along the track of the ionizing particle. A

larger time dispersion due to the field would increase the fluctuations seen due to this clustering and lower the intrinsic accuracy of the chamber.

8.5. Calculation of induced pulses

One important criterium in the design of a chamber is the crosstalk between neighbouring electrodes like sense wires and, in the DØ case, delay lines. A certain fraction of the signal seen on wire #1 will be induced with opposite sign on the neighbour wires. One goal of the design of the chamber is to minimize this induced signal between sense wires and maximize it for the case sense wire delay line.

The two cases –sense wire to sense wire crosstalk and sense wire to delay line crosstalk– should be looked at under slightly different circumstances. For the sense wires the crosstalk should be kept as small as possible. The parameters that influence the size of the induced pulse and which can be changed are the distance to the neighbour wire and the number and arrangement of the potential wires, separating the two sense wires. In the case of the delay line pulse it was found that two sense wires contribute to the signals: the one closest to the delay line and the next one in the cell. The contribution of the second wire should be kept as small as possible, while the closest wire should induce a large signal on the line.

Two things can be changed to improve the situation: The shielding between the second wire and the delay line can be improved. At the same time the gain on the wire closest to the line can be raised increasing the delay line signal. Now however care has to be taken to make sure that the crosstalk between the two sense wires does not increase to unacceptable levels.

In order to calculate induced pulses a simplified scenario is investigated. As discussed in the section on the physics of the drift chamber, the pulse seen on a sense wire is mostly due to the charge induced on this wire by the positive ions as they are moving away from the wire. Simplified the wire is surrounded by a sheet of positive charge which slowly expands and drifts away from the wire. The field of the wire is nearly radial for small distances from the wire, and falls off like $1/r$ with the distance r from the wire. The largest contribution to the current pulse comes from the first few wire radiuses of drift distance of the ions, and most of the pulses seen on other wires will have been induced during this initial time period. To calculate the relative induced pulse height on other electrodes, this dynamic situation is replaced by a static one, where the moving sheet of ions is replaced by a charge at the position of the wire. The induced charge is then determined by the capacitive coupling between this wire and the surrounding electrodes. This describes the process integrated over the initial part of the pulse. This is a very good approximation of the actual process because

the preamplifiers used are integrating amplifiers.

For example, consider the case where the charge q_1 induced on conductor 1 by a charge placed on conductor 2 shall be calculated. 1 and 2 are parts of a larger system of wires. The whole system is described by the equation

$$Q_i = \sum_{j=1}^{n} C_{ij} V_i \qquad (8-7)$$

To simplify the problem, a unit charge is placed on the conductor 2 and all other conductors are grounded. So $V_i = 0$ except for $i = 2$, and Eq.(8- 7) reduces to

$$Q_1 = C_{12} V_2$$
$$Q_2 = 1 = C_{22} V_2$$

or

$$q_1 = \frac{C_{12}}{C_{22}}$$

For a more complete description of this method see for example [43]:

To get the induced pulse on the delay line a wire was put at the position of the delay line. No information about the absolute pulse height will be obtained in this way, only relative pulses can be calculated.

This method of calculating induced pulses has a few drawbacks:

- it does not give any information about pulse shape or relative timing of original and induced pulse.
- the representation of the delay line with a single wire is a rather crude one and some discrepancy between calculated and experimental numbers are to be expected
- as stated above this method does not take into account the signal induced by the positive ions as they are drifting away from the sense wire.

8.6. Calculation of the Displacement of wires

Under the influence of the electric field and the gravitational field the wires in the chamber will deflect by a certain amount. This displacement has to be kept to a minimum if it should not seriously affect the position resolution of the wire and the uniformity of the gain along the wire.

The deflection of a wire in an electric field can be easily calculated: The two forces acting on the wire (for the moment electrostatic and gravitational force will

not be considered separately) are the electrical force and the opposing force due to the tension in the wire that tries to keep the wire in the position with zero deflection. If $\vec{T}$ is the tension at a point s on the wire and $\vec{F}$ the force per unit length due to the external field then

$$\begin{aligned} \vec{T}(s+\Delta s) - \vec{T}(s) &= \frac{d\vec{T}}{ds}\Delta s + O(\Delta s^2) \\ \frac{d\vec{T}}{ds} + \vec{F} &= \vec{0} \end{aligned} \qquad (8-8)$$

or, in components (where x is the coordinate along the wire, y perpendicular to it):

$$\begin{aligned} \frac{dT_x}{ds} &= 0 & \frac{dT_y}{ds} &= F_y \\ T_x &= const & T_y &= F_y(s-s_o) \\ &= T_o \end{aligned} \qquad (8-9)$$

Here it was assumed, that the force acts only in the direction of the y-coordinate and is constant along the wire. Solving these two first order differential equations and calculating the total tension as $T = \sqrt{(T_x^2 + T_y^2)}$ gives:

$$T = T_o\sqrt{(1+\alpha^2\,(s-s_o)^2)} \qquad (8-10)$$

where $\alpha = F/T_o$ and F the electrostatic / gravitational force. Eq.(8- 10) describes the tension as a function of the coordinate s along the wire.

With

$$\begin{aligned} T_x &= T\cos\alpha & T_y &= T\sin\alpha \\ &= T\frac{dx}{ds} & &= T\frac{dy}{ds} \end{aligned} \qquad (8-11)$$

one gets using Eq.(8- 11)

$$\frac{dx}{ds} = \frac{1}{\sqrt{(1+\alpha^2(s-so)}} \qquad \frac{dy}{ds} = \frac{\alpha(s-so)}{\sqrt{(1+\alpha^2(s-so)}} \qquad (8-12)$$

Solving these equations and eliminating $(s-so)$ yields:

$$(y-yo) = \frac{1}{\alpha}(\cosh\alpha(x-xo) - 1) \qquad (8-13)$$

For small deflections one gets

$$(y-yo) \approx \frac{1}{\alpha}\frac{\alpha^2(x-xo)^2}{2} \qquad (8-14)$$

At the center of the wire ($x = 0$ and $x_o = l/2$)

$$\Delta = y - y_o = \frac{\alpha}{2}\frac{l^2}{4} \qquad (8-15)$$

This formula is applicable for both the electrostatic deflection and the gravitational sagging. In the former

$$\alpha = \frac{\sigma g}{T_o} \qquad (8-16)$$

and in the electrostatic case

$$\alpha = \frac{\tilde{Q}E}{T_o l} \qquad (8-17)$$

where Q = charge per unit length on the wire, E the electric field at the position of the wire, T_o the mechanical tension, l the length and σ the linear mass density of the wire and g the gravitational acceleration.

This formalism works reasonably well as long as the deflections of the wires are small. For larger deflections an iterative process has to be employed, since moving the wire in principle changes the field on the wire and therefore the force it sees. The calculation of the deflection of each wire should be repeated using the displaced wire position and the field at the new position. However at this point the wire can no longer be treated at an infinitely long straight object in the third dimension, and the whole concept used for this program starts to break down.

The following table shows both the measured deflection of a sense wire and the calculated deflection. The wire used was an edge sense wire.

Chamber Voltages /kV				Deflection / μm	
V_{field}	V_{strip}	V_{sin}	V_{sout}	measured	calculated
0	0	0	0	0	0
0	0.35	0	0	- 42 ± 15	- 20
-4.2	0.35	0	0	- 0 ± 15	8
-4.2	0.35	1.00	1.00	56 ± 15	52
-4.2	0.35	1.40	1.40	42 ± 15	54
-4.2	0.35	1.50	1.50	42 ± 15	52
-4.2	0.55	1.50	1.50	167 ± 15	112

The calculated and the measured values are roughly in agreement. The discrepancies can be understood in the following way:

- The measurement error is rather large. The deflections were measured with a microscope with a scale in the ocular, but the overall calibration was estimated to be good to not better than $10\mu m$. In addition each measurement carries a measurement error of about the same order: $\pm 10\mu m$.

- The module which was used for these measurements was an early prototype. The mechanical tensions of the wires in this module were known only to within $\pm 20\%$.
- As pointed out above the calculations are not iterative and will break down the moment the deflections become large. This can actually be seen at the last entry in the table, where a measured deflection of $167\mu m$ is put against a calculated one of only $112\mu m$.

All these effects contribute to the discrepancies between the measured and the calculated value. However the table shows that for small deflection (small meaning less than $100\mu m$) the agreement between theory and experiment is acceptable. These calculations certainly can be used as an indication of the size and direction of deflections to be expected.

To get a better prediction of the wire deflection, a considerably more sophisticated program is needed. This program not only uses an iterative process to calculate deflections but should also take into account that the wire is no longer straight in its deflected state and the field along the wire is no longer constant.

8.7. Electrostatic Stability of Wires

If sufficient charge is put on a wire in a field the force experienced by that wire can become large enough to put the system in an unstable state. More than one metastable configurations might arise and the wire starts oscillating between them. Tom Trippe [44] shows that for a simple linear array of wires under equal tension and with equal charge there exists a critical tension T_c. which separates the stable configuration from the unstable one. In the following his results are expanded to the case of a wire configuration of the arrangement as the DØ chamber and to wires with different charges.

In a system of wires as sketched in Fig. [47] two different coherent displacement patterns can be found. In Fig a) the sense wires are deflected out of the sense wire plane. one up, one down. It is assumed, that the potential wires do not move, since they are strung at a much larger tension. Above a certain charge on the wires this pattern rather than the normal "design" pattern has a minimal energy for the system, and the transformation into this state will occur suddenly upon an infinitesimal deflection of any wire of the array. Fig b) shows the second mode: All sense wires are displaced by the same amount in the sense wire plane towards one side. The sense wires are sitting asymmetrical in the cage of potential wires, which again were assumed to be stationary. This position as well will be reached suddenly following a small disturbance of any one sense wire in the correct direction, if one goes beyond the so called limit of stability. Both modes have two separate solutions, because the

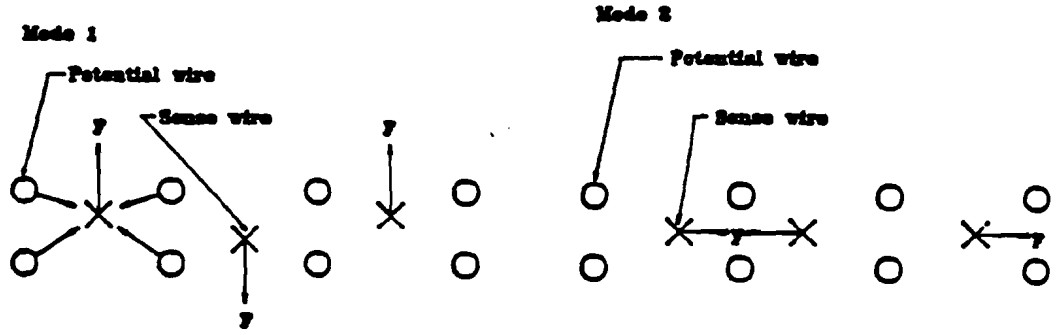

Figure 47 . Two coherent modes of displacements under the electrostatic force for sense- and potential wire arrays. Indicated are the forces acting in the two different cases.

directions of the disturbance that initiates the transition can be either up or down for the first type or left or right for the second type.

For the first type of instabilities three different contributions can be separated. The bottom row of potential wires acts on the sense wire, the top row counteracts this force somewhat, and every second sense wire has a non vanishing force component on the central wire. Only those sense wires which are at a different y-coordinate than the wire being looked at will contribute a net force. These different forces are

$$\begin{aligned} F_1 &= 2\frac{1}{2\pi\epsilon_0} q_s q_p \frac{1}{\sqrt{(b-\Delta)^2+a^2}} sin\alpha \\ &\approx \frac{1}{\pi\epsilon_0} q_s q_p \frac{b-\Delta}{(b+\Delta)^2+a^2} \\ F_2 &= -2\frac{1}{2\pi\epsilon_0} q_s q_p \frac{1}{\sqrt{(b-\Delta)^2+a^2}} sin\alpha \\ &\approx -\frac{1}{\pi\epsilon_0} q_s q_p \frac{b-\Delta}{(b-\Delta)^2+a^2} \end{aligned} \qquad (8-18)$$

where a is the inter wire spacing, b the offset of the potential wires out of the plane,

and terms not linear in Δ have been dropped. After adding both forces and expanding to order Δ one finds:

$$F = \frac{1}{\pi\epsilon_0} q_s q_p \frac{2\Delta}{a^2 + b^2} \qquad (8-19)$$

This is the force due to the four next neighbour potential wires. The force due to the two next sense wires can be obtained similarly:

$$\begin{aligned} F &= 2\frac{1}{2\pi\epsilon_0} q_s^2 \frac{1}{r} sin\alpha \\ &\approx \frac{1}{\pi\epsilon_0} q_s^2 \frac{\Delta}{2a^2} \end{aligned} \qquad (8-20)$$

Again the expression has been expanding to include all order Δ terms. The total force due to the next neighbours is the sum of Eq.(8- 20) and Eq.(8- 19):

$$F = \frac{1}{\pi\epsilon_0} \frac{\Delta}{2a^2} q_s \{ q_s + \frac{4a^2}{a^2 + b^2} q_p \} \qquad (8-21)$$

To derive the full force a sum over all wires in the array has to be done. For the special case of $b = 0$ and $Q_p = 2q_p$ the sum can be done for a very large wire array:

$$F = \frac{1}{\pi\epsilon_0} \frac{\pi^2}{8} q_s (q_s - 2Q_p) \frac{\Delta}{2a^2} \qquad (8-22)$$

The second type of instability can be treated in a similar manner. Here the sense wires - sense wire interaction does not contribute anything, since all sense wires are symmetric with respect to the one being investigated. After some algebra one finds that the force on a sense wire due to its immediate neighbours is given by:

$$F = \frac{1}{\pi\epsilon_0} q_s q_p 2 \frac{(a^2 - b^2)}{(a^2 + b^2)^2} \Delta \qquad (8-23)$$

Again for $b = 0$ and a very large array the summation to compute the total force can be done and the result is:

$$F = \frac{1}{\pi\epsilon_0} \frac{\pi^2}{8} q_s Q_p \frac{\Delta}{a^2} \qquad (8-24)$$

If the wire is being deflected the tension in the wire is producing a restoring force

$$F_r = -T \frac{d^2y}{dx^2} \qquad (8-25)$$

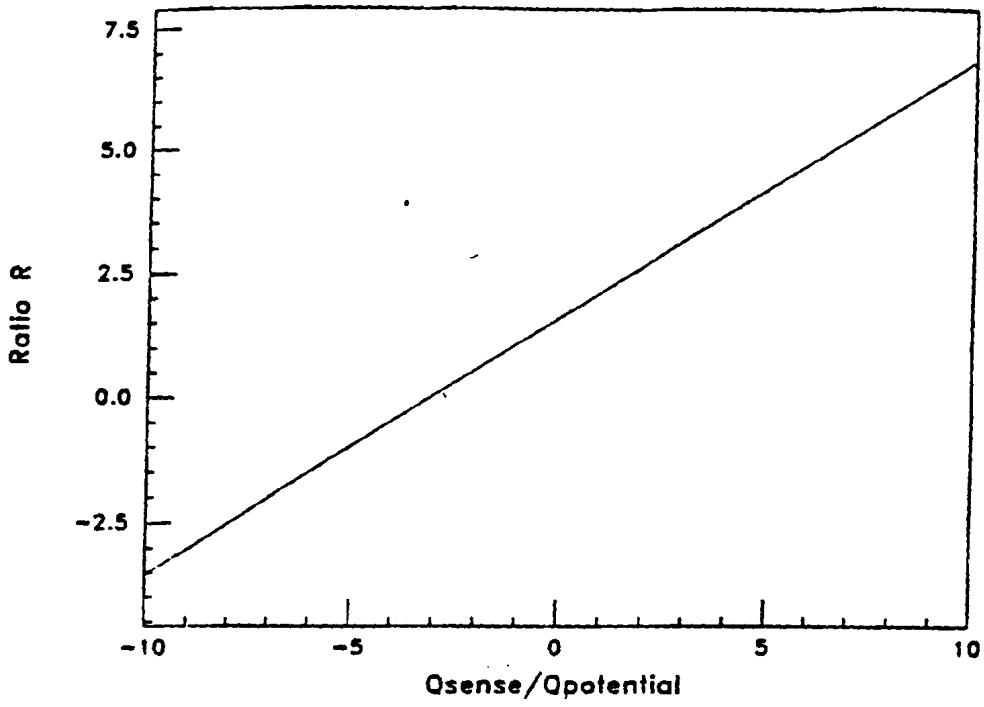

Figure 48 . Ratio of the two forces responsible for the two different modes of instabilities. Indicated is the point at which the DØ chamber will operate under nominal conditions.

For small deflections the electrostatic force can be linearized to the form

$$F_{el} = ky \tag{8-26}$$

so that the state of equilibrium is described by:

$$T\frac{d^2y}{dx^2} - ky = 0 \tag{8-27}$$

The solution to this equation with the boundary condition that $y = 0$ at $x = 0$ and at $x = l$ is given by:

$$y = y_0 \sin(\frac{\sqrt{k}}{T}x) \tag{8-28}$$

and the additional constraint:

$$\sqrt{\frac{k}{T}}l = \pi \tag{8-29}$$

or

$$T = \frac{kl^2}{\pi^2} \tag{8-30}$$

In the case of the DØ chamber $a = 2b$. Here for $q_s < -16/5|q_p|$ the second instability dominates. Fig. [48] shows a plot of the ratio of the two forces. The chamber is

operated in a region where the first instability dominates. However one should keep in mind that only next neighbour interactions have been taken into account here. Including wires further away might modify the results somewhat.

9. Electrostatic Simulation of the Chamber

9.1. Mechanical Tolerances

The mechanical skeleton of the DØ central drift chamber is made of light composite plates (see the section on the construction of the chamber for a more complete description). This construction method has the drawback that it introduces the possibility of misalignment between this walls and the adjacent wires. These displacements potentially are much larger than those expected in conventional "all wire" wire chambers.

To study the effect of these mechanical tolerances the electrostatic program was used to calculate the charge on the sense wires for different positions of the chamber wall. The charge on the wire determines the gain of this wire as $G = A \exp BQ$, where A and B are constants. Empirically a 4% change in the charge on the wire results in a change of the gain by a factor 2 for most Argon based mixtures.

Fig. [49] shows the charge on S1, S2 and S3 (in arbitrary units) as a function of the wall position x, measured with respect to the center of the chamber. One sees that, as expected, S1 is the most affected wire. The charges on S2 and S3 are hardly changed by moving the wall.

The charge on S1 shows a weak minimum around x=2.3 cm. Variation of the wall position around this value changes the charge by a rather small amount. The chosen chamber half width of 2.21 cm is close enough to this minimum, so that variations of $\pm$ 0.5 mm vary the charge on S1 by about $\pm$ 1 % .

Since the system is linear in the potential applied to the wires changes in the wire potentials will not affect the basic shape or position of this minimum. The bottom part of Fig. [49] confirms this statement. Also the gains of the wire changed substantially, the position of the minimum remained constant.

Hand in hand with the question of the sensitivity of the gain against movements of the wall goes the question how the electrostatic deflection of the wires depend on the mechanical tolerances. Fig. [50] shows the electrostatic deflection of the outer sense wire as a function of the wall position. The wall position again is measured from the center of the chamber. The deflection crosses $0.00\mu m$ at $x \approx 2.05cm$. At around x=2.1 cm the curve levels out and, although at nonzero total deflection, becomes rather insensitive to further changes in the wall position. The actual width x=2.21 cm is well within the flat region , so that no significant influence of the wall position on the wire deflection is expected.

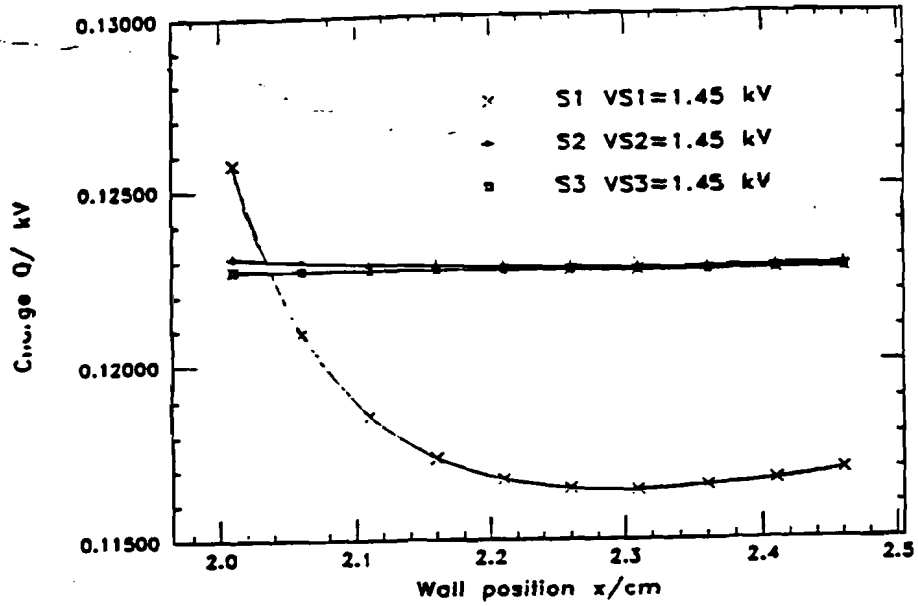

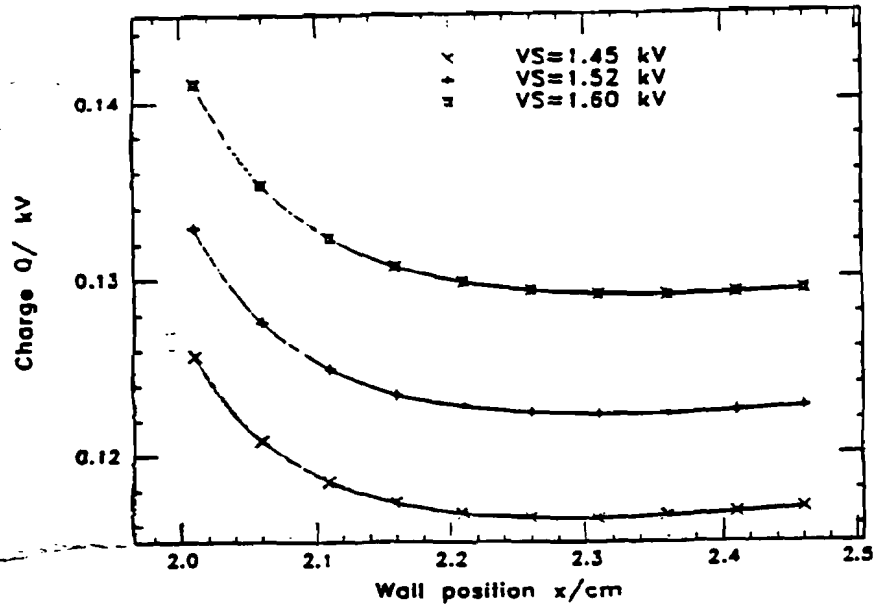

Figure 49 . top plot: Charge on the sense wires vs. wall position. The effect of moving the wall is shown for the sense wires 1, 2 and 3. bottom plot: Charge on the outer sense wire as a function of the position of the wall, for different potentials on the wire

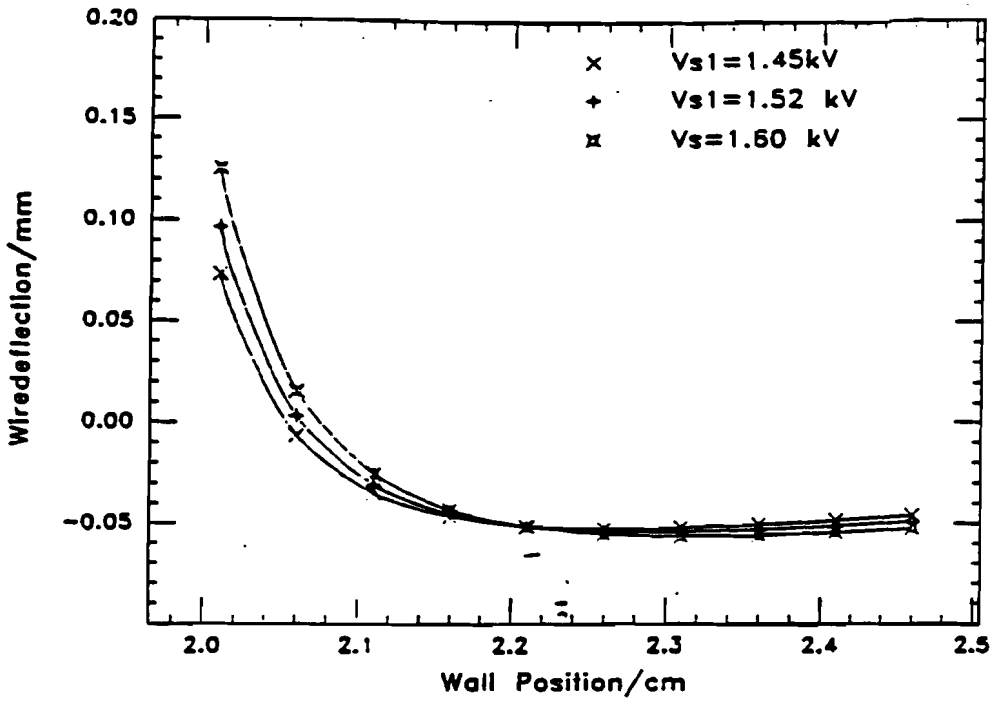

Figure 50 . Wire deflection vs. wall position for the outer sense wires for different voltages

Fig. [51] compares the normal chamber geometry in the top plot with a chamber, where the outer wall was moved by 0.5 mm and 5 mm away from the wires respectively. The field distortions are quite severe and can be seen to propagate nearly to the center of the chamber. The wire most affected by this is the second sense wire, whose collection region gets squeezed at large displacements. However for realistic numbers - displacements of less than $1/2mm$- the field distortions are limited.

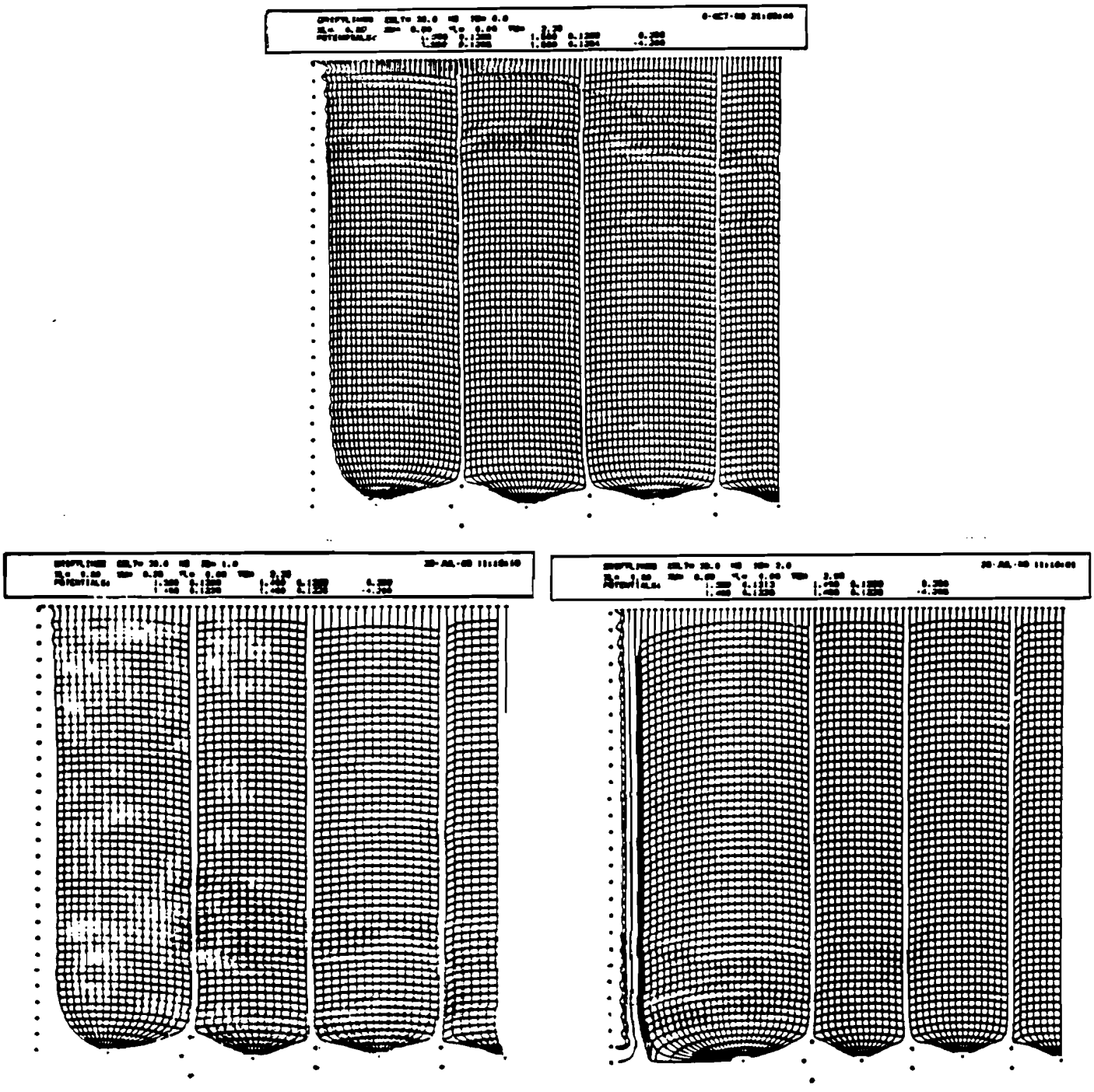

Figure 51 . Drift maps showing the chamber with moved outer walls. Three plots are shown. The top one shows the chamber under nominal operating conditions with the wall at its normal position. The second one depicts a chamber with a wall moved by 0.5 mm. In the lower plot the wall has been moved outwards by 3 mm

9.2. Crosstalk Measurements and Calculations

a) Sense wire Sense wire crosstalk

As pointed out in the introduction the crosstalk between the sense wires can be changed by changing the distance between wires and by varying the number and arrangement of the potential wires separating neighbour sense wires.

To compare the calculated predictions with measured values a small proportional chamber was built and used to measure induced pulses for different wire geometries. The signal in the chamber was obtained from a Fe 55 source, which has a monochromatic soft X-ray line at 5.9 keV. The signal was then amplified and digitized. The cited numbers for crosstalk are the area (=total charge) under the averaged pulse.

Three configurations were measured:

1) One potential wire separates two sense wires. The potential wire is located on a straight line connecting the two sense wires.

2) Two potential wires separate each sense wire pair. They are offset from the sense wire plane by half the sense wire spacing

3) Three potential wires separate the sense wires, one arranged as in geometry 1),the other two as in geometry 2)

4) Two potential wires out of the sense wire plane by one quarter of the sense wire spacing are separating neighbouring sense wires (no direct experimental data are available for this setting)

The quoted results are the relative pulses induced on wires or delay line measured in percent of the pulse on the inducing wire. The results of the measurements and the calculation are compared in the following table:

	Configuration	measured crosstalk	calculated crosstalk
1	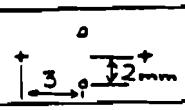	6.0 ± 1.0 %	6.0 %
2	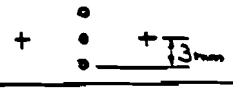	4.5 ± 1.0 %	5.6 %
3	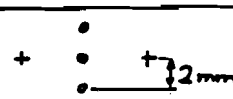	3.5 ± 1.9 %	3.1 %
4	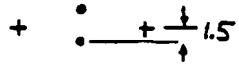	n/a	4.0 %

Table 1

As expected three potential wires give optimal shielding power, however 2 potential wires arranged as in geometry 4) are nearly as good. Table 1 also shows that the agreement between the measured values and the calculated crosstalk is very good and within the error of the experimental measurement. This shows that the simple method as described in the previous chapter is adequate for predictions of crosstalk in the chamber.

Fig. [52] and Fig. [53] show predictions for sense wire sense wire crosstalk for a pair of wires in the middle of the chamber (which are therefore insensitive to edge effects), and a pair of outer wires (S1 and S2). In both cases crosstalk for the case of two and of three potential wires separating the sense wires is shown.

Although in both cases 3 potential wires perform better than 2 the difference is rather small. In particular 2 wires can be somewhat closer to the sense wire plane than the 2 outer ones of a 3 potential wire geometry, therefore partially compensating for the loss of the shielding power of the inner potential wire. For the 2 wires being out of the sense wire plane by half the sense wire spacing a crosstalk of 4 % is achieved. This is a very acceptable level.

The situation is different for the two outermost sense wires. Here the aim is to reduce the crosstalk as much as possible because the outer wires will be run at about twice the gain of the inner ones, therefore making the crosstalk to S2 worse, and, in particular, the signal seen on the delay line from S2 has to be as small as possible. Therefore for the two outer wires the additional shielding provided by three potential wires is needed.

For mechanical reasons the spacing between three wires in a straight line cannot

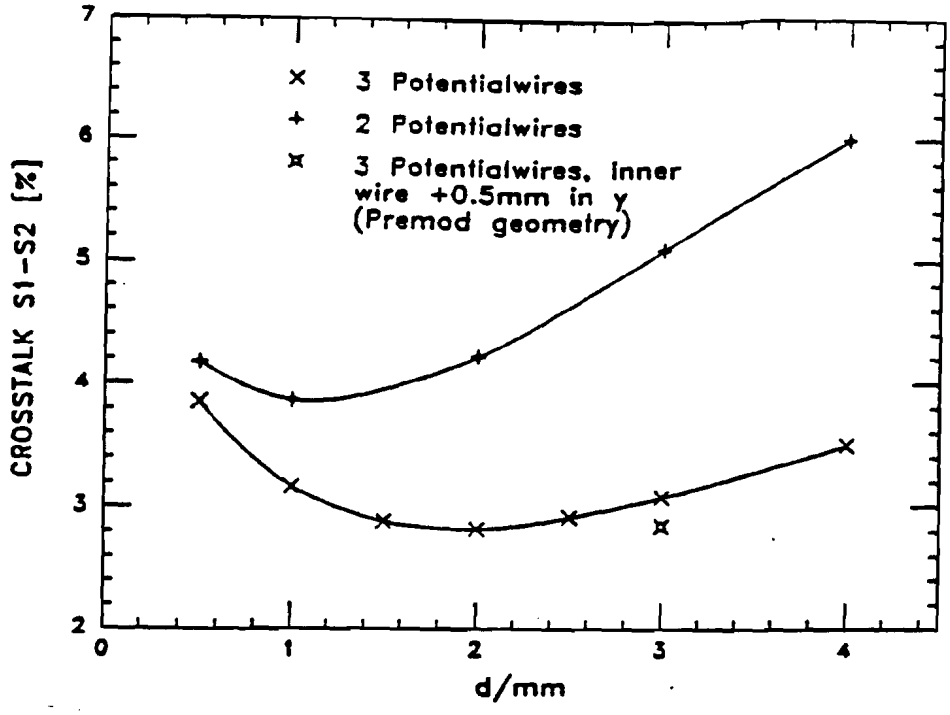

Figure 52 . Cross talk from S1 to S2 for different potential wire geometries as predicted by the program

be less than 3 mm. This forces the two outer potential wires further out into the chamber at $\pm$ 3 mm. The crosstalk calculated for this configuration is 3.1 %.

9.2.1. Delay line Signals

In order to maximize the pulses seen on the delay lines and to improve the shielding of the delay line from sense wires other than the one right next to the line the described methods of calculating induced pulses was used for delay lines as well.

Again the values predicted by the program described in the previous chapter were cross checked with actual measurements on the above mentioned proportional chamber, this time equipped with one delay line in addition to the sense wires.

Table 2) summarizes the results:

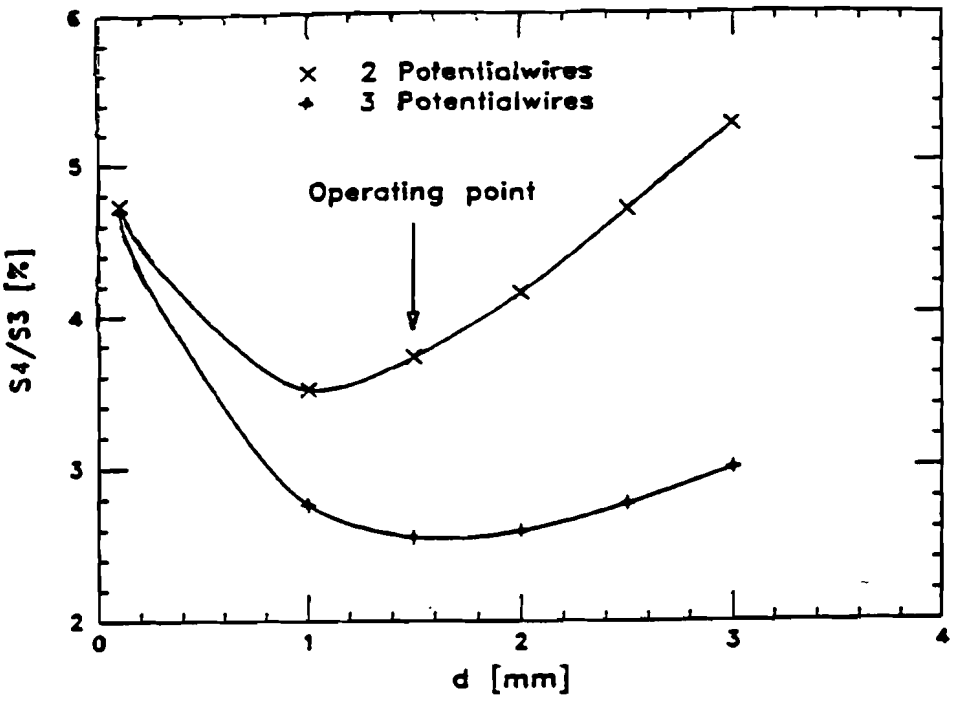

Figure 53 . Cross talk from S3 to S4 for different potential wire geometries as predicted by the program

Configuration	measured delay line signal	calculated delay line signal
d=2.5 mm	32 ± 1 %	34 %
d=4.0 mm	20 ± 2 %	27 %
d=11.0 mm	11 ± 1 %	14 %
2 pot wire d=2.5 mm	31 ± 1 %	33 %
3 pot wire d=2.5 mm	32 ± 1 %	31 %
3 pot wire d=3.0 mm	30 ± 1 %	31.7 %

Table 2

Table 3 . shows the signals induced on the delay line from the second sense wire. The measurements agree reasonably well with the calculated values showing that the predictions are reliable to about 20 %. It should be pointed out though that the absolute value of the induced signal can not be predicted well within this method. Only the relative size of *induced* pulses on the delay line are calculable. The reason for this is that within the context of a chamber simulated entirely by wires it is very difficult to introduce an extended object like a delay line. However the tables show that once the overall normalization has been fixed the relative sizes of induced pulses are predicted rather well.

	Configuration	measured delay line signal	calculated delay line signal
1	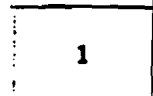	6.5 ± 2.2 %	6.6 %
2	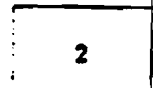	4.9 ± 1.5 %	6.0 %
3	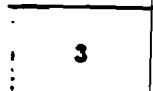	4.5 ± 1.3 %	4.5 %
4		3.5 ± 1.0 %	2.7 %
5	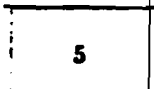	2.5 ± 1.0 %	3.4 %

Table 3.

To measure the height of signal induced from S1 on the delay line and to compare this with the signal induced by S2 it is convenient to introduce a ratio R such that

$$R = \frac{\text{pulse induced by S1 on delay line}}{\text{pulse induced by S2 on delay line}}$$

Ideally R would be ∞: no delay line signal is seen which is due to a signal on S2. This ,of course, is impossible, so the goal is to make R as large as possible. To do that S1 should be moved as close as possible towards the delay line while S2 should be as far away as possible. In addition the electrostatic shielding between S1 and S2 and therefore the shielding of the delay line from S2 should be as good as possible. However S1 can not be moved too close to the delay line, because at some point the electrostatic deflection of this wire will become too large - with the ultimate danger of the wire being pulled into the wall and becoming inoperative. A 3 mm distance to the wall appears to be a safe distance. Given the chamber height of 44.2 mm and the chosen sense wire spacing 6 mm 7.1 mm are left between S1 and S2. Fig. [54] shows the (calculated) ratio R as a function of the offset d of the potential wires from the sense wire plane. Both cases - 2 and 3 potential wires separating S1 and S2 - are shown. With 3 potential wires and d=3 mm R = 11.8 is achievable. It should be noted that R does not appear to be as sensitive to the number of potential wires as the sense wire sense wire crosstalk.

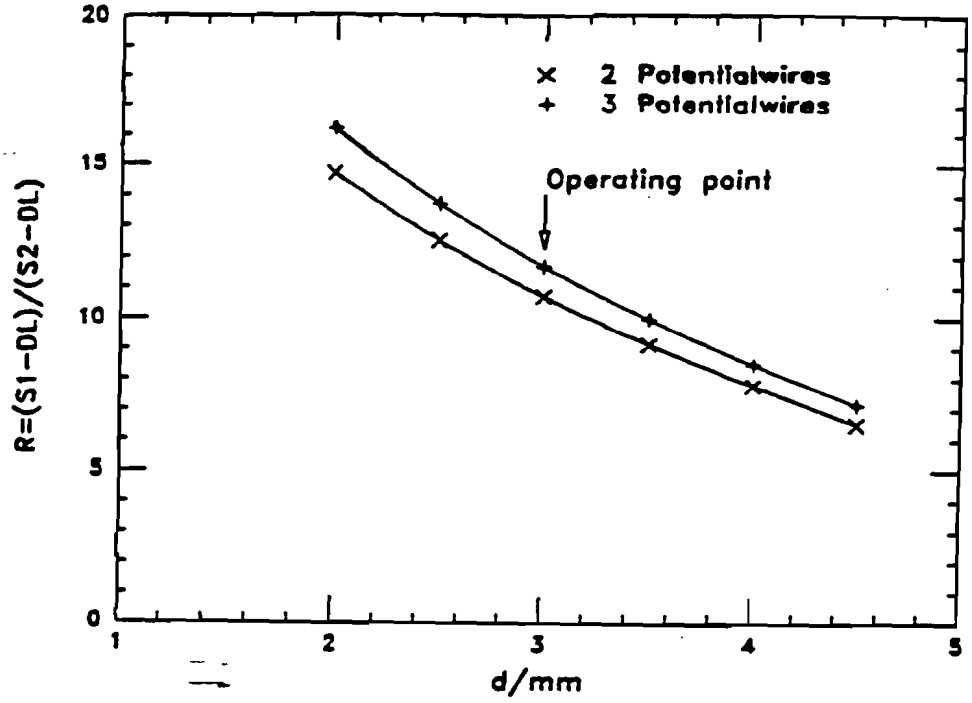

Figure 54 . Ratio R (signal induced onto the delay line from S1 over signal induced onto the delay line from S2) vs. the spacing of the potential wire separating S1 and S2

9.3. Electrostatic Stability

An important question is whether the chosen wire geometry is electrostatically stable and whether possible deflections are small compared to the intrinsic chamber resolution. S1 and S2 are both in a somewhat asymmetric situation and therefore potentially subject to large forces. To first order the deflection D depends on the sense wire voltage itself, the voltage applied to the central potential wire separating S1 and S2 and the voltage of the central field shaping strip. The following figures show some typical slices of the $V_{S1} - V_{potin} - V_{strip}$ deflection space.

Fig. [55] shows the deflection of S1 vs the strip voltage for different voltages of S1. The inner wires are kept at 1.45 kV. The dependance of the deflection on the sense wire voltage is not very strong and passes through zero for strip voltages between 250V and 300V. Fig. [56] shows the same situation in a different projection, with V_{strip} constant and the sense wire voltage varying. Fig. [57] shows the deflection of S2 vs the voltage on the outer sense wire for different voltages on the inner wires. The deflections are very small and do not vary strongly for quite a range of both V_{Sin} and V_{Sout}.

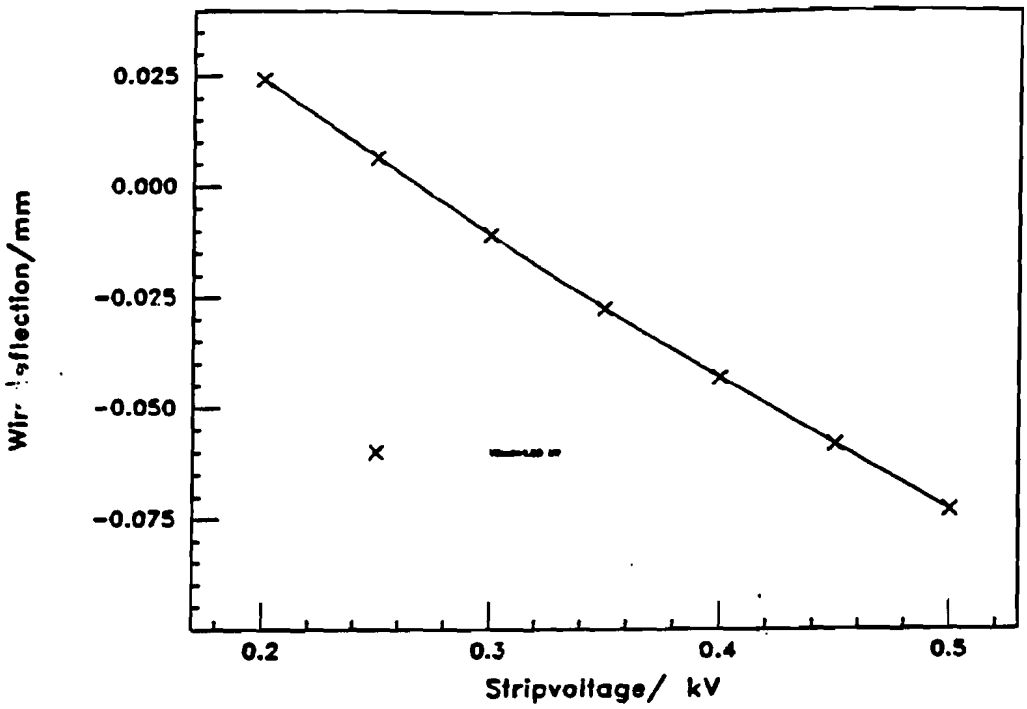

Figure 55 . Deflection of S1 vs. different strip voltages for VSout=1.55.

From the above discussions the following geometry seems to optimize both crosstalk and R while keeping the deflections small :

- 7 sense wires, the 5 inner ones spaced 6 mm apart, the two edge ones 7.1 mm away from the next neighbour.
- The 5 inner sense wires are separated by 2 potential wires each, which are offset from the sense wire plane by 1.5 mm
- The 2 edge sense wires are shielded by 3 potential wires, one in line with the sense wires, the other two offset by $\pm$ 3 mm. For mechanical reasons the inner potential wire of the three is moved towards the edge sense wire by 0.5 mm.

9.4. Time dispersion

A number of popular drift gases show a characteristic maximum in the drift velocity as a function of drift field. The velocity after passing through this maximum decreases and with increasing field levels out. This region of "negative slope" can be used to reduce the time dispersion seen by a sense wire.

In a typical drift map the electrons start out drifting on parallel trajectories

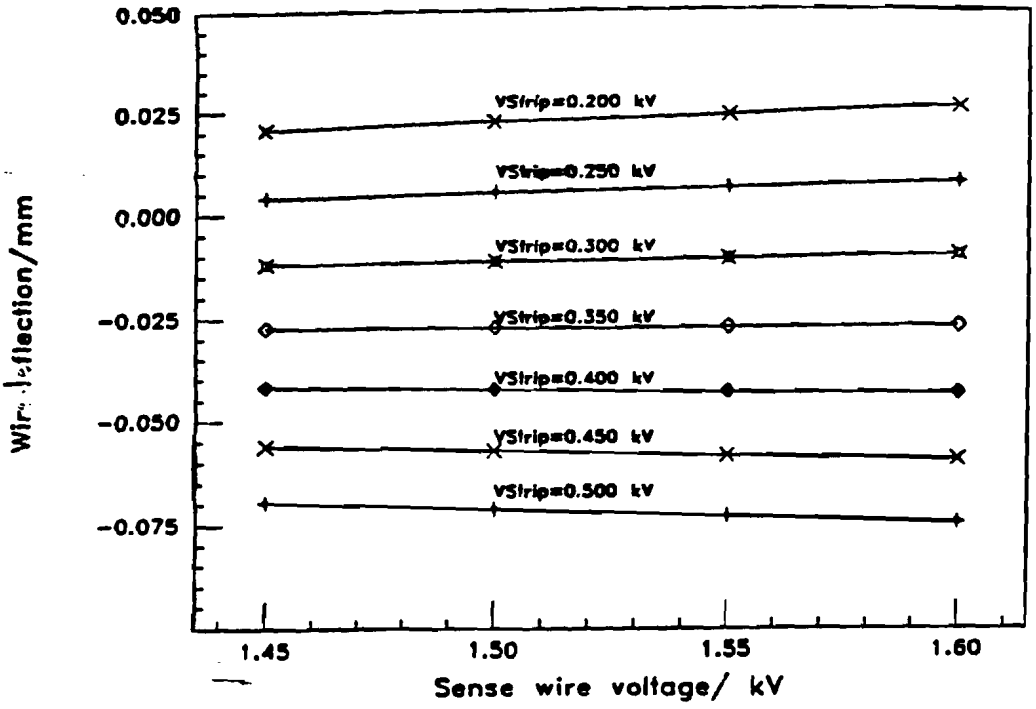

Figure 56 . Deflection of S1 vs. sense wire voltage for different strip voltages

towards the sense wire. Close to the wire the outer line start to bend inwards until close to the wire the field looks very much like the radial field of a single wire. The path length for electrons on the outer bending trajectories is considerably longer than for the inner ones. This translates into a longer drift time for the former. However, if the drift field is chosen to be within the region of negative slope, the outer electrons see in this inhomogeneous region a smaller field than the ones which are drifting straight to the wire. Therefore they are faster than the inner electrons and thereby partially compensate for the longer path length. Fig. [58] shows this effect quite clearly: The main plot shows the time dispersion for a track starting 2 cm from the sense wire plane as a function of the drift field. The curve has a clear minimum at about 500 V/cm drift field. In the inset the velocity-drift field plot for the used gas - MARK II in this case- is shown. The negative slope here extends from a field of about 300 V/cm toward 750 V/cm, which coincides with the region of minimum time dispersion on this wire. The two curves shown in the main plot are calculated for sense wires 2 and 3 respectively. They are different because of the staggering of the sense wires. Wire 3 is moved towards the track, which reduces the focussing effect of the potential wires and slightly increases the time dispersion.

The program was also used to try to answer the question of how far the geometry

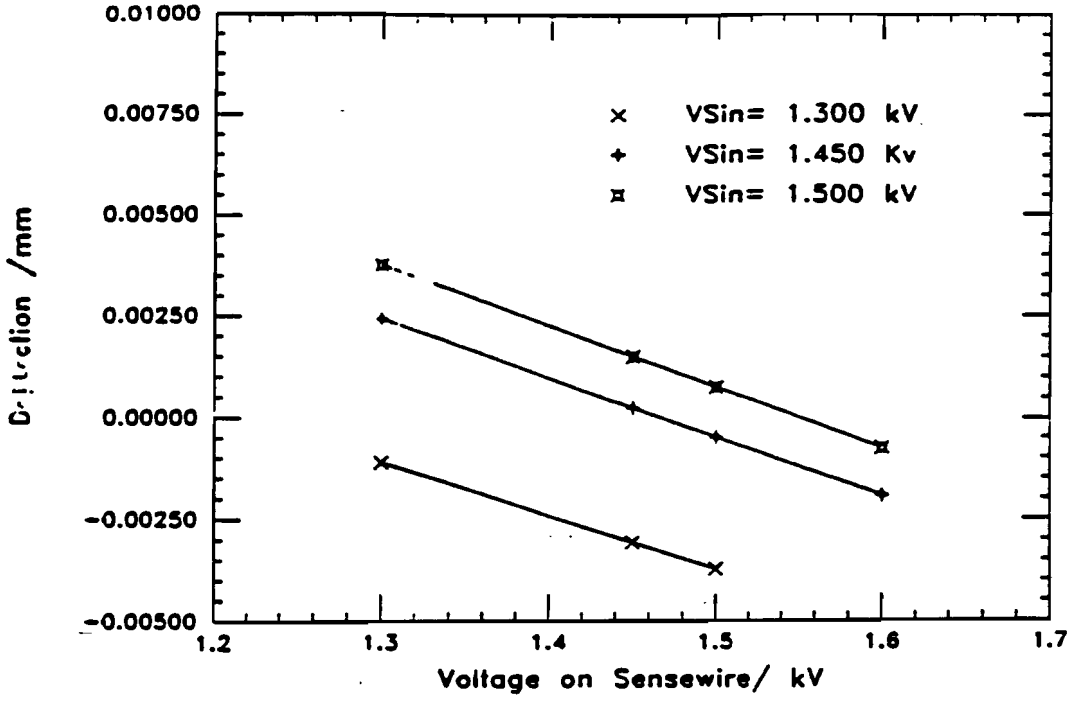

Figure 57 . Deflection of S2 vs. the voltage on the outer wire

and the running conditions of the chamber influence the time dispersion. In particular one seeks answers to the following questions:

- How does the time dispersion depend on the drift distances of the electrons.
- How does the time dispersion depend on the potential of the sense wires.
- Is sense wire 1 special in respect to its time dispersion, and by how much is it different.
- How much does the strip voltage influence the time dispersion, in particular on sense wire 1.

In Fig. [59] the time of arrival for electrons with different starting points in the chamber are shown. Each "cup" represents electrons which will end up on one sense wire. The edge sense wire is at $x = 1.91cm$, the inner one at $x = 0.0cm$. Plots for two gases are shown, the upper one for a constant drift velocity, the lower one for MARK II gas. The focussing effect of the MARK II gas and the staggering of the wires are apparent. In Fig. [60] the time dispersion is plotted as a function of the percentage of electrons in a particular bunch included in this time dispersion. In other words, to collect 100% of all electrons on SW 2 one has to wait about 45 ns, while for 90% one only has to wait around 15 ns. The time dispersion increases rapidly for the last

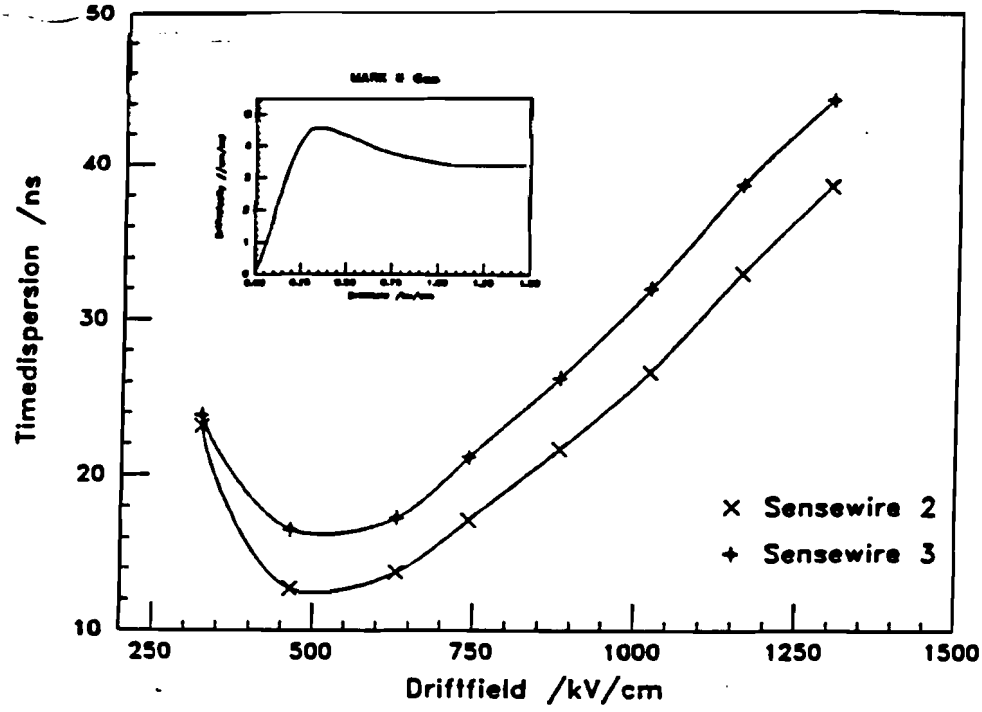

Figure 58 . Time dispersion vs. drift field for sense wire 2 and 3. In the insert the drift velocity as a function of the electric field for the MARK II gas is shown

few percent. In the following time dispersion always refers to the first 90% of the electrons collected.

The fact that some of the sense wires in the DØ geometry do not see a symmetrical surrounding can also be seen in the time dispersion. Looking at Fig. [59] the curves are not quite symmetric for x to the left or x to the right of the sense wire. This is particularly true for the edge sense wire and to some degree true for S2.

Fig. [61] is a summary of the time dispersion. Shown are plots for sense wires 1 to 3 of the time dispersion as a function of drift distances for different potentials of the sense wires. S2 and S3 show a basically flat behaviour, that changes only very little with either drift distances or sense wire potential. S1 has a little more structure at a slightly higher level, but still acceptable. The different behaviour of S1 can be understood because of the wider gap (7.1 compared to 6 mm for S1) and the closeness of the wall.

In no case, however, does the time dispersion rise above 25 ns, usually being less than 20 ns. This is below the normal rise time of a chamber pulse, which is around 30 to 40 ns. However, as was pointed out above, due to the statistical nature of the deposition of the charges along the track of the particle passing through the chamber

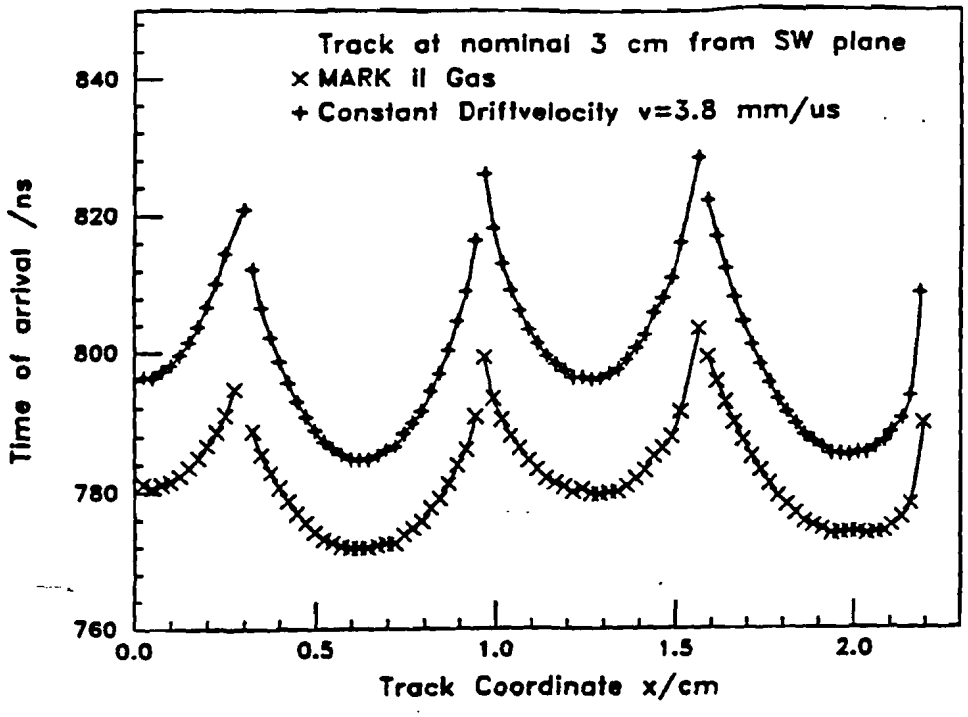

Figure 59 . Time of arrival of the electrons starting from different coordinates across the chamber vs. their starting coordinate

large time dispersion will introduce largely fluctuating contributions to the rise time and should be avoided.

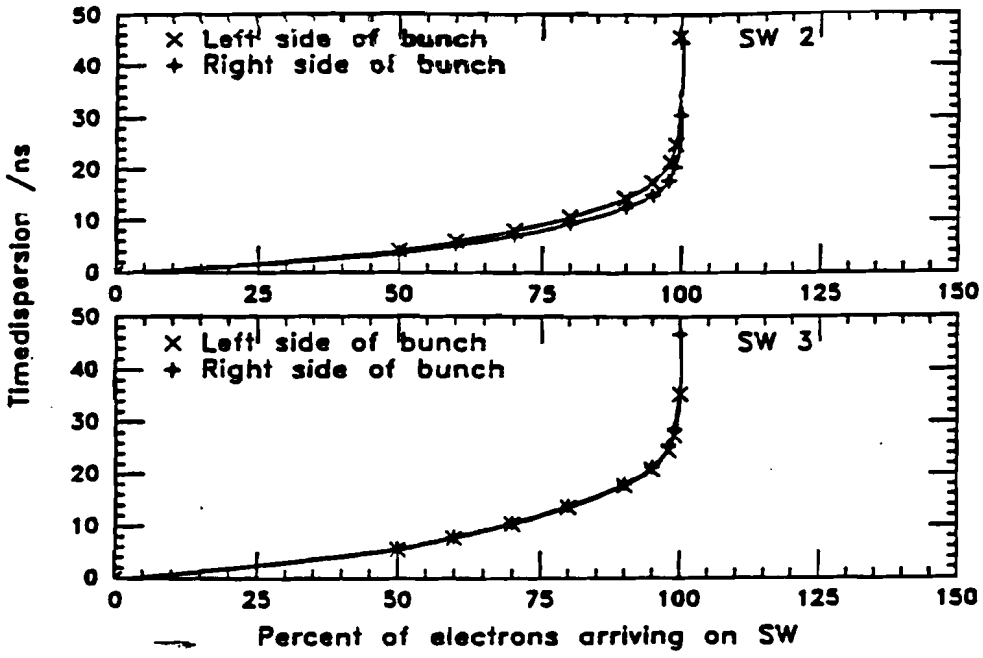

Figure 60 . Total time dispersion vs. percentage of electrons having arrived within this time

9.5. The Drift Field

9.5.1. Determination of the operating point

Every drift chamber of finite cell size has to live with distortions of the drift field close to the edges of the cell. This effect is particularly pronounced for the DØ chamber, since the walls are solid and insulating.

Two effects are observed: If no counter measures are taken, regardless of whether the chamber walls are solid or made of wires, the field close to the edges is going to be distorted. Ionization produced anywhere close to the walls is either going to be lost completely or will at least be mismeasured to some degree. Distortions of the field will also produce changes in the drift velocity in these region with resulting changes in drift times and pulse shapes. If, like in the DØ chamber, the walls are made of solid materials with exposed insulating surfaces, charges can be deposited on those surfaces and change the field in a "dynamic", time dependent, fashion. The larger the rate of primary ionization in the chamber volume, the more charge will be present in the drift region and the more of it will be deposited on the wall. This

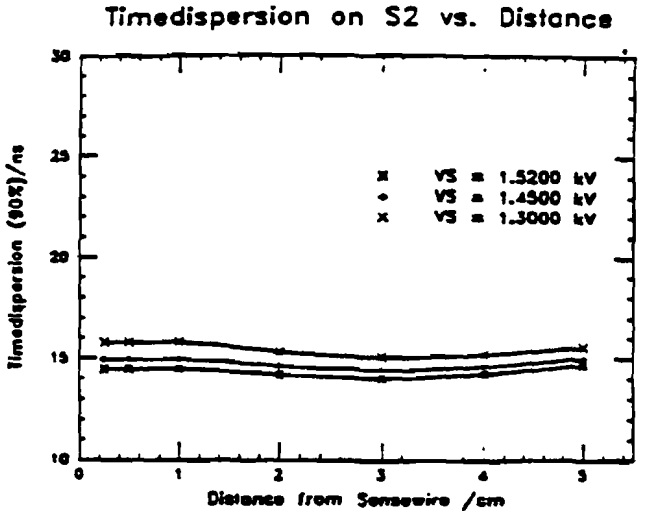

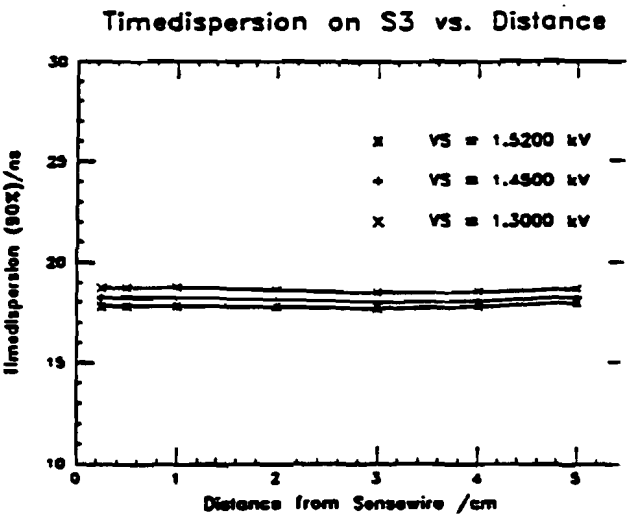

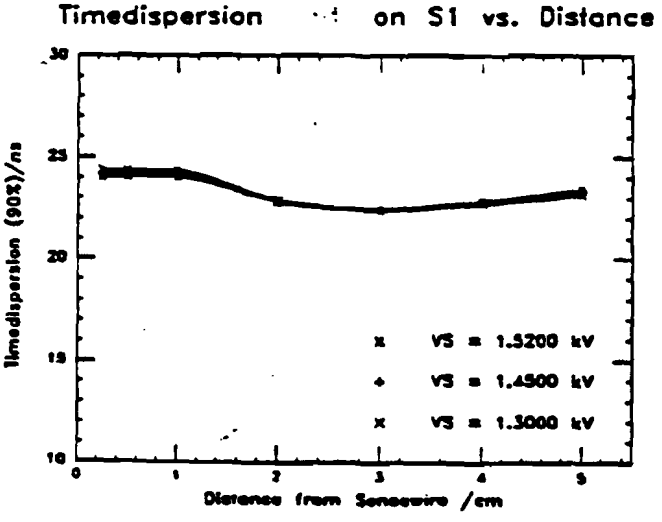

Figure 61 . Time dispersion on inner and outer sense wires as a function of drift distance of the electrons.

will change the field configuration which in turn will change the rate at which charge gets deposited on the wall. One gets a feedback mechanism which will either reach an equilibrium after some time or cause a breakdown of the chamber. Either way the normal functioning of the chamber will be impaired.

To alleviate these problems the chamber has to be designed in such a way that, electrostatically, the walls "do not exist". This is of course an idealized prescription (and a rather impossible one to achieve), but it describes the basic idea. The potential distribution and the charge buildup on the walls of the cell have to be controlled in a way that does not disturb the ideal drift field that one would have if the chamber was actually infinitely wide with no walls or edges. If this potential can be applied to the wall, the drift field will be essentially undisturbed up to very close to the wall. In the following the solution employed in the DØ chamber will be described together with a procedure to arrive at a set of operating conditions for different chamber parameters like gain of the wire, drift field, etc.

As mentioned before the walls of the DØ chamber are constructed of a light composite material with the outer skin made of Kapton foil. To fix the potentials on this (insulating) foil conductive lines are printed onto them. The center to center distance between the lines is 0.1 ", and they are 40/1000" wide. A resistive divider applies a potential to every line so that the potential distribution simulates the one seen in an infinitely wide chamber at the equivalent position as closely as possible.

Unfortunately this can only be done approximately. The potential will be steplike as opposed to the smooth behaviour in the ideal chamber. Also in between the lines strips of Kapton are exposed presenting the danger of charge being deposited there. Originally it was hoped that the application of a slightly conductive epoxy to the wall covering these open Kapton strips would solve this problem and allow the charge to dissipate. However no reliable and reproducible coating could be produced. All tested coatings would start out to be conductive in the right range, but would gradually increase in resistance after exposure to dry gas for some time and finally end up being nearly as insulating as Kapton. The use of these epoxies was consequently abandoned.

The process of establishing a working set of voltages proceeds as follows:

The first step is to establish the size of the drift field. In the case of MARK II gas (see Fig. [62] for V-E curve) the field is chosen to be around 620 V/cm. This places the drift field just past the maximum on a part of the curve with a negative slope. This negative slope helps in focussing the electrons and decreasing the time dispersion.

Sense wire and cathode voltages are set to produce the intended drift field and

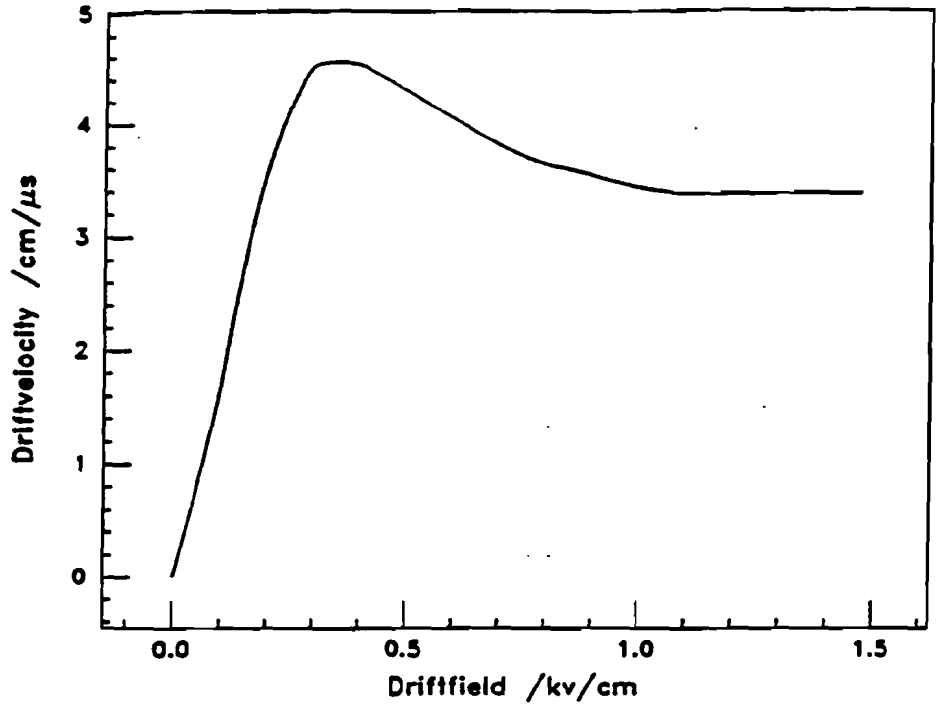

Figure 62 . Drift field vs. drift velocity for Mark II gas

gain respectively. Both are interconnected somewhat- changing the drift field will change the gain and vice versa. The gain is determined experimentally by using test chambers. Once the charge to achieve a specific gain is known the program is used to determine the appropriate set of sense and cathode voltages to get both drift field and gain correct.

The last step is to find the correct potential for the central strip. As discussed earlier the central strip is the field shaping strip which is located directly under the edge sense wire, right on top of the delay line. This strip is the end of the voltage divider, which grades the potential down starting from the cathode voltage.

A rather good approximation for this potential may be obtained in the following way. First one plots the potential in the middle of the chamber away from any wall effect along a straight line starting in the middle between two sense wires in a direction along the drift field, perpendicular to the wire plane. The resulting plot is shown in Fig. [63] . A straight line is fitted to the potential for $x > 0.4cm$. The intersect of this straight line with the sense wire plane is calculated and the resulting value is used as the first order strip voltage.

The final set of voltages is obtained by repeating the described steps, until a

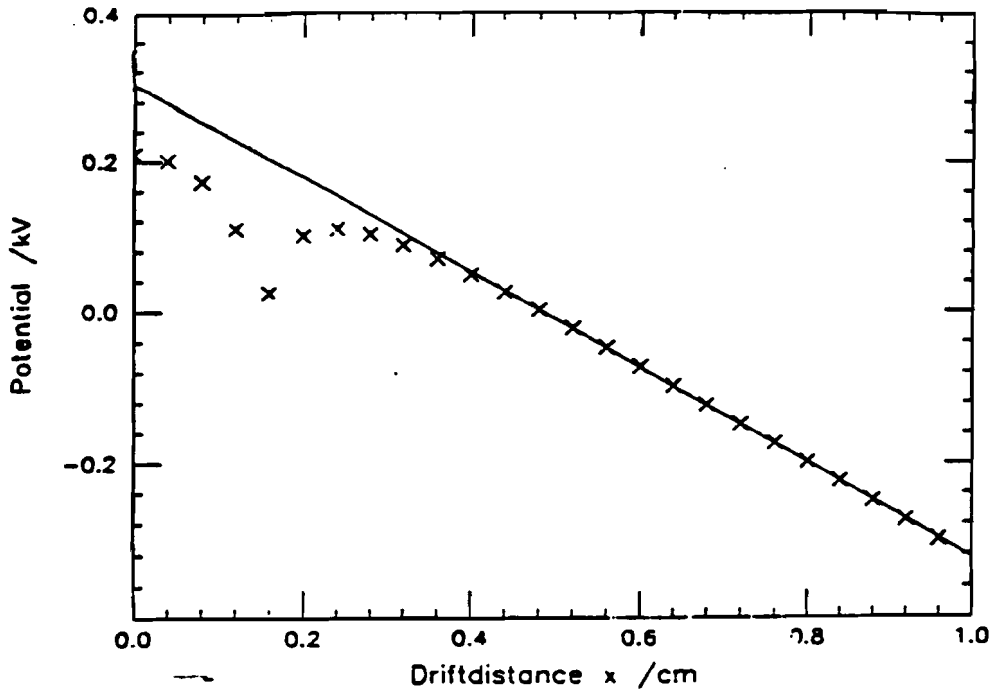

Figure 63 . Calculated potential along a line perpendicular to the wire plane starting in the middle between two sense wires, vs. distance from the sense wire plane.

decent field map is obtained for an acceptable set of charges on the sense wires. The final set also has to satisfy the stability criteria for the wire and the other points discussed in the chapter on the electrostatics of the chamber.

It should be noted that changing any of the chamber parameters, e.g. the gain ratio between outer and inner sense wires, changes all the other parameter and requires a new optimization of them.

9.5.2. The Behaviour of the Drift field

Fig. [64] show a series of drift plots, where the strip voltage was varied while all the other voltages were kept constant. The sense wire voltages were the "standard" settings from the summer '88 cosmic ray test:

$$VS_{in} = 1.45kV$$
$$VS_{out} = 1.58kV$$
$$V_{cath} = -4.2kV$$

The maximum drift distance was the one for layer 3 in the chamber: $d = 7.079cm$. The plots start with $V_{strip} = 0.00kV$ and end at $V_{strip} = 0.65kV$. The main effect

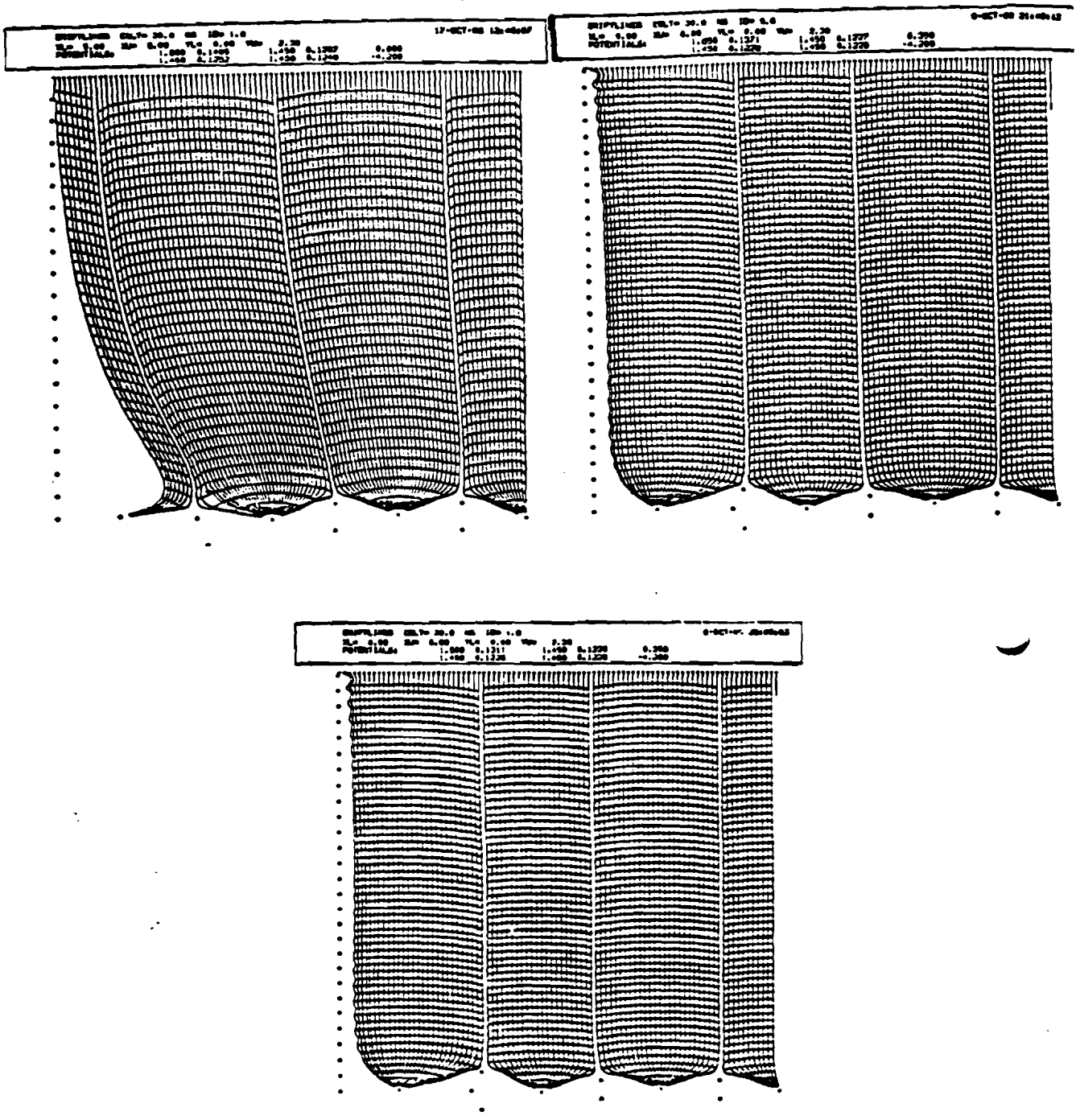

Figure 64 . Drift maps for 3 different strip potentials. Top plot: Vstrip=0.0kV, middle plot: Vstrip = 0.35 kV, bottom plot: Vstrip = 0.65 kV

of this is to tilt the drift field of the outer wires away or towards the wall. For $V_{strip} = 0.00kV$ the field of sense wire #2 is tilted quite heavily towards the wall at large drift distances. This considerably reduces the amount of charge that will end up on wire #1. For large drift distances only about 1/4 of the normal charge will be collected by wire #1, the rest will end up on wire #2. The field for wire #3 is still slightly deformed. The situation is just the opposite for $V_{strip} = 0.65kV$. Here the field tilts away from the wall for large drift distances and compresses the space available to the drift lines which will end up on wire #2. The gap of wire #1 collects now a disproportionally large part of the primary ionization, however a sizable part of that charge will not end up on the wire, but gets pulled into the wall of the chamber.

The optimum drift field seems to be around $V_{strip} = 350V$, which is in agreement with the previously shown number.

Fig. [65] shows a set of drift maps for constant wire and strip voltage, but changing cathode voltage. The cathode voltage is changed from its nominal value of -4.2 kV to -10kV. The overall pattern of the field remains unchanged, but around $V_{cath} = -6.00kV$ the charge on the potential wires changes sign and drift lines ends up on them. At $V_{cath} = -10kV$ a sizeable number of the drift lines end up on the outermost potential wire. In order to retrieve these lines the potential on the sense wires has to be increased with a corresponding increase of the charge difference between the sense and the potential wires, which eventually will result in a breakdown of the chamber.

In addition the equal time lines (spaced at 30.0 ns on each of these plots) are considerably more curved in the -10kV setting than they are in the nominal setting. This is also a consequence of the now positively charged potential wires, which loose their focussing ability.

9.6. Summary

A drift cell with 7 sense wires and 14 potential wires was selected for the final DO drift cell. The 5 inner sense wires are spaced by 6 mm, with 2 potential wires in between each pair. The potential wires are arranged in two rows $\pm 1.5mm$ off the sense wires plane. The 2 edge sense wires are 7.1 mm away from the next sense wire, with 3 potential wires in between. The surface of the shelves is 3 mm from the first and last sense wire. Electrostatic simulations indicate that a geometry like this is mechanically stable for wire tensions well below the elastic limits of the wires. It is possible to find a suitable set of operating voltages so that the drift map shows only very little distortion close to the edges of the chamber. The chosen drift field minimizes the time dispersion and results in the proper gain for the sense wires. The

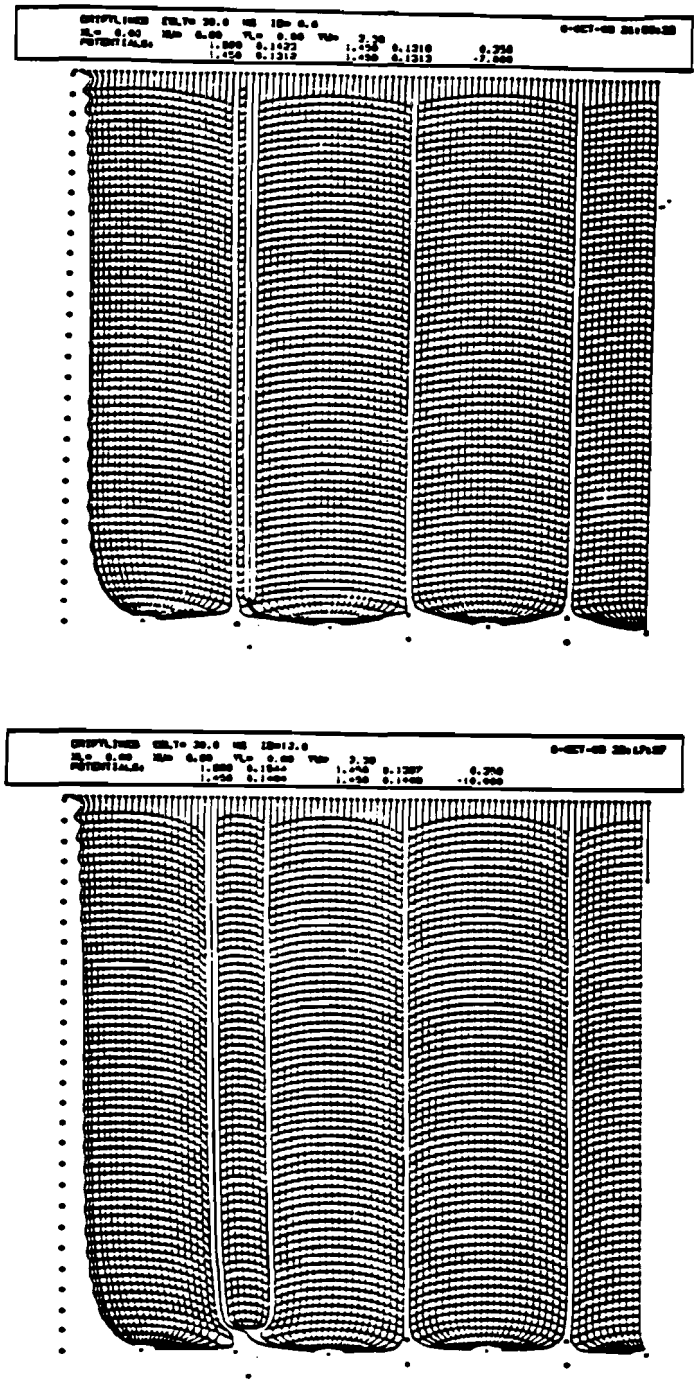

Figure 65 . Driftmaps for constant wire voltages, but the cathode voltage changing. Plots for (in order) -4.2kV, -7.0kV and -10kV are shown.

geometry of the edge wires is such that small mechanical displacements of the walls do not lead to catastrophic consequences for gain or drift field.

10. Early beam tests

10.1. Introduction

During the design and construction phase of the central drift chamber two major test beam efforts were undertaken. During the spring and early summer of 1985 two early prototypes were tested in a beam at the Alternating Gradient Synchroton at the Brookhaven National Lab. The chambers tested were close to the final cell configuration, but were made from different materials using methods different from the eventually adopted ones. In June of 1986 a larger effort encompassing a large part of the collaboration took place, in which a prototype of the Vertex Chamber and a larger prototype of the central chamber were tested. The so called TC5 CDC prototype was a close approximation of a two module piece of the final chamber, however with only two layers and flattened out.

The goals of both tests were to gain a basic understanding of the proposed cell design, measure its characteristic behaviour and gain some insight into the influence of the readout electronics on the results. In the following a short summary of the two tests is presented. No details of the analysis are discussed, they can be found in [45], [46],[47].

10.2. The Spring 1985 BNL test

The 1985 Testbeam took place in the A2 testbeam at the Alternating Gradient Synchroton at the Brookhaven National Laboratory on Long Island. A momentum separated secondary beam of 0.8 to about 5 GeV of mostly pions and protons with some electrons was used. Following a lead collimator with an opening of 1x1" and two gas filled Čerenkov Counters the chambers were mounted on a remotely movable table. A lead glass calorimeter was mounted behind the chamber allowing the identification of electrons in the beam. A number of scintillation counters provided a beam trigger and a time of flight system to distinguish pions from protons at 800 MeV.

The moving table was controlled from the counting house and could position the chamber in two directions perpendicular to the beam axis. A digitizer provided an accurate readout of the chamber position.

Two chambers were tested in this setup. Both were single cell prototypes of 1.50 m length- the at this time current length of the DØ chamber. They were equipped with 8 sense wires and two delay lines each. The chambers were different in the

spacing of the sense wires (2.5 and 3 mm respectively) and in the way the delay lines were surrounded by the field cage. Cases with and without central strip did exist.

Different to the final DØ design the sense wires in either cell were separated by one potential wire only. Also no extra steps were taken to insulate wires 1 and 8 specially to minimize the crosstalk and to maximize the delay line signal.

Two types of runs were taken. Most runs were done with the beam energy set to 4 GeV, close to the maximal energy of the beam. In this setting intrinsic chamber parameters like resolution were measured. A number of runs were taken at 800 GeV however. At this energy, the smallest energy at which the beam was stable, it was possible to separate the beam into protons, pions or electrons and trigger on them individually. These data were used for studying the dE/dx behaviour of the chamber.

The readout electronics consisted of a Fujistu preamp, followed by a shaping amplifier(which did minimum shaping, essentially only compensating for cable losses), a LeCroy 10X photo multiplier amplifier and a LeCroy 100 MHz Wave form digitizer.

10.2.1. Resolution of the chamber

The resolution of the sense wires was determined from a set of three sense wires. The time measured on the two neighbour wires was compared to the time of the central wire. The sigma of the resulting distribution is called the intrinsic resolution of the wire:

$$\sigma = \sigma(\frac{t_{n+1} - t_{n-1}}{2} - t_n) \qquad (10-1)$$

To convert the timing resolution into a spatial resolution the drift velocity has to be measured. This was done using the movable table, moving the chamber by a known amount, measuring the drift time difference, and converting this into a velocity. From a least square fit to the data a value of $v = 32.5\mu m/ns$ for P10 gas (10% Methane, 90% Argon) was found.

A fit to the measured resolution as a function of drift distance x with

$$\sigma = \sqrt{a^2 x + b^2} \qquad (10-2)$$

yields for the parameters a and b (from [46]):

$$\begin{aligned} a &= 44 \pm 24\mu m \\ b &= 112 \pm 4\mu m/\sqrt{cm} \end{aligned} \qquad (10-3)$$

For sense-wires at the edge of the chamber the resolution was found to be worse by about 11%.

For the delay lines the difference in time measured on the right side of the chamber and on the left side of the chamber is a measure of the z-position. The width of the distribution is the intrinsic resolution of the line.

$$z = \frac{v_{dl}}{2}(t_l - t_r)$$
$$\sigma = \frac{v_{dl}}{2}\sqrt{\sigma_l^2 + \sigma_r^2} \qquad (10-4)$$

For the delay line this approach using single particle can be used, because contribution to the σ due to the width of the beam was small compared to the resolution of the line itself. This is not the case for the sense wires.

For one line which had no resistive strip on top a resolution of $\sigma = 2.5mm$ was found, for the other line, which had a $1k\Omega/\square$ line on top the resolution was somewhat worse with $3.3mm$.

10.2.2. dE/dx performance

Since the DØ detector has no central magnetic field one of the purposes of the drift chamber is to help in the separation of single electrons from overlapping double electrons. The later one will be produced mostly by conversions in the chamber material. This differentiation will be made by measuring the specific ionization of a track and comparing it to the one of a minimum ionizing particle (MIP). Since the test chambers had only one cell four consecutive events were overlaid in software to simulate a multi cell event. It was found, that at a 95% confidence level the 2π contamination in the 1π sample is less than 1%.

10.2.3. Two particle separation

An attempt was made to measure the two particle resolution of the chamber again using simulated events. Single hit data were overlaid and shifted in time to model a double hit event, and then passed through the hit finder. For 100Mhz 8bit digitization the efficiency to find a second hit drops below 90% at 2mm separation.

10.2.4. Resolution with reduced sampling rate and reduced digitization accuracy

To understand more about the digitization process and the needed accuracies etc. a number of tests were made with analyzing data with reduced digitization rates and accuracies. The following table summarizes the requirements for the different performance criteria:

	nominal value	resolution frequency	deteriorates at accuracy
Sense wires	$120\mu m$	60 MHz	6bit
Delay lines	2.5 mm	80 MHz	8 bit
2 particle sep.	2 mm	80 MHz	8 bit

Table 1

Table showing the nominal values for resolution, dE/dx and 2 particle separation and the frequencies and digitization accuracies required to achieve this performance.

10.3. The June 1986 BNL test

During June of 1986 a second beam test effort was undertaken in which a prototype of the CDC was tested. This time a larger part of the collaboration participated. Besides the chamber this test was meant to be a system test for the DØ data aquisition system and online software. For this a first version of the level 2 system was installed. Chambers tested were a new CDC prototype and a test chamber of the vertex detector. The setup was very similar to the one described for the previous test beam. It took place using the same beam with a very similar triggering system. This time no lead glass Čerenkov calorimeter was present because of other experiments downstream from the DØ setup. For the CDC the goals of this test were twofold. The results from the last year test beam were to be confirmed, if possible, and supplemented on some points. More important though the overall performance of the new prototype called TC5 was to be tested. This was a very important milestone, because TC5 was the first chamber built of the same materials as the final chamber would be, and which was geometrically very close to the real chamber. The performance of TC5 was hoped to give a good indication how the DØ chamber would eventually perform, including questions like aging, stability etc.

TC5 was a "flat" version of the final chamber. It consisted of the equivalent of two modules, each having two layers. Two complete cells were formed by this configuration, with four delay lines. The cells were constructed using a flat version of

the Rohacell-Kevlar-Epoxy-Kapton sandwich described in the section on construction of the chamber. The overall mechanical layout was the same as it is used in the big chamber. The tension of the wires was supported by the Al- frame, but the endplugs which are positioning the individual wires were also used to key in the two module and position them relative to the Al- frame. The field shaping cage was made by printing resistive lines onto the surfaces of the shelves. The wires were pulled up to the correct potential by a surface mounted resistor strip mounted inside the chamber on the surface of the shelf. The wire arrangements inside a cell were slightly different from the final cell. Every sense wire was separated from its neighbours by 2 potential wires. The potential wires were offset out of the plane by half the distance between neighbour sense wires. The edge sense wire was treated in the same way as the other wires, with two potential wires separating it from the next wire. The distance from the edge wire to the surface of the shelf was a little bit larger than half the distance between neighbour sense wires.

The results of the test were mostly compatible with the earlier beam test. The sense wires resolution was found to be around $125\mu m$ at 1 cm, increasing like $\sqrt{x}$ with the drift distance. Close to the sense wires the resolution increases again due to field imperfections. dE/dx resolution for separation of 1π events from 2π is similar to the one measured before. The contamination of 2π events in a 1π sample is below 1% for the 65% truncated mean.

The main difference between this and the earlier beam test was found in the delay lines. The resolution of the lines was found to be 3.4, 4.0 and 4.0 mm for DL1, DL3 and DL4 respectively. One sense wire which was driving the fourth delay line was not functioning properly. This is somewhat worse than the previous number. 2.5mm was found there to be the intrinsic resolution. The reason for the deterioration was determined to be the resistive strip on top of the delay lines in connection with the contribution from the strips on the cathode. In this chamber for the first time more than one layers of cells were used, with cathodes mounted very close to the delay lines. The resistivity of both types of lines was chosen to be a few $k\Omega/\square$. This turned out to be too low and worsened the resolution considerably. Another contribution to the resolution was a non negligible crosstalk from the second sense wire onto the delay line. The ratio *pulse induced from S1 onto delay line / pulse induced from S2 onto delay line* was measured to be only 4. This tends to smear out the pulse on the delay line and worsen therefore the resolution. These results triggered a careful redesign of the cell geometry, which is described elsewhere.

10.3.1. Conclusion

The first full scale beam test of a DØ drift chamber prototype took place at the BNL alternate gradient synchroton. Data collected there were used to establish the basic performance parameters of the proposed cell. It was found that the chamber performed within specifications. Spatial resolutions of better than $200\mu m$ in drift and $2.5mm$ in z were obtained.

The second beam test supported the results achieved in the first test. The chamber performed reliably and without major problems, proving that the method of construction and the materials used are compatible with use in a drift chamber. Problems in the design were found with the way the outer sense wires drive the delay lines and with the shielding between the inner and the outer sense wires.

11. The Premod - the cosmic ray tests

During the 1986 DØ summer workshop it was recommended to the CDC group to construct a chamber using 10% of the finished parts from the whole chamber production and test this chamber thoroughly. Although a lot of test data did exist at this point as described in the chapter on early beam tests, and although the performance data of the chamber were quite well established, it was felt that the methods used in the construction of the chamber were sufficiently novel and untested to warrant a full scale system test. Besides once more confirming the basic performance data for the chamber this test was geared towards better understanding questions of stability of the chamber, operating parameters and, last but not least, to actually see and experience the little details in constructing a complicated object like the CDC.

During the following month a test chamber called Premod was built at Stony Brook. The premod consists of three final modules– modules which have been taken out of the production line– put into a specially built Aluminum drum and equipped with a nearly finalized version of the electronics. This chamber was used in two major tests: During the summer of 1988 a series of detailed cosmic ray studies were undertaken. In the fall of 1988 the chamber was shipped to the Fermi National Accelerator Laboratory and installed in the DØ interaction hall at close to the final chamber position. During the winter and spring of 1989 data were taken at Fermi Lab using the Tevatron Proton Antiproton collider and the DØ data acquisition system. In the following the chamber, the cosmic test setup and test results and the DØ Hall test will be described.

11.1. Premod: The chamber

The premod test chamber is made up from three standard CDC modules. They are held in an Aluminum drum with two removable end plates. Exactly as in the final chamber the end plates are machined to receive the oval end plugs from the modules. An "O"-ring seals the drum against the atmosphere. Once the modules are inserted the tension of the sense- and potential wires is transferred onto the Al- drum with the help of little bridges as described in the section on the construction of the CDC. Fig. [66] shows a cross section of the premod. In each layer two cells are complete, and one cell is incomplete. Since adjacent layers are staggered these incomplete cells are alternating on the right and on the left side of the chamber. This means that they overlap with complete cells. Track reconstruction in these edge region might be problematic, if the field is highly distorted. However no evidence was found that this is the case. In the following the full 28.625° opening angle of the chamber, which

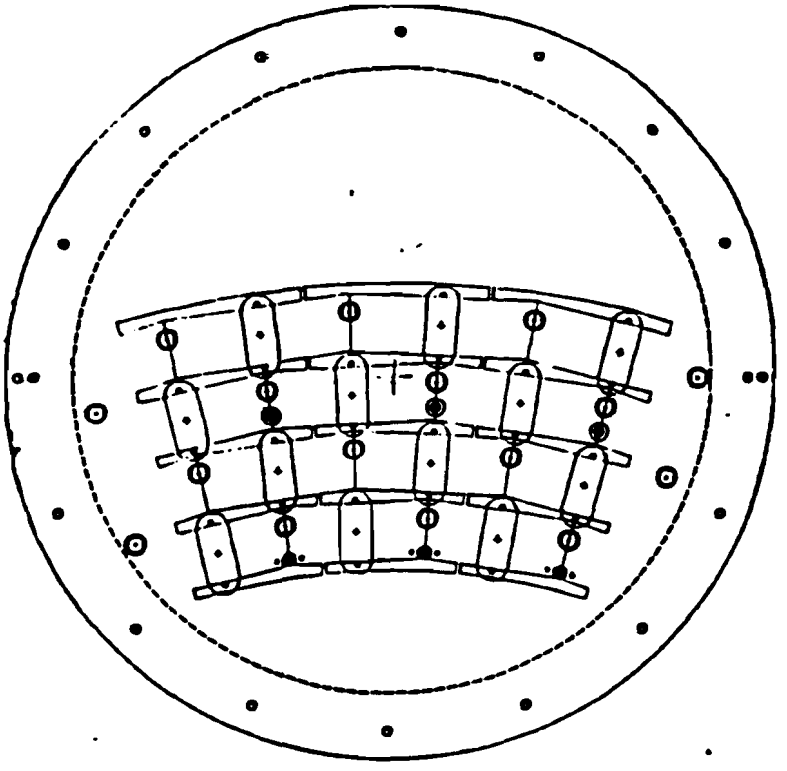

Figure 66 . Cross sectional view of the Premod with the outline of the three modules. Clearly visible are the "unfinished" cells on either side of the chamber.Fully useable are only the eight inner cells.

includes the inner half of the incomplete cells, are used.

The construction details are exactly the same as for the full chamber. The only difference is in the way the gas flows through the chamber. Since the three modules were put into a round drum, there are large spaces above and, to a lesser extent, below the modules. Gas flowing into the space between the Al- end plate and the G10 end plate from the top will see a low impedance for a path bypassing the actual chamber. This path is much less important in the real CDC because the modules are fitted inside the ring of outer shell and inner shell. For the premod that has the consequence that for the same flow rate the exchange of gas in the actual chamber volume is slower, so that the chamber has to be operated at a higher flow rate. Typically 0.5 l/min were used for the premod. For comparison the CDC during its cosmic tests at Stony Brook operated at typically 1.5 l/min for 32 modules without problems.

Construction of the Premod was started in the late winter of 1987. At this time the techniques for molding the shelves etc were more or less established. A first set of modules were inserted into the chamber in May of 1987, and the chamber was

operated successfully during the summer and fall of the same year. In late 1987 it was discovered that the chamber became unstable under high currents- currents of the order of 10 times the nominal DØ currents. As the most likely explanation of this effect the above mentioned Malter effect was eventually identified. A high resistivity coating which was used on the walls of the early modules to help dissipate static charges is thought to be the source of these breakdowns. The resistive layer on top of the electrodes would charge up and the charge would not be able to leak through to the electrode fast enough under sufficiently high currents. A high charge built–up on the electrode occurred and at some point a breakdown happened. This breakdown freed a few electrons which drifted to the anode wire and started another avalanche, which in turn increased the charge on the resistive layer. A positive feedback mechanism was established and the chamber broke down. Only after removing the HV entirely would the chamber recover.

This discovery led to the abandoning of the coating for all the production modules. The modules in the premod were exchanged against good ones in early 1988. After this the chamber performed without problems under high currents. In the section on the analysis of the test data implications due to the removal of the coating are discussed.

The electronics used to instrument the premod was very close to the final version. On the readout side of the chamber boards with sense wire amplifiers serving one module or 28 wires alternate with delay line amplifier boards serving 8 delay lines each. Signals are brought to the outer radius of the chamber and flat coaxial cables carry them on towards the outside. On the HV side every second board is a delay line amplifier board of the same type as used on the readout side. In between G10 boards distribute the HV to the sense wires and the central strips. The cathode voltages are distributed with thin teflon insulated HV cable directly to the HV feed through in the end plate.

11.2. The cosmic ray test setup

For the cosmic ray test a simple test station was built at Stony Brook. It consisted of a trigger formed by three scintilation counters, a Fastbus based FADC system (the system used for the June 1986 test beam) and a PDP 11/24 mini computer. The PDP read out the data from the FADC, simulated the zero suppress circuit and sent the suppressed data on towards a VAX 11/780, where they were stored and analyzed.

The trigger was made up of three 1.8 m long 10 cm wide scintillation counters. One was mounted on top of the chamber, one directly below and another one about one meter below the chamber. 15cm of Iron provided a momentum filter in front of

the last counter. For a trigger a coincidence of all three counters was required. The trigger time was set by the middle counters, which was closest to the active chamber volume.

The analog signals from the preamps were brought via thin coaxial cables to a set of DØ shapers. Theses shapers were an early version of the later used model, with many fewer features. They were set up to do basically no shaping but to simply compensate for the distortions of the signals due to the cables. From the shapers the signals were routed to the FADC, where they were digitized and then sent on to the PDP11/24. This version of the FADC did not have a zero suppression chip nor a bilinear response. On the PDP11/24 the missing zero suppress chip was simulated in software and the suppressed data were sent to the VAX 11/780 via a fast parallel link. There the data were stored and analyzed.

11.3. The Cosmic ray data

The data presented in this section were taken during the summer of 1988 using the cosmic ray setup at Stony Brook (see also [48]). Questions addressed in this analysis were:

- Efficiency of the chamber
- Resolution in the drift coordinate and in z and uniformity of the resolution along the drift distance and along z.
- stability of t_0 and velocity with time and with changing gas mixtures.

11.3.1. Efficiency of the chamber

A number of effects contribute to inefficiencies in a drift chamber.

- Loss of charge along the drift direction. A large loss of charge will decrease the efficiency of the chamber.
- Inefficient hit finding. Hits might be missed because the hit finding algorithm is not optimized, because the Hv is set wrongly or because of poor internal chamber alignment.

In the following each of the above effects will be discussed in detail.

Loss of charge along drift and z

Two different sets of modules were tested in cosmic rays. They differed in the treatment of the walls within a cell. For the early set the walls were covered with a thin layer of an antistatic epoxy. For the reasons outlined above this epoxy made

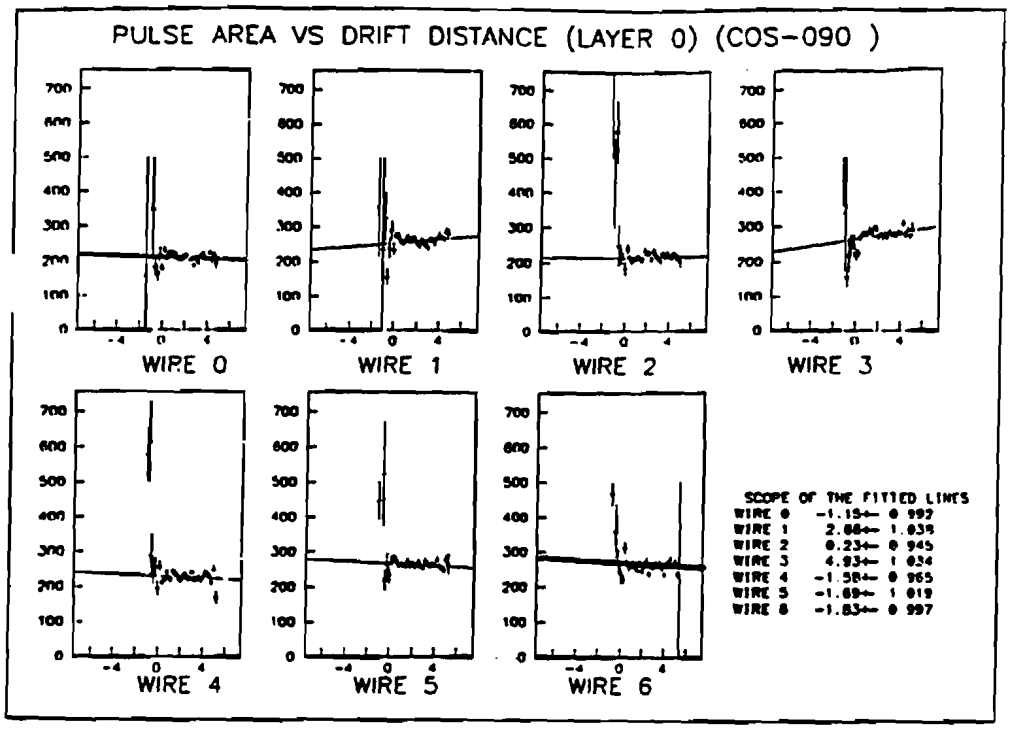

Figure 67 . Charge on the sense wire as a function of drift distance for an old module with walls coated with antistatic epoxy

the chamber unstable under high currents and was abandoned for the later modules. Fig. [67] shows the charge as a function of drift distance for the early set of modules. The distributions are flat, no significant loss of charge is observed. Fig. [68] shows the same plot but for one of the new modules. The operating conditions are the same as for the previous plot ($V_{sw\_i} = 1450V$, $V_{sw\_o} = 1550V$, $V_{cath} = -4200V$, $V_{strip} = 220V$.). A dramatic drop of the charge with drift distance for the outer wires is observed. The inner wires remain flat. Fig. [69] shows a drift plot for this setting. A number of lines from the edge sense wire end up on the wall of the chamber. This affects the signal on this wires in two ways. With increasing distance from the anode the width over which charge from a track will be collected on the outer wire decreases. For the field configuration shown in Fig. [69] this is a 15% effect for 6.8cm of drift. Secondly some part of the ion charge will be deposited on the walls instead of drifting towards the cathode. It is possible that this charge interacts with the drifting electrons and reduces the amount of charge arriving on the sense wires.

These measurements show that for the chosen operating conditions the loss of charge is connected to the deposition of ion charge on the walls of the chamber. The antistatic coat used in early modules prevented this problem, but it can not be used

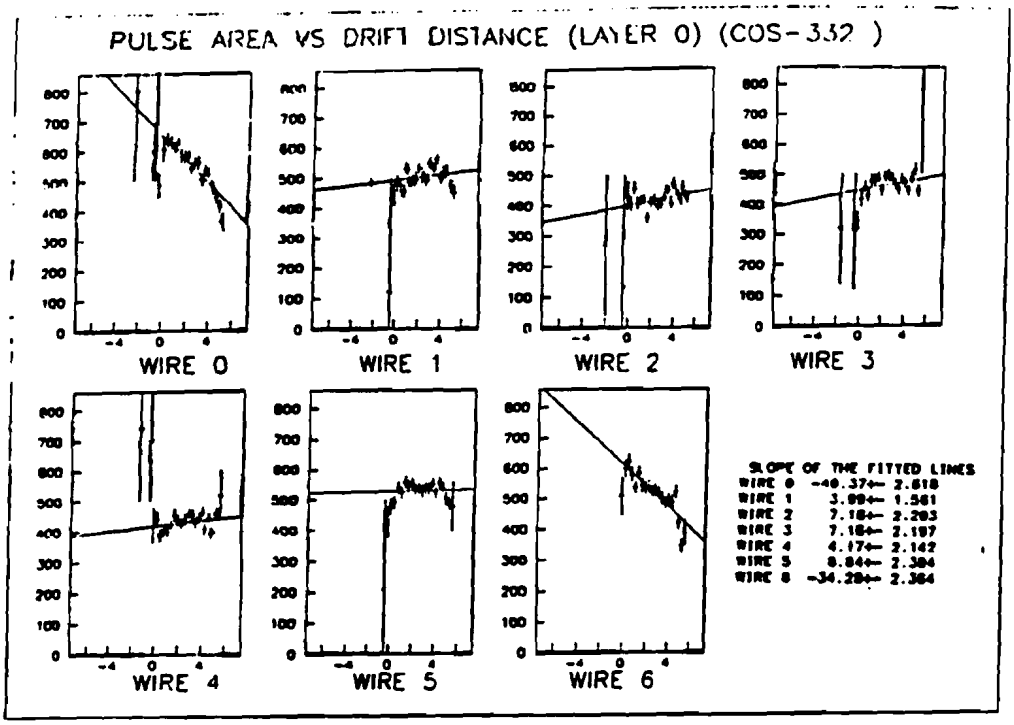

Figure 68 . Pulse area vs. drift distance for layer 0 of module 7

for other reasons discussed above. An alternative solution is to change the field in the chamber in a way that no or as few as possible drift lines end on walls. This can be achieved by changing the potential of the central strip. Changing this potential will change the charge on each field shaping strip and, depending on the sign, tilt the field towards or away from the wall. The second plot in Fig. [69] shows the resulting drift field for a central strip voltage of 350 V. The effect on the drift lines in the outer gap is clearly visible, no more lines end on the wall. 350 V might actually be a slight over compensation, since the field lines for the outer wire are now tilted away from the wall, compressing the lines for the next wire. In Fig. [70] the resulting pulse area vs. drift distance plots are shown. They are much more similar between the outer and the inner wires, with all dropping around 5% over the full drift distance. Table 1 lists the exact numbers before and after the corrected potentials:

Using the adjusted potentials for the central strip the charge distribution on the outer sense wires as a function of z was measured. This is an equally important distribution because a non flat response here will introduce region of possibly lower efficiency in z and will influence the delay line signal. Fig. [71] shows the plot for the inner module in the premod. The response is basically flat for all wires. Some structure may be present at either end of each line, which can be understood because

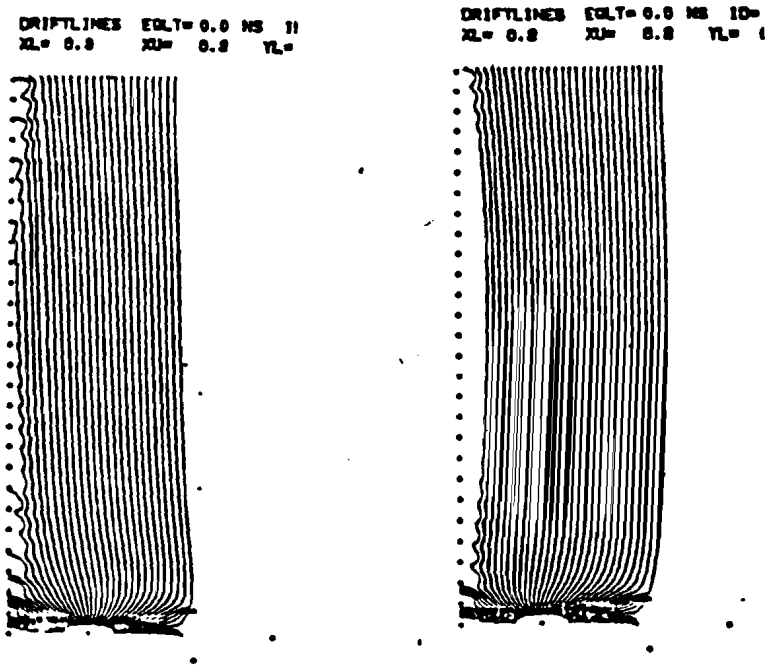

Figure 69 . Drift Lines for the chamber settings used to calculate the loss of charge presente table 1. The left plot shows the lines for a strip voltage of 290 V, the right one for 350 V

of effects close at the end of the chamber.

These data show that the loss of charge with drift distance observed in some cosmic ray data are mostly due to improper settings of the potentials on the electrodes, in particular on the central strip. This stresses again the need for a careful optimization of the chamber voltages as described in the section on the electrostatics of the chamber. No evidence for attachment has been observed.

Hit finder related effects on the efficiency

Software plays in important role in the determination of efficiencies. The variables used in the pulse finding have to be close to optimum in order not to influence the efficiency. Closely related to the efficiency of the pulse finder is the correct high voltage on the sense wires. Too low a voltage might let some pulses disappear into the noise and lower the efficiency as well.

Efficiency in the following is defined as the ratio

$$E = \frac{\#\text{ of hits on a track}}{\#\text{ of expected hits on the track}}$$

Only full tracks were used to calculate efficiencies.

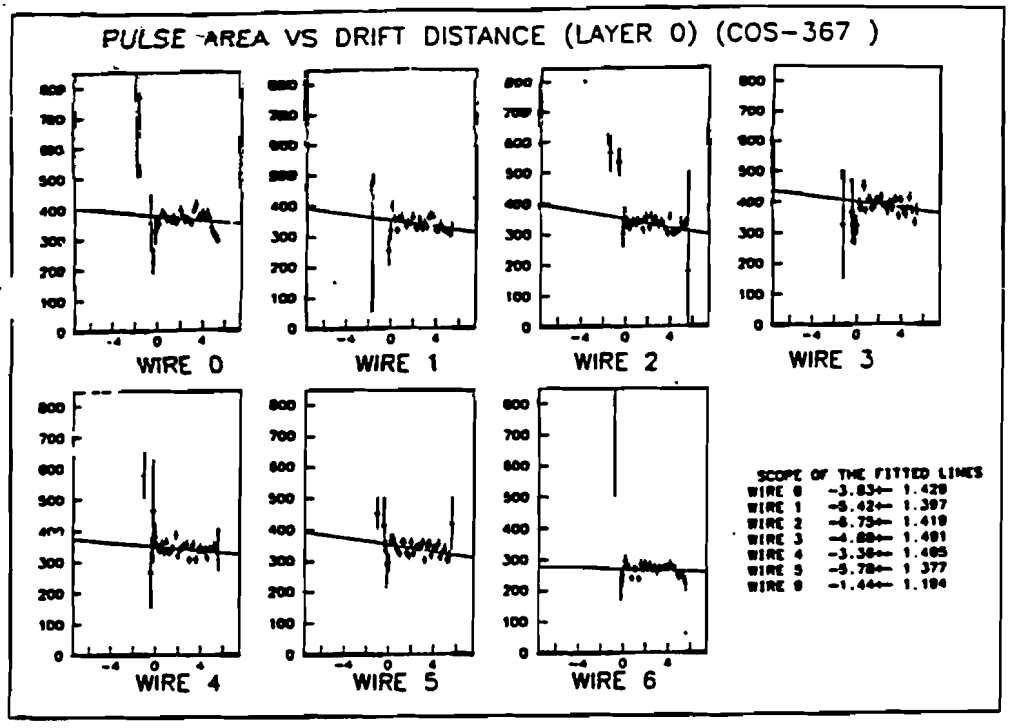

Figure 70 . Pulse area versus drift distance for the strip voltage raised to 350V

Wire #	drop over drift distance /% before correction	σ/%	drop over drift distance after correction	σ/%
0	-40.4	±2.6	-3.8	±1.4
1	4.0	±1.6	-5.4	±1.4
2	7.2	±2.2	-6.8	±1.4
3	7.1	±2.2	-4.9	±1.5
4	4.2	±2.1	-3.4	±1.4
5	0.6	±2.3	-5.8	±1.4
6	-34.3	±2.4	-1.4	±1.2

Table 1

Drop in charge seen by the different sense wires in layer 0 before and after the central strip potential was corrected.

Fig. [72] shows efficiencies on the sense wires of layer 0 as a function of different high voltages. Fig. [73] shows the same plot for two different threshold settings. For the setting with Thres1=3, Thres2=9 and Thres3=9 FADC counts the plateau is reached the earliest at 1.4 kV for inner and outer wires.

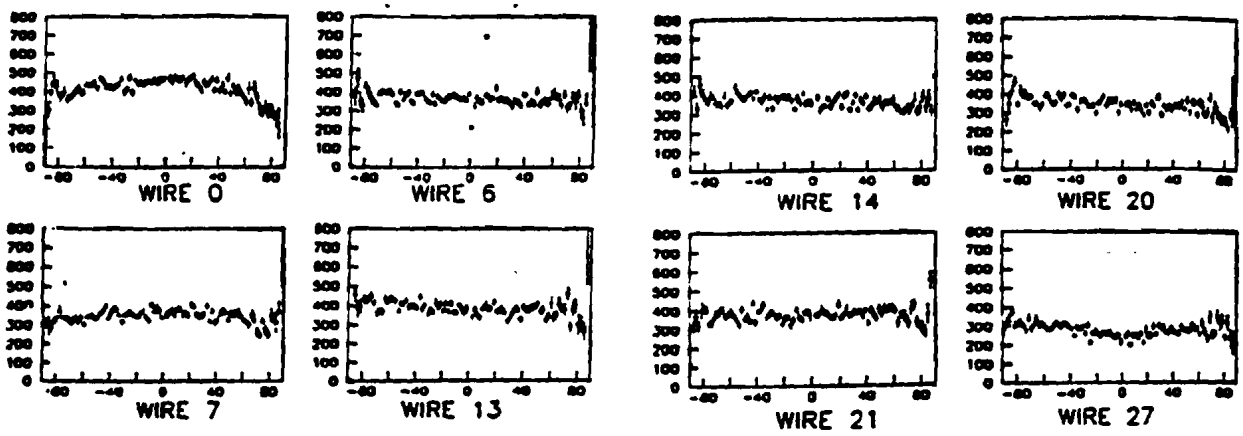

Figure 71 . Charge on the outer wires vs. z

Fig. [74] shows sense wire efficiencies if one uses the optimum settings obtained above. It was required that 4 segment tracks are present for a full track to be formed.

The efficiency is basically flat within the four layers of the chamber. No wire is particularly bad or good. Some variations from wire to wire might be due to a not ideal alignment file. The average efficiency for the 4-segment track is $94 \pm 2\%$.

Conclusions

After optimizing the High Voltage of the chamber and the threshold parameters in the hit finding routine and after setting up the drift field in a way to minimize the loss of charge with drift distance a single wire efficiency of 94% is obtained. There a a number of reasons which might contribute to an efficiency lower than 100%: A finite noise level will make the hit finder miss some small pulses even in the optimized settings. In events with more than one track, e.g. due to conversions, the pulse finder might not correctly separate the two hits and might miss or mismeasure a hit which otherwise would participate in a track.

11.3.2. Resolution and residuals for sense wires

The single wire resolution is defined here as the width of the distribution of the

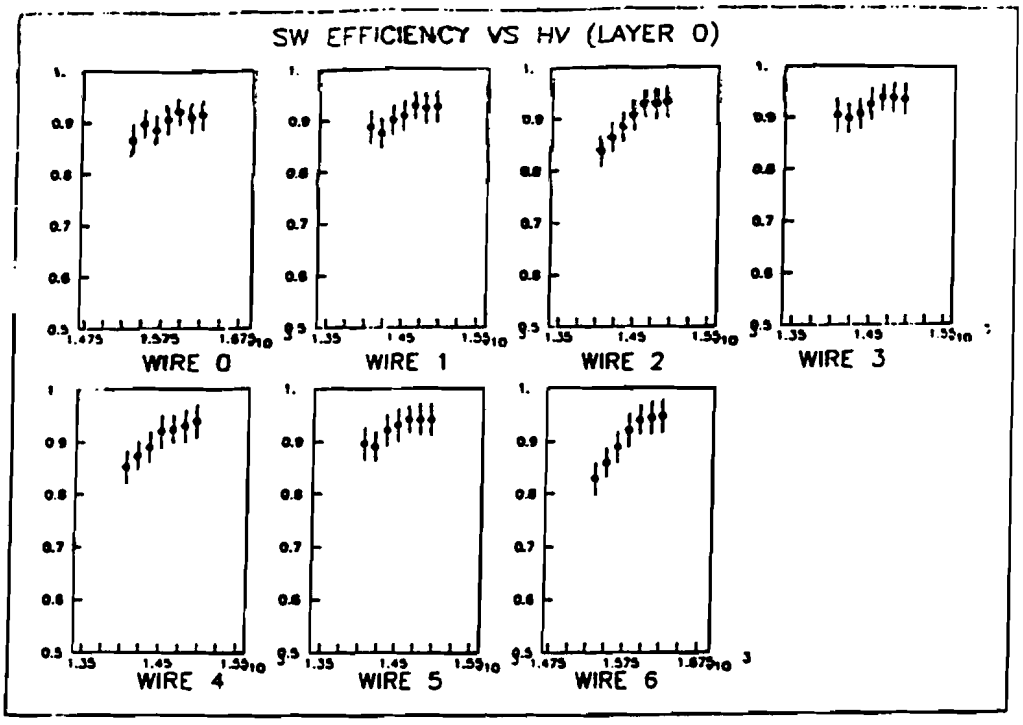

Figure 72 . Sense wire efficiency as a function of the high voltage on the wire. The voltage has been varied around the standard setting by -3%,-2%,-1%,0%,+1%,+2%,+3%. Threshold settings are Thres1=5, Thres2=10 and Thres3= 10

deviations of the measurements of the drift coordinate from the "nominal" coordinate obtained from a line fit to the points within one layer. The residuals are defined as the average of this distribution. For all these measurements the wire measured was included in the fit. This was done to save computer time, because if the wire would not be included in the fit, the fitting would have to be repeated for every wire measured.

The residual of this same wire is the mean value of this distribution. While the width is a quantity that is mostly inherent to the chamber- a measure of diffusion, ion statistics and uniformity of the drift field, to just mention the most important contributions–, the residuals are a mixture of external and internal influences. A bad drift field, besides increasing the resolution, might also introduce a non zero residual. More probable though a wrong t_0 or a wrong drift velocity will shift the points systematically and produce non vanishing residuals. Two effects on the residuals can be distinguished: An overall wrong t_0 will move the residual up or down independent of the drift distance. A wrong drift velocity will introduce a slope on the residuals. Problems with the drift field however will put some structure on the residuals as will a nonuniform drift velocity.

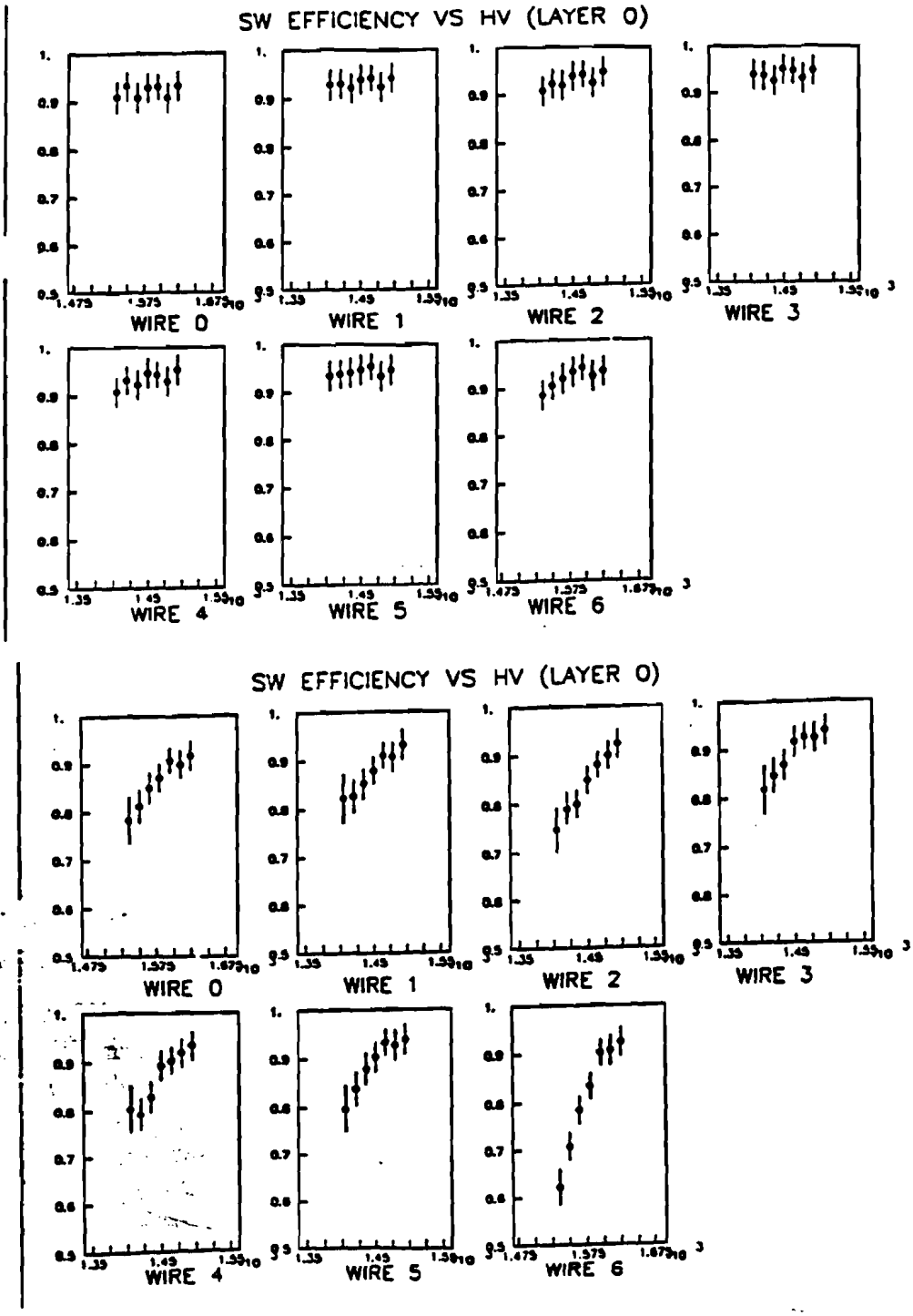

Figure 73 . Sense wire efficiency under the same conditions as in the previous figure, but with different threshold settings in the pulse finder algorithm. For the top plot Thres1=3, Thres2=9 and Thres3=9 FADC counts, for the bottom one Thres1=7, Thres2=20 and Thres3=20 FADC counts

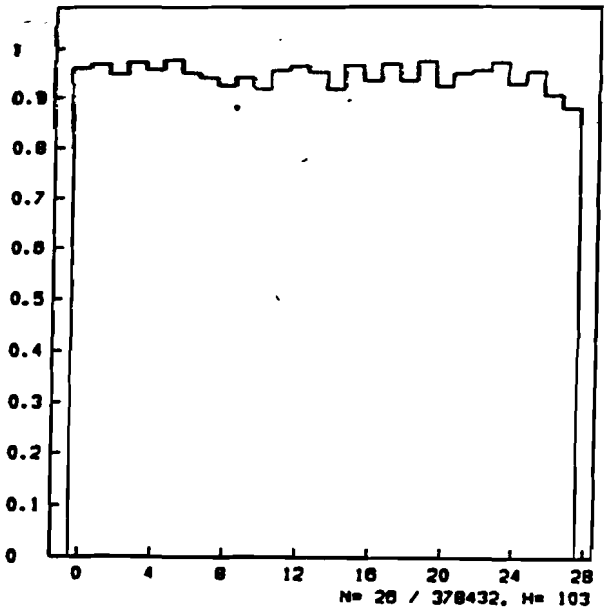

Figure 74 . sense wire efficiencies for all 4 layers in the chamber. 4 segment tracks are required to form a full track

Obviously the measured resolution depends on the hit finding algorithm used. In determining the time each difference between adjacent bins of a cluster which has been recognized as belonging to a pulse is weighted with a fixed factor times the bin number, and the time is computed as the center of gravity of the positive part of the difference pulse:

$$T = \frac{\sum_{i=1}^{N} w^{i-1} D(i) * i}{\sum^{N} w^{i-1} D(i)} \qquad (11-1)$$

where $D(i) = D(i+1) - D(i)$ is the difference between adjacent FADC bins, and N is the number of positive differences in the pulse. Fig. [75] and Fig. [76] show how the residuals and the sigma of the residuals depend on this weight. Both show clear flattening out for a weight larger than about 1.1. The sigma of the residuals actually display a minimum. Averaging the minimum positions one finds a weight of 1.2 to be optimal. In the following all times have been measured with a pulse weight of 1.2.

Fig. [77] shows the resolution as a function of the drift distance for the wires in layer 0. As expected the resolution rises with increasing drift distance. A fit of the function

$$\sigma = (a^2 x + b^2)^{1/2} \qquad (11-2)$$

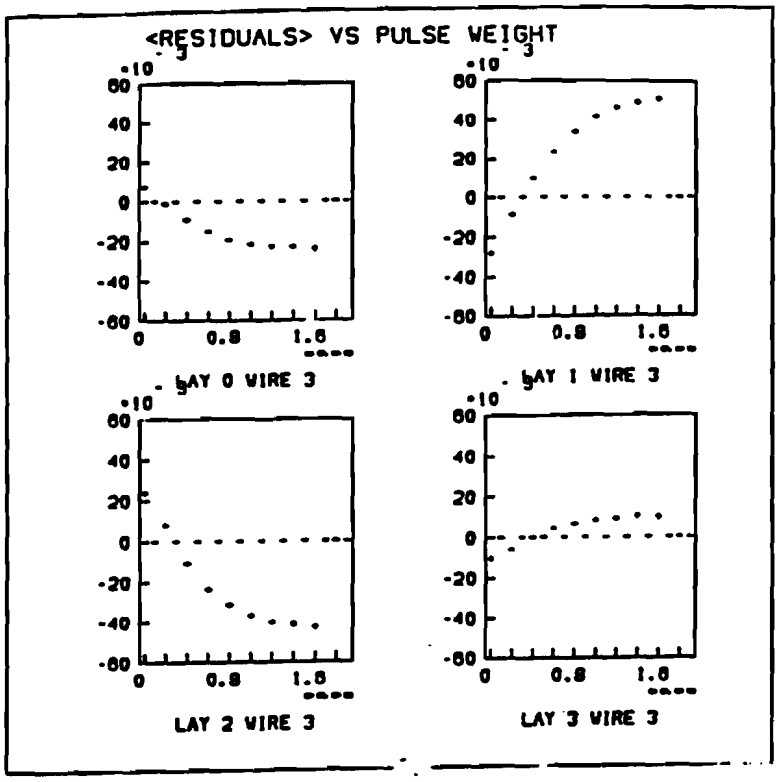

Figure 75 . Average residuals for the innermost wire in each layer as a function of the pulse weight applied in the hit finding

gives

$$a = 68\mu m/\sqrt{cm}$$
$$b = 108\mu m \qquad (11-3)$$

A is a measure of the diffusion, b of the intrinsic resolution of the chamber. Close to the sense wires the resolution worsens because of field inhomogeneities. At a drift distance of 3 cm the average resolution of a single wire within a segment track is about $170\mu m$.

Fig. [78] shows, for the same data as the previous plot, the resolution as a function of the drift distance, but this time derived from full tracks. The resolution on the inner wires became flatter with drift distance, but increased slightly. The average resolution at 3 cm is now about $200\mu m$. The flattening out of the resolution curve is an indication that other effects external to the chamber start to dominate the accuracy with which a track can be fitted. In particular critical is the alignment from layer to layer. Bad alignment here refers to a not ideal set of t_0's or a wrong velocity. In particular a wrong velocity will make a good track fit for all drift distances impossible.

Looking at the residuals one sees the same effect there. In Fig. [79] the residuals

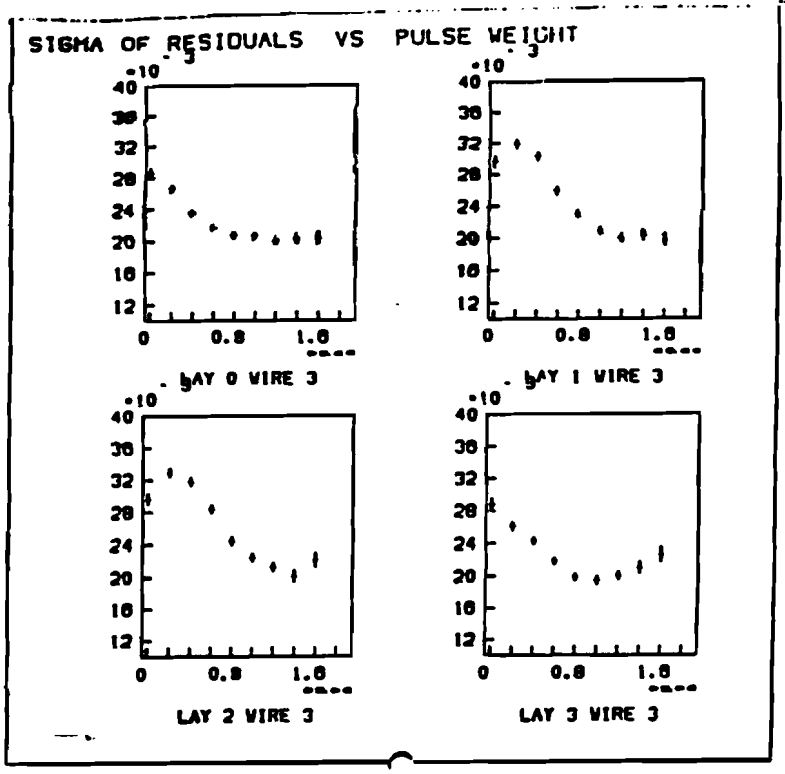

Figure 76 . Sigma of the residuals for the innermost sense wire in each layer as a function of the pulse weight applied in the hit finding

for a segment fit to the wires in layer 0 are shown. They are centered around zero, but show some definite structure. The peak to peak variations are below $\pm 1\sigma$. It is interesting to note that the outer and the inner wires show the opposite behaviour, with the second and second to the last wire exhibiting transitional behaviour. While the residuals of the inner wires have a negative slope for most of the drift distance, the outer wire residuals slope positive in the same region. This is an indication that the field for the outer wires is not the same as for the inner ones.

Fig. [80] shows the same wires, but this time for the case that a full track has been fitted. The maximum deviation from zero is larger by 50% compared to the segment track fit supporting the observation from the resolution measurement that the alignment for full tracks is not perfect.

Other layers and other modules exhibit similar behaviour with resolution and residuals of the same magnitude.

Another interesting question is how the chamber behaves under large currents. In order to study this runs were taken under normal cosmic ray fluxes and with the chamber illuminated by a strong source. The resolution of the sense wire was measured in both cases. Fig. [81] shows the results. The resolution remains

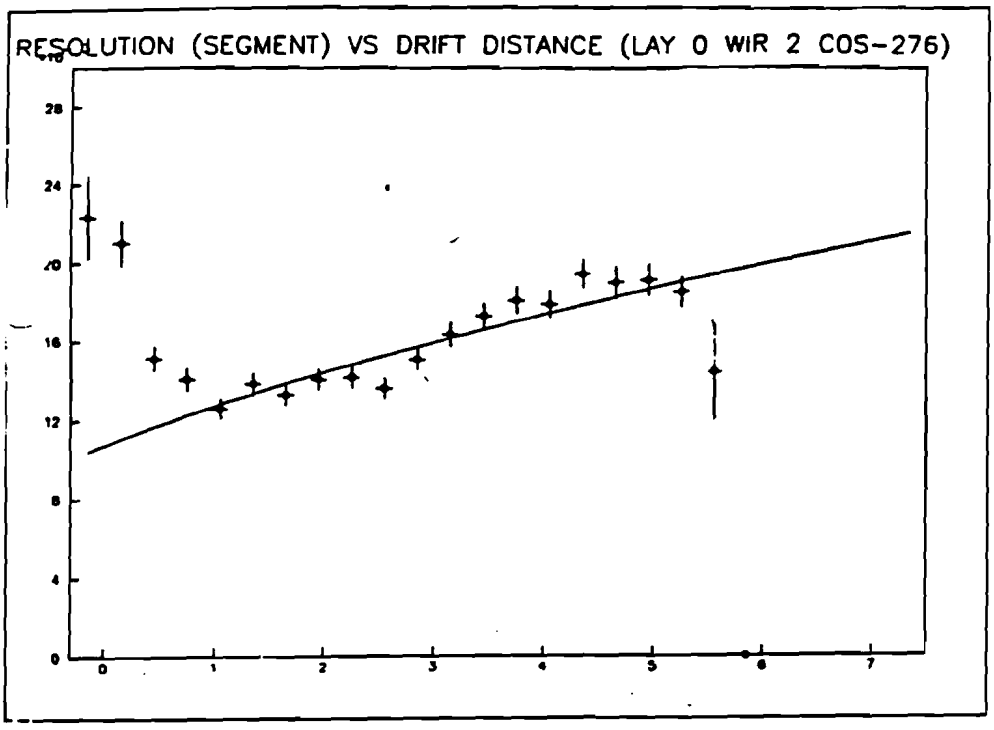

Figure 77 . Resolution of the individual sense wire within one cell (from segment tracks) vs d· distance for layer 0 in module 7

unchanged.

To summarize it has been shown that the chamber is capable of intrinsic resolutions $170\mu m$ for 3 cm drift. If a full track fit is done this deteriorates to about $200\mu m$. This is due to uncertainties in the absolute value of the drift velocity, to mechanical misalignments, to nonlinearities in the field and to a drift velocity which is not constant with drift distance. All these effects make the connection of segment track to full tracks less precise. With a better alignment and a more complete understanding of the inaccuracies in the chamber it is hoped that this number can be improved to narrow the gap or even make it totally disappear.

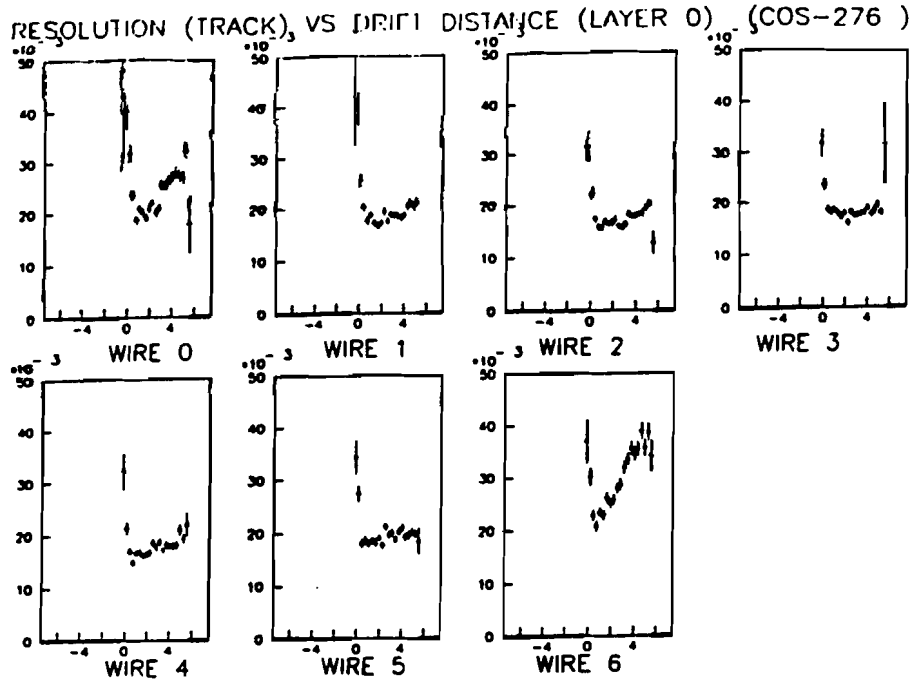

Figure 78 . Resolution of the individual sense wire derived from full tracks, vs drift distance, for layer 0 of module 7

11.3.3. Delay line resolution and residuals

A careful study was done of the residuals and the resolution of the delay lines as a function of z. The resolution is of course of interest because this indicates the intrinsic accuracy with which the z coordinate can be measured. It is also a good indicator whether the newly adopted resistances of the field shaping lines as described in the section on the construction of the chamber are in the right range and do not interfere with the signals. Fig. [82] shows the resolution of the delay lines in module 5. They are basically flat in z with an average value of $(2.0 \pm 0.2)mm$.

The residuals for the same module are shown in Fig. [83] . Here a clear structure in z is visible. The changes in residuals along z are mostly due to inhomogeneities of the delay lines along z. These have been measured before the modules are inserted into the chamber. Fig. [84] shows the results of these calibration measurements for module 5 after they have been processed with a monte carlo to smear them out due to the different angles of tracks passing through the real chamber. Both curves show a very similar structure indicating that a correction of the measurements along z according to the calibration measurements will improve the residuals and possibly

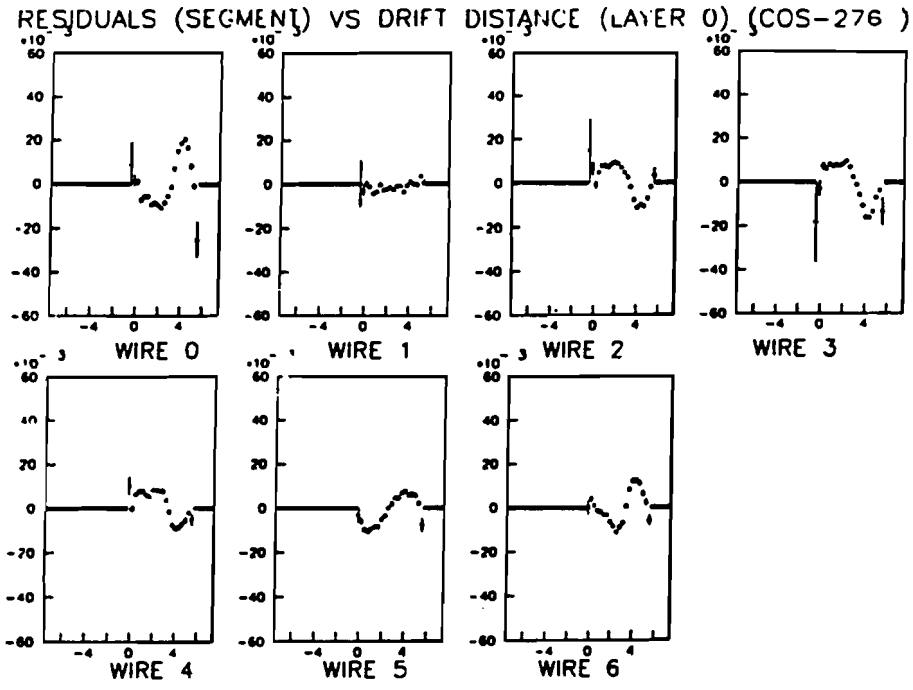

Figure 79 . Residuals for the sense wires in layer 0 for a segment track, vs drift distance

the resolution.

11.3.4. Stability of the operation of the chamber

A number of effects influence the stability of the chamber with time. Since the pressure and to some extent the temperature of the chamber gas are not independent of the environment changes of these quantities will change the behaviour of the chamber. Another source of uncertainty is the mixture of the gas used. Small impurities or changes in the composition might change the drift velocity drastically. In the following consequences of the later problem will be discussed.

To measure the influence of the changing gas mixture on the chamber a long run was taken. After some initial data taking to establish a stable starting platform the mixture of the gas was changed. The percentage of CO_2 was reduced from 3% to 2%, with the balance taken by Argon. The whole run was taken over 22 hours, with the gas flowing at a rate of $1/2l/min$. With the volume of the premod being $330\,l$ this flow rate is equivalent to one volume exchange in $10h$. Over the time of the run the whole chamber volume will have been exchanged about 2 times, with the gas inside the actual drift cells changed at a possibly somewhat slower rate due to the fact that

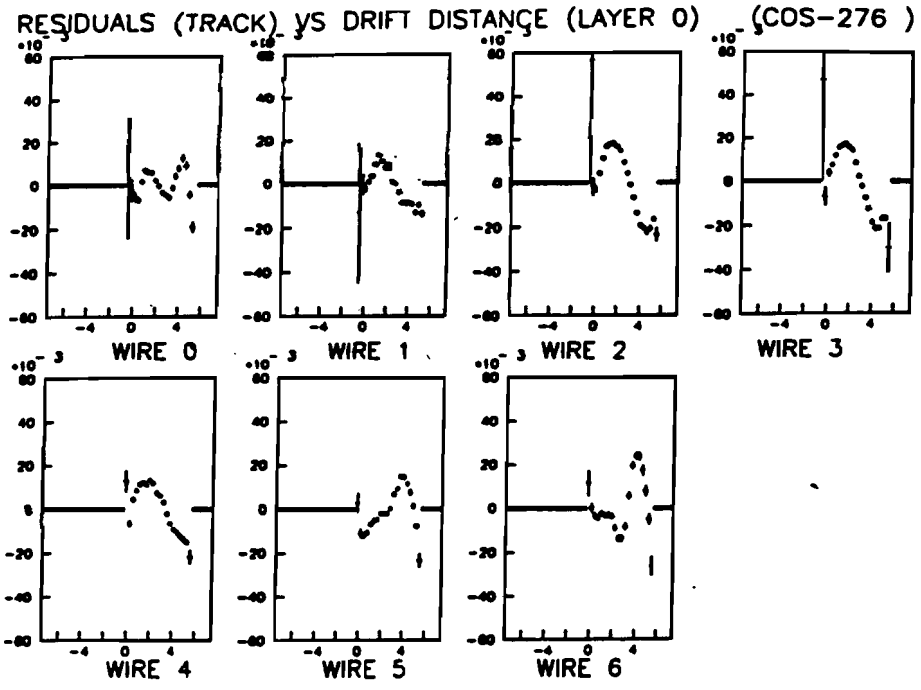

Figure 80 . Residuals for the sense wires in layer 0 of module 7 for a full track fit

they are communicating with the main gas volume only through narrow slots. The run was subdivided into sub runs with 500 events each. For each part the chamber was realigned- that is a new set of $t_0's$ was computed. t_0 here is not the normal t_0, but includes the change of drift velocity:

$$\Delta t_0 = \frac{< \text{residuals} >}{v_{drift}(nominal)} \qquad (11-4)$$

Fig. 85 shows the resulting t_0 distribution. Plotted is the accumulated change in t_0 as a function of the event number. The event number is essentially a measure of time, except for one lap in time around event number 10000, where the data taking was interrupted briefly. The first 5 runs are very stable. After the introduction of the new gas mixture the t_0 starts to change. Since the velocity is absorbed into a time measurement, a raising t_0 means a decreasing velocity. After event number 15000 the Δt_0 curve flattens out indicating that the gas has changed completely and that the chamber is stable again.

In order to translate the change in t_0 into a change of velocity the t_0 from the beginning of the run were used and the velocity varied, until the apparent offset in t_0

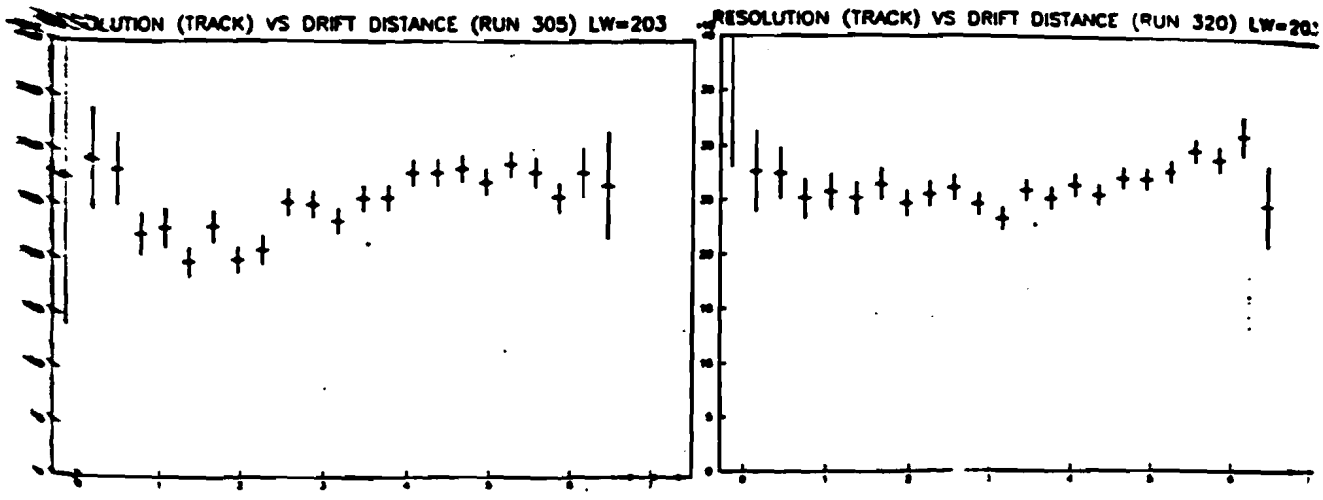

Figure 81 . Resolution of sense wire 3 in layer 2 of module 7 with and without illumination by a strong source

between the original t_0 and the ones needed to align the chamber with the changed velocity were zero. Starting from a velocity of $40\mu m/ns$ it was found that a velocity

$$v = v_{old} * F$$

with

$$F = 0.865 \pm 0.005$$

gave the best agreement with the starting t_0's. Converting this into a relative change of the velocity due to a 1% decrease in the CO_2 concentration one finds:

$$\frac{\Delta v}{v} = -(13.5 \pm 0.5 + 6.5 - 3)\%$$

where the first error is the statistical error in calculating F, the second one an estimate of the error due to the change in HV around event number 13500 and due to the end of the run before the flattop was reached completely. This result is compatible with the measurement of [49], where $\Delta v/v = -(17 \pm 4)\%$ for a -1% change in CO_2 was predicted. To retain an accuracy of $200\mu m$ in the chamber the drift time should be

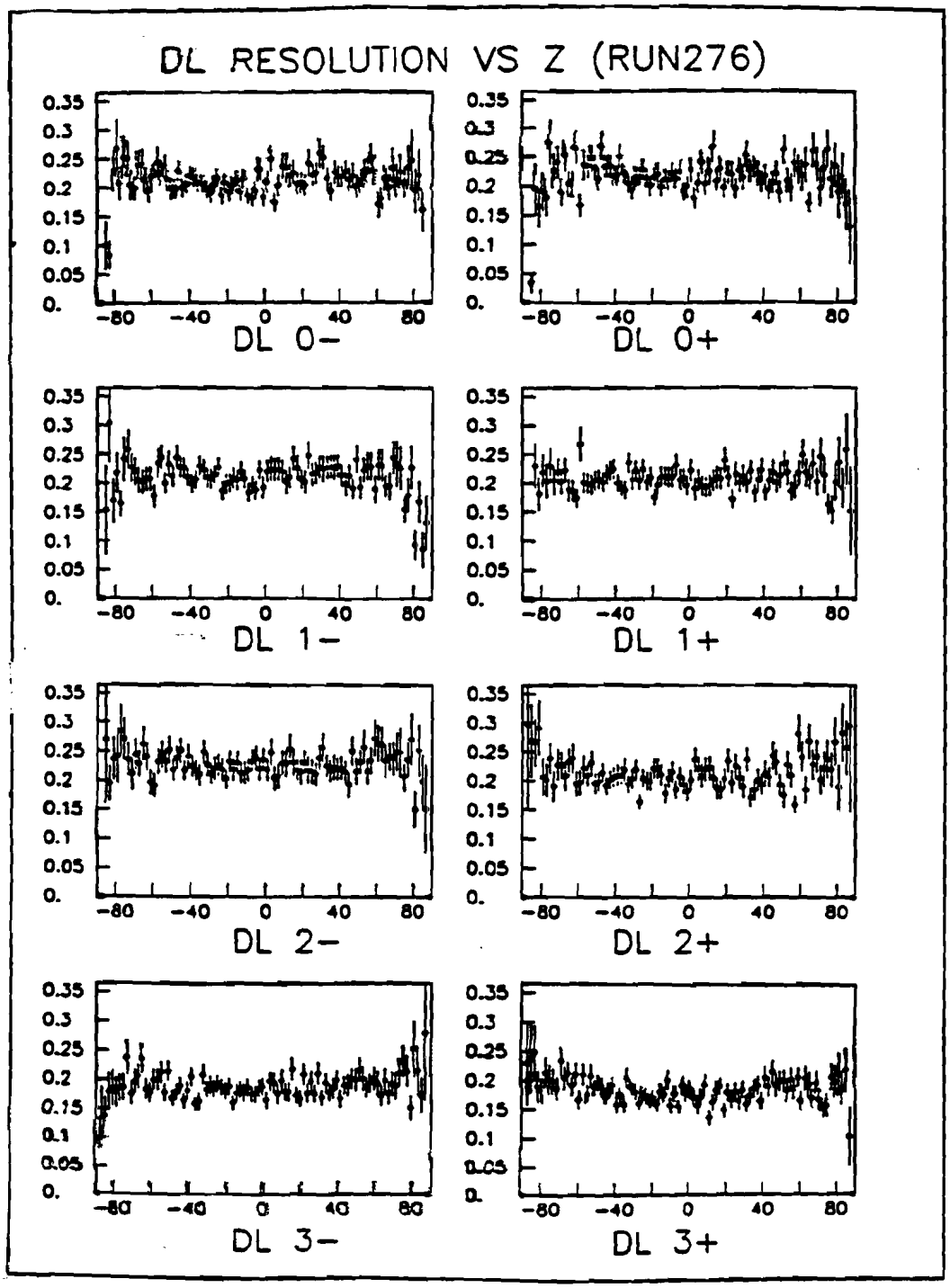

Figure 82 . Resolution of the eight delay lines in one module as a function of z, for module # 5

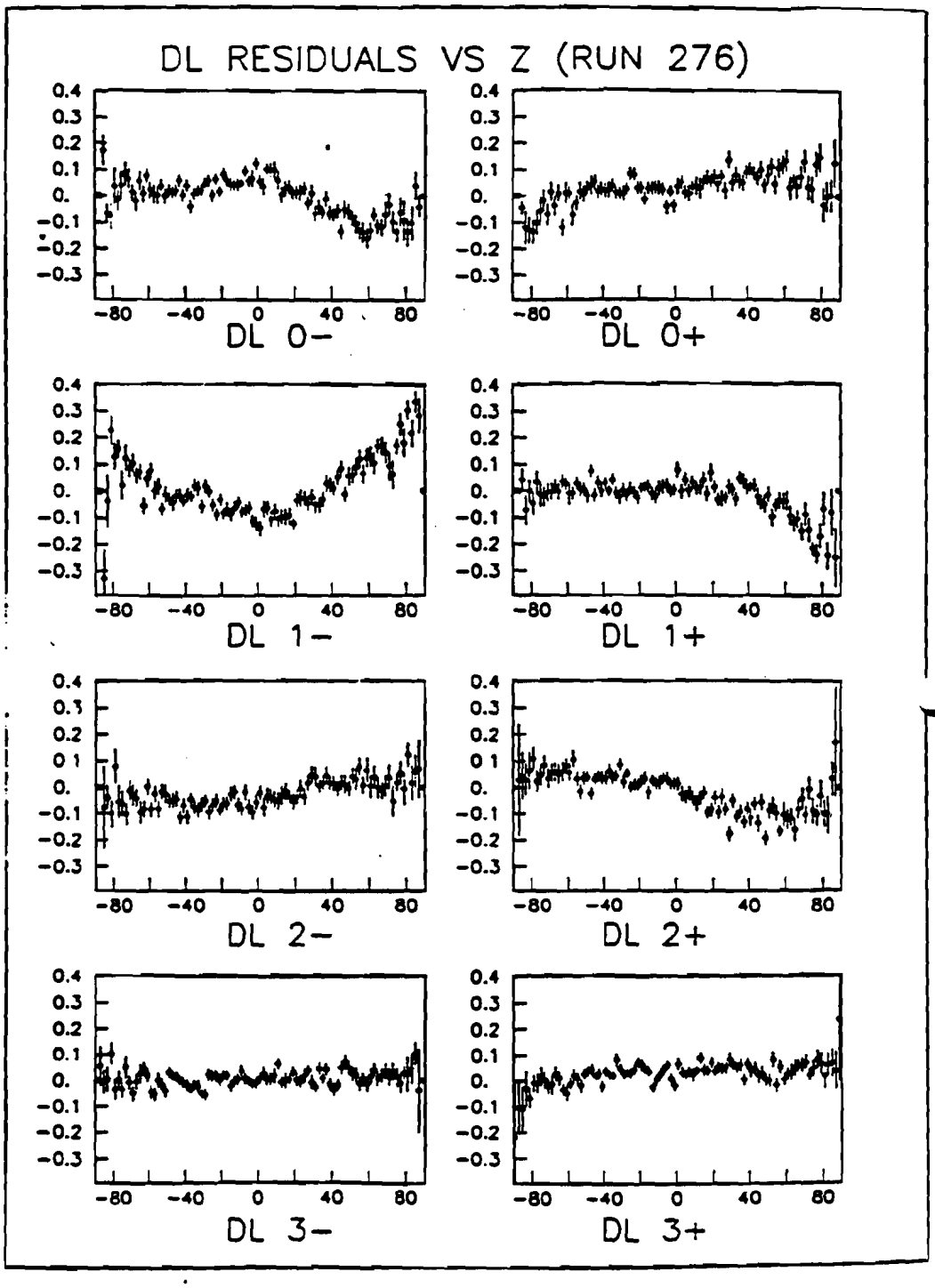

Figure 83 . Residuals of the delay lines in the same module as the previous plot (module 5), vs z

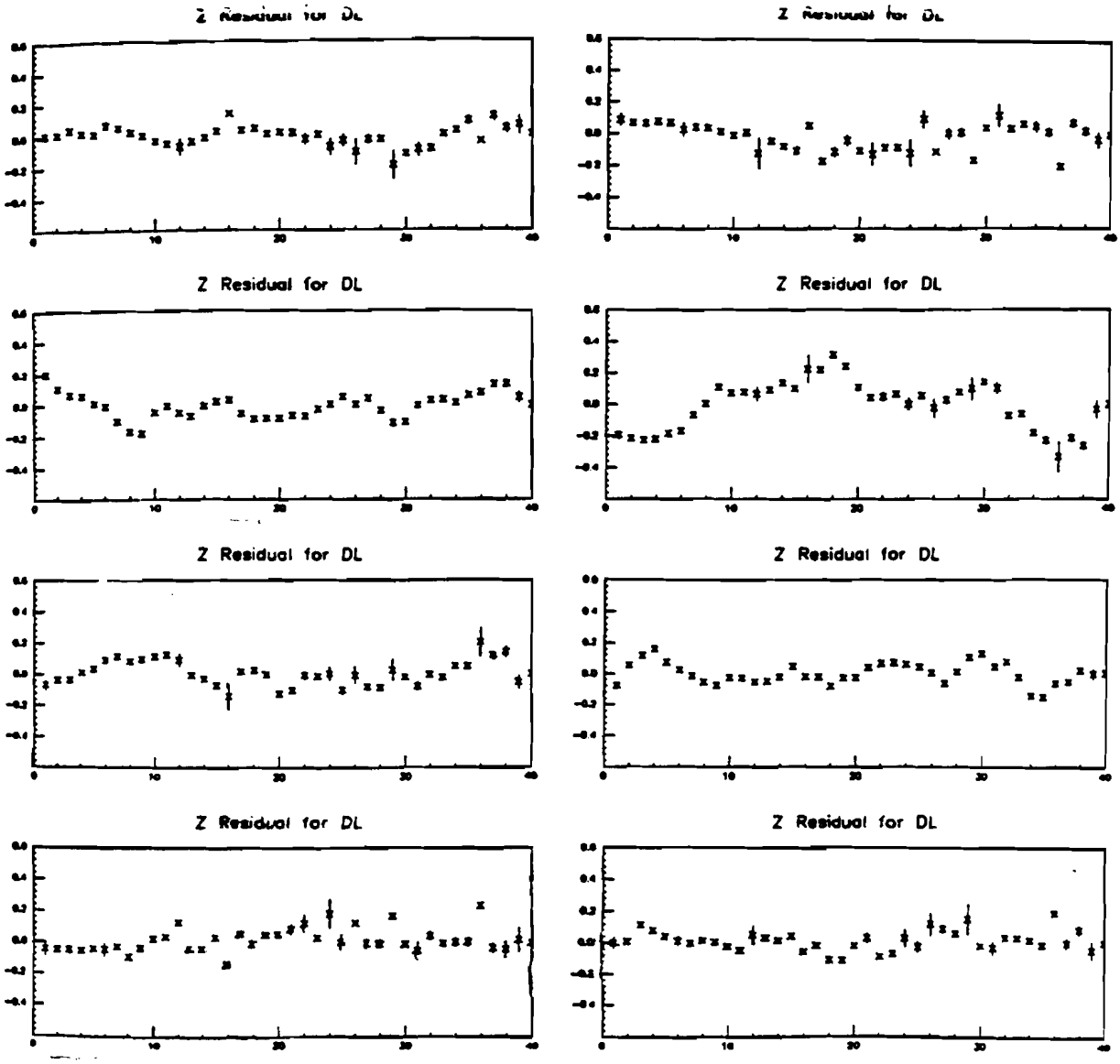

Figure 84 . Residuals for the lines in module 5 as measured during the calibration

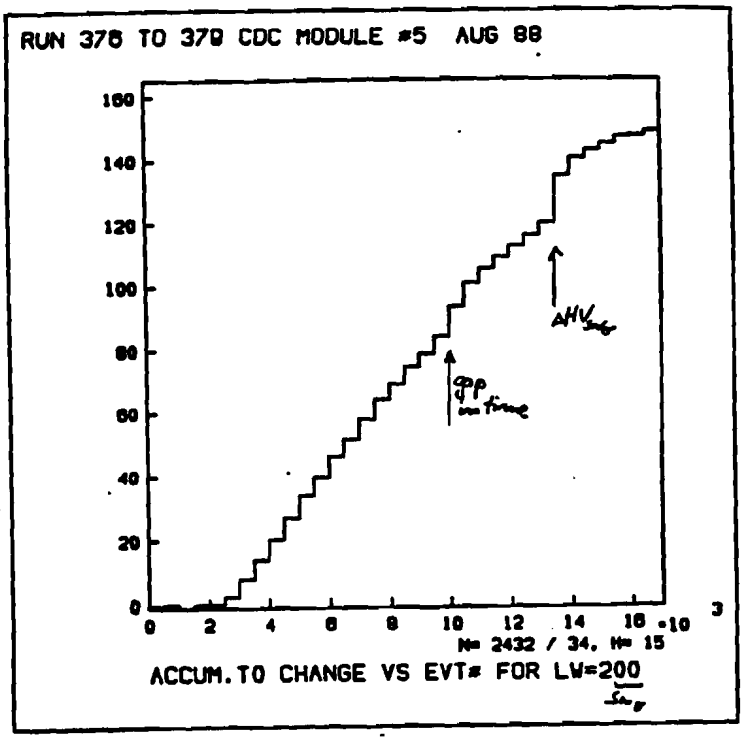

Figure 85 . Change in Δt_0 vs event number. The event number is a measure of the time since the beginning of the run. The first step in the curve is due to a gap in time, the second one due to a slight change in HV on the outer wires and the strip.

stable to better than 5 ns for an average drift distance of 3 cm. This translates into a necessary stability of the velocity of $\Delta v/v < 0.67\%$. The concentration of the CO_2 gas has to be kept constant at better than 0.05% of the total gas flow.

In [49] the change in velocity due to a decrease in the CH_4 concentration from 4 to 3 % was measured to be $-(8 \pm 3)\%$. This would translate for the same stability requirement of t_0 of $5ns$ as in the CO_2 case into a requirement on the stability of the concentration of the CH_4 of better than 0.08% of the total gas flow.

The influence of the environmental factors like pressure, temperature etc. will show up in the t_0's as well. A rough study was done to estimate the size of the effect over a long time. Fig. [86] shows a plot of t_0 of one sense wire (wire 2 in layer 2) measured repeatedly over a period of one month. During this period the module read out was changed twice- the first 6 points were taken with module 5, the next two ones with module 6 and the remaining ones with module #7. The point to point variations are between 5 and 10 ns. It is hoped that a very careful calibration of the chamber and a stable gas system will make a stable operation of the chamber over longer periods of time possible. It might be necessary to change the overall velocity,

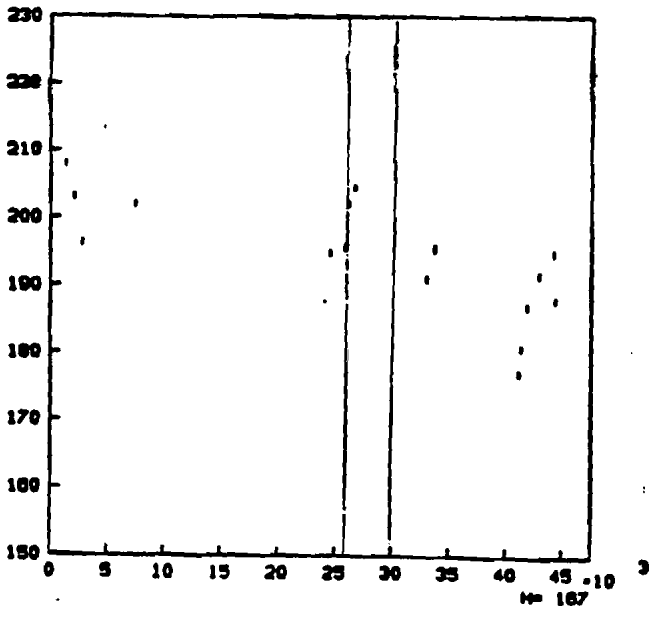

Figure 86 . Average t_0 for wire 2 in layer 2 as a function of time. The first 6 points were taken with module # 5. the next 2 with #6 and the remaining ones with module 7

but the hope is that no adjustments of $t_0's$ are needed.

11.3.5. dE/dx measurements

Similarly as described for the 1985 BNL test the dE/dx resolution of the chamber was measured. Again because no real double track events are available this was done by superimposing two consecutive events in software. The ionization of the events was measured as the 66% truncated mean of the charge of the hit, averaged over all hits participating in a track. The pulse area was corrected for the angle Θ in the rz-plane. Fig. [87] shows the resulting distributions. With 28 sense wires single and double ionizing particles can be clearly distinguished. For a cut at 1.3*minimum ionizing particle charge, the 1 MIP efficiency is 96%. The rejection factor for a 2 MIP event over a single ionizing particle is found to be 55 ± 12

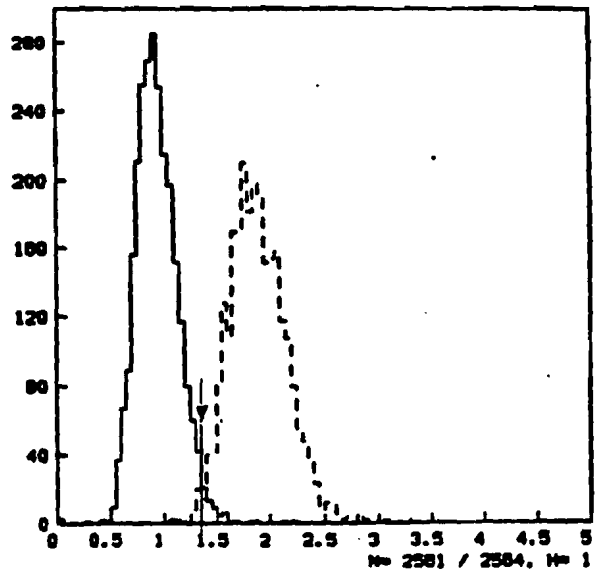

Figure 87 . Plot of the charge of a track normalized to a minimum ionizing particle, for single MIP particles and for simulated double MIP particles

12. The Offline analysis program

12.1. Introduction

The offline analysis of the data from the test chamber was done with a general purpose analysis program called DØuser developed for the DØ experiment [50] The DØUSER program provides a framework from which data taken previously and stored in a disk file may be read, processed and summary information be obtained. The program, written in Fortran 77, interacts with the user via a menu driven interface [51] Three principal stages are to be distinguished during the execution of the program. During the setup stage parameters for the upcoming analysis run are collected. The input file is set and possible output streams are opened, if selected files are to be saved. After the setup the event processing task starts. If the program is run interactively another menu provides access to a number of features like event display, histogram display, event dump etc. The event display in itself is a menu driven program which allows the user to interactively access different views of the detector, redefine them, split the screen into different windows etc.

The last stage of the program is reached once all events in the input file or a preset number of events have been processed. The user can either reinitialize the program with a new input file, exit directly or produce the desired output of histograms etc. with the help of a dialog.

Each of the above mentioned tasks is accessed via a so called user hook. A user hook is a logical function which is called at the appropriate place in the program, and which is used by the user to hang his/her specific applications from. For example during the event processing a routine USREVT is called for each event, from which, in the case of the central detector, the complete hit finding and tracking package is called in turn. Each user hook exists for every subsystem of the detector. For example the routine USREVT exists for the CDC, the FDC, the TRD, the VTX, the calorimeter and the muon system. With the help of a special tool, the so called program builder, the user sets up a special package for his/her particular needs, in which only the necessary user hooks are actually called. This allows to build a comparatively small executable version of the program by avoiding calling and processing many unneeded routines. At the same time adding other detector parts to an existing package is easy and entails only a session with program builder and a relinking of the program. For example for the analysis of the central chamber test data no other part of the detector was needed (or even present), so that a version of the program was built which only

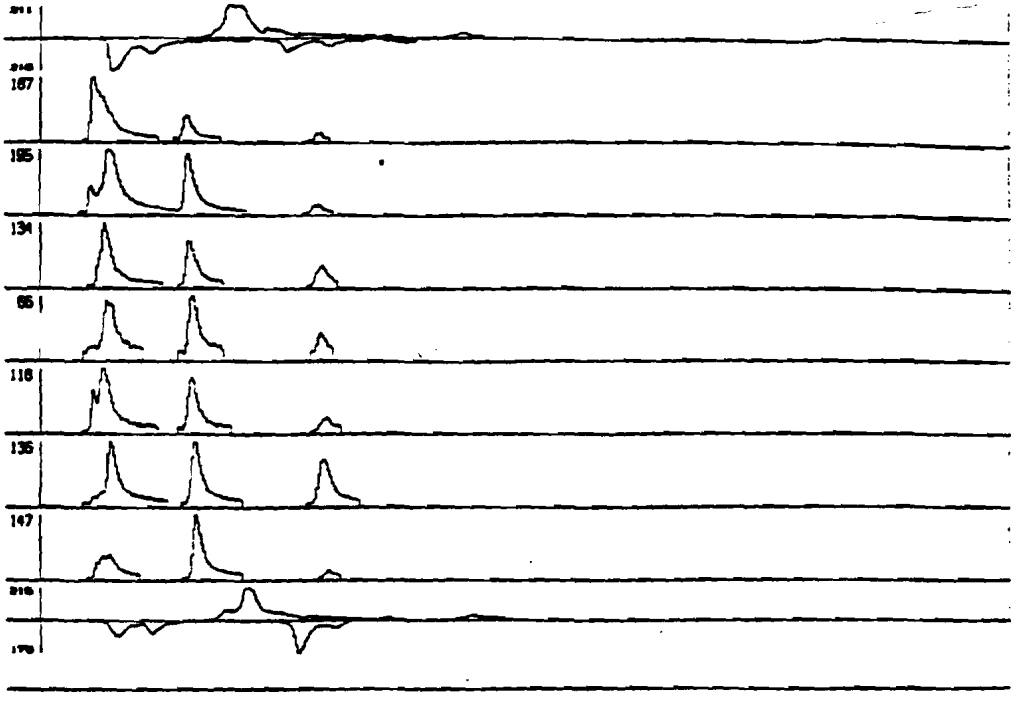

Figure 88 . Raw data for a set of seven sense wires and two delay lines. The top two and the bottom two traces are the delay lines, the other ones sense wires.

called the routines relevant for the central detector.

Data in DØ are stored using the ZEBRA utility package from CERN. Zebra allows dynamic data storage and management in a Fortran based program. The data coming from the level 2 nodes are written onto file in a binary format preserving the Zebra structure. The DØ user program reads this file, decodes the informations and makes it accessible for the user subroutines. For each event additional zebra banks are filled containing for example the hit and track information.

12.2. The reconstruction program for the CDC

Reconstructing an event in the CDC is done in three steps. First the raw FADC data are scanned for hits. Fig. [88] shows a typical example of a set of raw hits as digitized by the FADC's. Once the hits are found and the basic parameters like time, area and width are determined, so called segment tracks are found. A segment track is a track within one layer formed by at most seven sense wire hits. Fitting of these tracks is done on the r-Φ projection of the chamber. Once all segment tracks are found, the program tries to connect as many as possible to form complete tracks

over four layers and tries to fit the accompanying z-information.

In the following the procedures used for these three tasks are described in some detail. Most of the routines were written by Olivier Callot, Stony Brook and Orsay, France.

12.2.1. Hit Finding

Data for the CDC are digitized signals from the sense wires and delay lines. In each channel the raw data are zero suppressed by a hardware circuit. DØuser reads the suppressed data from the file. The first task to be done in order to be able to reconstruct the event is to find the hits in the traces. The algorithms used follows closely one developed for the OPAL experiment at CERN [52].

Pulse finding and definition of the pulse time is done using the first difference of the data rather than the actual FADC data. Two different conditions exist for the hit finder to recognize a pulse. Three consecutive differences are scanned and have to be larger than a threshold or two consecutive differences have to be larger than a threshold and the sum of both has to be larger than some other threshold. For any data to be used in this selection process it has to be above the previously defined pedestal of this particular wire.

The trailing edge of the pulse is found by requiring three consecutive differences to fall below the leading edge threshold. If this condition is not met within a fixed number of bins after the leading edge the pulse is truncated at a fixed length. If a second pulse arrives before the trailing edge of the first pulse was found, an overlap flag is set and the first pulse is ended at the beginning of the second one.

The area of the pulse is calculated by summing the bins between the leading and the trailing edge. If a second pulse arrives before the first ends the area calculation stops at the beginning of the second pulse. The width is defined as the distance in time between the leading edge and the trailing edge bin of the found hit. Again if a second pulse arrives before the first ends the calculation is stopped at the beginning of the second pulse.

The time of the pulse is determined by finding the center of gravity of the positive portion of the difference pulse after the leading edge bin.

$$T = \frac{\sum_{i=1}^{N} w^{i-1} D(i) * i}{\sum_{i=1}^{N} w^{i-1} D(i)} \qquad (12-1)$$

where i starts at the beginning of the cluster and runs over all positive differences D(i). w_i is a weight applied to each bin. It is currently a constant number independent

of i. This shifts the time towards the larger bins and reduces the time jitter due to noise fluctuations. Once the appropriate bin is found it is converted into a time by multiplying it with the time for one bin in the FADC. In DØ, since the clock is synchronized with the accelerator clock, this time is 9.43ns (the clock is running at 106MHz).

Using the difference rather than absolute thresholds makes the hit finder more independent of pedestal fluctuations. This is important because although care was taken to make the electronics as stable as possible with respect to the baseline in order to avoid an unstable pedestal, fluctuations in the chamber current due to fluctuations in the density of particles traversing the chamber will move the baseline around somewhat.

More important though this algorithm does recognize a pulse by its rise time and will reject pulses which are vastly too slow or too fast. Spikes due to faulty bits in the FADC will not be recognized as pulses, nor will some slowly rising pulses due to discharges pass the selection. This powerful feature makes the hit finder very useful in not filling up the hit banks with spurious hits.

This hit finder was first programmed for the early cosmic ray test, which were done without a sophisticated zero suppression circuit. Test will be made to determine to what extent this complicated algorithm is necessary if the full zero suppression is implemented.

At the moment the same hit finder is applied to the sense wires and to the delay lines. Because the delay line pulse is somewhat slower than the sens wire pulse a different hit finding routine might give a larger efficiency. For reasons of simplicity however no distinctions is made at the moment between hit finding on sense wires or delay lines.

For delay lines however one additional constraint has to be fullfilled, before a hit can be called a good delay line hit. For every hit there are two delay line measurements, one on either side of the line. The sum of the times corrected for the drift time on the sense wire which drives the line has to be equal to the total delay of the delay line. The program first finds all hits on the delay lines for both sides. It then compares both sides and finds the best match for a given hit. The condition for a hit to pass is that

$$t_{left} + t_{right} - 2 * t_{sense} = T_{sum} \qquad (12-2)$$

within a given tolerance ΔT.

12.2.2. Fitting Segment Tracks

In order to find the tracks within one layer all hits found in that layer are sorted in Φ. A list is built up which contains the hits for each wire (0:6) arranged in Φ from 0 to 2π. Each hit enters twice into the list as the "real" point and its mirror image on the other side of the sense wire. This has to be done because no information exists at this stage which would distinguish one side from the other. The discontinuity at $\Phi = 2\pi$ is being taken care of by copying the last hits over to the beginning of the list. Starting from a hit on the lowest plane (first wire in the cell) a hit in one of the higher planes, e.g. plane 6, is chosen. This second hit has to lie within an angular range $\pm\Delta\Phi$ from the first point. This is done in the $r - \Phi$ projection. A road of certain width is opened connecting both points, and a line is fitted to the points lying within this road. The fitting is no longer done in the $r - \Phi$ plane, but in the x-y projection, since this is the coordinate system in which the final result is being stored. The points which result in the best fit are used for the segment track. Since the individual hit has no information from which side of the sense wire it originates each hit will show up twice: once on the left side of the sense wire plane, once on the right side (The "real" hit and the mirror hit). Segment tracks are fitted on both sides, but only the track with the better χ^2 is retained. They are tagged together with their mirror images so that they are not used again for another track. A track is fitted only if a minimum number of wires out of the possible seven have passed the criteria and are being used for the actual fit. Typically two wires out of seven are allowed to be missing.

12.2.3. Connecting segments to full tracks

The last step in the reconstruction is to connect the segment tracks to form a full track. Starting from the outer radius of the chamber a segment track is used as a "seed" similar as it is done in the segment track finding itself. Tracks in the next lower layer which are within a maximum distance in $r - \Phi$ and whose angle Φ does not vary more than a preset angle are selected. The one which is closest to the original one is added to the list of segments on a track. Usually one layer is allowed to be missing from the list. Once the list is complete a line is fitted to all hits participating in the segment tracks selected. The track is stored in the form

$$\begin{aligned} x &= x_0 + s * \cos\Phi \sin\Theta \\ y &= y_0 + s * \sin\Phi \sin\Theta \\ z &= z_0 + s * \cos\Theta \end{aligned} \qquad (12-3)$$

The track is first fitted in $r - \Phi$, then in z. For the fit in z each point has to have a xy-component, for the fit in xy the z-points may be missing. All errors in xy- and in z

are assumed to be perpendicular to the projection of the track into the xy plane and the rz plane respectively. The points participating in the fit are entering weighted with the inverse of the square of the error of this point. The final track is stored by its center of gravity point of all used hits, the angle Φ in the $x-y$ plane and the angle Θ between the z-axis and the track.

12.3. Constants

In order to be able to convert the timing information obtained from the hit finder routine to a space information needed in the reconstruction of the event a number of additional informations are needed. In the case of the sense wires these informations are the drift velocity, an offset time called t_0 and a more detailed space to time relation for fine corrections to the time. The drift distance x is determined from the drift time t by the relation:

$$x = v_{dr} * (t - t_0) \qquad (12-4)$$

t_0 is a time offset between the time measured with the FADC and the actual time at which this particular event happened. In particular due to slightly different delays in the cables and in the electronics this time may vary somewhat from channel to channel. Using data from test pulse runs these electronic contributions to the differences in t_0 can be corrected. There are however other effects which might change t_0. The field for the outer wires might be slightly different from the one for the inner wires. This might result in a shift in t_0 for the inner wires relative to the outer ones. These changes are very hard to predict, but they have to be taken into account if a good resolution of the chamber should be achieved. An iterative process is employed to minimize the differences in t_0. This is described in more detail in the section on alignment.

In the case of the delay lines a t_0 exists in the same way as it does for the sense wires. However additional information is needed to be able to pinpoint the time to space relation ship more precisely. First the active part of the delay lines might not start always at exactly the same position within the chamber. Measurements taken on the finished lines showed this to vary by about $\pm 0.125''$. This will shift the apparent center of the delay line and cause misalignment in the track fitting. The lines do show some changes in propagation speed along z. This was measured prior to the wiring of the individual modules for sixteen points along the line. From this an average speed and a correction table were derived. For the data discussed here the velocities as measured in the calibration were used, but no attempt was made to utilize the point by point calibration.

Using the test pulse data the t_0's for both delay lines and sense wires may be

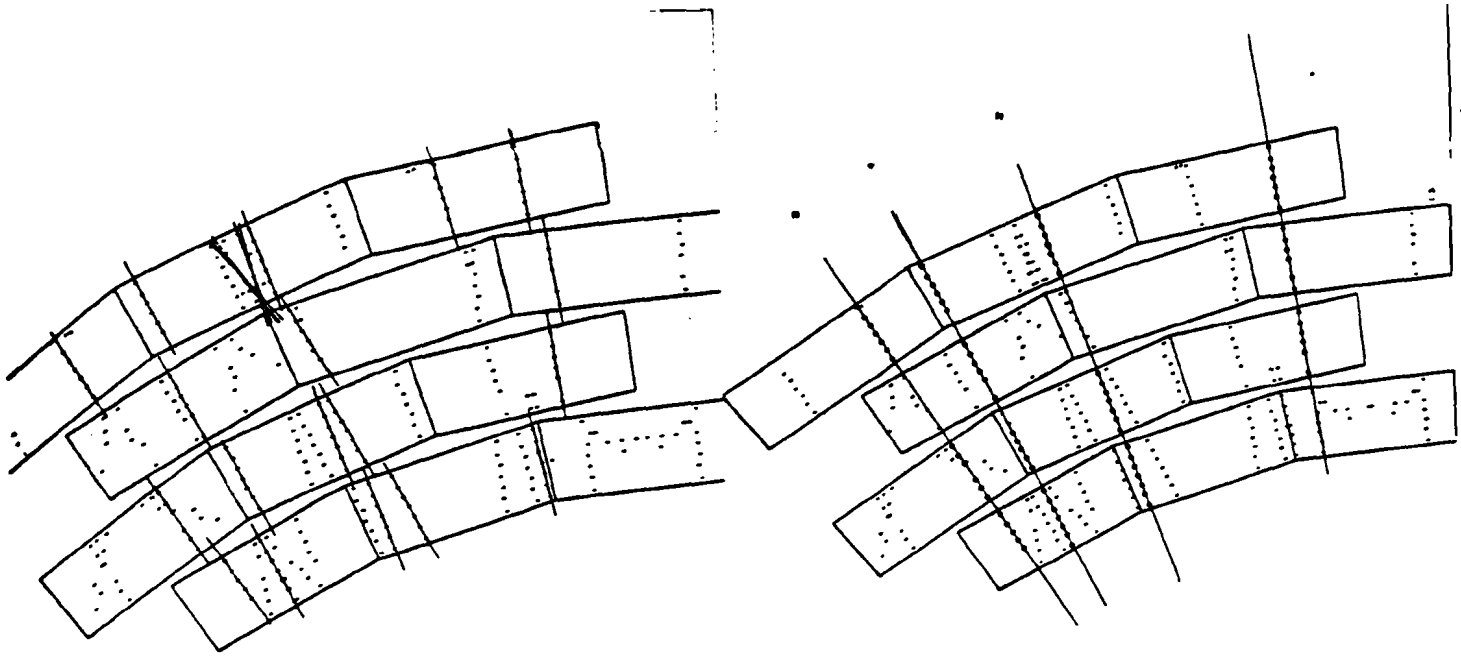

Figure 89 . $r - \Phi$ view of the same event with two different overall t_0. The relative t_0's are identical. In the left picture segment tracks do not line up properly because of a wrong $T0$. In the right picture all t_0 are corrected by a time corresponding to half the mean time separating two neighbour segment tracks. The segment tracks line up properly and full tracks are found.

determined relative to each other, but an overall factor remains unknown. This global shift is fairly easily determined in the case of the sense wires. Due to the staggering of neighbour layers track segments will be pulled apart if an overall time offset is introduced. In such a case the fit within a segment will be good, since the relative t_0 are known, but large distances will separate segments tracks in different layers. The overall shift in t_0 is determined as the time needed to shift the two segments on top of each other. Fig. [89] shows two different views of the same event. In one view the overall t_0 was not adjusted properly. Since the relative channel to channel t_0 are nearly correct many segment tracks are found. However segments between neighbour layers are offset by a large time $T0$ and do not line up to form full tracks. The second view shows the same event after the overall t_0 has been moved by $0.5 * T0$. The segment tracks did shift on top of each other and full tracks are found.

For delay lines the situation is slightly more complicated. Nothing directly comparable to the staggering of cells in the case of sense wires exists. However an overall t_0 will change the sum of left and right times for each hit on the delay line. In order to find the shift tracks were fitted to the left hits and to the right hits separately.

One half of the time difference between the two fits was then used as the additional t_0.

For the final DØ chamber the exact position of each delay line and its active region is known. Here the t_0 can be derived much more precisely from pulser data and the geometrical measurements than it was possible for the Premod used in the DØ hall test.

For each delay line a fairly large number of constants is needed. The velocity as obtained from the calibration and the measurements referencing the line to the chamber have to be known. In addition the sixteen calibration points have to be stored, or a polynomial fit to those , to allow for high precision reconstruction in z.

All the static parameters are kept in a special zebra bank. They are read in at the beginning of each run. They are changed only during the alignment phase (see section on alignment).

12.4. Alignement of the chamber

As briefly discussed in the section on the constants used in recontructing tracks the t_0 needed to link tracks up can be measured to some accuracy with a test pulse. These measurements together with the known geometry of the chamber allow for a first set of constants which usually allows a quite good reconstruction efficiency fo tracks.

For the tests done so far (the previously described cosmic ray test and the to be described DØ hall test) the operating conditions and the geometry of the chamber were not known well enough to allow a good determination of the t_0's based purely on pulser calibrations etc.. An internal alignement procedure is used to find an average set of t_0's for the chamber.

The basic idea is as follows. First a set of t_0 for the sense wires is derived. In a first pass tracks in the segments are fitted as described above, but the χ^2 for the fit is allowed to be fairly large. The residuals for these tracks are accumulated and the mean and sigma are determined. At the end of the run the t_0's are corrected with half the mean residuals. The same procedure is repeated a number of time, each time tightening up the cut on χ^2. If the determination of the electronic t_0 was done properly, this process converges fairly quickly if the events are clean.

For the delay lines a very similar method is employed. After the overall $t_0's$ are determined in the way described above residuals are computed and corrected over a number of consecutive passes. At this point no attempt was made to use the individual calibration measurements for each line except in using the individual line

velocity. It is hoped that the inclusion of these corrections will improve the quality of the fit to the delay line hits.

It is hoped that this internal alignment procedure can be replaced by a better pulser alignment and a better and more complete understanding of the chamber.

13. The Premod - the DØ HALL test

13.1. Introduction

In late September of 1988 the premod was shipped to FNAL to be installed in the DØ interaction region. After a preliminary test of the chamber in the counting room with cosmic rays the chamber could finally be moved into the beam in the middle of November of 1988. The delay was partially due to slowly coming electronics for the readout, but for the most part due to a Tevatron which functioned without major problems for an extended period. This quite remarkable performance of the collider however kept the premod out of the interaction region, because no beam access was possible.

On the 23. of November 1988 the first events from the DØ interaction point were recorded. During the next couple of month the trigger was gradually improved to discriminate against beam gas events and to maximize the trigger rate. During the collider shutdown over Christmas a new set of Scintillation counters was installed to provide a set of counters at small angles to the beam far away from the interaction point.

For the next 5 month until the end of may 1989 the test was running intermittently. A large fraction of the time the system was not fully operational. The reasons were many and were not connected to the chamber- some of them will be discussed in the following sections. Very often however problems in the data aquisition chain made the taking of data impossible.

In the following the setup used to take data is discussed. The data aquisition system is briefly described, together with an overview of the software needed to operate it. Finally data from this test are presented and some results are shown.

13.2. The Tevatron collider

This section very briefly discusses the main characteristics of the Tevatron proton-antiproton collider as far as they are relevant for the chamber test at DØ. The Tevatron is a proton anti proton storage ring at the Fermi National Accelerator Laboratory in Batavia, Illinois. The basic parameters are summarized in the following list:

Max beam energy	0.9 – 1.0 TeV
Injection energy	0.15 GeV
Circumference	6.28 km

No of interaction regions	1 high L, 3 low L
Luminosity	$0.5 - 1.5 * 10^{30} cm^{-2} s^{-2}$ at the high L region, about a factor 80 less at the low L region.
Luminosity lifetime	typically around 20 hours
No of particles per bunch	$p : 6 * 10^6; \bar{p} : 2 * 10^6$
No of bunches in ring per species	6
Average beam current per species	$p : 1.4mA, \bar{p} : 0.5mA$
Crossing angle	$0°$
Energy spread	$0.15 * 10^{-3}$
Transverse emittance	$2.6 * 10^{-9} \pi rad - m$
RF frequency	$53MHz$
Acceleration period	$44s$
Bunch length	$50cm$
Beam radius	$43 * 10^{-6} m$

The quoted numbers were mostly taken from [53], page 50, and were updated to correspond to the actual performance of the collider during the 1988/1989 run.

Since the RF frequency is 53MHz, particles can be trapped in principle every 18.86ns around the ring. For six bunch on six bunch operation an equal spacing between all bunches is not possible, but it varies by one "bucket". Bunches are spaced 185 or 186 RF buckets apart alternating between the the numbers. The first (leading) bunch is called the "A"-marker, the third one the "B" marker and the sixth one the "C" marker.

At injection the Tevatron is running at 150 GeV. First the six proton bunches, then the six antiproton bunches are injected. If everything succeeds the ring will then ramp up to its normal energy of 1.8TeV CM, the so called flat top.

During this run only one interaction region was equipped with mini beta magnets to increase the luminosity. This was the B0 interaction region with the CDF experiment. Here luminosities up to $1.5 * 10^{30} cm^{-2} s^{-1}$ were obtained. In the other three interaction region the luminosity is about a factor 80 less than the CDF luminosity [54].

13.3. The DØ interaction region

During the 1988/1989 collider run a temporary setup was installed in the DØ interaction region. The interaction hall for the DØ detector was already finished.

but no detector was installed. A steel bridge crossed the space for the detector as a temporary support for the beamline.

The FNAL collider really consists of two rings: The so called main ring, a synchroton with conventional magnets, and the Tevatron itself with super conducting magnets. The main ring is used for two purposes. During the filling of the Tevatron with protons and anti protons it is used as a preaccelerator, ramping the protons/ antiprotons to 150 GeV/c before they are injected into the Tevatron. Once the Tevatron is filled the main ring is used as a proton synchroton to provide protons needed in the antiproton source. Every 2.25 seconds the main ring will ramp for appr. 1.75 seconds and then dump the accelerated protons onto a target.

In the tunnel both rings are placed on top of each other. As they enter the DØ interaction hall they separate to a distance of about 2 m at the collision point. A number of magnets are placed on the Tevatron inside the interaction hall, which are used for beam extraction during fixed target running. A space of about 1.80 m around the interaction point is left clear of magnets etc.

Around the collision point the standard 4 inch diameter stainless steel beam pipe of the tevatron was replaced by a thin extruded stainless pipe for $\pm 8.5''$. The wall thickness of this pipe was 6/1000", as opposed to 34/1000" for the standard beam pipe.

Besides the premod a monopole experiment shared the DØ collision point. It introduced considerable amounts of material in front of the premod. Its main parts are 1" thick pieces of glass mounted inside the beam pipe and an array of plastic scintillator like materials about 1" thick just at the outside of the beam pipe. This detector intends to find very heavy particles by the damage they do to the material in the detector when traversing it. It requires no external electronics or connections.

13.4. The chamber setup

13.4.1. The Beam trigger

Fig. [90] shows an end view of the premod as it is mounted in the DØ interaction region. The chamber sits between two magnets, slightly to the side of the perfect vertical due to space restrictions. The chamber is supported by two "unistrut" bars which run parallel to the beamline. These bars are placed in a way that a particle from the beam which would go through the active chamber volume will not traverse either of them. Two scintillation counters are placed beneath the chamber between the beam pipe and the premod, another one on top of it. These three counters form

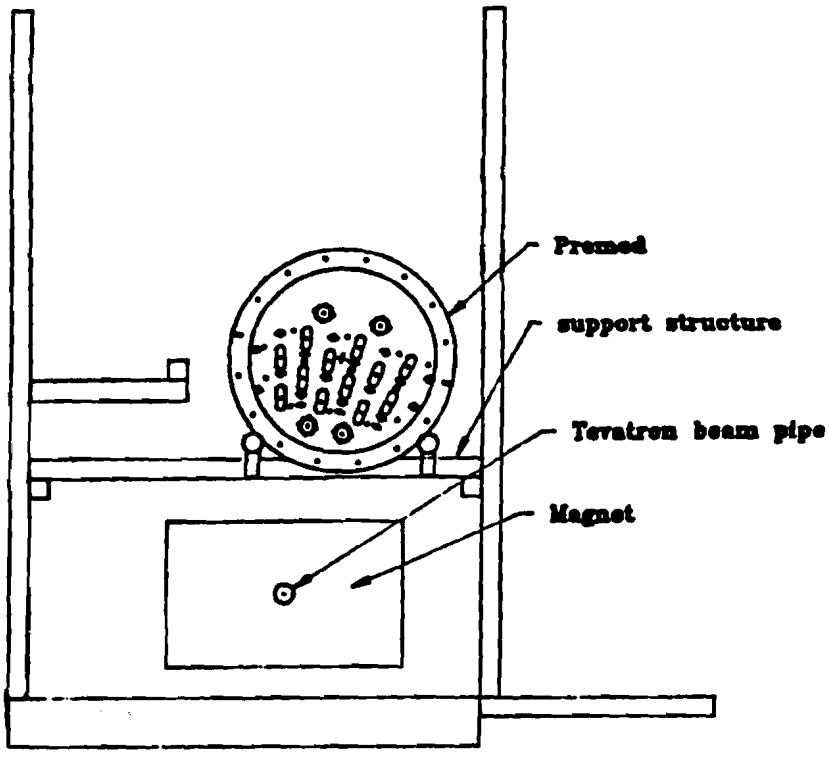

Figure 90 . Endview of the premod mounted in the DØ interaction region.

the so called inner set of counters referred to later in discussing the trigger. Two scintillation counters are placed in front and behind the chamber, covering the ends of the counters on top and right below the chamber. At different times these counters were used as veto counters to discriminate against particles travelling parallel to the beam pipe, or as crude interaction triggers by requiring a coincidence between both of them.

In addition two sets of two counters each were positioned to the left and the right of the beam pipe 7.06 m away from the nominal interaction point on the anti proton side and 9.72 m away from DØ on the proton side. Fig. [91] shows the position of the different counters with respect to the interaction point and the chamber. Unfortunately two large dipole magnets and one quadrupole are placed around the interaction region. In particular on the $\bar{p}$ side the dipole will blank out most of the particles for the far counter on this side. The counter essentially will see only those particle which just "graze" the edge of the dipole magnet and produce particles hitting the counter.

Fig. [92] shows the finally adopted schematics for the trigger. Essentially a trigger is formed in two steps. First a coincidence between the three inner counters is

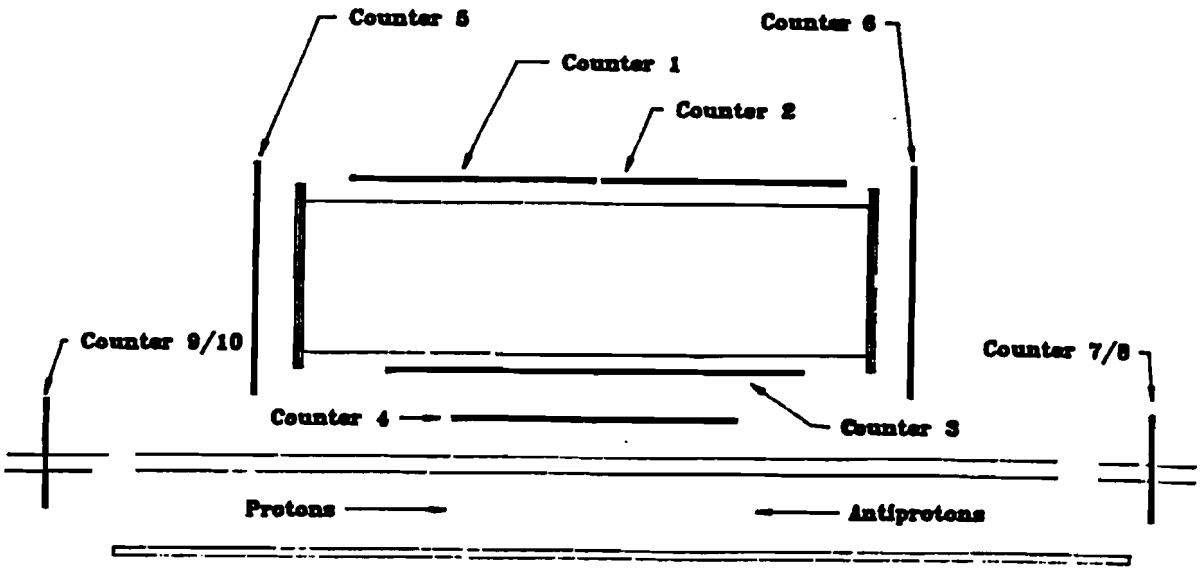

Figure 91 . Schematics of the different scintillation counters used for trigger purposes

made and vetoed by an "or" between the two endcap counters (counters 5 and 6). The timing of this coincidence is set by the counter closest to the chamber, counter #3. A second coincidence is made between the two far side counters. More precisely the "or" between the two far counters on either side is formed, and the coincidence between these two signals is made. A coincidence between this and the inner coincidence is used to form the final trigger signal. Finally the trigger is once more retimed with an appropriately delayed signal from counter # 3 to minimize the jitter in time, and vetoed with an "or" of the 4 far counters timed in early with respect to the expected interaction.

The machine provides two types of signals which are used in addition to the counter signals. The first is a pulse signaling the beginning of an acceleration cycle in the main ring. During the ramping of the main ring a lot of background from this is expected. The trigger is blanked out during this period of 1.75 s out of a total cycle time of 2.25s. The other signal is the so called Tevatron Beam Synchronization signal. It is a signal occurring every $7\mu s$ whose frequency is synchronized to the Tevatron interaction rate. An appropriate delay is introduced to put this signal exactly at that point in time at which an interaction at DØ would happen. The actual interaction rate is twice as high, collisions occur every 3.5 μs, so the trigger will loose half the

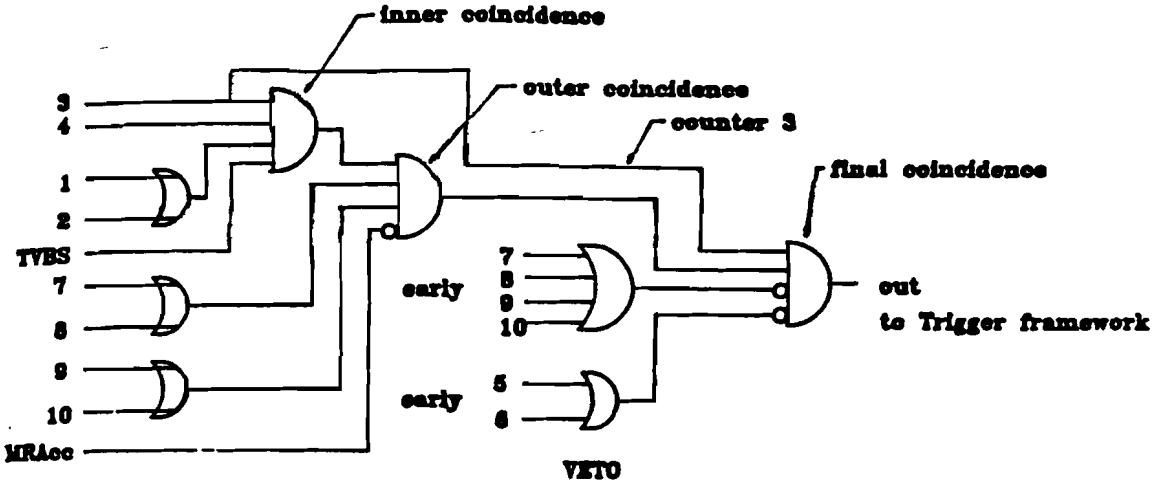

Figure 92 . Schematics of the trigger logic used for the final runs. For reasons of clarity all delays have been omitted.

possible interactions. This signal is introduced as an additional signal into the first, the inner coincidence.

The trigger was set up to try to reject as many beam gas events as possible and to be as insensitive as possible to halo particle from both the proton and the anti proton beams. As the beams travel down the beam pipe in their respective directions, they are surrounded by a cloud of particles. THeses originate from beam gas collisions, interactions with parts of the beam transport system etc. If ones calls the time of the "real" interaction $t = 0$, then the proton will pass by counters 9/10 at time $-t_1$. Most probably some of the halo particles will hit the counters and produce a signal. The same is true for the anti protons and counters 7/8. These halo hits can be easily rejected by the fact that they are too early compared to the nominal interaction time. At $t = 0$ the interaction occurs at DØ and the fragments starts to fly apart. Only a small fraction of all particles in the beam actually interact so most protons/ antiprotons will just continue on. They will now pass the opposite far counters at the same time as any fragments from the real interaction. Discrimination between the real event and the halo is possible by requiring a simultaneous hit on both far counters, upstream and downstream of the chamber. However there will be always

some background due to accidental halo hits in both counters which fall within the time window of the coincidence.

The trigger sketched out in Fig. [92] does essentially the following thing: The inner coincidence requires at least one particle at large theta. The veto with the two close outer counters (counters 5 and 6) removes any hits from particles flying parallel to the beam axis and also events with a large number of particles. At the same time two very low angle "beam jets" are required to trigger the coincidence of the two far counters. A very tight timing on the coincidence is meant to lower the chance of accidental signals from two halo hits at the same time on either side. The veto on the early signal from the far counters removes the first set of halo interactions and some beam gas events. The whole trigger is retimed with the counter closest to the chamber to remove as much time jitter as possible. It is synchronized to the Tevatron crossing signal. During the main ring accelerator cycle no triggers are allowed. Although background from the main ring is not very likely to fake a trigger, it does produce many low energy particles whose tracks overlap the real event in the chamber and make the reconstruction difficult.

There are several sources of possible background triggers. An interaction can occur but without producing a particle at high theta. The two low angle beam jets are present and trigger the far coincidence. The high theta trigger however is done by an simultaneous beam gas event from either the proton of the anti proton beam. Some similar events might happen in which not one beam gas particle produces the trigger but a number of them hit the inner counters more or less at the same time. Again if the far counters are present the trigger will fire. Some of these events will be rejected by the veto from the counters 5 and 6, because they will rather likely spill over into counters 5 and/or 6.

The hits in the far counters will with some probability be faked by simultaneous hits of the p and the $\bar{p}$ halo respectively. The inner coincidence might be present due to a real event or, more likely, due to a beam gas event.

13.4.2. The signal path: From the chamber to the event display

After the preamp the signals from the wires are sent to the outside of the interaction hall via a flat coaxial cable. There they are amplified and shaped in the DØ shaping amplifiers, which are described elsewhere in more detail. The shaping headers were set up to do no real shaping, but to compensate for the losses and distortions in the cable only. The headers also allowed for a limited adjustment of relative gains between individual channels. This was used to supply a lower electronic gain to the outer sense wire, which were operated at a higher chamber gain, and to amplify

the delay line signals more than sense wire signals. From the shaper the signals are sent up to the movable counting house into the FADC. At the Input of the FADC a coupling transformer inverts the signal and decouples the grounds. The signal is AC coupled into an amplifier with a bilinear response curve. For large signals (larger than FADC bin 192 above pedestal) the gain is 11 times smaller than for the main part of the pulse. The bilinear response is essentially achieved by using the knee voltage of a diode. The FADC is a 100 MHz 8bit SONY chip, running at 106 MHz. This frequency was chosen in order to be able to synchronize the FADC clock with the Tevatron timing signals. Data are next passed through the DØ zero suppression chip, a custom designed gate array described in more detail in the section on the readout electronics. The zero suppress chip tries to find clusters of data which are not base lines in the raw digitized hits passed over from the FADC. Only those clusters are saved and sent out onto the data cable. From there the data are processed by the level 2 system and picked up by the main data aquisition program on the host computer.

13.5. The Data acquisition system

During the test of the premod a complete version of the DØ data acquisition system was in place in the DØ hall. This system, which is described in detail elsewhere [55] will eventually consist of a dedicated fast trigger processor (trigger framework), a farm of 50 μVax computers (the level 2 farm) and a VAX 8820 host computer. The Trigger framework does the first level of precessing of some selected set of the data from the detector to decide whether a good event happened or not. Level two takes all the good events and does a first processing of them and a reformating. Finally the 8820, the host computer, stores the good events and does any kind of online analysis.

A certain time after every beam crossing trigger framework checks whether any valid trigger condition is met. In the simplest case a valid trigger would be a set bit in the 32 bit trigger word. In more realistic situations any combination of those may be used for a specific trigger. The trigger conditions will be programmable in software by the user to allow for maximum flexibility. In the final experiment trigger framework will actually build the trigger from a number of inputs- like information from the calorimeter, from the trigger counters or other parts of the detector. During the 1988/89 run the actual trigger was formed outside trigger framework by the above described trigger logic and was processed and timed by trigger framework.

If a valid trigger condition is met, a signal is send out to the different front end crates to suspend the taking of additional data. In the case of the CDC a flag is set at the FADC indicating that the data in the fast buffer are to be transferred into the zero suppress chip (start digitize signal). Another flag is set, the "hold transfer" flag,

which can be used to abort the processing of the data, if for some reason the trigger system marks a initially valid trigger as invalid. This is the so called level 1.5 trigger decision, which would mean that the front end is dead for one intersection, during which data are being processed and the final trigger decision is reached. It allows the trigger computer some more time to arrive at a more sophisticated trigger decision without unnecessarily slowing down the whole system by introducing a lot of dead time. If the hold transfer flag drops before the start digitize flag, the FADC stops processing, empties out its buffers and is ready for a next event.

Trigger framework also sends a signal to the level 2 farm indicating that a valid trigger occurred and that the system should prepare for data to come in.

To guarantee that the timing between the different components of the system is consistent everything up to the level of trigger framework is timed from the same clock. This master clock is driven by a synchronization signal received from the accelerator, which retriggers the system every 21 μs (every full revolution of the beams). Starting from this signal the clock generates a 106 MHz square wave which is phaselocked to the main timing signal and resynchronized every 21 μs. This clock drives all the FADC's. In this test the 106 MHz signal as received from the clock was distributed to the FADC's directly via the VMS back plane. In future versions repeaters are foreseen on each FADC board to minimize the dependance of the system on the signal quality received from the clock. The clock also sent a Tevatron crossing signal to trigger framework, which is used by the trigger computer as its main synchronization signal. Every check trigger framework does on trigger bits is timed relative to this timing signal. All the signals originating in the clock system are controlled by a local computer. They can be delayed with respect to the main timing signal from the accelerator, so that e.g. the acquisition of data with the FADC starts shortly before data actually start arriving from an interaction on the input. Care has to be taken to time this on the correct bunch passing by in DØ. Since bunches are not equally spaced, but vary in distance by 18.8 ns, the start acquire signal sent to the FADC should be timed in the correct sequence to match up the sequence of the bunches passing by at DØ.

Data from the detector are send to the μVaxes via fast data cables. Each part of the detector is served by one data cable. At the farm a supervisor computer decides which of the μVax nodes is not busy and sends the data to this node for processing. The cable is directly mapped into a part of the processor memory avoiding repeated copying of the data from one memory location to another. Once data are being processed they are send on towards the host for storage and, if so desired, online processing.

The actual system available at DØ was a scaled down version of the final acquisi-

tion system. Four μVax computers formed the level 2 farm- one as a supervisor, the other three as actual nodes. Three data cable were installed, one for the chamber test, one for the muon chamber test and one for the calorimeter electronics test. The level two system was essentially only used as an intelligent data router without doing any actual data processing. It did receive the data from the VME crates, checked them for parity errors and consistency by comparing the information in the data header with the actual data package (e.g. length of the data package) and held them in a buffer until it was able to ship them off to the host.

On the host a number of things are happening. Most importantly data arriving from the level 2 farm will be recognized according to the trigger type – in this test, the distinction was entirely detector related: central chamber data, muon data or calorimeter data, in real running this might mean a missing p_t trigger, or an electron trigger– and saved into appropriate disk files. The disk storage is only used as a spooler for the tapes- once a certain file size is met, data will be automatically written to tape.

At the same time the host allows the online analysis of the data. If this is enabled data are being put into a common block, the so called global shared common, where they can be accessed by an online analysis program and used for event display etc.. Again the online program will pick out only those events from the global shared common which fall into certain trigger categories.

13.5.1. DAQ Software

A number of programs have to be present in order for the Data acquisition system to function properly. This section does not attempt to provide a users guide to the system, but rather to give a short description of the programs involved. For the user three programs are visible. One is a low level program running on the 68000 μProcessor that controls the VME crate with the FADC's. This program upon receiving a trigger signal will start and control the routing of data from the FADC buffers on the data cable driver. The other two visible programs are running on the Host. One is the control program for the taking of data, the program "Taker", which defines the type of trigger used, switches recording of events on and off etc. The other visible program is the online analysis/ event display package called "Examine". Examine is the online version of the previously described DØuser program. It provides a subset of the functions of DØuser, which are meaningful for interactive data analysis. Histograms may be booked and filled, and the standard event display package is present.

In the background a number of other processes have to be active. The central

task running is the Coordinate program, which "coordinates" the flow of data from the level 2 farm to the host. COOR, as the program is called, will with the help of two other processes fill the global shared common and write data onto disk for those triggers for which a Taker is active.

Each of the other parts of the DAQ, the level 2 farm and the trigger framework, have their own control programs, which may be accessed from the host. They allow the user to interact, mostly for debugging purposes, with the different systems. A more detailed description of these can be found elsewhere.

13.6. Performance of the Premod in the DØ interaction region

During the collider run the premod was continously in the beam for about 7 month. About half of this time the chamber was actually under HV, some undetermined small fraction of this taking good data. However the chamber performed very good over the whole period. No problems were encountered which were due to the chamber. In particular no HV breakdowns occurred, nor did the chamber trip spontaneously. The only time the HV had to be lowered was during the injection of p and $\bar{p}$ into the Tevatron, when a very large background radiation increased the chamber currents to more than $20\mu A$ per wire (the limit of the current meters).

In the following a short summary of the general performance of the chamber is given. For a more detailed discussion refer to the previous section on the cosmic ray tests. This section is intended only to show that the chamber operated correctly.

Fig. [93] shows the number of full $r-\Phi$ tracks in every event, the number of hits which participated in the track and the number of hits on the $r-z$ track. Only 3 layers were required for a full track in $r-\Phi$. Of the 10643 events processed in this run, 1610 did not reconstruct any full track at all in $r-\Phi$. For about twice as many events no track in r-z was found (3650). Conditions for a track were as follows:

Max χ^2/N for segment tracks	5
number of missing wires on a segment	2
minimum numbers of segments in full track	3
max χ^2/N for full tracks	30
number of missing delay lines	4

Fig. [94] shows an efficiency plot for the sense wires and the delay lines. This plot was obtained by requiring 4 layers to participated in a track fit. The results agree with the measurements done using cosmic rays. Two delay lines did not work properly in the premod. This explained the lower efficiency for delay line #15 and #27 in the plot. Fig. [95] shows the χ^2 per degree of freedom for the track fits in both views, $r-\Phi$ and $r-z$. Fig. [96] shows distributions for the ϕ and the

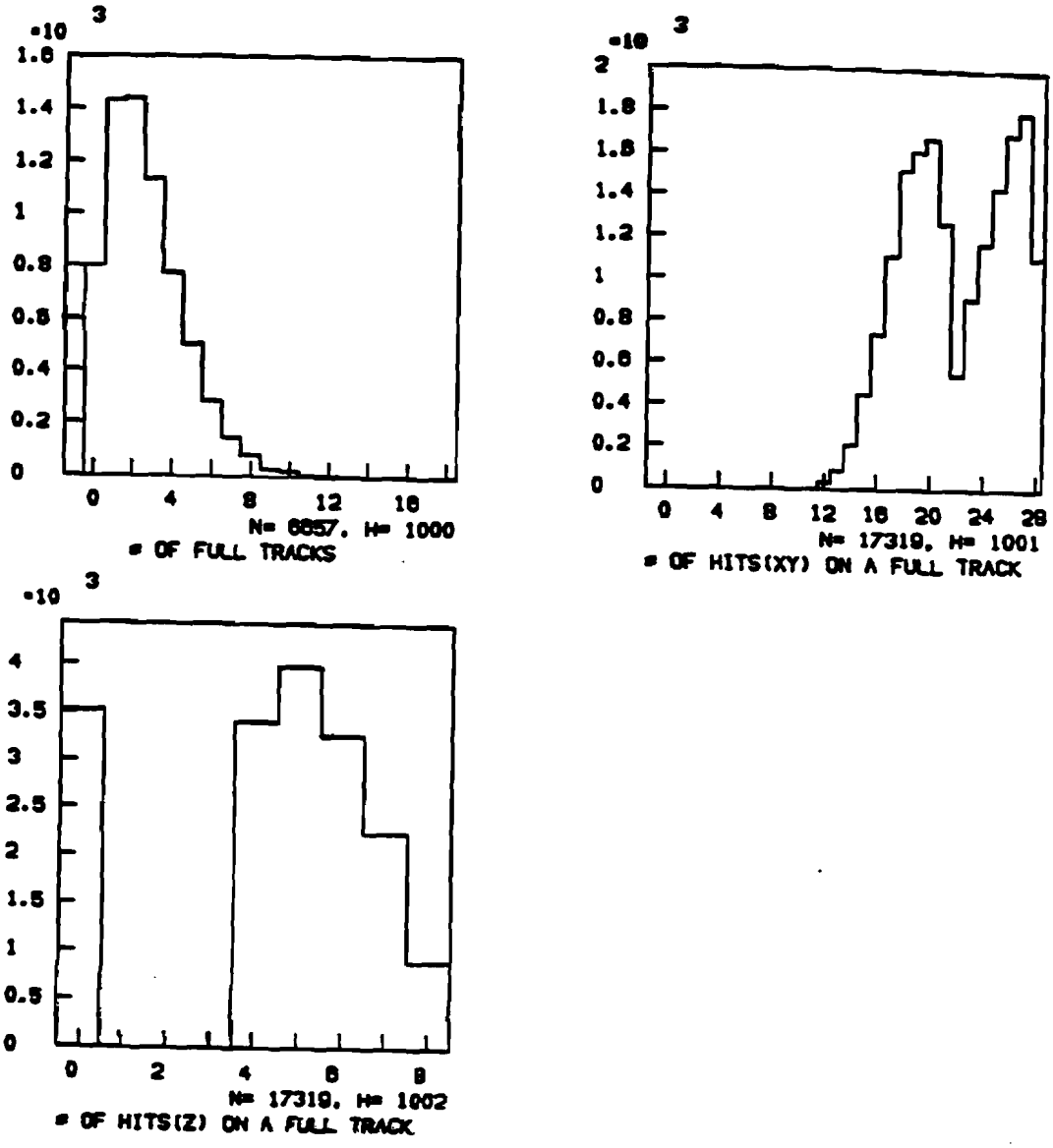

Figure 83 . Number of full tracks/event, number of hits on a full track and number of hits on a r-z track for run 3584

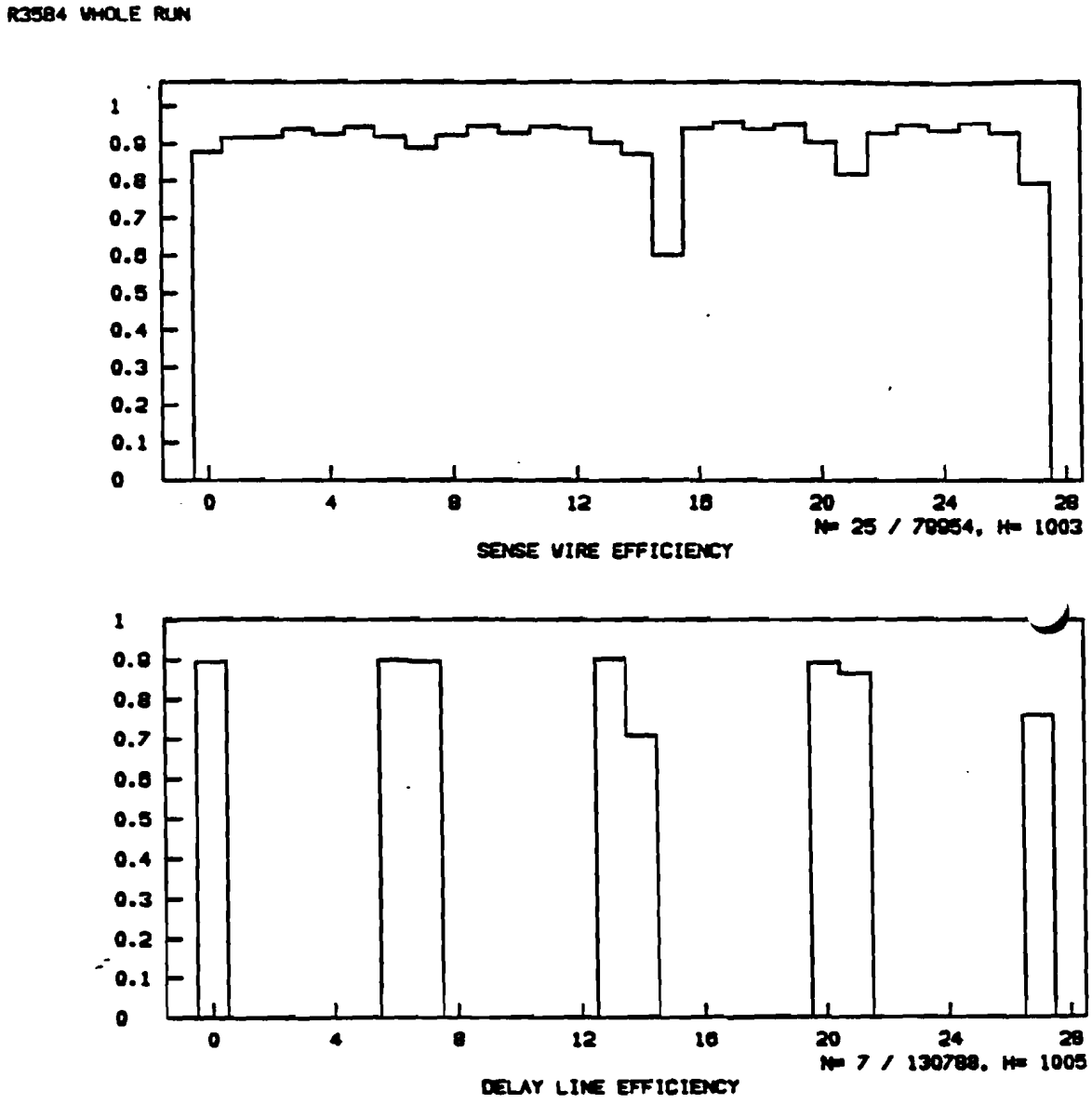

Figure 94 . Efficiency for sense wires and for delay lines. Two delay lines were not functioning (# 15 and #27) in one sector.

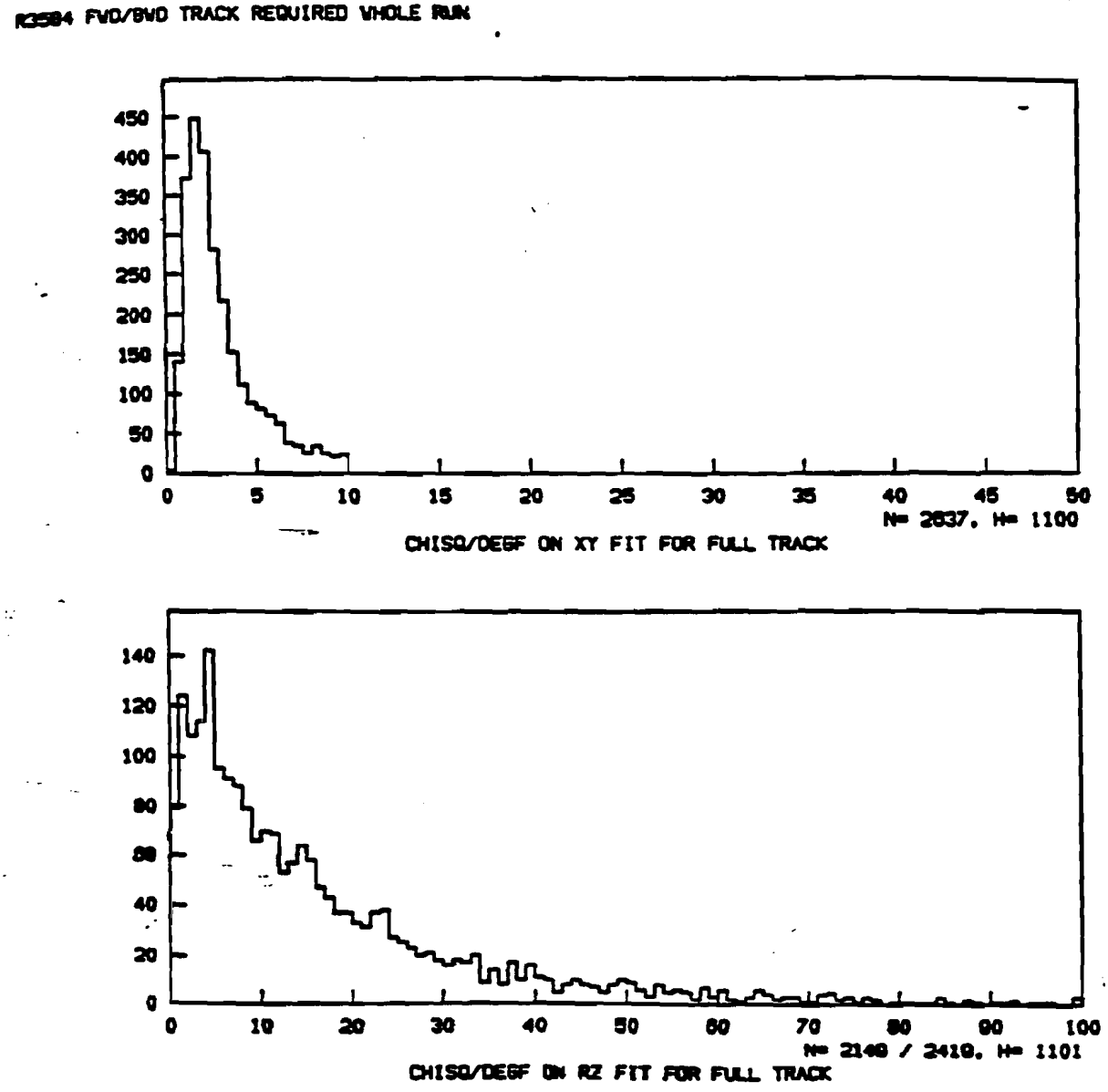

Figure 95 . χ^2/N for the fit in $r-\Phi$ and in $r-z$. For the calculation of χ^2 in $r-\Phi$ a constant time error of 4 ns was assumed, for the $r-z$ calculation the actual fitting error was used.

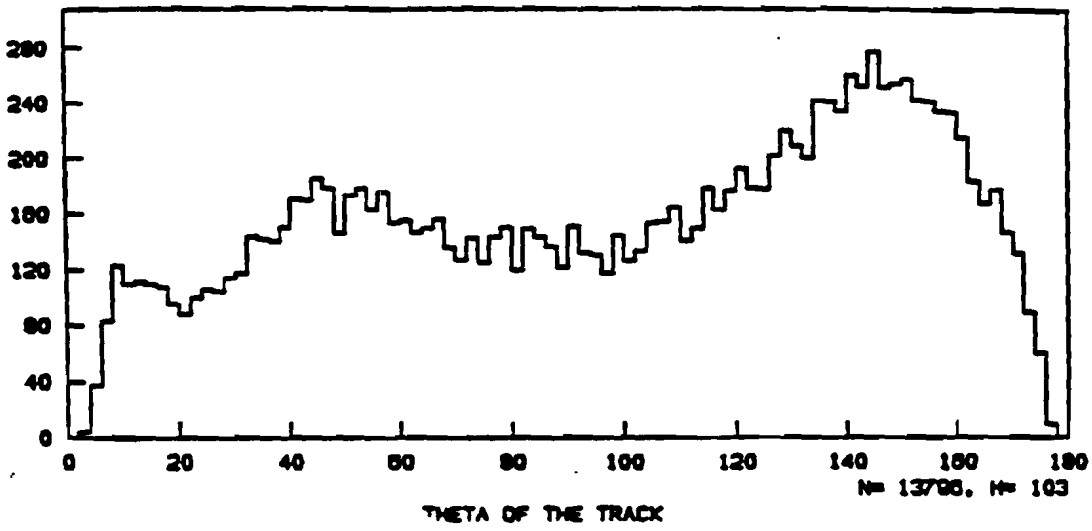

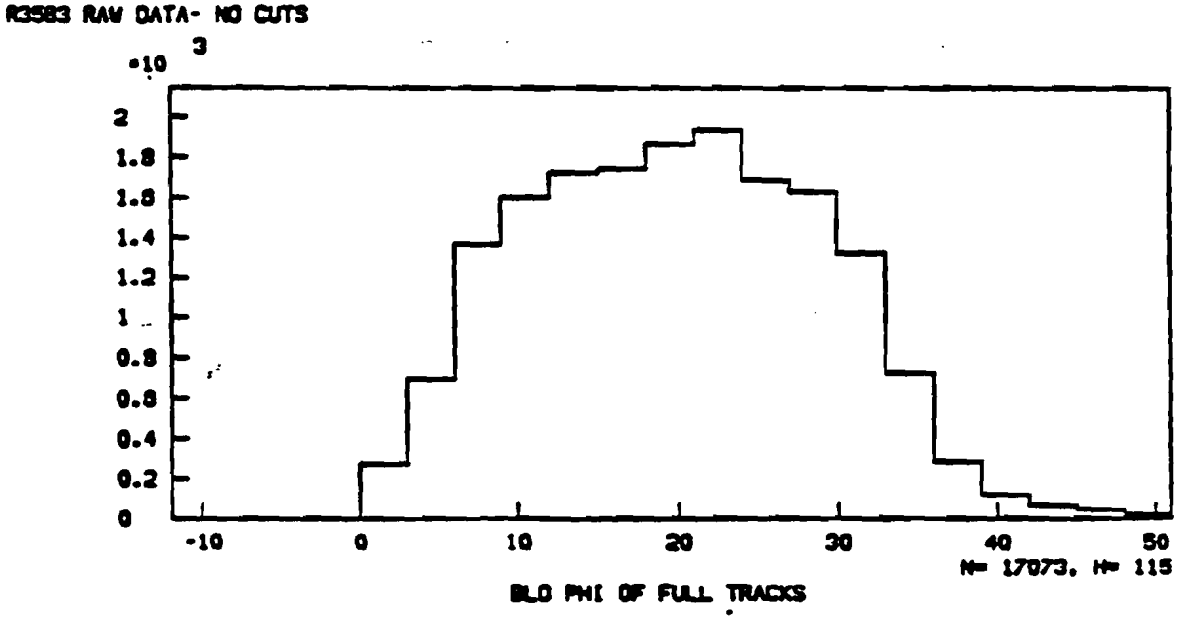

Figure 96 . Distribution of the angle Φ seen in the chamber and of Θ

Theta angle measured in the chamber. The Φ distribution is flat indicating that the chamber is *illuminated* uniformly in Φ. Θ shows two peaks due to forward and backward events, to a large extent probably due to beam gas interactions. A more detailed discussion of this is given in the next sections.

13.7. Analysis of the DØ hall data

The data discussed in the following section were taking during the last part of the DØ hall premod test. At this point the trigger as outlined in the last section was in place and functional. The data acquisition chain was working most of the times, and the online program was in a state which allowed a quick feedback on the incoming data. Two large runs were taken during the last days of collider running which yielded useable data: run 3583 and run 3584. If not otherwise noted data presented here come from either of these two runs.

They were taken under "nominal" conditions: Tevatron running at 1.8 TeV center of mass energy with six proton bunches colliding with six antiproton bunches. The Luminosity at the begin of each run was $1.2 * 10^{30} cm^{-2} s^{-1}$ for run 3583 and $1.0 * 10^{30} cm^{-2} s^{-1}$ for run 3584 respectively. 31380 triggers were taken in run 3583, 15640 in run 3584.

The analysis presented in the following proceeded in three steps. First a rough alignment of the chamber was done using data from a pulser run. A first pass over the data was done, using this alignment, in which very clean events were picked out. The file of so selected events was used to improve the alignment of the chamber. Once the alignment was satisfactorily the raw data were once more passed through the analysis program. This time events with good tracks in z were selected. In a third pass finally the selected events were further reduced by requiring a fully reconstructed vertex in three dimensions. In the following the different steps will be discussed in detail together with the methods used, cuts applied etc..

13.7.1. The alignment phase

Fig. [97] shows a few typical events directly from the raw data tapes. Clearly there are many hits present besides those which were recognized as participating in a full track. Due to low energy particles from various background sources many incomplete tracks form in the chamber. They will be reconstructed as segment tracks, but will usually not pass the criteria to participate in a full track. The automatic alignment procedure described in the chapter on the offline analysis program will take any segment track and try to find the best matches for full tracks. Without

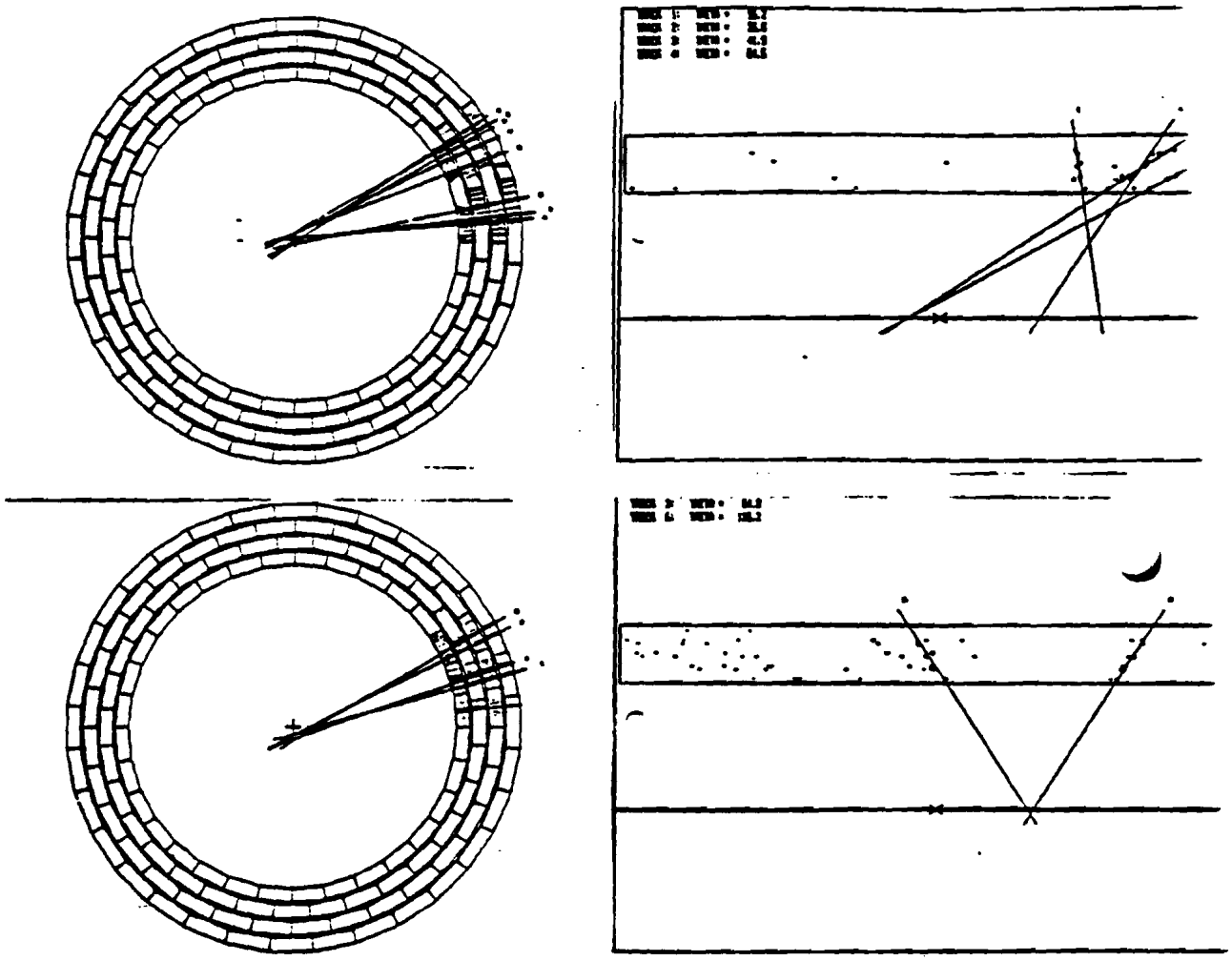

Figure 97 . Some typical raw events directly from the tape. No cuts or selections have been made. In the left view the projections of the tracks into the $r - \Phi$ plane are plotted, in the right one the tracks in the $r - z$ plane are shown.

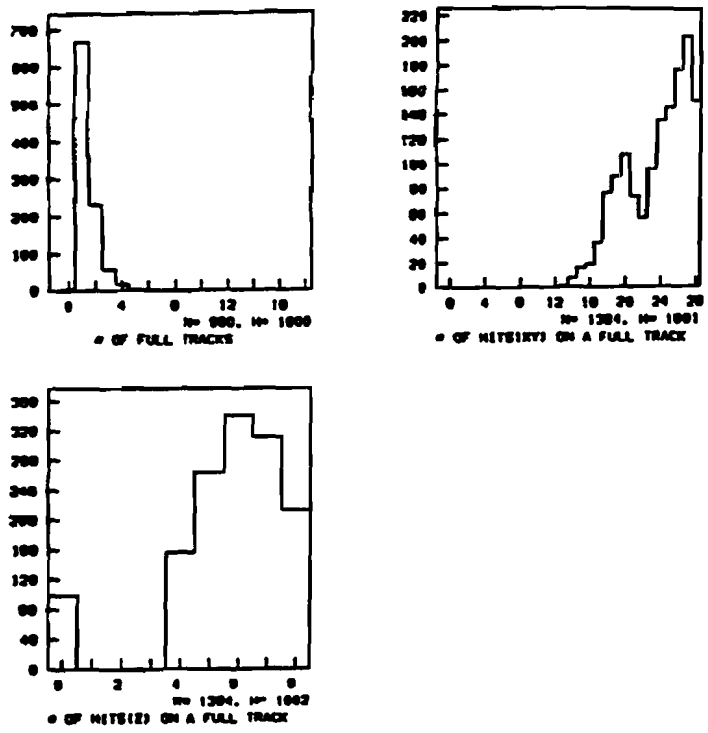

Figure 98 . Number of $r - \Phi$ tracks (full tracks), number of hits on a r - Φ track and number of hits on a $r - z$ track for the clean event sample

any absolute reference using these noisy events will yield unpredictable results. The program might attempt to connect "wrong" segments into tracks, broadening the residual distributions considerably and making an accurate determination of the t_0's very difficult. In order to make the alignment more reliable a special sample of the data was produced that included only very clean events. All cuts were applied to segment tracks only, because their alignment is mostly fixed by the pulser data.

For an event to pass the selection criterium at least one segment track had to be present in each layer. No condition was placed that this track had to line up with other ones in the chamber. If any segment track was found within 1 cm of the anode, the event was rejected. This was done to avoid problems with a non linear field shape close to the sense wire. Every segment was next checked for other hits near by. If more than 3 hits were found for any segment track to be closer than 5 mm to the segment the event was rejected. This way events with tracks close to each other or crossing each other were not included in the sample. In the next step when segment tracks were joined into full tracks, the maximal allowed distance between two segment tracks was chosen to be smaller than 5 mm. The alignment program was forced in this manner to align only the correct tracks together. Fig. [98] shows the resulting

plots for number of tracks found and number of hits on a track in $r-\Phi$ and $r-z$ for the clean sample of events from run 3584. Nearly all events in the sample are single track events with the track reconstructed in both views. Of the 15640 initial triggers in run 3584 980 or 6.3% passed the cuts. Fig. [99] shows the change in the t_0's for sense wires and for delay lines due to the alignment. The changes are not big- they are of the order of a few ns- but important enough to increase the number of tracks found considerably. Fig. [100] shows the t_0 plots for the two consecutive runs, run 3583 and 3584. The first run was a rather large one extending over approximately 9 hours (at a trigger rate of 2.4 Hz). It is clear that a realignment of the chamber is necessary frequently.

13.7.2. Data Reduction: first pass and background rejection

Most events recorded turn out to be beam gas or other background events. The final goal of this analysis is to find those events in the whole data sample that are real $p-\bar{p}$ interactions. This was done in a two step process which is described in detail in this and the following section. To be able to separated the events from the background a more complete understanding of the background events themselves is helpful.

In order to understand the background better, data were taken during a proton only run with a slightly modified trigger. The arm of the far counters which is the side of the protons was not included into the trigger, and the veto of 5 and 6 was removed. The resulting triggers are expected to be entirely due to beam gas events from the proton beam. Fig. [101] shows the distributions for the angle Θ of the track and the intersection with the beamline z. The z-distribution shows a clear peak at z=115 cm and a peak in Θ at 150°. Looking back at the setup in the beam one sees that at z=1m one of the dipole ends- most triggers seen in this run are due to beam gas events scattering at the face of this magnet.

Looking at Fig. [101], it is clear that most background originates from events with $|z|> 1m$ and $\Theta < 40°$ or $\Theta > 140°$. For the next step in selecting good events only those events with tracks with $-75cm < z < 75cm$ and $40° < \Theta < 140$ were accepted. At least two tracks had to pass the z- criterium, and one of the two had to satisfy the Θ criterium. Fig. [102] shows the resulting z- and Θ distributions for the selected events from run 3583. A small peak at z=110 cm survives because some events which have two good tracks in z - and therefore passed the selection cut- also have other bad tracks originating at z=110 cm. 11132 events out of the 31380 raw triggers passed this cut (35 %). Fig. [103] and Fig. [104] show a few events which passed the cuts.

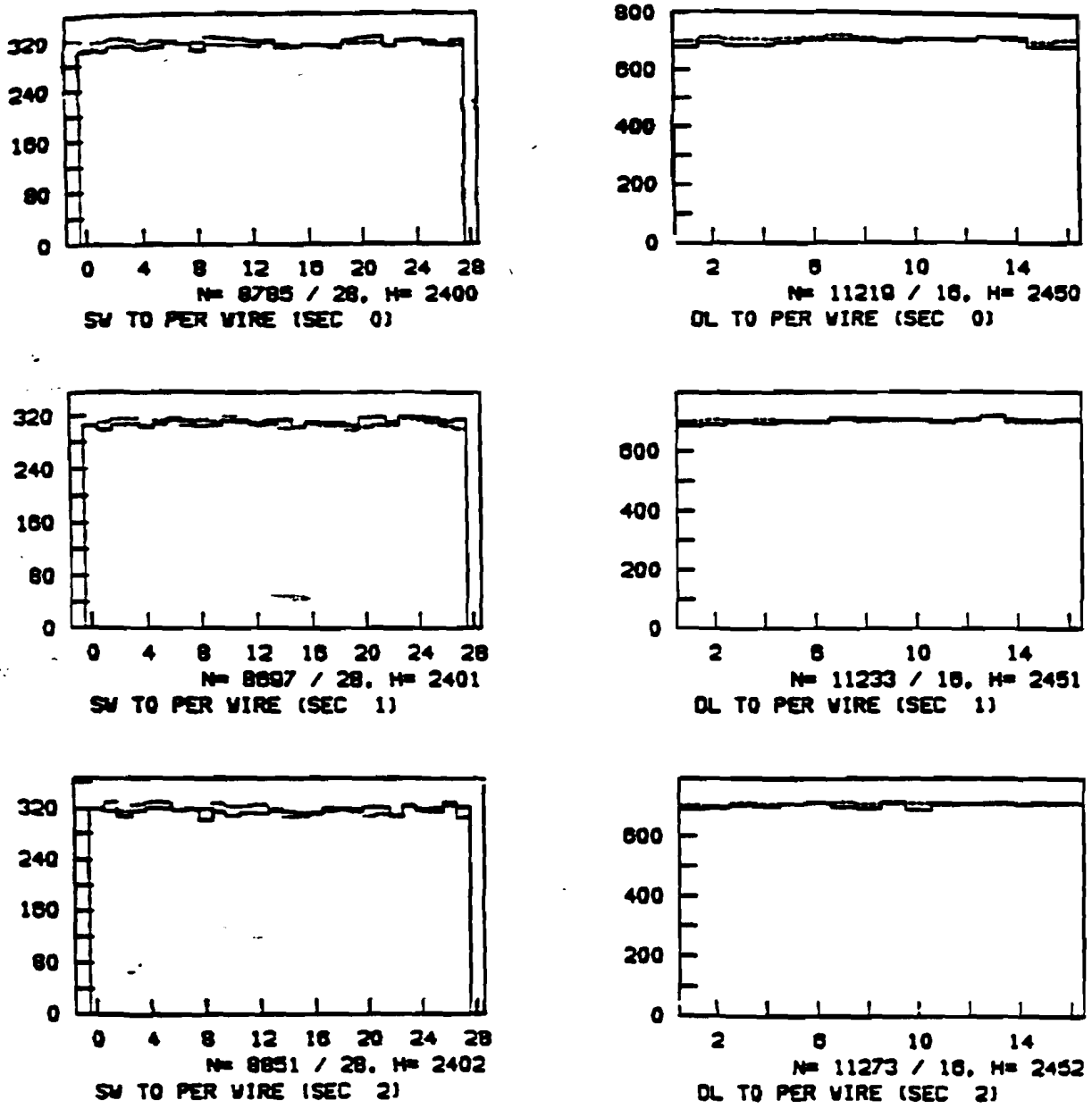

Figure 99 . t_0 before (solid line) and after alignment of the chamber using the clean data sample for run 3584. The left plot shows the sense wire t_0's as a function of wire number, the right one the delay line t_0's.

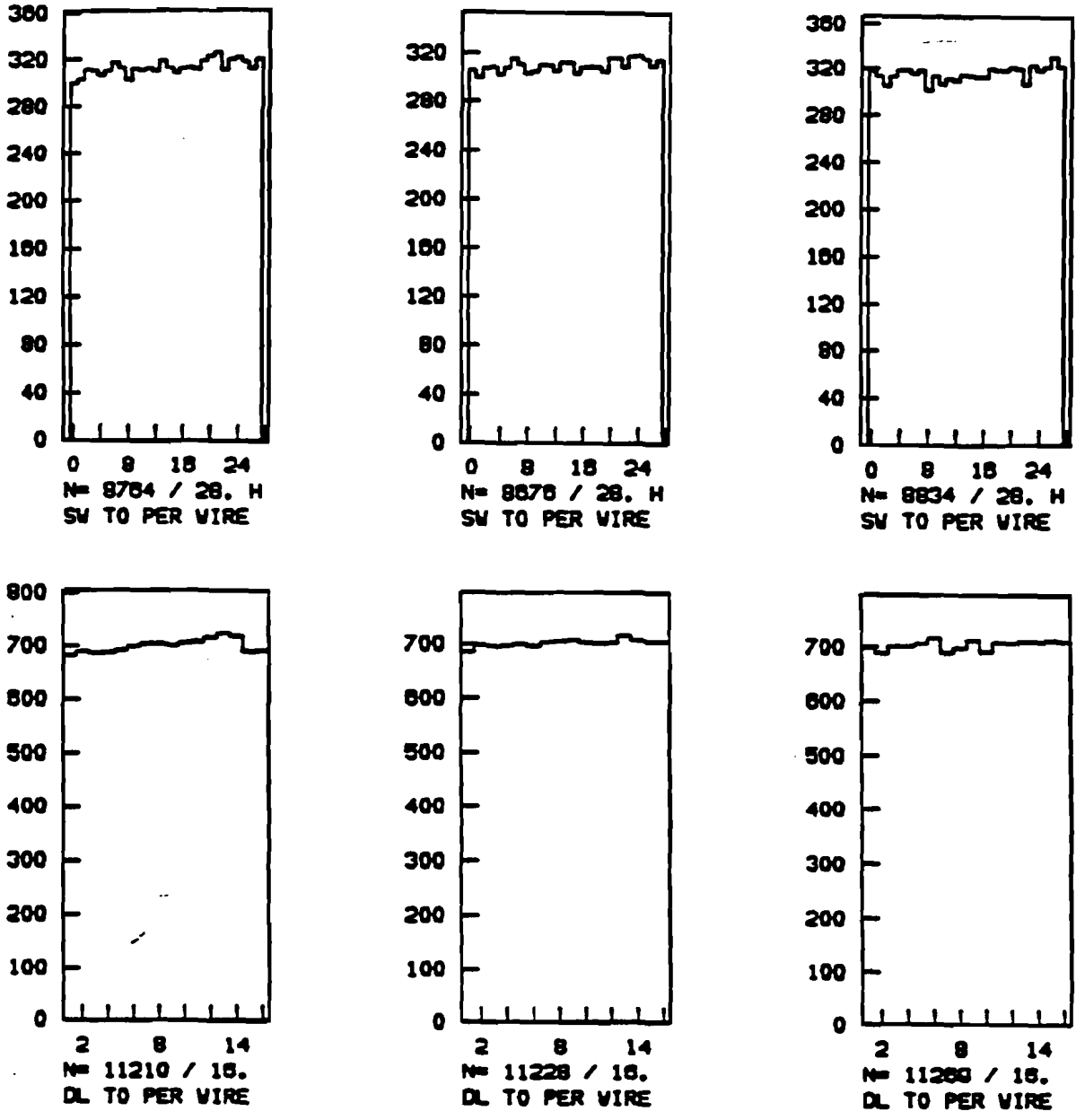

Figure 100 . T_0 **for sense wires and delay lines for run 3583 and 3584.**

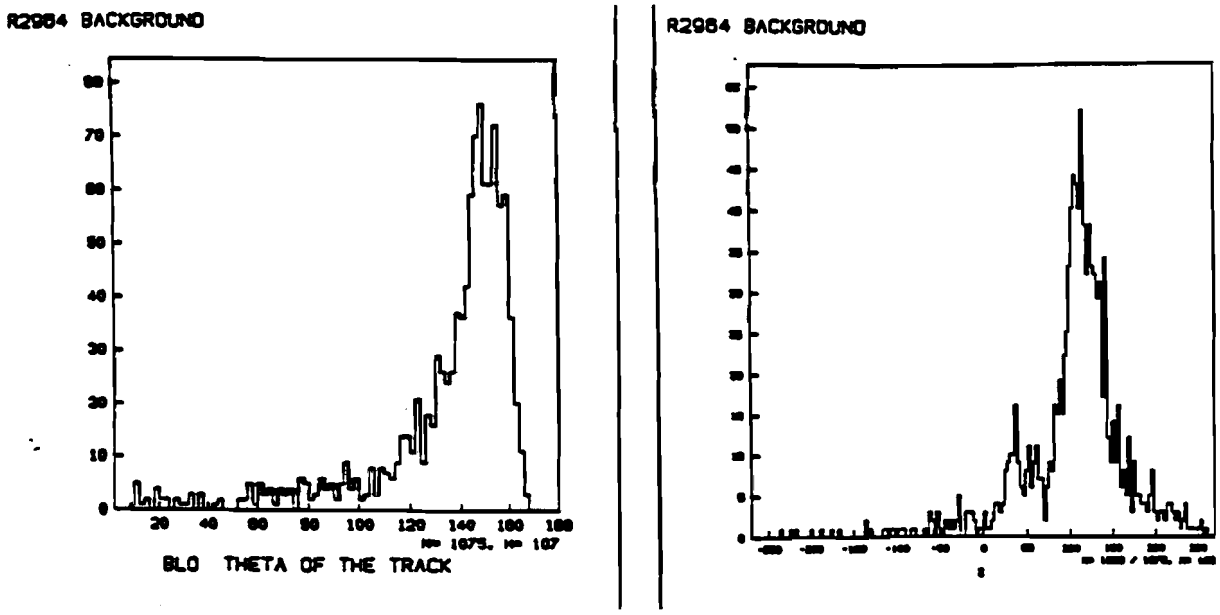

Figure 101 . z and Θ distributions for the background run (proton only store)

13.7.3. Vertex reconstruction

The final selection criterium for real events was that at least two tracks must fully reconstruct a vertex in three dimensions. In the following the cuts used and the method to calculate a vertex are discussed in detail. Since the premod covers only 28° in Φ, the vertex in the xy- projection can be measured much more precisely in one direction than in the other one. This will not be a true for the final chamber, since it will cover 2π in Φ. Since z is known with much less precision than x-y, this makes it impractical to attempt a real simultaneous fit in three dimensions to find the vertex. The method adopted for the DØ Hall data uses the xy vertex as the starting point for a vertex and tries to find a best z-vertex for this xy-vertex.

In detail the procedure is as follows. The first thing done is that the coordinate system of the chamber is changed. Normally the $\Phi = 0$ direction coincides with the outer edge of the cells in the most counterclockwise wise position possible in the chamber. In this way all angles Φ are always positive and start at 0. However for reconstructing a vertex the precision with which that can be done depends on the opening angle of the tracks used for the measurements and on the orientation

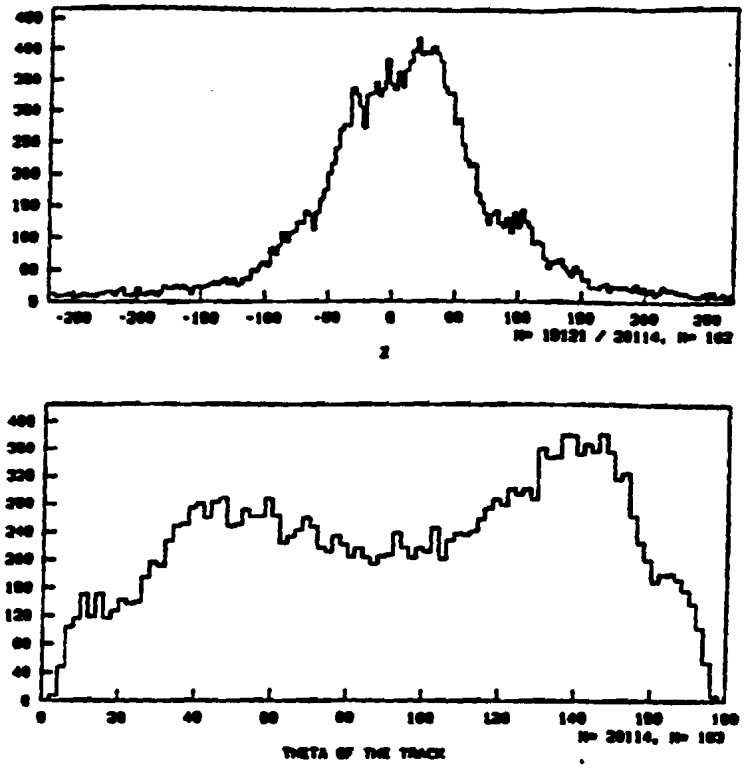

Figure 102 . Z- and Θ distributions of a part of the sample after passing the first pass cut: at least 2 tracks with $-75cm < z < 75cm$ and at least one of these tracks with a Θ within $40 - 140°$.

of the axis with respect to which the vertex is being measured. The most precise measurement can be done in a plane perpendicular to the symmetry axis of the chamber. The coordinate system is rotated in a way that the y-axis is along the symmetry axis. X is now the direction in which the vertex position will be measured most accurate, y the one in which the determination will be worst. Fig. [105] shows a sketch of the used coordinate system.

After rotating the tracks into the new coordinate system the distance of closest approach between each track in the $r - \Phi$ plane and the nominal vertex position in xy is calculated. Only tracks which are closer than 5cm to this point will be included in the following. Next it is required that participating tracks are reconstructed in $r - z$ as well and that the intersection of the $r - z$ projection with the r=0 axis is within $\pm 75cm$ of the nominal vertex position in z. For every possible combination of two tracks which pass these cuts the intersection in the x-y plane is calculated and stored in an array. The distance in x and in y from this intersection to the nominal vertex position is checked and has to be less than a certain limit. Since the x-coordinate can be determined much more precisely than the y-coordinate, a tighter cut is applied to x. At the position of the xy vertex on the track the distance in z is calculated

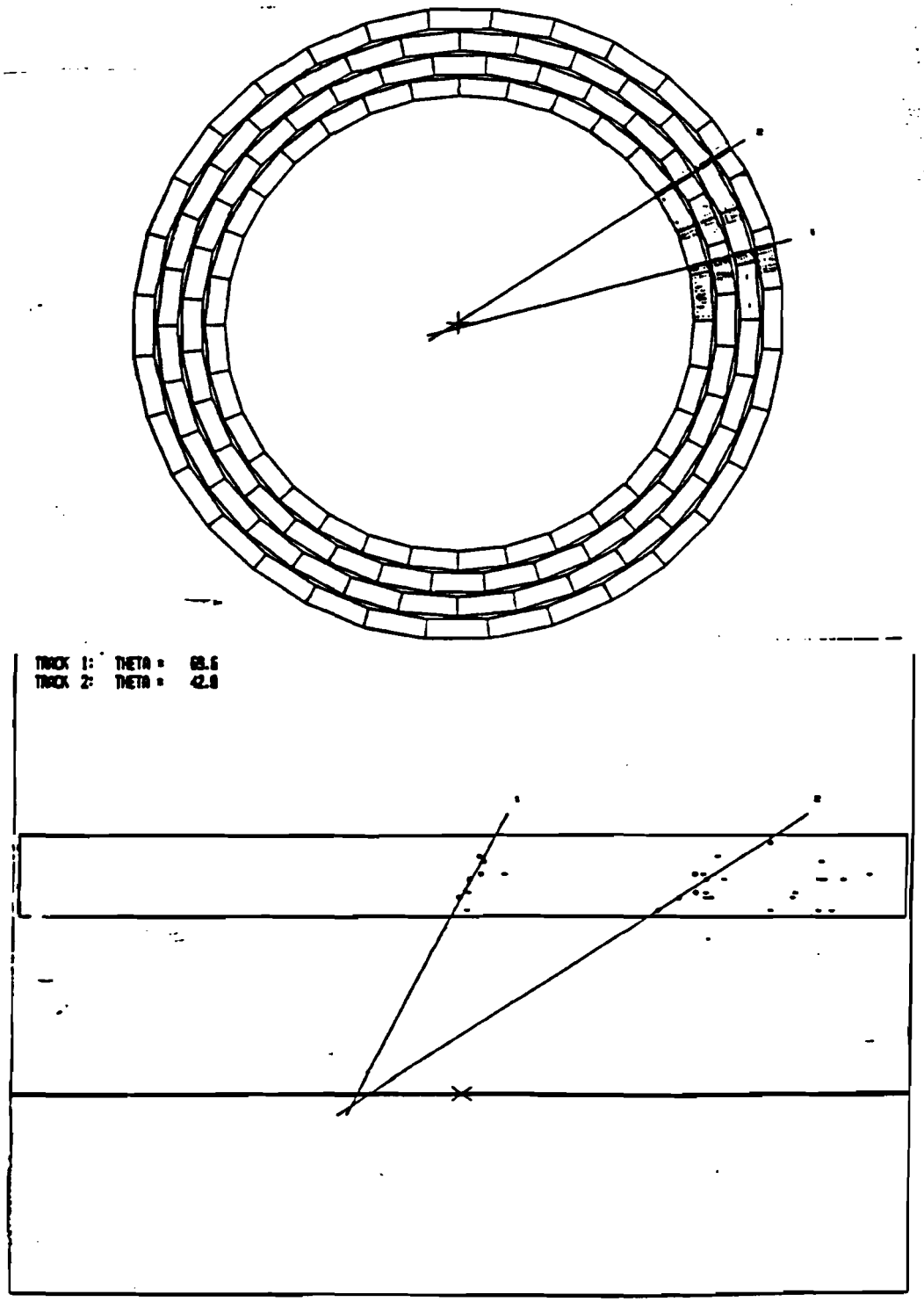

Figure 103 . A typical event display after the first pass cut

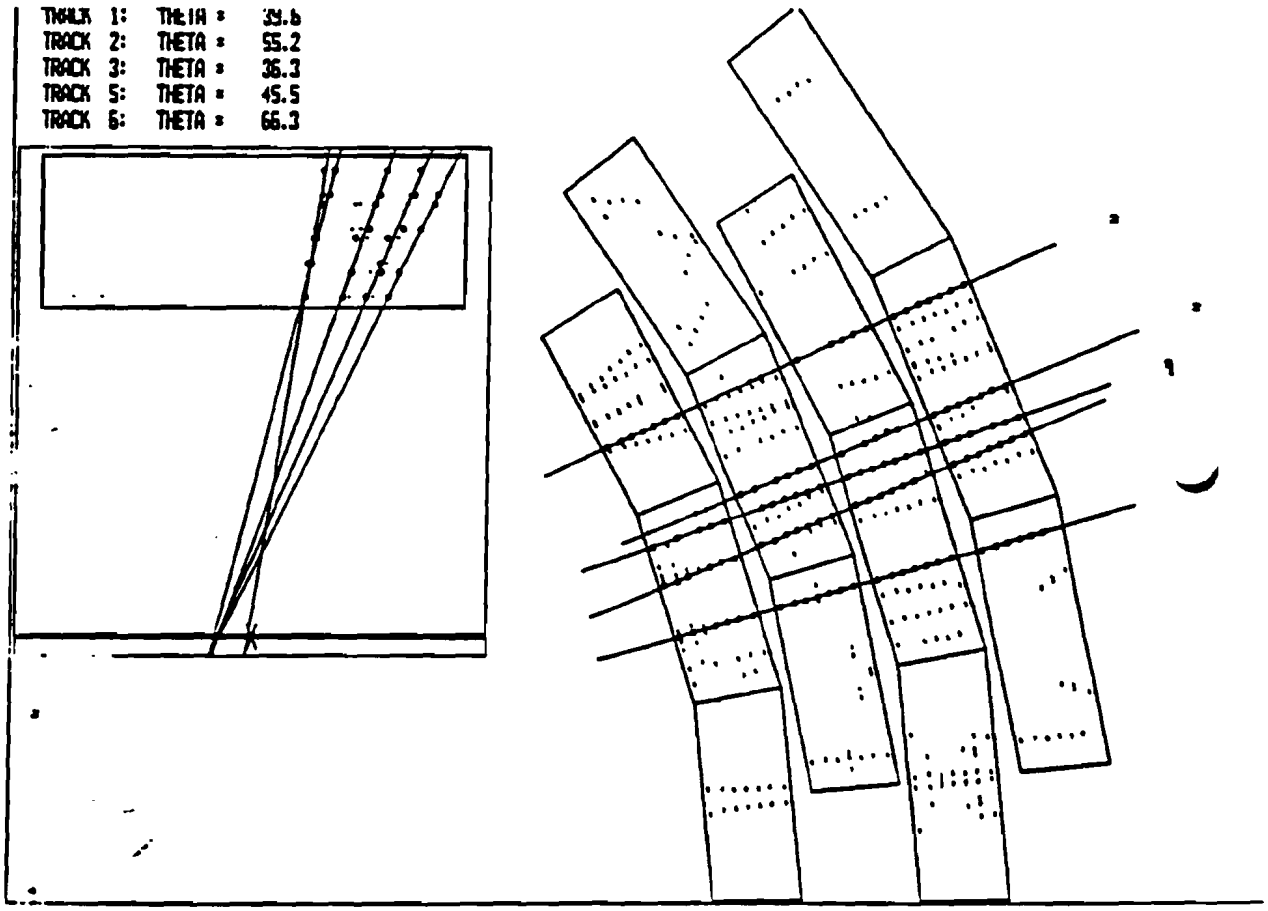

Figure 104 . A typical event display after the first pass cut

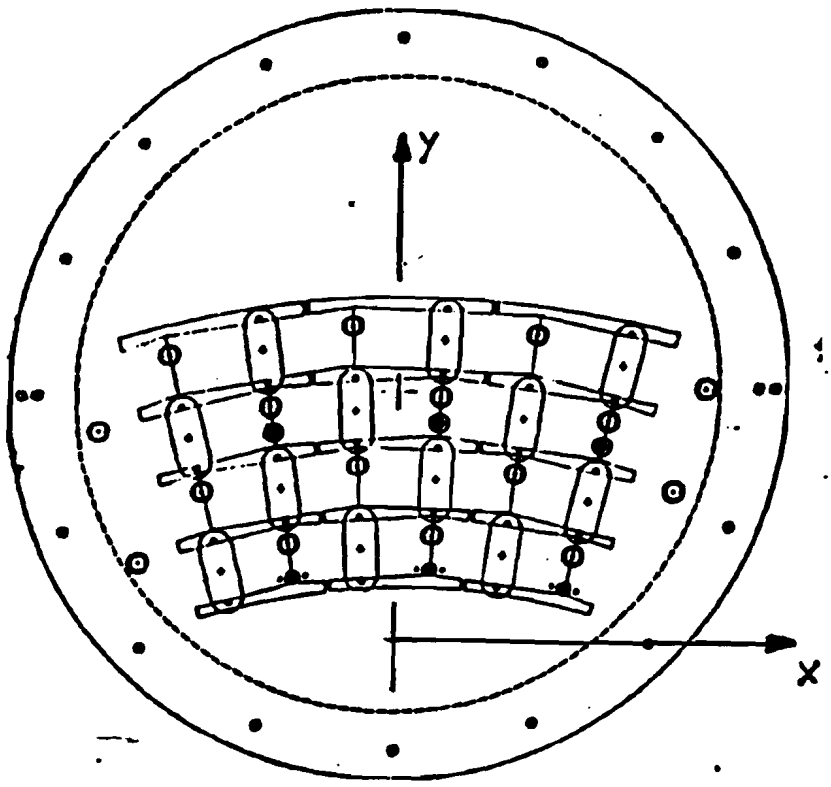

Figure 105 . Coordinate system used in calculating the vertex position

between the two tracks and stored in an array as well. If this distance is less than a limit, the z-tolerance, the two tracks are tagged as possible vertex track candidates. This procedure is repeated for every combination of two tracks in the event.

Once all tracks are processed a list is made which gives for every track tagged as a vertex track candidate the number of neighbours in z which are within the z-tolerance. The track which has the most neighbours is chosen and all the neighbour tracks which are listed with this track, are identified as participating in a real vertex.

The actual vertex position is calculated differently for the $r-\Phi$ projection and for the $r-z$ projection. For the $r-\Phi$ view a fit is done to find the point in the plane which is simultaneously the closest to all the tracks participating in the vertex. This is done by maximizing the Probability:

$$P = \prod_{i=1}^{N} e^{\frac{-d_i^2}{2\sigma^2}} \qquad (13-1)$$

where d_i denotes the distance between the $i-th$ track and the common point (x,y), and sigma is assumed equal for all tracks. The distance between a point and a track

given by the equation $y = mx + b$ is given by:

$$d_i = \frac{|m_i x - y + b_i|}{\sqrt{1 + m_i^2}} \qquad (13-2)$$

The point of common closest approach is then calculated by the following equation:

$$\begin{aligned} y &= \frac{a_1 c_2 - a_2 c_1}{a_2 b_1 - a_1 b_2} \\ x &= -\frac{c_2 + b_2 y}{a_2} \end{aligned} \qquad (13-3)$$

where the coefficients are given by :

$$\begin{aligned} a_1 &= \sum \frac{m_i^2}{1 + m_i^2} \quad & b_1 &= \sum \frac{m_i}{1 + m_i^2} \quad & c_1 &= \sum \frac{m_i b_i}{1 + m_i^2} \\ a_2 &= \sum \frac{m_i}{1 + m_i^2} \quad & b_2 &= \sum \frac{1}{1 + m_i^2} \quad & c_2 &= \sum \frac{b_i}{1 + m_i^2} \end{aligned} \qquad (13-4)$$

For the z-vertex this approach can not be used. A point of common closest approa to all participating tracks in the $r-z$ projection is not necessarily the best 3-d vertex. This is because in the process of projecting the tracks into the $r-z$ plane they are not only rotated but also shifted if the are not lying in the plane. Spurious vertices will show up in the display which are not present in reality. To circumvent this problem, the distances between any two z-tracks obtained at the point of the xy vertex are used. The simple average of these values is calculated and is called the vertex position.

13.7.4. Sources for error on the vertex calculation

Two main phenomena contribute to an uncertainty of the calculated vertex position. The chamber has an intrinsic measurement error which will limit the precision with which the vertex can be calculated. Secondly material in front of the chamber will multiple scatter the tracks and broaden the vertex distribution as well.

The quantities measured on a track are the center of gravity in $r-\Phi$ and in $r-z$ and the two angles Φ and Θ. The errors on these quantities are known from the fitting routines. Using the error propagation law the error on the two track intersection in two dimensions can be calculated. With $x = m_i y + b_i$ one finds after some algebra:

$$
\begin{aligned}
\sigma_x^2 &= \left(\frac{m_1+m_2}{m_1-m_2}\right)^2 \sigma_{y0}^2 \\
&+ \frac{1}{(m_1-m_2)^4}\{(m_1^2+m_2^2)(x_1-x_2)^2 - 2(x_1-x_2)(y_1-y_2)(m_1^3-m_2^3) \\
&+ (y_1-y_2)^2(m_1^4+m_2^4)\}\sigma_m^2 \\
\sigma_y^2 &= \frac{m_1^2+m_2^2}{(m_1-m_2)^2}\sigma_{y0}^2 \\
&+ \frac{1}{(m_1-m_2)^4}\{2(x_1-x_2)^2 - 2(m_1+m_2)(x_1-x_2)(y_1-y_2) \\
&+ (m_1^2+m_2^2)(y_1-y_2)^2\}\sigma_m^2
\end{aligned}
\qquad (13-5)
$$

A special case is the one when the two tracks are symmetric about the x-axis ($m_1 = -m_2$). This corresponds to the sightly idealized situation discussed above, where the vertex can be measured most precisely in a direction perpendicular to the symmetry axis of the chamber. In this case the y direction is the one which may be measured most precisely. For this special case the equation simplifies considerably:

$$
\begin{aligned}
\sigma_x^2 &= \frac{1}{8m^2}((x_1-x_2)^2 + m^2(y_1-y_2)^2)\sigma_m^2 \\
\sigma_y^2 &= \frac{1}{2}\sigma_{y0}^2 + \frac{1}{2m^4}\{(x_1-x_2)2 + m^2(y_1-y_2)^2\}\sigma_m^2
\end{aligned}
\qquad (13-6)
$$

For a hit in the center of the chamber ($y0 = 55cm, x0 = \pm 10cm$), and an $\sigma_{y0} = 200\mu m, \sigma_m = 0.002$, one finds

$$\sigma_x = 0.08cm$$
$$\sigma_y = 0.46cm$$

It is interesting to note, that $\sigma_x/\sigma_y = 6$ for tracks with an opening angle of 20°.

The effect of multiple scattering may be estimated with the following formula describing the width of the anglular distribution after multiple scattering as [56]:

$$\Theta_0 = \frac{14.1MeV/c}{p\beta} Z_{inc}\sqrt{\frac{L}{L_R}}[1 + \frac{1}{9}\log(\frac{L}{L_R})] \qquad (13-7)$$

where p is the momentum of the particle (in MeV), β its velocity in units of c and Z_{inc} its charge number, L/L_R the thickness of the scattering medium in radiation length. This formula assumes that the angles after the scattering are gaussian distributed. This is not exactly true, in particular at low energies the distribution has non gaussian tails. For an estimate of the magnitude of the effect however Eq.(13- 7) is adequate.

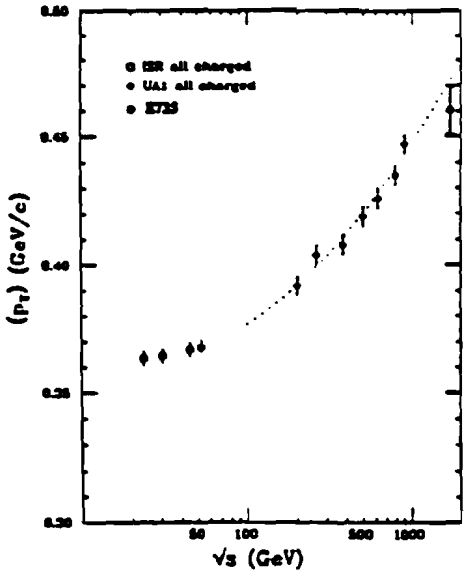

Figure 106 . Average transverse momentum of charged particles as a function of center of m energy

To calculate the multiple scattering angle for the premod a measurement of CDF was used to determine the average transverse momentum for minimum bias particles at 1.8Tev. Fig. [106] shows a plot of the average transverse momentum of charged particles as a function of the center of mass energy [57]. From this the average p_T is found to be 460 MeV at 1.8 TeV.

The following table lists the contributions of the different materials found in front of the chamber:

Material	D/cm	L/L_R	$\Theta_0/^\circ$	σ/cm
1" glass (monopole)	5	0.2	0.78	0.1
1" Scintillator (monopole)	10	0.06	0.4	0.09
1/16" SS Monopole skin	13	0.09	0.5	0.1
1/4" Trigger counter	20	0.02	0.15	0.05
1/4" Trigger counter	30	0.02	0.15	0.08
3/16" Al- drum (premod)	45	0.05	0.4	0.31

Table 1
Material in front of the premod, thickness in radiation length and contribution to the vertex smear due to multiple scattering. D is the distance between the beam and the material

If one adds all the individual contributions in quadrature the resulting sigma is

$$\sigma_{total} = 0.36cm$$

due to multiple scattering. This shows that multiple scattering is the dominant effect and will limit the accuracy of the vertex measurement.

13.7.5. Results

Of the 43535 raw triggers in run 3583 and the 19902 triggers in run 3584 1207 and 545 respectively passed all the cuts. This corresponds to 2.8% of the data sample. Fig. [107] shows the distribution for the three views of the vertex. A gaussian fit was done to the distributions with the following results:

View	Average position/cm	σ/cm	χ^2/N
x	-0.43 ± 0.02	0.40 ± 0.1	1.40
y	-0.9 ± 0.1	2.9 ± 0.1	1.82
z	4.5 ± 1.0	30.8 ± 0.6	1.10

The results are compatible with the expected errors discussed in the previous section. A σ_x of 0.404 cm has to be compared to an error due to multiple scattering of 0.34 cm. The measured width in y is $7.5 * \sigma_x$ as opposed to a predicted ratio of 6. However this prediction was calculated for an ideal track opening angle of 20°. In reality smaller angles will contribute as well and increase the error in y.

The width of the vertex distribution in z of 31 cm agrees with measurements done by other experiments at the tevatron during the last run [58].

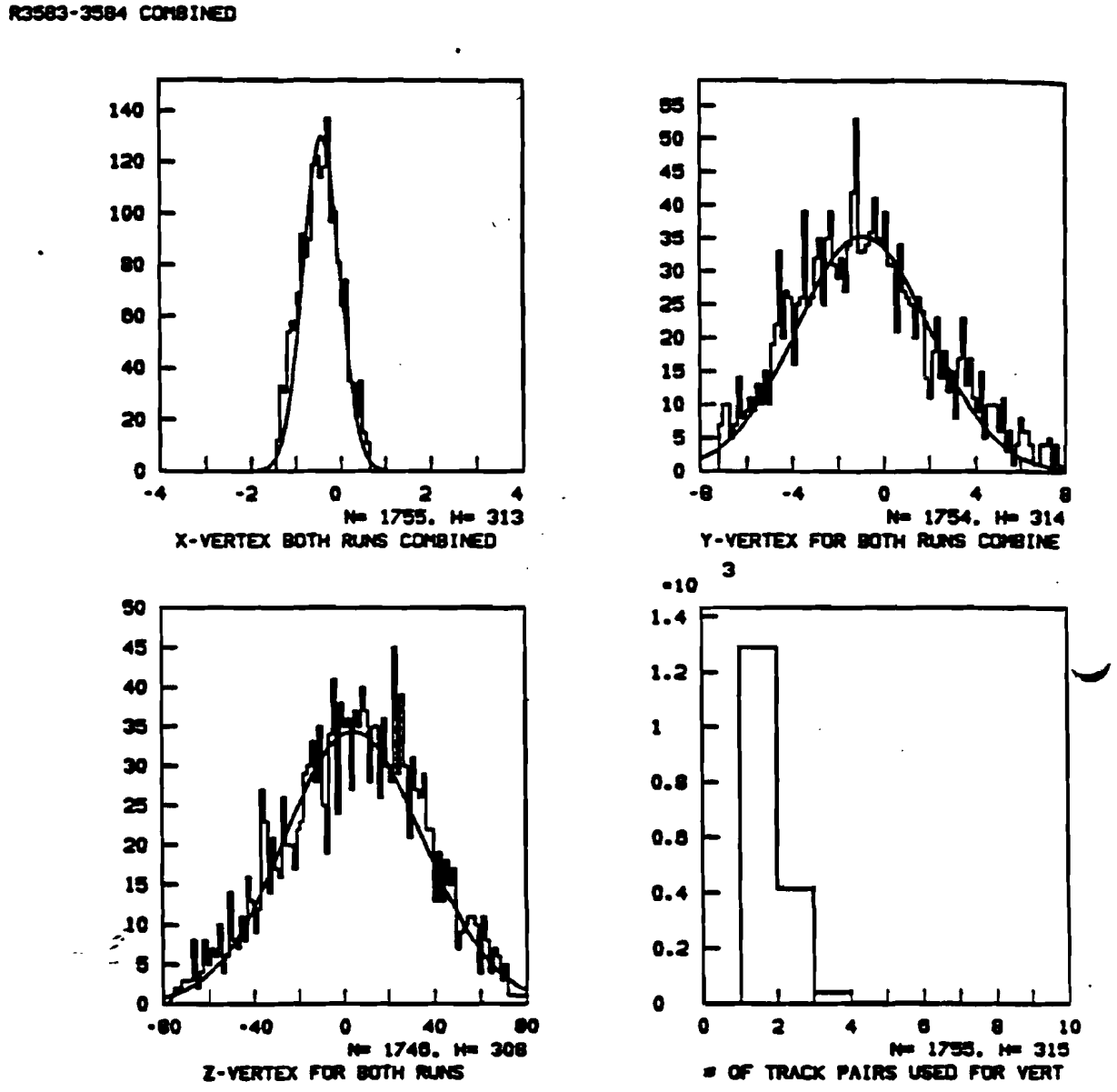

Figure 107 . Vertex distributions for run 3583 in x, y, and z, and number of pairs of tracks participating in the reconstruction of the vertex

13.7.6. Conclusion

The premod has been operated in the $p - \bar{p}$ collider at Fermi Lab for a number of month. During this time no problems with the chamber were found. Using the data from the last part of the run a reconstruction of the vertex was done. It was found that about 5% of all events reconstructed a complete vertex in space. The measured dimensions of this vertex are consistent with measurements of other groups (z-distribution) or can be explained by multiple scattering (x-vertex) or by geometric effects together with multiple scattering (y- vertex). It has been shown that the CDC chamber design is capable of operating reliably in a collider environment, that the chamber efficiently can measure tracks even in a high noise environment and that a stable operation over extended periods of time is possible.

List of References

[1] R. Raja Theoretical Implications of the W-Z mass difference and the capabilities of the DØdetector in measuring it *Proceedings of the $p - \bar{p}$ workshop in Fermilab, 1988*

[2] J.D.Jackson Classical Electrodynamics *John Wiley & sons 1975, p 685f*

[3] P. Grannis Specifications of the DØdetector *DØnote 560*

[4] Paul Grannis The DØdetector at the Fermilab collider *DØnote 558 1987*

[5] A. Zylberstein The transition radiation detector for the DØexperiment *proceedings from the $p - \bar{p}$ workshop 1988, p482*

[6] A.R.Clark et.al. A high precision drift chamber for DØ *NIM A261 (1987) 420*

[7] B. Gobbi et.al. The DØforward drift chamber *DØnote unpublished*

[8] SLD group SLD design report *SLAC report 273, May 1984*

[9] B. Hubbard Jet fragmentation properties at CDF *Proceedings ogf the $p - \bar{p}$ workshop 1988*

[10] G.Charpak et al The use of Multi Wire Proportional Chambers to select and localize charged particles *NIM 62,235 (1968)*

[11] e.g. G.Charpak et. al Some features of large Multi Wire Proportional Chambers *NIM 97,377 (1971)*

[12] G. Marel Large planar drift chambers *NIM 141, 43 (1977)*

[13] see e.g. W Bartel et.al. *Phys. Lett. 87b, 171 (1979)*

[14] see e.g. H. Drumm et.al. Experience with the Jet chamber of the Jade Experiments at Petra *NIM 176, 333 (1980)*

[15] Al Clark et.al. Test results from a high precision Drift Chamber *DO note 562*

[16] K Kleinknecht Detektoren für Teilchenstrahlung *Teubner Studienbücher 1984*

[17] Tom Ferbel, editor Experimental Techniques in High Energy Physics, especially the articles by K. Kleinknecht and F. Sauli *Addison Wesley 1987*

[18] H.A. Bethe *Annalen der Physik 5, 325 (1930)*

[19] L.D. Landau *J. Exp. Phys (USSR) 8,201 (1944)*

[20] V. Palladino, B.Sadoulet Application of classical theory of electrons in gases to drift proportional chambers *NIM 128, 323 (1975)*

[21] L. Malter *Phys.Rev. 50, 48 (1936)*

[22] Mark II note *unpublished*

[23] see e.g. Parker Seals O-ring reference guide *Parker technical publication ORD 5703*

[24] Riccardo De Salvo et.al. The CLEO wiring system *Note and private communications*

[25] Jim Cochran, Michael Rijssenbeek A computer based system to measure wire tensions in drift chambers *DØnote unpublished, 1989*

[26] SLD group SLD design report *SLAC-Report 273, May 1984*

[27] Camilleri et.al. A system of cylindrical drift chambers in a superconducting solenoid *NIM 156 (1978)275-281*

[28] H. Krehbiel et.al Delay Line readout for Drift Chambers *NIM 156 (1978) 347-351*

[29] R. Grove et.al Phase compensated electromagnetic delay lines *NIM 99 (1972) 381-385*

[30] V.Radeka Second coordinate readout in drift chambers by charge division *IEEE Trans. Nucl. Sci. NS-26 (1979)*

[31] V. Radeka Signal, Noise and resolution in position sensitive Detectors *IEEE Trans. Nucl. Sci. NS-21 (1974) 51*

[32] Rohlix linear actuator *Zero Max industries, Minneapolis*

[33] Jim Cochran et.al. The Delay Line Calibration system *to be published as a DØnote*

[34] Michael Rijssenbeek et.al. 8 channel preamp hybrid based on the Fujitsu MB43458 quad charge amplifier *DØnote 563, 1987*

[35] Dough Howard DØshaper specifications *DØNote unpublished*

[36] G. Saewert et.al Central Tracking Detector flash A/D converter buffer circuit summary *DØnote 669*

[37] D. de Groot DØCentral Tracking zero suppress chip description *DØnote 500*

[38] J Vav'ra Measurement and Simulation of the drift pulses and resolution in the micro-jet chamber *NIM 217,322 (1983)*

[39] G. Erskine Electrostatic Problems in Multiwire Proportional Chambers *NUM 105 (1972)565-572*

[40] T.J. Killian Accurate Computer simulation of a drift chamber *BNL-28160, CERN/EP-800-35*

[41] Alan Weinstein Some results from the drift chamber electrostatics program *MARK II/SLC note 66, March 1984*

[42] Wlodek Guryn and Irvin Sheer Drift chamber simulator *BNL-TN 84 March 1984*

[43] Mathieson et.al. Induced charges in a multi wire proportional chamber *NIM 154(1978) 189-191*

[44] Tom Trippe Minimum tension requirements for Charpak wire chamber wires *CERN NP internal report 69-19*

[45] Matteo Carcano Masters thesis *unpublished 1986*

[46] D. Buchholz et.al. The Use of Waveform Digitizers with Drift Chambers for DØ *NIM A257(1987)556*

[47] B. Good et.al Proceedings from the Summer 1986 Brown DØworkshop *DØnot 471, 1986*

[48] Qizhong Lee Demarteau CDC Tests in cosmic rays *DØnote 760, 9/28/88*

[49] Ralph Bilger Measuring drift velocities with a drift chamber *Stony Brook HEG internal note, 1988*

[50] S. D. Protopopescu User's guide to the DØUSER program *DØnote 476 1988*

[51] J. Hoftun Compack, a command input package for interactive programs, programmer's manual *DØnote 543 1987*

[52] Opal Optimization of a pulse finding algorithm *Opal note unpublished*

[53] Particle Data Group Review of particle properties *PYLBA 204, 1-486(1988)*

[54] Frank Turkot, E731 *private communication*

[55] Dave Cutts et.al. DØdata acquisition system *DØnote unpublished*

[56] Particle Data Group Review of particle properties *PYLBA 204, 1-486(1988)*

[57] J.D.Dowell Inclusive physics results from the UA! experim